MND1 and PSMC3IP control PARP inhibitor sensitivity in mitotic cells

Anabel Zelceski

2023

The Institute of Cancer Research
University of London

Submitted for the degree of Doctor of Philosophy

Abstract

The PSMC3IP-MND1 complex stimulates the formation of D-loops during meiosis in both yeast and mammals by facilitating the recombinases' DNA strand exchange activity. Surprisingly, genome-scale CRISPR-Cas9 mutagenesis and interference screens in mitotic cells revealed that depletion of either *PSMC3IP* or *MND1* led to sensitivity to clinical Poly (ADP-Ribose) Polymerase inhibitors (PARPi). Additionally, a retroviral mutagenesis screen in mitotic cells identified *PSMC3IP* and *MND1* as genetic factors for ionising radiation (IR) sensitivity. Depletion of either *PSMC3IP* or *MND1* led to an accumulation of toxic RAD51 foci in response to DNA damage, a reduction in homology-directed DNA repair, and sensitivity to PARPi. Despite replication fork reversal also being affected, the disrupted D-loop formation could be the major cause of PARPi sensitivity; a *PSMC3IP* p.Glu201del D-loop formation mutant linked to ovarian dysgenesis was found to be ineffective in reversing PARPi sensitivity. These findings suggest that meiotic proteins like MND1 and PSMC3IP could play a greater role in determining the response to therapeutic DNA damage in mitotic cells.

Statement of contribution

I confirm that I designed and carried out all the work presented in this thesis with the following exceptions (I have acknowledged all contributions in the main text, as well as in the appropriate Figure legend):

Feifei Song (ICR) and Joseph Baxter (ICR) assisted with execution of the genome-wide CRISPRn and CRISPRi screens presented in Chapter 3. The CRISPR screens were designed by me, with the assistance of Rachel Brough (ICR). The analysis of these CRISPR screens was performed by colleagues in the ICR Bioinformatics department, Aditi Gulati and John Alexander. Aditi Gulati performed the quantile normalisation required to compare the results from multiple published CRISPR screens. I subsequently analysed the quantile normalised CRISPR screen data, as presented in Figure 3.12.

Feifei Song, Rachel Brough and Sandhya Sridhar (ICR) executed the additional CRISPR screen presented in Figure 3.11.

Paola Francica (University of Bern) designed and executed the HAP1 retroviral mutagenesis screen presented in Chapter 3. I performed the analysis of the HAP1 retroviral mutagenesis screen data, as presented in Chapter 3.

Rachel Brough (ICR) executed the drug sensitivity assays for characterisation of the cell models to be used for CRISPR screening purposes in Figure 3.3.

Chris Lord performed the analysis of the expression data presented in Chapter 4, which I subsequently plotted.

Dragomir Krastev provided advice for the generation of the cell models presented in Chapter 4, including AlphaFold modelling.

Paola Francica (University of Bern) generated and characterised (Figure 4.19) the murine cell models for MND1 deficiency. With the assistance of Lea Lingg and Merve Mutlu (University of Bern), these cell models for drug sensitivity assays (Figure 4.20, Figure 4.21C, D), immunofluorescence micronuclei detection (Figure 5.5), and PLA.

Colin Stock (University of Groningen) performed the DNA fibre assays using the cell models generated by Paola Francica (University of Bern).

Maya Raghunandan provided general scientific advice and contributed to project management of the work in this thesis.

Stephen J. Pettitt provided scientific advice in a supervisory capacity and contributed to project management of the work in this thesis.

Andrew Tutt and Chris Lord provided scientific advice in a supervisory capacity and contributed to project management of the work in this thesis.

Signature of candidate.....

Acknowledgements

I would like to thank my supervisory team, Prof. Chris Lord, Prof. Andrew Tutt and Dr Stephen Pettitt for their continued support during this Ph.D. I sincerely thank them for providing the opportunity to study under their guidance.

An additional thank you to everyone in the Gene Function and Target Validation and DNA Damage Response teams for providing an inspiring work environment during my PhD – as well as cake and badminton, sometimes.

Finally, I would like to thank my friends and family for their encouragement and support.

Table of contents

List of figures

List of tables

Abbreviations used

3AB	3-aminobenzamide
ALT	Alternative lengthening of telomeres
ART	ADP-ribosyl transferase domain
ATCC	American Type Culture Collection
ATM	Ataxia Telangiectasia mutated
ATR	Ataxia Telangiectasia and Rad3-related
AP	Apurinic/apyrimidinic
BARD1	BRCA1-associated RING domain protein 1
BER	Base excision repair
b.i.d.	*bis in die* (twice daily)
BLM	Bloom syndrome
BRCA	Breast and ovarian cancer associated
BrdU	Bromodeoxyuridine
BSA	Bovine serum albumin
BTR	BLM-Topoisomerase IIIα-RMI1-RMI2
CAT	Catalytic (domain)
CDK1	Cyclin dependent kinase 1
CDK12	Cyclin dependent kinase 12
cGAMP	Cyclic GMP-AMP
cGAS	Cyclic GMP-AMP (cGAMP) synthetase
CHEK1/2	Checkpoint Kinase 1/2
CHFR	RING finger domain protein
CHK1	Checkpoint Kinase 1
CHO	Chinese hamster ovary (cells)
CI	Confidence interval
CIdU	5-chloro-2'-deoxyuridine
CML	Chronic myelogenous leukaemia
CO	Crossover
CRISPR	Clustered Regularly Interspaced Short Palindromic Repeats
CRISPRi	CRISPR interference
CRISPRn	CRISPR mutagenesis
CRPC	Castration-resistant prostate cancer
crRNA	CRISPR RNA
CtIP	CtBP-interacting protein
DAPI	4',6-Diamidino-2-Phenylindole, Dihydrochloride
DBD	DNA-binding domain
dCas9	Catalytically-inactive Cas9
DDR	DNA damage response
DE	Drug-effect
DMEM	Dulbecco's Modified Eagle Medium

DMSO	Dimethyl Sulphoxide
DNA	Deoxyribonucleic Acid
DNA Polymerase Theta	Polθ
dNMP	Deoxyribonucleoside monophosphate
DNPH1	2′-deoxynucleoside 5′-monophosphate N-glycosidase
DSB	Double-strand DNA break
DSBR	Double-strand DNA break repair
dsDNA	Double-stranded DNA
DYNLL1	*Dynein light chain 1* protein
EGF	Epidermal growth-factor
EMA	European Medicines Agency
ES	Embryonic stem (cells)
EXO1	Exonuclease 1
FA	Fanconi's Anaemia
FBS	Foetal bovine serum
FCS	Foetal calf serum
FDA	Food and Drug Administration
FEN1	Flap endonuclease I
FFPE	Formalin-fixed paraffin embedded (FFPE)
FHA	Forkhead-associated (domain)
GFP	Green Fluorescent Protein
GTEx	Genotype-Tissue Expression (project)
H3K4me3	trimethylation of histone H3 on lysine 4
H3K36me3	trimethylation of histone H3 on lysine 36
HBOC	Hereditary breast and ovarian cancer
HD	Helical domain
HER2	Human epidermal growth factor receptor 2
HGSOC	High-grade serous ovarian cancer
HJ	Holliday junction
hmdU	Hydroxymethyl-deoxyuridine
HORMAD1	HORMA (Hop1, Rev7, Mad2)-domain protein
HR	Homologous recombination
HRD	Homologous recombination deficiency
HRR	Homologous recombination repair
HU	Hydroxyurea
IC	Inhibitory concentration
ICL	Inter-strand crosslink
IdU	5-iodo-2′-deoxyuridine
IMDM	Iscove's Modified Dulbecco's Medium
Indel	Insertion/deletion (mutations)

IR	Ionising radiation
ITPA	Inosine triphosphatase
KRAB	Krüppel associated box
LAM (PCR)	Linear Amplification Mediated (PCR)
LIG1	DNA ligase I
LIG3	DNA ligase 3
LOH	Loss of heterozygosity
MAD	Median Absolute Deviation
MAGeCK	Model-based Analysis of Genome-wide CRISPR/Cas9 Knockout
mCRPC	metastatic castration-resistant prostate cancer
MeiCT	Meiosis-specific cancer/testis
MHRA	Medicines and Healthcare products Regulatory Agency
MMC	Mitomycin C
MMEJ	Microhomology mediated end joining
MMR	Mismatch repair
MND1	Meiotic Nuclear Division Protein 1 Homolog
MOI	Multiplicity of infection
MRN	MRE11-RAD50-NBS1
mRNA	messenger RNA
MTD	Maximum Tolerated Dose
NAD	nicotinamide adenine dinucleotode
NBS1	Nibrin
NCO	Non-crossover
NER	Nucleotide excision repair
NGS	Next-generation sequencing
NHEJ	Non-Homologous End Joining
NLS	Nuclear localisation signal
NSCLC	Non-Small Cell Lung Cancer
OB	Oligonucleotide/oligosaccharide-binding
ORF	Open reading frame
ORR	Objective response rate
PAM	Protospacer Adjacent Motif
PAR	Poly(ADP-ribose)
PARG	PAR glycohydrolase
PARP1	Poly (ADP-ribose) polymerase 1
PARPi	Poly (ADP-ribose) polymerase inhibitor
PBST	PBS with tween-20
PCR	Polymerase Chain Reaction
PD	Pharmacodynamics
PDAC	Pancreatic ductal adenocarcinoma
PDX	Patient-derived xenograft

PFS	Progression free survival
PK	Pharmacokinetics
pptm	parts per ten million
PSMC3IP	PSMC3 Interacting Protein, HOP2
RER	Ribonucleotide excision repair
RF	Replication fork
RFP	Red fluorescent protein
RNA	Ribonucleic Acid
RNAi	RNA interference
ROS	Reactive-oxygen species
RPA	Replication protein A
RPM	Rotations per minute
RRA	Robust ranking aggregation
RT-qPCR	Quantitative Reverse Transcription Polymerase Chain Reaction
SCE	Sister chromatid exchange
SD	Standard deviation
SDSA	Synthesis-dependent strand annealing
SF	Survival fraction
sgRNA	Single-guide RNA
shRNA	Short hairpin RNA
siRNA	Short interfering RNA
SLX-MUS	SLX1-SLX4-MUS81-EME1
SRB	Sulphorhodamine B
SSA	Single-strand annealing
SSB	Single-strand DNA break
SSBR	Single-strand break repair
ssDNA	Single-stranded DNA
STING	Stimulator of interferon genes
T_0	Timepoint 0
T_1	Timepoint 1
TCA	Trichloroacetic acid
TIDE	Tracking of Indels by Decomposition
TIGAR	*TP53*-induced glycolysis and apoptosis regulator
TNBC	Triple-negative breast cancer
TOP1	Topoisomerase I
TPM	Transcripts per million
tracrRNA	Trans-activating CRISPR RNA
TSS	Transcriptional start site
UV	Ultraviolet
V	Volts
VCP	Valosin-containing protein

VE	Viability effect
VEGF	Vascular endothelial growth factor
VPR	VP64-p65-Rta
γH2AX	Histone H2A, Serine 139 phosphorylated
ZnF	Zinc finger (domain)

Work arising from this thesis

Publication:

Anabel Zelceski[1,2+], Paola Francica[3,4+], Lea Lingg[3,4], Merve Mutlu[3], Colin Stok[5], Martin Liptay[3], John Alexander[2], Joseph S. Baxter[1,2], Rachel Brough[1,2], Aditi Gulati[2], Syed Haider[2], Maya Raghunandan[2], Feifei Song[1,2], Sandhya Sridhar[1,2], Josep V. Forment[6], Mark J. O'Connor[6], Barry R. Davies[6], Marcel A.T.M. van Vugt[6], Dragomir B. Krastev[1,2], Stephen J. Pettitt[1,2*], Andrew N. J. Tutt[2*], Sven Rottenberg[3,4,7,8*], Christopher J. Lord[1,2]

[1]The CRUK Gene Function Laboratory and [2]Breast Cancer Now Toby Robins Breast Cancer Research Centre, The Institute of Cancer Research, London, SW3 6JB, UK.

[3]Institute of Animal Pathology, Vetsuisse Faculty, University of Bern, 3012 Bern, Switzerland

[4]Departement of Biomedical Research (DBMR), Cancer Therapy Resistance Cluster, University of Bern, 3012 Bern, Switzerland

[5]Department of Medical Oncology, University Medical Center Groningen, University of Groningen, Hanzeplein 1, 9713GZ, Groningen, The Netherlands.

[6]Oncology R&D, AstraZeneca, Cambridge, United Kingdom.

[7]Division of Molecular Pathology, The Netherlands Cancer Institute, 1066CX Amsterdam, The Netherlands

[8]Bern Center for Precision Medicine, University of Bern, 3012 Bern, Switzerland

(2023) "MND1 and PSMC3IP control PARP inhibitor sensitivity in mitotic cells." **Published in Cell Reports**

Presentation:

June 2021: Institute of Cancer Research annual conference, Royal Holloway, Egham. **Oral presentation:** "MND1 and PSMC3IP control PARP inhibitor sensitivity in mitotic cells." Anabel Zelceski[1,2+], Paola Francica[3,4+], Lea Lingg[3,4], Merve Mutlu[3], Colin Stok[5], Martin Liptay[3], John Alexander[2], Joseph S. Baxter[1,2], Rachel Brough[1,2], Aditi Gulati[2], Syed Haider[2], Maya Raghunandan[2], Feifei Song[1,2], Sandhya Sridhar[1,2], Josep V. Forment[6], Mark J. O'Connor[6], Barry R. Davies[6], Marcel A.T.M. van Vugt[6], Dragomir B. Krastev[1,2], Stephen J. Pettitt[1,2*], Andrew N. J. Tutt[2*], Sven Rottenberg[3,4,7,8*], Christopher J. Lord[1,2]

Chapter 1. Introduction

1.1. The DNA damage response

The human genome is constantly damaged by a variety of intrinsic or exogenous factors. For example, exogenous environmental sources of DNA damage include ultraviolet (UV) light (Wang & Smith, 1986) and ionising radiation (IR) (Ward, 1988). Intrinsic factors that cause DNA damage include the reactive-oxygen species (ROS) formed by oxidative respiration (Lindahl, 1993; Lindahl & Nyberg, 1972). If this DNA damage is not repaired, or if cells with persistent DNA damage continue to divide, the overall fitness of cells is compromised and/or faithful transmission of genetic material from parent to daughter cell is impaired (Jackson & Bartek, 2009). For example, breaks in both strands of the DNA double helix (DNA double-strand breaks, DSBs) can either lead to chromosomal translocations that alter the overall structure of the genome (Gaillard et al., 2015) or, in extreme cases, can stimulate the cell to enact a form of programmed cell death to prevent the transmission of damaged DNA to daughter cells (Roos & Kaina, 2006; Wyllie et al., 1980). Given the potentially critical effects of DNA damage, organisms have evolved a series of molecular processes that sense and repair DNA damage, collectively referred to as the DNA damage response (DDR) (Jackson & Bartek, 2009).

In broad terms, the DDR includes proteins that detect DNA damage (sensors), proteins that are stimulated by sensors to recruit additional proteins to the site of DNA damage (mediators or transducers) and proteins that enact the repair of the double helix, upon recruitment to the site of DNA damage (effectors) (Zhou & Elledge, 2000). In reality, many of the proteins involved in the DDR have multiple functions, for example acting as both sensor and transducer or transducer and

effector (Zhou & Elledge, 2000). For example, two key regulators of the DDR, the closely related kinases Ataxia Telangiectasia Mutated (ATM) and Ataxia Telangiectasia and Rad3-related (ATR) (Jackson and Bartek 2009), sense DNA damage and recruit DNA repair effectors to the site of damage by phosphorylating substrates (Lovejoy & Cortez, 2009). ATM is recruited to and activated at DSBs (Andegeko et al., 2001), while ATR is activated by a broad spectrum of DNA damage (examples of which will be discussed shortly in this thesis) in addition to DSBs (Lovejoy & Cortez, 2009). In addition to repairing DNA, multiple proteins within the DDR interact with proteins involved in distinct processes in the cell that are also critical to maintain cellular homeostasis. For example, ATM and ATR also instigate signalling pathways that either prevent the firing of latent DNA replication forks (RFs) or stimulate the stalling of the cell cycle (Banin et al., 1998; Tibbetts et al., 1999). The prevention of additional DNA replication and the stalling of the cell cycle, whilst not directly involved in DNA repair *per se*, allow DNA repair to occur prior to the normal progression of the cell cycle once repair is complete.

The range of different DNA lesions resulting from DNA damaging agents requires a diverse set of DNA repair processes for their repair. Specifically, DNA damage can manifest as breaks in one strand of the double helix (single-strand breaks, SSBs), breaks in both strands of the double helix (DSBs), the oxidation of bases (Demple & Harrison, 1994), the formation of covalent cross links between bases on one strand of the helix, (intra-strand crosslinks), or between those on opposing strands (inter-strand crosslinks), the imprecise replication of DNA leading to DNA base mismatches or the covalent linking of proteins or small molecules to the double helix. Matching this array of DNA lesions, a variety of ostensibly distinct

molecular processes has evolved including single-strand break repair (SSBR) (Caldecott, 2014) and double-strand break repair (DSBR) (Szostak et al., 1983) pathways, for repair of SSBs and DSBs, respectively. Details of DSBR will be discussed in detail in a subsequent section of this thesis. Base excision repair (BER) pathway (Lindahl, 1974) repairs base adducts and oxidative lesions that can occur upon base oxidation (Demple & Harrison, 1994). While inter-strand crosslinks are repaired with a dedicated DNA repair pathway, inter-strand crosslink (ICL) repair (Clauson et al., 2013), intra-strand crosslinks are repaired with nucleotide excision repair (NER), which also removes bulky lesions (Clauson et al., 2013; Sancar, 1996). Mismatch repair (MMR) repairs base mismatches that occur during replication (Modrich & Lahue, 1996). In brief, BER, NER and MMR pathways involve the excision of a damaged region and insertion of new DNA bases to fill the gap.

As well as maintaining the overall fitness of the cell, the DDR also acts as a barrier to tumourigenesis. Indeed, defective DDR, and the resulting genomic instability that it causes, are regarded as one of the characteristic hallmarks of cancer (Hanahan & Weinberg, 2011). Defective DDR can result in the accumulation of DNA lesions and increase the mutational burden, contributing to tumour evolution (Negrini et al., 2010). For example, many solid tumours exhibit either aneuploidy (an abnormal number of chromosomes) (Taylor et al., 2018), a structurally disordered genome (e.g. multiple copy number alterations, chromosome deletions, translations, etc.) and/or a relatively high mutation rate (Beroukhim et al., 2010; Zack et al., 2013). As such, it is suggested that the processes that maintain the

integrity of the genome, such as the DDR, might be dysfunctional in tumours (Loeb et al., 1974; Nowell, 1976).

The publication from Peter Nowell (Nowell, 1976) established the concept of tumour progression as a genetic evolution process governed by Darwinian principles of diversification and natural selection, referred to as clonal evolution. The clonal evolution model postulates a series of clonal expansions, dependent on the acquisition of oncogenic mutations which confer a fitness advantage (Fidler, 1978). As such, the mutant clones are able to outcompete and outgrow cells lacking the specific mutation, so clonal selection drives the expansion of subclones with distinct phenotypic traits and growth advantages (McGranahan & Swanton, 2017). The selection pressure exerted by the tumour microenvironment, therapeutic interventions, and immune responses further shape the clonal composition of the tumour, favouring the survival of subclones with specific advantageous features. As in nature, genetic diversity is essential for evolution in tumours. As such, DNA damage acts as a driver of genetic diversity, introducing random mutations, chromosomal rearrangements, and copy number variation, leading to tumour heterogeneity; the presence of diverse subpopulations of cancer cells within a tumour. In addition to genetic alterations, DNA damage can influence tumour heterogeneity through epigenetic modifications. DNA methylation patterns, histone modifications, and chromatin remodelling can be altered in response to DNA damage, leading to changes in gene expression patterns and cellular phenotypes (Marusyk et al., 2012). A major consequence of the tumour heterogeneity, which can be caused by a continuous cycle of DNA damage and repair, is the development of subpopulations of cancer cells with different growth

rates, migratory capacities, and responses to therapy (Marusyk et al., 2012). This heterogeneity poses challenges in clinical management, as certain subclones may acquire resistance to treatment while others remain sensitive, as such the survival and expansion of treatment-resistant subclones can lead to disease relapse and metastasis (Dagogo-Jack & Shaw, 2018). Moreover, the presence of diverse subpopulations can contribute to the failure of targeted therapies, as specific genetic alterations may only be present in a subset of cells (Lord & Ashworth, 2017).

Many of the high penetrance genetic disorders that are associated with cancer predisposition, such as Bloom's Syndrome (German, 1993; Wu & Hickson, 2003), hereditary breast and ovarian cancer (HBOC) (Miki et al., 1994; Wooster et al., 1995), and Fanconi's Anaemia (FA) (Schroeder & Kurth, 1971), are caused by deleterious mutations in genes that encode DDR proteins (e.g. the *BLM* (Wu & Hickson, 2002), *BRCA1* or *BRCA2* (Miki et al., 1994; Wooster et al., 1995), and the *FANC* family of proteins (de Winter & Joenje, 2009)). Many of the highly recurrent somatic gene mutations that are now known to be "driver" effects in cancer, i.e. those mutations that are required for tumourigenesis (Stratton et al., 2009) are in genes involved in the DDR; *BRCA1* and *BRCA2* are two such examples (Cancer Genome Atlas, 2012). Finally, many of the approaches successfully used to treat cancer work by exploiting DDR defects that exist in tumour cells, but are largely absent in normal cells. These approaches include radiotherapy, DNA damaging chemotherapy and more recently discovered targeted agents, such as Poly (ADP-ribose) Polymerase inhibitor (PARPi) (Lord & Ashworth, 2017).

1.2. Homologous recombination

Homologous recombination (HR) is a relatively error-free sub-pathway of DSBR, which mediates the exchange of genetic information between the broken region of DNA and identical or similar DNA sequences elsewhere in the genome (Szostak et al., 1983). HR is conservative, restoring the pre-damaged DNA sequence back at the site of the DSB. HR in somatic cells, summarised in Figure 1.1, aims to repair DNA damaged-induced DSBs on one chromosome by using the undamaged sister chromatid DNA as a template. Therefore, somatic HR occurs in S/G_2 phase, after chromosomes have been replicated and the sister chromatid generated (Kadyk & Hartwell, 1992). Although less favoured than the sister chromatid due to possible impact on genome integrity, homologous chromosomes can also be used as a template for HR (Johnson & Jasin, 2000). Aside from its role in the repair of DNA damage, HR is also used in meiotic cells, the process of which is summarised in in Figure 1.2. Meiotic HR aims to recombine homologous regions of DNA on paternal and maternal homologous chromosomes, as part of crossing over and the generation of genetic variation during gametogenesis (Baudat et al., 2013).

HR is distinct from other, more mutagenic, forms of DSB repair. These include non-homologous end joining (NHEJ), which involves direct ligation of broken DNA ends independent of sequence homology (Lieber, 2010), or microhomology mediated end joining (MMEJ), where DNA sequences with microhomology on either side of a DSB align as a prelude to DNA ligation (Kramer et al., 1994; Robert et al., 2009). Another form of DSB repair, single-strand annealing (SSA), involves the alignment and annealing of regions of homology on either side of the DSB (Lin et al., 1984). Although SSA successfully repairs the DSB, the intervening sequence

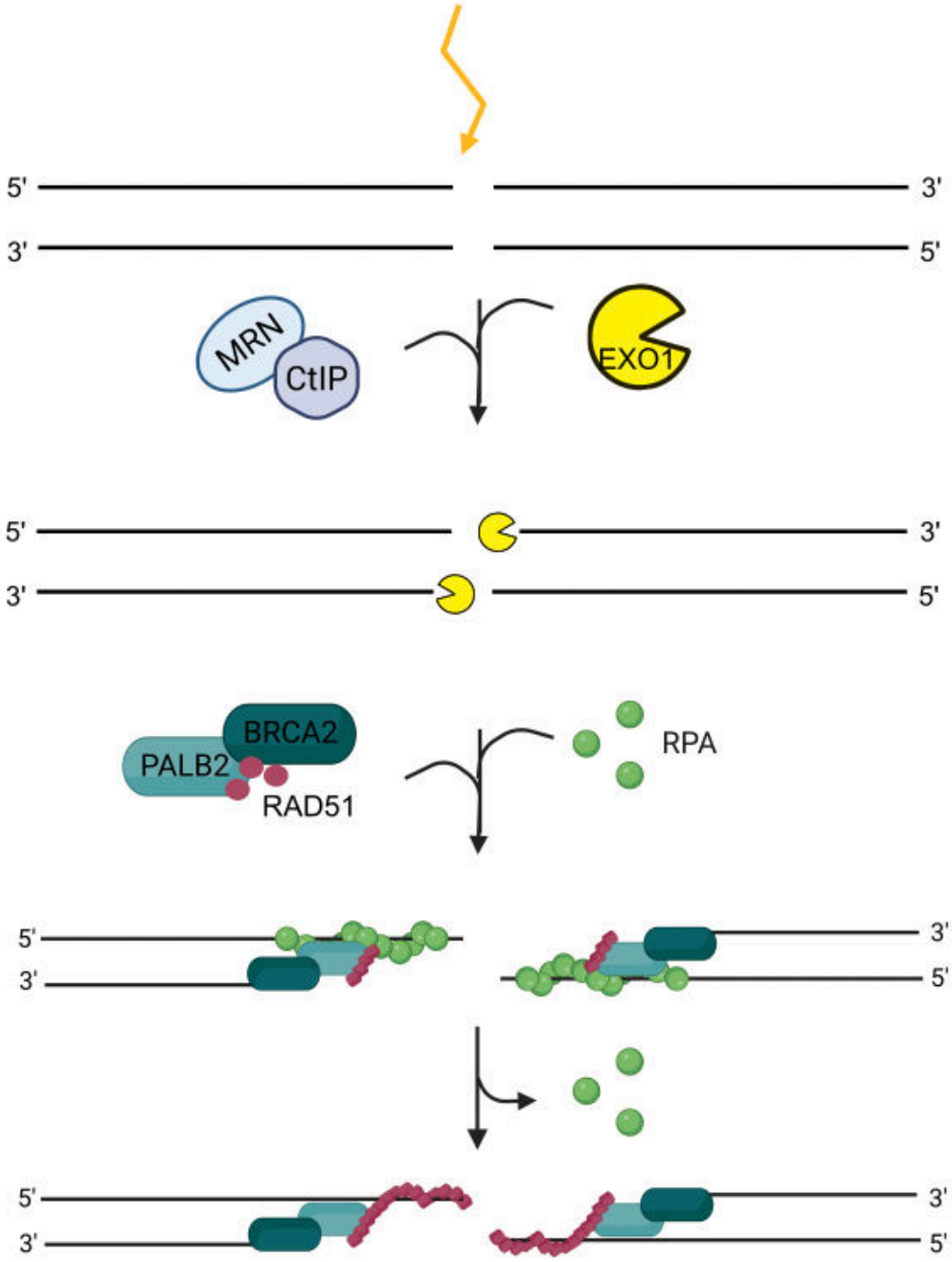

Figure 1.1 Simplified schematic of initial stages of somatic homologous recombination.
Somatic homologous recombination (HR) is initiated with resection of DNA ends at the DSB to generate a DSB with single-stranded DNA (ssDNA) overhangs via MRN-CtIP, then exonuclease 1 (EXO1). Replication protein A (RPA) rapidly coats and stabilises the resulting 3'-ssDNA to protect it from degradation. In order to terminate DNA end resection, RPA is replaced with the DNA recombinase, RAD51, by BRCA2, with the help of PALB2. RAD51 is required for the later homology search and strand invasion step of HR. Figure adapted from (Jiang & Chu, 2018).

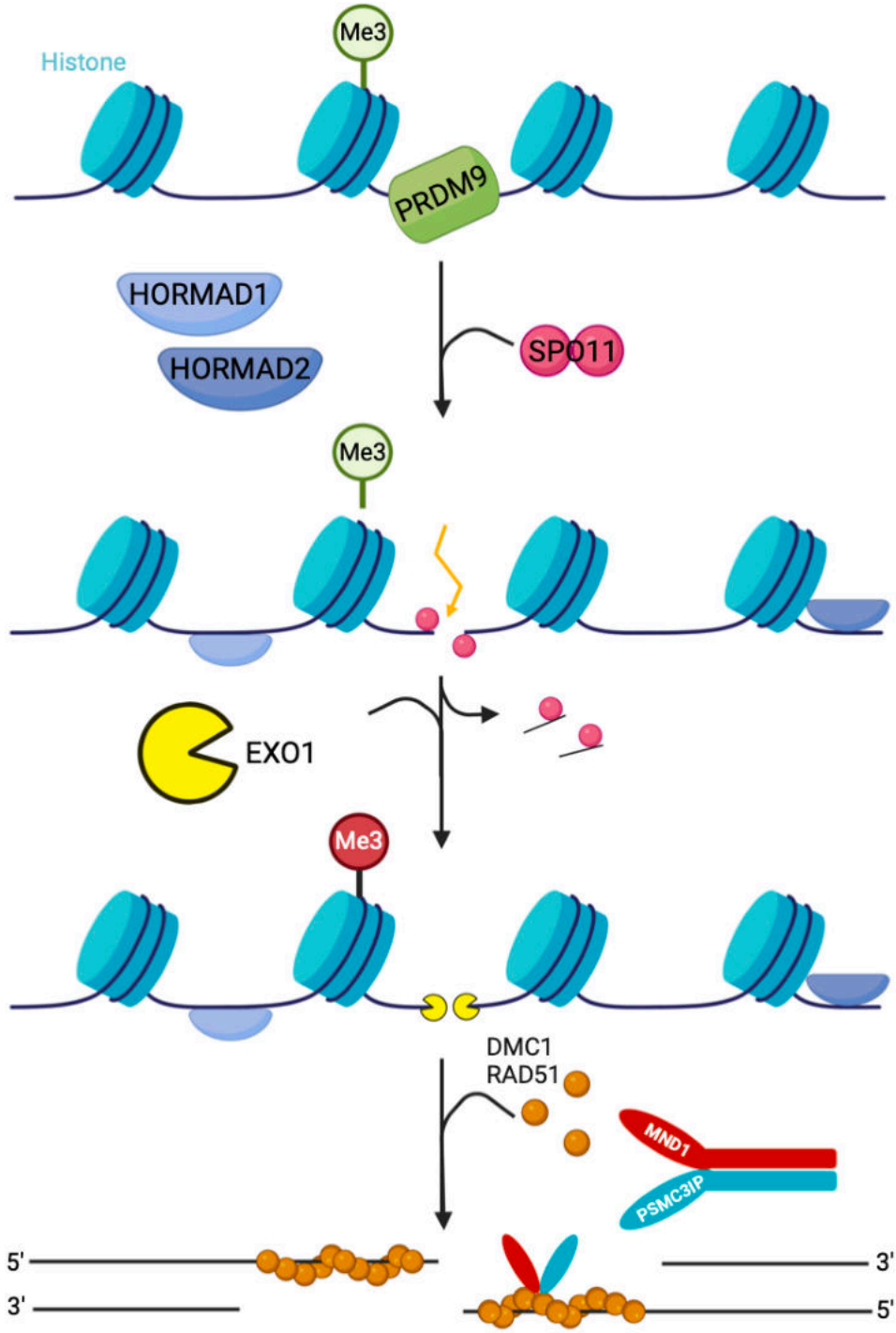

Figure 1.2 Simplified schematic of initial stages of meiotic recombination. Meiotic homologous recombination (HR) is initiated by programmed introduction of SPO11-mediated double-strand breaks (DSBs) (signified by yellow arrow). Target sites for DSB induction by SPO11, recombination hotspots, are marked epigenetically by PRDM9. DSB induction is further promoted by HORMAD1 and HORMAD2. Following exonuclease 1 (EXO1)-mediated resection of DNA ends, RAD51 and DMC1 DNA recombinases bind single-stranded DNA (ssDNA). As such, nucleoprotein filament can be formed, which recruits downstream factors to stimulate initiation of HR. PSMC3IP-MND1 heterodimer aids DSB resolution by promoting RAD51/DMC1-mediated homology search in meiotic HR. Figure adapted from (Sansam & Pezza, 2015) and (Feichtinger & McFarlane, 2019).

is deleted, which result in deletions between repetitive elements. In the case of DSBs occurring on more than one chromosome, chromosome translocations could even result from SSA (Richardson & Jasin, 2000). As such, mammalian cells with repetitive genomes would be at risk of genome instability with SSA. Although there are multiple sub-types of HR, including the classical DSBR sub-pathway (Szostak et al., 1983), and the synthesis-dependent strand annealing (SDSA) sub-pathway (Nassif et al., 1994), as summarised in Figure 1.3, the initial steps are similar. HR is initiated by resection of DNA ends at the DSB to generate a DSB with single-stranded DNA (ssDNA) overhangs. This DNA structure provides a platform for the recruitment of proteins required for HR, and also prevents loading of Ku70/Ku80 heterodimer onto the DNA ends, which are required for NHEJ (Lieber, 2010). As such, initiation of HR via resection blocks NHEJ. Following DNA damage, the MRN complex, which consists of three subunits MRE11, RAD50 and Nibrin (NBS1), is recruited to the DSB site and binds DNA via RAD50 (Lisby et al., 2004). BRCA1 tumour suppressor protein (described in detail later) further promotes HR by ubiquitylating CtBP-interacting protein (CtIP), which when also phosphorylated by cyclin dependent kinase 1 (CDK1), stimulates MRE11 endonuclease activity (Yun & Hiom, 2009). As CDK1-mediated phosphorylation of CtIP is restricted to S/G_2 phase, this ensures the availability of the sister chromatid for use as a DNA template (Sartori et al., 2007). MRE11 endonuclease activity generates a nick in double-stranded DNA (dsDNA), from which MRE11 3′-5′ exonuclease activity subsequently generates short (~100 nucleotides) 3′-ssDNA overhangs (Mimitou & Symington, 2008). MRE11 has limited exonuclease activity.

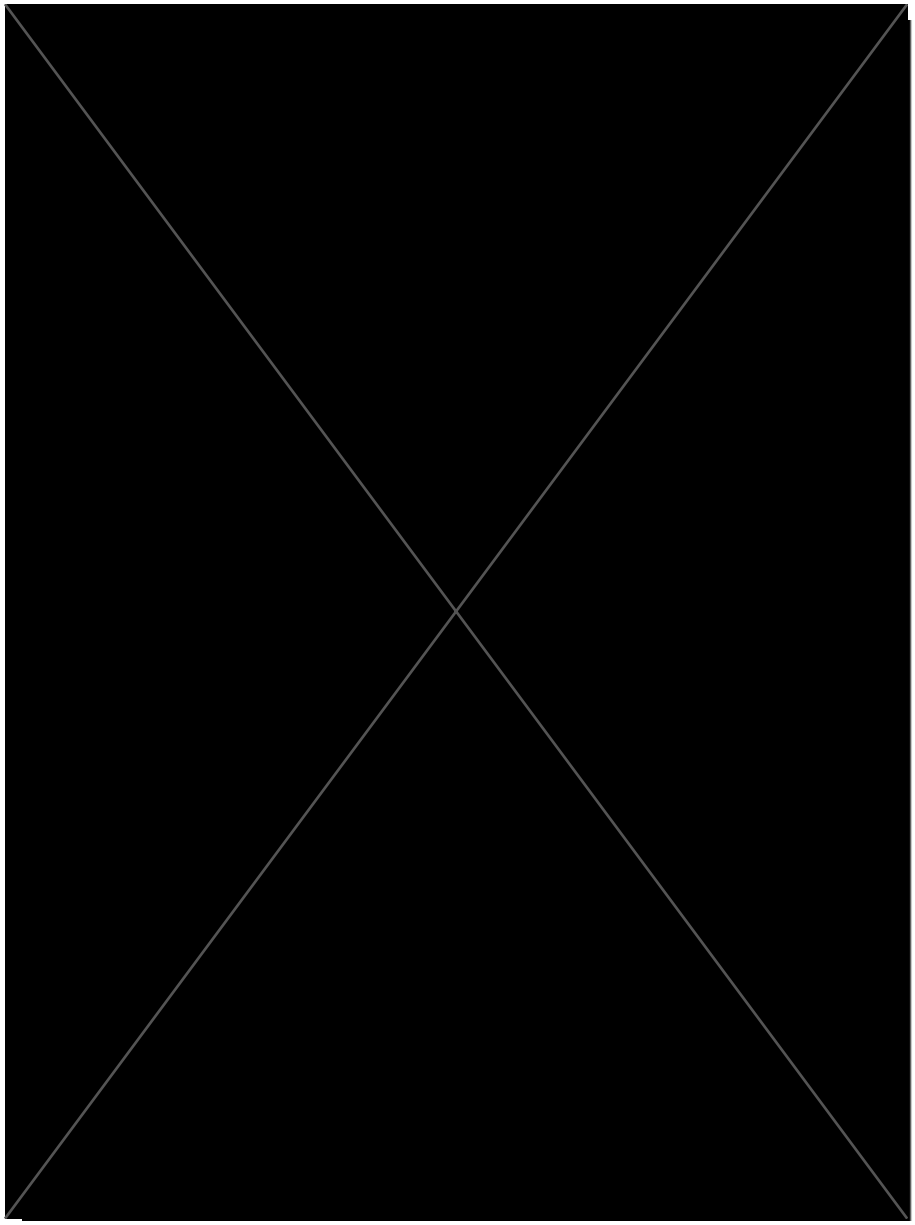

Figure 1.3 Schematic summarising the multiple sub-types of HR.
Following initial stages of homologous recombination (HR) comprising end resection, strand invasion and DNA synthesis (A), HR can either proceed via the synthesis-dependent strand annealing (SDSA, B) or the classical double-strand break repair (DSBR, C) sub-pathway. (A) Following DSB formation, the DNA ends are resected to generate 3'-single-stranded DNA (ssDNA) overhangs, which allows HR-related proteins to mediate homology search and strand invasion of the DNA template to form a nascent D-loop structure. This step is followed by DNA synthesis. (B) In SDSA, the D-loop is dissolved, i.e., the D-loop is unwound, and the freed ssDNA strand anneals with the complementary ssDNA strand associated with the other DSB end. Gap-filling DNA synthesis and ligation concludes SDSA, to generate only non-crossover products. (C) In DSBR, the second end of the DSB can be captured, via second end capture, to form an intermediate with two Holliday junctions (HJ)s. Gap-filling DNA synthesis and ligation concludes DSBR, to generate either non-crossover products, if dissolved (black triangles), or crossover products (grey triangles), if resolved with specialised endonucleases. Figure from (San Filippo et al., 2008).

The MRN complex, therefore, recruits exonuclease 1 (EXO1) and DNA2, which are indeed capable of generating the long 3′-ssDNA overhangs required for the later step of HR, involving strand invasion into a homologous template (Zhu et al., 2008). Unlike MRE11 or EXO1, which are capable of degrading single strands within dsDNA, DNA2 is only able to degrade ssDNA (Kao et al., 2004). As such, DNA2 requires helicase activity of Bloom syndrome (BLM) protein (Mimitou & Symington, 2008; Nimonkar et al., 2011) and Werner syndrome ATP-dependent helicase (WRN), another RecQ family helicase for DNA unwinding (Sturzenegger et al., 2014). Replication protein A (RPA) rapidly coats the ssDNA that is generated during DNA resection to protect it from degradation (Sugiyama et al., 1997). RPA also mediates checkpoint activation by ATR (Zou & Elledge, 2003), which functions to prevent the firing of latent DNA RFs or stimulate the stalling of the cell cycle (Tibbetts et al., 1999), as mentioned earlier in this thesis. In order to terminate DNA end resection, RPA needs to be removed to allow localisation of the DNA recombinase, RAD51, which mediates the subsequent step of HR; homology search and strand invasion into the homologous template (Sharan et al., 1997; Yang et al., 2002). RPA removal is regulated by BRCA2-DSS1 (Marston et al., 1999). DSS1 is a small (70 residues) and highly acidic protein that allows removal of ssDNA via ssDNA mimicry (Zhao & Sung, 2015). Furthermore, PALB2 plays a role in ensuring the proper localisation of BRCA2 through its interaction with the N-terminus of BRCA2 (Xia et al., 2006). BRCA2 interacts with DNA via its DNA-binding domain (DBD) and RAD51 via its BRC repeat domain, to facilitate the recruitment of RAD51 to the DSB to form RAD51-ssDNA filaments for strand invasion (Sharan et al., 1997; Yang et al., 2002). RAD51, in its ATP-bound form, undergoes a conformational change required for DNA binding via its N-terminus.

Once localised, RAD51 monomers bind to the ssDNA in a cooperative manner, forming small complexes of 2-5 monomers (Candelli et al., 2014; Hilario et al., 2009; van der Heijden et al., 2007). These initial complexes serve as nucleation sites for further RAD51 monomer binding. Only a subset of nucleation events result in productive outcomes, as only a fraction of short RAD51 clusters that initially bind to ssDNA in an unstable manner will undergo elongation through the addition of RAD51 subunits at the filament ends (Kowalczykowski, 2015). As more RAD51 monomers are added to the complex, a helical nucleoprotein filament structure begins to form on the ssDNA (Sharan et al., 1997). The filament grows in a 5'-3' direction, with RAD51 monomers aligning along the ssDNA. This assembly process is facilitated by the interaction between RAD51 and the BRC repeats of BRCA2, which act as a scaffold for filament formation (Sharan et al., 1997). BRCA2 also stabilises RAD51 filaments by protecting RAD51 filaments from premature disassembly and degradation (Sharan et al., 1997). The assembly of RAD51 into filaments is also influenced by various regulatory factors. Cyclin-dependent kinase 13 (CDK13) has been implicated in promoting RAD51 filament formation, via phosphorylation-mediated mechanisms (Quereda et al., 2019). E2F1, one of the E2F family members which regulate cell cycle progression, have also been observed to modulate RAD51 filament dynamics. E2F1 knockdown correlated with loss of RAD51 expression and RAD51-dependent DSB repair in colon cancer cell models (Choi & Kim, 2019). EGR1 (Hine et al., 2014) and p53 (Arias-Lopez et al., 2006) have also been identified as RAD51 regulators. RAD51 monomers are arranged into nucleoprotein filaments to allow homology search and strand invasion of the 3' overhang into the homologous template, yielding a DNA joint referred to as a D-loop (Sigurdsson et al., 2002).

The DSBR sub-pathway of HR proceeds with the engagement of the second end of the DSB, in a process referred to as second end capture, which is achieved either by a second independent invasion or DNA annealing to the displaced strand of the D-loop (Nimonkar & Kowalczykowski, 2009). RAD52 catalyses the annealing of the second end, via its unique ability to anneal complementary ssDNA bound to RPA (Sugiyama et al., 2006; Sugiyama et al., 1998). As a result, a joint DNA molecule comprising two Holliday junctions (HJ)s, is formed (Holliday, 2007), which requires removal prior to the onset of mitosis for faithful chromosome segregation (West et al., 2015). HJs can be "dissolved" by BLM-Topoisomerase IIIα-RMI1-RMI2 (BTR) complex, to promote the migration of the two HJs towards each other, giving rise to a hericenone (a conjoined DNA duplex) that can be processed by topoisomerase-mediated dissolution (Wu & Hickson, 2003). In the DSBR sub-pathway of HR, the HJs can alternatively be "resolved" by the SLX1-SLX4-MUS81-EME1 (SLX-MUS) complex (Wyatt et al., 2013) or GEN1 nuclease (Garner et al., 2013; Ip et al., 2008) to cut HJs (Figure 1.4B). Gap-filling DNA synthesis and ligation concludes the DSBR sub-pathway of HR. In the SDSA sub-pathway of HR, the D-loop is dissolved after DNA synthesis, whereby the D-loop is unwound, and the freed ssDNA strand anneals with the complementary ssDNA strand associated with the other DSB end (Orr-Weaver et al., 1981; Szostak et al., 1983). Gap-filling DNA synthesis and ligation concludes the SDSA sub-pathway of HR. Similarly to BTR-mediated dissolution of a HJ within the DSBR sub-pathway of HR, the D-loop dissolution within the SDSA sub-pathway of HR results in the two ends of the DNA break being re-joined to the original sister chromatid template; a "non-crossover event" (NCO) (Figure 1.4A). Although NCO are also possible with HJ resolution, mediated by either SLX-MUS or GEN1, within

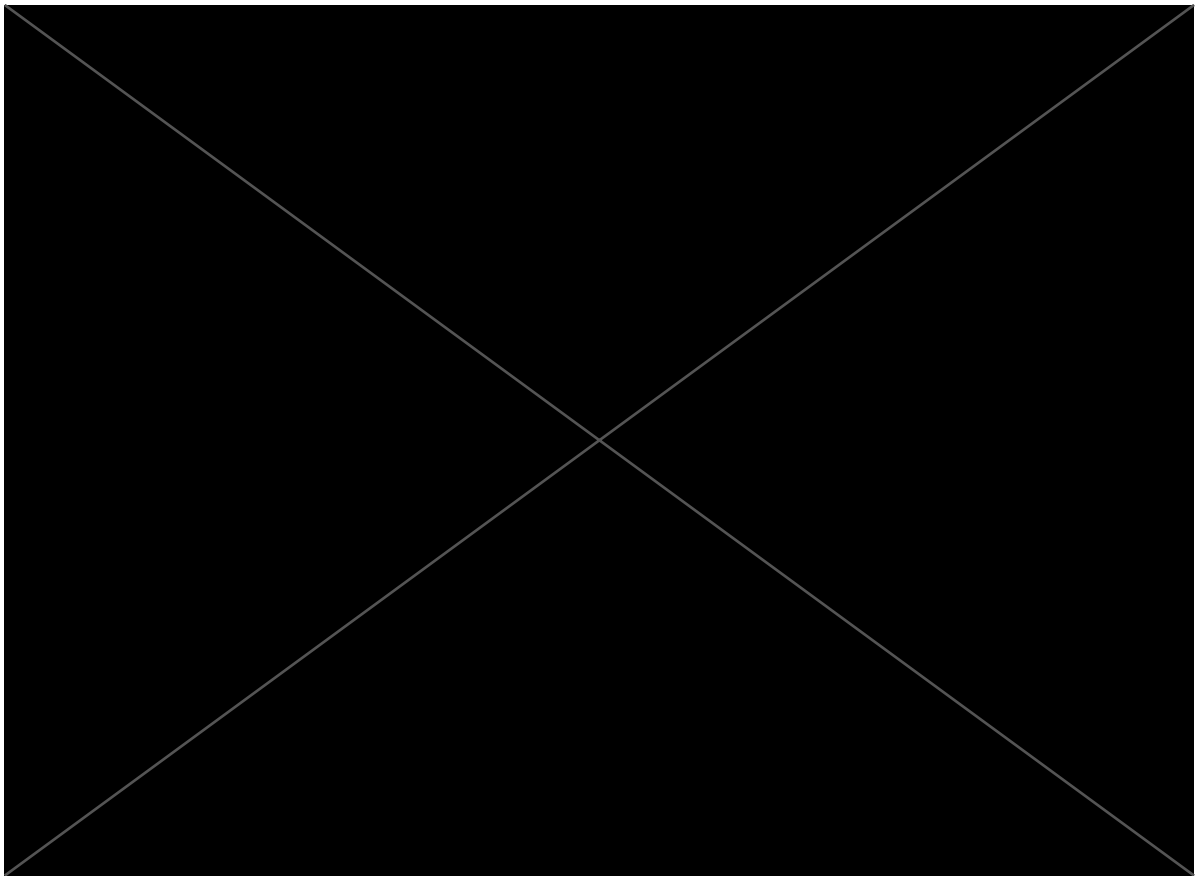

Figure 1.4 Simplified schematic for the processing of Holliday junctions (HJs). (A) Holliday junctions (HJs) can be "dissolved" by BLM-Topoisomerase IIIα-RMI1-RMI2 (BTR) complex, to promote the migration of the two HJs towards each other, giving rise to a hemicatenane (a conjoined DNA duplex) that can be processed by topoisomerase activity. Dissolution generates non-crossover (NCO) products, which avoids sister chromatid exchanged (SCE) and the potential for loss of heterozygosity (LOH) upon recombination between homologous chromosomes. (B) HJs can alternatively be "resolved" by the SLX1-SLX4-MUS81-EME1 (SLX-MUS) complex or GEN1 nuclease, which cut HJs. HJ resolution results in either NCO or crossover (CO) products. Figure from (West et al., 2015).

the DSBR sub-pathway, the DNA ends of opposing sister chromatids can also be re-joined, resulting in a “crossover event” (CO) or “sister chromatid exchange” (SCE) (Figure 1.4B). HR-mediated DNA repair between sister chromatids is genetically silent, even when associated with CO. However, despite their importance for meiosis, CO between chromosome homologs can result in loss of heterozygosity (LOH). As such, despite its reputation as an accurate form of DSB repair, HR can be mutagenic (Al-Zain & Symington, 2021). Given the risk to genome integrity from generating COs, the resolution pathways for HJ removal are tightly regulated to favour BTR-mediated dissolution in the DSBR sub-pathway of HR (Al-Zain & Symington, 2021). Despite the common outcomes of meiotic and mitotic HR, the exchange of genetic information between the broken region of DNA and identical or similar DNA sequences elsewhere in the genome, many factors are uniquely expressed in meiotic HR, as summarised in Figure 1.2. In contrast to the DNA lesions that occur sporadically in somatic cells, that require repair to minimise the risk of DNA alterations, DSBs are introduced in a programmed manner in meiotic cells to initiate the process of crossing over. PRDM9 mediates epigenetic marking of recombination hotspots (Grey et al., 2011; Parvanov et al., 2010; Powers et al., 2016), which are target sites for DSB induction by SPO11 (Neale & Keeney, 2006). The PRDM9 zinc-finger domain binds DNA, bringing the PR/SET domain in a conformation to allow the trimethylation of histone H3 on 189 lysine 4 (H3K4me3) and histone H3 on lysine 36 (H3K36me3), resulting in the disassembly of the nucleosomes and allows SPO11 binding (Grey et al., 2011; Parvanov et al., 2010; Powers et al., 2016). SPO11 tyrosine residue attacks DNA phosphodiester backbone, which ultimately disrupts the DNA backbone and introduces a break site (Keeney et al., 1997). Besides SPO11, which is the

catalytically active unit, IHO1, MEI4, MEI1 and REC114 are also required for DSB introduction (Libby et al., 2003; Kumar et al., 2018; Kumar et al., 2010; Stanzione et al., 2016); HORMA (Hop1, Rev7, Mad2)-domain protein HORMAD1 allows the recruitment of IHO1 (Stanzione et al., 2016). Similarly to somatic HR, the process of DNA end resection is then initiated, as previously described; the DNA ends at the DSB are resected to generate a DSB with ssDNA overhangs, which are in turn eventually bound by RAD51 (Sharan et al., 1997). In contrast with somatic HR, another DNA recombinase, DMC1, is also involved (Bugreev et al., 2011). As such, DMC1 is exclusively expressed in meiotic cells. As in the process of DNA recombination in somatic cells, BRCA2 is required for proper loading of DNA recombinases RAD51 or DMC1 (Sharan et al., 1997). RAD51 and DMC1 retain ~54% identical amino acid sequence in humans (Davies et al., 2001) and possess shared functions of mediating homology search and strand invasion in meiotic HR, as reported with strand exchange and strand assimilation (D-loop) assays (Baumann et al., 1996; Li et al., 1997). However, the catalytic activity of RAD51 is reportedly not required for the completion of meiosis, but rather has been suggested to facilitate the loading of DMC1 onto the ssDNA (Cloud et al., 2012). DMC1 functions as the predominant strand exchange protein during meiosis (Cloud et al., 2012) to promote strand invasion, recombination between homologous chromosomes and crossing over (Hong et al., 2013; Schwacha & Kleckner, 1997). RAD51 also functions to repair residual DSBs after recombination between homologous chromosomes and synapsis are complete (Cloud et al., 2012; Da Ines et al., 2013). In contrast to somatic HR, accessory proteins MND1 and PSMC3IP support RAD51 and DMC1 functions in meiotic HR. MND1 and PSMC3IP form a heterodimer complex, which acts in concert with RAD51 and

DMC1 to facilitate the homology search process (Chen et al., 2004; Tsubouchi & Roeder, 2002). The C-terminus of PSMC3IP-MND1 interacts with RAD51/DMC1 and PSMC3IP binds ssDNA to orchestrate the localisation of DMC1 on the ssDNA (Zhao et al., 2015), while the N-terminus of PSMC3IP-MND1 binds dsDNA to bring the chromosome homologs in close juxtaposition together (Chen et al., 2004; Pezza et al., 2007). As such, PSMC3IP-MND1 promotes recombination between homologous chromosomes, rather than sister chromatids, which is desired for meiotic recombination (Leu et al., 1998). This function of PSMC3IP-MND1 also condenses dsDNA surrounding the filament to enhance the homology search (Pezza et al. 2010). Overall, PSMC3IP-MND1 promote homology search and facilitates stabilisation of the nucleoprotein complex, which ultimately allows DSB resolution.

1.3. The DNA damage response in meiosis

As previously detailed, the DDR is a highly conserved mechanism that safeguards genome integrity by sensing, signalling, and repairing DNA lesions (Jackson & Bartek, 2009). While not as extensively studied as in somatic cells, the DDR in meiosis, the specialised cell division process responsible for gamete formation, is also important. Meiosis is a crucial biological process that ensures the faithful transmission of genetic material from one generation to the next, via production of genetically diverse and competent gametes (Zickler & Kleckner, 1999). The interplay between the DDR and meiosis is crucial for maintaining chromosomal stability and facilitating accurate genetic recombination. Besides ensuring faithful transmission of DNA by actively repairing DNA damage that arises during meiosis, the DDR also actively influences the meiotic recombination process by regulating

DNA repair pathways, with a predominant emphasis on HR (Hunter, 2015). HR facilitates the recombination of homologous regions of DNA on paternal and maternal chromosomes, as part of crossing over and the generation of genetic variation during gametogenesis (Baudat et al., 2013).

The DDR is also crucial for the initiation of meiotic recombination via DSB formation by SPO11 (Keeney et al., 1997). The DSB ends are resected to release SPO11 and generate a DSB with ssDNA overhangs, which are in turn bound by either RAD51 (Sharan et al., 1997) or meiosis-specific DMC1 (Bugreev et al., 2011), forming a helical presynaptic nucleoprotein filament. During meiosis, DMC1 functions as the predominant strand exchange protein (Cloud et al., 2012) to promote strand invasion, recombination between homologous chromosomes and crossing over (Hong et al., 2013; Schwacha & Kleckner, 1997). RAD51, on the other hand, functions to repair residual DSBs after completion of recombination and synapsis between homologous chromosomes (Cloud et al., 2012; Da Ines et al., 2013). Accessory proteins MND1 and PSMC3IP support the functions of RAD51 and DMC1 in meiotic HR. Early studies regarding *Hop2* and *Mnd1* genes (orthologs of the human *PSMC3IP* and *MND1,* respectively) were performed in yeast. Hop2 was found to be meiosis-specific (Leu et al., 1998), and subsequent studies showed that Hop2 forms a stable heterodimer with Mnd1 (Hop2-Mnd1); co-purification of Hop2 with affinity-tagged Mnd1 was observed independent of other proteins (Chen et al., 2004). Physical interactions between Hop2-Mnd1 and Dmc1 were demonstrated (Pezza et al., 2007), and later confirmed to also involve interactions with Rad51 via affinity pulldown experiments (Zhao et al., 2015). Zhao et al. further identified specific domains in Hop2 and Mnd1 responsible for the

interaction with Rad51 and Dmc1, showing that C-terminal deletions, but not N-terminal deletions, impaired the interaction (Zhao et al., 2015). Moreover, studies using DNA binding assays revealed that Hop2 and Mnd1 also bind DNA; Hop2 binds ssDNA through another C-terminus domain (Zhao et al., 2014), while Hop2-Mnd1 directly binds dsDNA (Chen et al., 2004), specifically at the N-terminus (Zhao et al., 2014). Together, these *in vitro* studies provide a functional model of PSMC3IP-MND1 function in meiotic recombination, where the C-terminus of PSMC3IP-MND1 interacts with RAD51/DMC1 and PSMC3IP binds ssDNA to orchestrate the localisation of DMC1 on the ssDNA (Zhao et al., 2015), while the N-terminus of PSMC3IP-MND1 binds dsDNA to bring the chromosome homologs in close juxtaposition together (Chen et al., 2004; Pezza et al., 2007). As such, PSMC3IP-MND1 promotes recombination between homologous chromosomes, rather than sister chromatids, which is desired for meiotic recombination (Leu et al., 1998). PSMC3IP-MND1 also condenses dsDNA surrounding the filament to enhance the homology search (Pezza et al. 2010). Overall, PSMC3IP-MND1 complex supports the functions of RAD51 and DMC1, facilitating homology search and strand invasion during meiotic recombination (Chen et al., 2004; Tsubouchi & Roeder, 2002).

Defects in the DDR during meiosis can result in profound consequences for chromosomal stability and gamete formation via persistent DNA lesions, genomic stability and aneuploidy (Hassold & Hunt, 2001). As previously detailed, SPO11 is a key protein involved in the initiation of meiotic recombination by generating DNA DSBs during meiosis; *SPO11* mutations can lead to impaired or deficient DSB formation during meiosis, disrupting the recombination process and compromising

genetic exchange between homologous chromosomes. Studies have demonstrated that infertility can arise from *SPO11* mutations. In mice, *Spo11* disruption results in lack of DSB formation (whereby no Rad51/Dmc1 foci were detected in meiotic chromosome spreads), and spermatocytes fail to undergo synapsis, so ultimately undergo apoptosis (Romanienko & Camerini-Otero, 2000). Preliminary studies have also indicated infertility in humans with *SPO11* mutation (Karimian et al., 2015). The infertility associated with *SPO11* mutations highlights the essential role of the activation of the DDR via the generation and repair of DSBs in ensuring the proper segregation of chromosomes and the generation of genetically diverse and competent gametes in meiosis. Without functional *SPO11*, the meiotic process is disrupted.

1.4. Cancer driver genes involved in homologous recombination

A number of the genes that encode proteins involved in HR and DSBR are recurrently mutated in human cancers. These are now considered as cancer driver genes that play “caretaker” roles, i.e., genes that contribute to the tumourigenic phenotype by maintaining the integrity of the genome (Kinzler & Vogelstein, 1997; Stratton et al., 2009). For example, *BRCA1, BRCA2, PALB2, RAD51C, RAD51D, BAP1, CDK12, ATM, FANCA, FANCC, FANCD2, FANCE, FANCF, NBS1, MRE11, BLM, BRIP1* are either somatically mutated in cancer, or are causative mutations in inherited disorders associated with a high degree of cancer predisposition (Lord & Ashworth, 2016).

Included in this list are *BRCA1* and *BRCA2*, originally identified by analyses of families at high risk of breast and ovarian cancer (Miki et al., 1994; Wooster et al.,

1995). *BRCA1* and *BRCA2* genes encode very large nuclear proteins of 1,863 and 3,418 amino acid residues, respectively. BRCA1 contains an N-terminal RING domain, nuclear localisation signals (NLSs), and two C-terminal BRCT domains of approximately 110 residues. Similarly to BRCA1, BRCA2 contains NLSs. BRCA2 also contains eight repeats of the ~40 residue BRC motifs. The fundamental roles of *BRCA1* and *BRCA2* within HR were initially established with the observation that mouse and human cells deficient for wild-type *BRCA1* or *BRCA2* demonstrated increased sensitivity to DNA lesions which rely on HR for their repair (Patel et al., 1998; Scully et al., 1999; Shen et al., 1998; Yu et al., 2000). BRCA1 N-terminal RING domain, interacts with BRCA1-associated RING domain protein 1 (BARD1) to form an E3-ubiquitin ligase (Hashizume et al., 2001), which mediates ubiquitylation of CtIP (Yun & Hiom, 2009). CtIP is involved in the initial DNA DSB resection step of HR through its association with the MRN complex (Lisby et al., 2004). CtIP also interacts with the two BRCT domains located at the C-terminus of BRCA1, which facilitate phospho-protein interactions. BRCA1-BARD1 interaction with the DNA recombinase RAD51 (Zhao et al., 2017), to promote RAD51-mediated homology search and strand (Sharan et al., 1997; Yang et al., 2002), indicates an additional downstream function of BRCA1 within HR. Following DNA end resection, and the resulting generation of 3′-ssDNA overhangs, BRCA1 coiled-coil domain (residues 1393–1424) binds N-terminus coiled-coil domain (residues 9-42) of PALB2 (Sy et al., 2009) which is bound to N-terminus BRCA2. Given that RAD51 is bound to BRCA2 via BRCA2 BRC repeats, and BRCA2 binds DNA via its DBD, RAD51 can be recruited to the DSB to form RAD51-ssDNA filaments for strand invasion. In contrast to the HR-specific function of BRCA2, BRCA1 possesses more diverse functions, such as in checkpoint activation

(Yarden et al., 2002). BRCA1 BRCT domains regulate the phosphorylation status, and consequential activation of CHK1, which partly regulates G_2/M checkpoint control.

The discovery that *BRCA1* and *BRCA2* contribute to cancer predisposition through roles in DNA repair originated from the observation of spontaneous chromosome aberrations in cells deficient in the murine *BRCA1* (Shen et al., 1998) or *BRCA2* (Patel et al., 1998) homologs. Similar observations were reported in human cancer cells deficient in either *BRCA1* or *BRCA2* (Tirkkonen et al., 1997). These observations established the function of BRCA1 and BRCA2 as caretakers which suppress genome instability. *BRCA1* and *BRCA2* contribution to cancer predisposition has also been reported clinically. *BRCA1* or *BRCA2* mutation carriers exhibit up to 80% risk of developing breast or ovarian cancer prior to reaching 70 years of age (Easton et al., 1995). The risk of ovarian cancer up to the age of 80 is 44% and 17% for *BRCA1* and *BRCA2* mutations carriers, respectively (Kuchenbaecker et al., 2017). The risk of breast cancer is also increased; 72% for *BRCA1* and 69% for *BRCA2* mutation carriers (Kuchenbaecker et al., 2017). A single defective copy of *BRCA1* or *BRCA2* is sufficient for predisposition of breast and ovarian cancers (Tutt & Ashworth, 2002; Tutt et al., 1999). Somatic loss of the remaining wild-type allele has been confirmed in primary breast tumours from individuals with *BRCA1* and *BRCA2* mutations (Collins et al., 1995; Cornelis et al., 1995; Merajver et al., 1995). In general, individuals with germline mutations in either *BRCA1* or *BRCA2* typically present with disease earlier in life, compared to those whose disease occurs sporadically (Lux et al., 2006; Petrucelli et al., 1993). In addition, the risk of developing prostate cancer for *BRCA1* mutation carriers is

8.6% by the age of 65 (Leongamornlert et al., 2012), while the lifetime risk of prostate cancer in *BRCA2* mutation carriers has been estimated to be 20% (Breast Cancer Linkage, 1999). Compared to the general population, a two- to three-fold increased risk of pancreatic cancer has been estimated in *BRCA1* mutation carriers (Stadler et al., 2012; Thompson et al., 2002). The estimated cumulative risk in *BRCA2* mutation carriers for pancreatic cancer by the age of 80 is 6.9% for males and 2.8% for females (van Asperen et al., 2005). 15-30% of all *BRCA1* and *BRCA2* mutations represent somatic mutations, which are only detected in tumour cells. Somatic *BRCA1* or *BRCA2* mutations have been associated with 3% of breast cancer cases (Winter et al., 2016), and over 12% of advanced prostate cancer cases (Decker et al., 2016). In a study containing 235 ovarian cancer cases, *BRCA1* or *BRCA2* somatic mutations were detected in 19% of patients (Hennessy et al., 2010).

1.5. PARP1 function

As I will describe later, one of the more recent advances in the treatment of *BRCA1/2*-associated cancer has been the discovery and development of small molecule inhibitors of a DNA repair protein, Poly (ADP-Ribose) polymerase 1 (PARP1), as a treatment for cancers with defects in HR.

PARP1 is a DNA-binding protein from the poly (ADP-ribosyltransferase) (ART) family (Luscher et al., 2022). Although multiple functions have been reported for PARP1, its role in DNA repair is the most well-studied (Fisher et al., 2007; Heale et al., 2006). As part of this process, PARP1 binds damaged DNA (Bramson et al., 1993; D'Silva et al., 1999; Weinfeld et al., 1997), having a particularly strong affinity

for apurinic/apyrimidinic (AP) sites, also known as abasic sites (Khodyreva et al., 2010). AP sites are one of the more frequent lesions in the genome, occurring >10,000 times per mammalian cell per day (Lindahl, 1993). DNA binding activates PARP1's catalytic activity; once active, PARP1 uses nicotinamide adenine dinucleotode (β-NAD+) to add multiple ADP-ribose units (originally termed "(ADP-ribose)n") onto substrate proteins, generating poly (ADP-ribose) chains (PAR), as part of the process of PARylation (Hilz & Stone, 1976; Luscher et al., 2021; Purnell et al., 1980). Early studies identified PARP1's function in the DDR by showing that DNA damaging agents decreased cellular levels of β-NAD+ and increased levels of PAR (Davies et al., 1978; Durkacz et al., 1980; Skidmore et al., 1979). This phenotype was reversed by toolbox PARP1 inhibitors, such 3-aminobenzamide (3AB) (Durkacz et al., 1980; Purnell et al., 1980). Inhibition of PARP1 activity with 3AB also enhanced sensitivity of cells to alkylating agents, such as dimethyl sulphate, which was reasoned to be caused by inhibition of PARP1-mediated DNA repair (Durkacz et al., 1980). A PARP1 "shuttle mechanism" was proposed, whereby PARP1 catalytic activity was originally attributed to its DNA binding and dissociation (Zahradka & Ebisuzaki, 1982).

When not bound to DNA, the catalytic activity of PARP1 is inhibited by an interaction between the autoinhibitory helical domain (HD) and the catalytic (CAT) domain (Dawicki-McKenna et al., 2015). When PARP1 binds DNA (which occurs via N-terminal zinc fingers (ZnF)), a conformational change in PARP1 disturbs the HD/CAT interaction, such that β-NAD+ can now access the CAT domain and catalysis ensues (Dawicki-McKenna et al., 2015; Eustermann et al., 2015). This

increase in PARylation of substrate proteins enables their recruitment to- and retention at the site of DNA damage, or in the case of histone PARylation, drives changes in chromatin structure that facilitate DNA repair (Leung, 2014; Ray Chaudhuri & Nussenzweig, 2017). At the end of the repair process, PARylation of PARP1 itself (autoPARylation) results in the dissociation of PARP1 from DNA. The negatively charged PAR has been suggested to cause electrostatic repulsion of PARP1 from DNA (Satoh & Lindahl, 1992). Correspondingly, PAR glycohydrolase (PARG), which counteracts PARylation by hydrolysing ribose-ribose bonds within PAR (Hatakeyama et al., 1986; Wielckens et al., 1982), increases the retention of PARP1 on DNA. Although structurally unrelated to PARG, ARH3 also degrades poly (ADP-ribose) to generate ADP-ribose monomers, albeit at only ~10% of the activity observed for PARG (Oka et al., 2006). Another proposed mechanism by which cells regulate PARP1 activation in response to DNA damage, involves the E3 ubiquitin ligase called checkpoint with forkhead-associated (FHA) and RING finger domain protein (CHFR). CHFR is recruited to DSBs by PAR, where it ubiquitinates PARylated, but not unPARylated, PARP1. As such, CHFR has been proposed as important for PARP1 dissociation from DNA damage sites (Kashima et al., 2012; Liu et al., 2013). More recently, PARP1 SUMOylation/ubiquitinylation has been reported to regulate removal of PARP1 from chromatin. The PIAS4-mediated SUMOylation and subsequent RNF4-mediated ubiquitinylation of PARP1 promotes the recruitment of p97 ATPase (also known as valosin-containing protein, VCP), which has been shown to promote the removal of PARP1 from chromatin (Krastev et al., 2022).

We now know that PARP1 plays a role in several DNA repair processes (reviewed by (Ray Chaudhuri & Nussenzweig, 2017)), such as repair of SSBs, DSBs, stabilisation of RFs, and chromatin modification. For example, SSBs can result from failed ligation of Okazaki fragments, which are discontinuous DNA fragments synthesised on the lagging strand of DNA during replication. Single-strand DNA (ssDNA) gaps in-between Okazaki fragments are normally filled by the activity of DNA ligase I (LIG1) and flap endonuclease I (FEN1). In instances where Okazaki fragments are incompletely processed, the resultant ssDNA gaps are normally bound by PARP1 and repaired by a PARP1-dependent process (Hanzlikova et al., 2018; Maya-Mendoza et al., 2018). Upon sensing DSBs, PARP1 promotes repair via HR, which is the relatively error-free sub-pathway of DSB repair, by inhibiting the alternative error-prone DSB repair pathway which I described in Section 1.2, NHEJ. PARP1-mediated PARylation of Ku70/80 NHEJ complex decreases Ku70/80-DNA affinity (Li et al., 2004). PARP1 also competes with Ku70/80 for DNA ends, which may provide additional suppression of NHEJ activity (Wang et al., 2006). Upon binding to DSBs, PARP1 is involved in the prompt recruitment and activation of MRE11 and NBS1 factors of the MRN complex (Haince et al., 2008), which are involved in sensing DNA damage and generating the 3'-ssDNA overhangs required for HR, as described in a previous section of this thesis (Lisby et al., 2004). Another major activator of DSB repair pathways, ATM, is influenced by PAR chain interaction (Aguilar-Quesada et al., 2007; Haince et al., 2007). PAR chains are also recognised by BRCT domain of BRCA1, thus the recruitment of BRCA1 to DSBs is also highly dependent on PARP1 activity (Li & Yu, 2013).

1.6. PARP inhibitors

After establishing the function of PARP1 in DNA repair, as well as that of the closest related paralog, PARP2, small molecule PARP1/2 inhibitors were discovered with the initial intention of being used to potentiate chemo- or radiotherapy. In 1980, a PARP1/2 inhibitor, 3AB, was identified that enhanced the cytotoxicity of the DNA methylating agent, dimethyl sulphate (Durkacz et al., 1980; Purnell et al., 1980). As part of the PARylation reaction, β-NAD+ is consumed and PAR chains are produced, with nicotinamide generated as a by-product. 3AB has a nicotinamide structure, suggesting that it inhibited PARP1 by competing with β-NAD+ for binding within the catalytic site (Durkacz et al., 1980; Purnell et al., 1980). However, the chemical properties of 3AB do not make it suitable for use as a drug, so, later, drug-like PARPi were designed to structurally mimic nicotinamide, including rucaparib (AG014699, PF-01367338/Pfizer/Clovis, now Rubraca), veliparib (ABT-888/Abbott Pharmaceuticals), olaparib (AZD2281, KuDOS/AstraZeneca, now marketed as Lynparza), and niraparib (MK-4827, Merck/Tesaro, marketed as Zejula) (reviewed in (Lord & Ashworth, 2017)). These first-generation clinical PARPi have PARP1 IC_{50} within the nanomolar range. A more potent PARPi, with a PARP1 IC_{50} within the picomolar range, was later discovered – talazoparib (BMN 673, Biomarin/Medication/Pfizer) (Shen et al., 2013). Each PARPi differs in its ability to trap PARP1 onto DNA (Krastev et al., 2021; Murai et al., 2012), which correlates with cytotoxic potency (described in more detail later); talazoparib is the most potent PARP1 trapping inhibitor and veliparib is the least potent. Recently reported agents pamiparib (BeiGene) (Xiong et al., 2020) and AZD5305

(AstraZeneca) (Johannes et al., 2021) are not only highly potent, but are also highly selective for PARP1.

1.7. PARPi mechanism of action

By structurally mimicking the PARP1/2 product, nicotinamide, pharmacological PARPi have two general mechanisms of action for its anti-tumour activity (i) catalytic inhibition of PARP1, which abrogates PARylation responsible for recruitment and retention of DNA repair proteins at the site of damage; (ii) “trapping” or locking PARP1 onto damaged DNA, which induces PARP1 conformational changes to increase DNA avidity (Murai et al., 2012; Murai, Zhang, et al., 2014). The nucleoprotein complex caused by PARP1 trapping was proposed to provide a steric barrier to the normal function of DNA and impair the normal progression of the RF, resulting in replication stress and ultimately RF collapse (Krastev et al., 2021; Murai et al., 2012). A correlation between trapping ability and cytotoxicity has been proposed; the scale of cytotoxicity observed with a weak trapper, such as veliparib, is diminutive compared to an effective trapper, such as talazoparib, even if PARP activity is effectively inhibited by both (Shen et al., 2013; Murai, Huang, et al., 2014; Pommier et al., 2016). Recent work has demonstrated PARPi-mediated trapping of PARP1 at Okazaki fragments (Hanzlikova et al., 2018; Maya-Mendoza et al., 2018). As detailed in the earlier section regarding PARP1 function, PARP1 functions in the repair of DNA lesions resulting from failed ligation of Okazaki fragments, ssDNA breaks. Upon PARPi exposure, and therefore PARPi-mediated PARP1 trapping, ssDNA gaps remain unrepaired, and the cells undergo mitosis with persistent SSBs. In the proceeding S phase, fork stalling and collapse results from the trapped PARP1 at the persistent SSBs, forming a

replication barrier (Hanzlikova et al., 2018; Maya-Mendoza et al., 2018). This model of PARPi-mediated cytotoxicity has been observed in cells deficient in either *LIG1*, which ligates Okazaki fragments or *FEN1*, which processes Okazaki fragments to allow their re-ligation. Enhanced PARPi sensitivity has been observed upon deficiency of genes which result in increased ssDNA gaps, providing further evidence for this model of PARPi-mediated cytotoxicity. Loss of *RNASEH2*-family genes, *RNASEH2A, RNASEH2B or RNASEH2C,* which are usually involved in ribonucleotide excision repair (RER), results in accumulation of topoisomerase 1 (TOP1)-cleaved ribonucleotides, and ultimately increased ssDNA gaps. This increase in PARP1-trapping lesions, ssDNA gaps, results in increased PARPi efficacy (Zimmermann et al., 2018). The trapping model of PARPi-mediated cytotoxicity is supported by observations of PARPi resistance with point mutations in *PARP1* DNA-binding ZnF domain (Pettitt et al., 2018) or upon genetic depletion of *PARP1* (Murai et al., 2012). In addition, a *PARP1* mutation, which resulted in failure to trap to DNA upon PARPi exposure, has also been identified in a patient with *de novo* PARPi-resistance (Pettitt et al., 2018).

PARPi therapeutic efficacy has also been attributed to the activation of the immune response. Innate immune response stimulation via cyclic GMP-AMP (cGAMP) synthetase (cGAS)- stimulator of interferon genes (STING) signalling, has been reported upon PARPi exposure (Chabanon et al., 2019; Ding et al., 2018; Oh et al., 2020; Pantelidou et al., 2019; Parkes et al., 2017). PARPi promote the accumulation of cytosolic DNA fragments, due to unresolved DNA lesions. Following recognition of cytosolic DNA generated via PARPi-induced DNA damage, cGAS activates the STING signalling pathway, which in turn activates

innate immune signalling responses (Chabanon et al., 2019; Ding et al., 2018; Oh et al., 2020; Pantelidou et al., 2019; Parkes et al., 2017). The adaptive immune system has also been suggested to participate in the anti-tumour activity of PARPi; anti-CD8 antibody-mediated neutralisation or depletion of $CD8^+$ T cells in tumour-bearing mice abrogates PARPi activity on tumour growth (Ding et al., 2018; Pantelidou et al., 2019).

1.8. PARP inhibitor synthetic lethality

In 2005, two studies demonstrated that PARPi selectively killed tumour cells lacking *BRCA1* or *BRCA2* (Bryant et al., 2005; Farmer et al., 2005). Farmer and colleagues demonstrated that RNA interference (RNAi)-mediated silencing of PARP1 resulted in reduced cell survival specifically in *BRCA1*- and *BRCA2*-deficient cells (Farmer et al., 2005). Enhanced PARPi sensitivity was also observed upon RNAi-mediated depletion of *BRCA1* in MCF7 human breast cancer cells (Farmer et al., 2005). *BRCA1*- or *BRCA2*- deficient cell lines were sensitive to PARP1 inhibitors, while cells with only heterozygous loss of *BRCA1* or *BRCA2, or* those without *BRCA1/2* defect, were not (Farmer et al., 2005). Compared to wild-type embryonic stem (ES) cells, *BRCA1*- or *BRCA2*-deficient cells demonstrated 57-fold or 133-fold enhanced sensitivity, respectively. Similar results were demonstrated in *BRCA2*-deficient Chinese hamster ovary (CHO) cells, which demonstrated 1000-fold enhanced sensitivity compared to BRCA2-complemented CHO cells (Farmer et al., 2005). Similar conclusions were reported in a back-to-back publication, whereby depletion of *BRCA2* levels via short interfering RNA (siRNA) sensitised cancer cells to PARPi (Bryant et al., 2005).

The concept of synthetic lethality, whereby a cell can tolerate the loss of function of either one of two genes, but not both (Lucchesi, 1968), was proposed as the underlying explanation of PARPi-mediated cytotoxicity in *BRCA1*- or *BRCA2*-deficient cells (Bryant et al., 2005; Farmer et al., 2005). These studies showed that treatment of cells with PARP inhibitors resulted in a large increase in DNA damage that required HR for repair, demonstrated by induction of RAD51 foci (in *BRCA1*/*2* wild-type cells). Therefore, it was hypothesised that PARP inhibitors result in an increased level of damage that persists into S phase where it impairs RF progression that needs to be repaired by HR, which *BRCA1/2* mutant cells are not capable of. This damage may result from deficient SSB repair in the presence of PARPi, lack of Okazaki fragment ligation or PARP1 trapping, as described above. Cells deficient in other HR mediators (such as *RAD51C* or *PALB2*) were also reported to be sensitive to PARPi treatment, referred to as BRCAness (Hoppe et al., 2018; Lord & Ashworth, 2017). Deficiency in genes involved in HR increases the dependency for other DDR pathways. In the absence of functional HR, repair is instead attempted with alternative DNA repair mechanisms, primarily via NHEJ. While HR-mediated repair would accurately restore the native DNA sequence, NHEJ is an error-prone DNA repair pathway. Therefore, *BRCA1* and *BRCA2* deficiency, or BRCAness, also renders the cells vulnerable to PARPi-mediated cytotoxicity via PARP trapping and NHEJ.

1.9. PARPi clinical development

Given the ability of PARPi to potentiate the effects of alkylating chemotherapies, the first PARPi clinical trial assessed the PARPi rucaparib in combination with the alkylating agent temozolomide (Plummer et al., 2013). However, following the

observation of PARPi synthetic lethality with either *BRCA1* or *BRCA2* defects (Bryant et al., 2005; Farmer et al., 2005), the prospect of using PARPi as a single agent was regarded as feasible, as assessed in a phase I trial using olaparib as a single agent (NCT00516373) (Fong et al., 2009). In this trial, the dose-limiting toxicities, such as myelosuppression and fatigue, was determined to be relatively minor compared to standard chemotherapy. In addition to safety, analysis of pharmacokinetic and pharmacodynamic characteristics of olaparib was performed. Pharmacokinetic (PK) studies determined that olaparib absorption was rapid, with peak plasma concentrations between one and three hours after dosing. Pharmacodynamic (PD) studies confirmed PARP inhibition in tumour tissue, whereby a reduction in PAR chain formation was used as a PD biomarker. PD analysis was also carried out by measuring γH2AX foci formation following PARPi treatment, indicative of DNA damage (Mah et al., 2010), as predicted by the preclinical model (Farmer et al., 2005). The maximum tolerated dose (MTD) was established as 400 mg twice daily. Within the expansion phase, which involves recruitment of additional patients with different eligibility criteria, cancer patients with germline *BRCA1* or *BRCA2* mutations (*gBRCAm*) were included (NCT00516373) (Fong et al., 2009). 12/19 of the patient population (63%) were reported to demonstrate clinical benefit with single agent PARPi (Fong et al., 2009), providing clinical evidence for the preclinical observation of PARP-BRCA synthetic lethality (Bryant et al., 2005; Farmer et al., 2005).

Following the phase I trial, two parallel phase II trials assigned patients into two cohorts with different olaparib doses to test PARPi efficacy and expand insights into PARPi tolerability, in the separate contexts of ovarian cancer (Audeh et al.,

2010) and *gBRCA*m breast cancer (Tutt et al., 2010). In the phase II trial conducted in the context of *gBRCAm* HGOC (NCT00494442), those who received the MTD, 400 mg twice daily (b.i.d.) had a higher objective response rate (ORR) of 33%, compared to the 13% reported in those who received the biologically active dose (100 mg b.i.d.) (Audeh et al., 2010). Similar findings were reported from the phase II trial comprising women with confirmed *BRCA1* or *BRCA2* mutations and recurrent, advanced breast cancer (NCT00494234). Subjects who received the MTD, 400 mg b.i.d.) had a higher ORR of 41% compared to the 22% reported in those who received the biologically active dose (100 mg b.i.d.) (Tutt et al., 2010).

The promising results from all these trials led to additional trials, including Study 19 (NCT00753545), the results of which ultimately led to the first clinical approval of a PARPi, olaparib. This randomised phase II trial assessed maintenance treatment using olaparib 400 mg twice daily versus placebo in high-grade serous ovarian cancer (HGSOC) patients who had previously demonstrated platinum-sensitivity. In this trial, patients with germline or somatic *BRCA1/2* deleterious mutations were included, as well as "wild-type BRCA" patients, which includes patients with no known *BRCA1* or *BRCA2* mutation, and those with a *BRCA1* or *BRCA2* mutation of unknown significance. As shown in Figure 1.5A, all patients (n=265) who received olaparib MTD, rather than placebo, exhibited superior progression free survival (PFS) (8.4 months vs. 4.8 months, hazard ratio, 0.35) (Ledermann et al., 2012; Ledermann et al., 2014). Stratifying patients for germline or somatic *BRCA1/2* deleterious mutations revealed the most pronounced improvement in PFS, as shown in Figure 1.5B (11.2 months vs. 4.3 months, hazard ratio 0.18) (Ledermann et al., 2012; Ledermann et al., 2014). As shown in Figure 1.5C, even

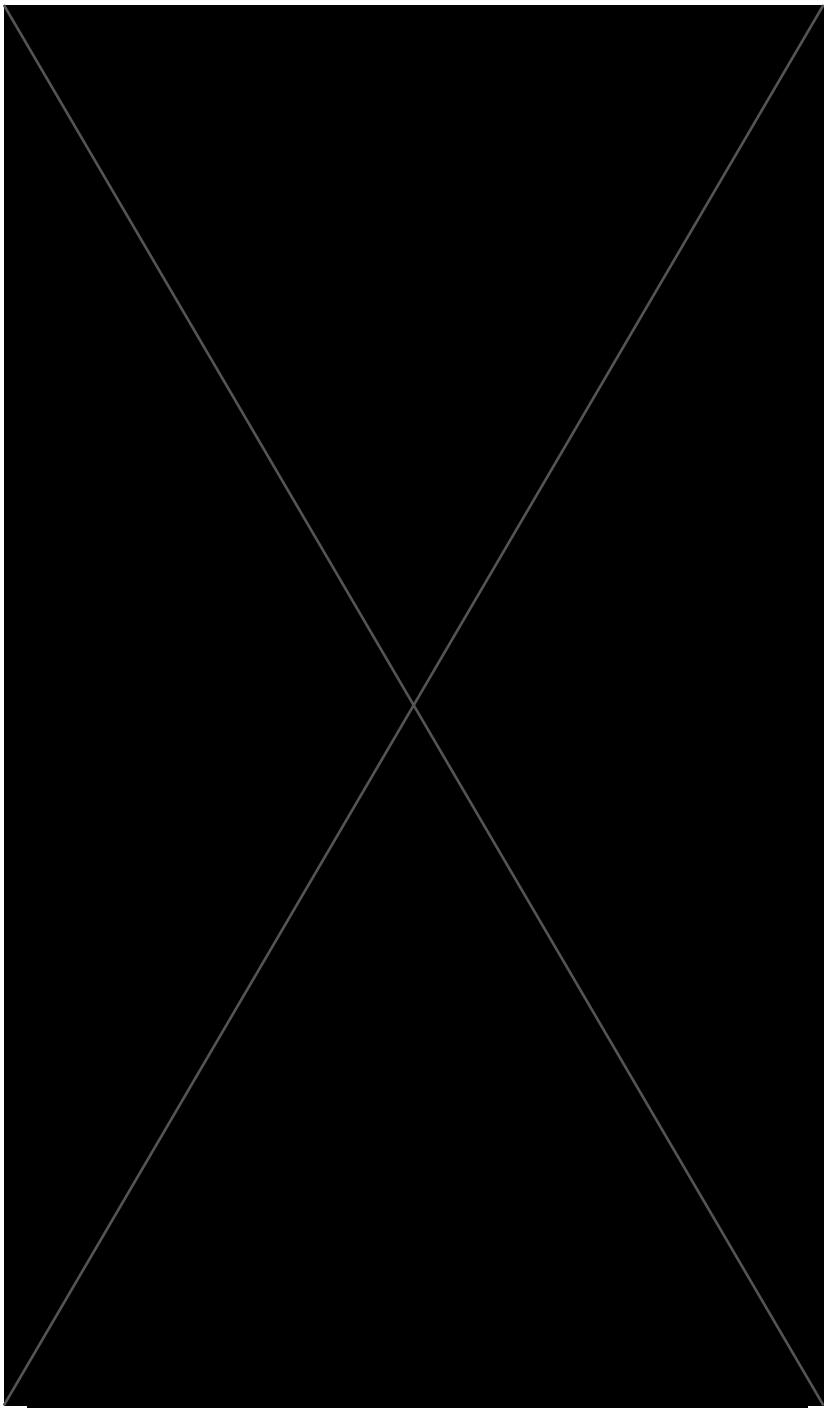

Figure 1.5 Kaplan-Meier survival plots of progression free survival (PFS) in all patients and according to *BRCA1* or *BRCA2* mutation status in Study 19.
265 patients in total were included in the study and the progression free survival (PFS) for olaparib (blue) vs. placebo (red) cohorts for all patients was summarised (A). 136 patients were stratified for germline or somatic *BRCA1* or *BRCA2* deleterious mutations and classified as "patients with BRCA mutation". PFS for olaparib (blue) vs. placebo (red) cohorts for "patients with BRCA mutation" was summarised (B). 118 patients were stratified into "patients wild-type BRCA" group which includes patients with no known *BRCA1* or *BRCA2* mutation and those with a *BRCA1* or *BRCA2* mutation of unknown significance. PFS for olaparib (blue) vs. placebo (red) cohorts for "patients with wild-type BRCA" was summarised (C). Figure from (Ledermann et al., 2014).

"wild-type BRCA" subjects who received olaparib MTD rather than placebo exhibited superior PFS (7.4 months vs. 5.5 months, hazard ratio, 0.54) (Ledermann et al., 2012; Ledermann et al., 2014). Results from this trial led to the licensing of olaparib. Initially, olaparib was granted approval for maintenance treatment of *BRCA1/2*-mutated patients in 2014, and this eligibility was expanded to all platinum-sensitive patients in 2018, regardless of *BRCA1* or *BRCA2* mutation status. Approvals beyond olaparib to other PARPi, as well as beyond ovarian cancer, has followed since the landmark Study 19. The eligibility criteria for PARPi have also refined with the compendium of data from the numerous clinical trials. As of the time of writing, clinical use of PARPi has been approved by the Food and Drug Administration (FDA) for several indications, as summarised in Table 1.

The following subsections will summarise the phase III clinical trials from which PARPi clinical approval was granted, according to each histology; ovarian, breast, metastatic prostate cancer and pancreatic ductal adenocarcinoma.

1.9.1. Development of PARPi for ovarian cancer

Based on the results of the phase III SOLO-2 trial (NCT01874353) trial (Pujade-Lauraine et al., 2017), and those of SOLO-1 (NCT01844986) (Moore et al., 2018), olaparib was approved as maintenance therapy for ovarian cancer patients who had demonstrated recurrent platinum sensitivity (Pujade-Lauraine et al., 2017). Beyond the maintenance setting, olaparib was also approved for advanced ovarian cancer patients with germline *BRCA1* or *BRCA2* mutations, progressing with prior treatment using three or more lines of chemotherapy (Moore et al., 2018). Another PARPi, niraparib (Zejula) was approved by the EMA and FDA as maintenance

therapy for platinum-sensitive HGSOC, regardless of *BRCA1* or *BRCA2* status, following a double-blind phase III trial (ENGOT-OV16/NOVA) (NCT01847274). A superior PFS was reported in the niraparib-treated patients compared to placebo in both cohorts of patients, regardless of *BRCA1* or *BRCA2* mutation status (21 months vs 5.5 months in g*BRCA*m patients, 9.3 vs 3.9 in patients with no detectable *BRCA* mutation) (Mirza et al., 2016). The ARIEL3 phase III trial (NCT01968213) aimed to assess the PARPi rucaparib as a potential maintenance therapy for platinum-sensitive HGSOC (Coleman et al., 2017). The placebo PFS was reported to be 5.4 months. An improved PFS was reported in all rucaparib-treated cohorts: 16.6 months in *BRCA1*- or *BRCA2*-mutation positive; 13.6 months in HR defect-associated signature based on LOH; and 10.8 months in the intention-to-treat population. The association between rucaparib sensitivity and an LOH-based signature was identified in the rucaparib phase II trial ARIEL2 trial (NCT01891344), whereby patients with high LOH had a much higher PFS compared to those with low LOH (10.2 months vs 5.6 months) (Swisher et al., 2017). The FDA and the EMA approved rucaparib as a maintenance treatment for HGSOC regardless of *BRCA1* or *BRCA2* mutation status based on these results. Rucaparib is additionally approved for *BRCA1*- or *BRCA2*-mutated HGSOC with prior treatment of two or more lines of chemotherapy (Oza et al., 2017).

1.9.2. Development of PARPi for breast cancer

The promising results from the previously mentioned initial proof of concept phase II trial (Tutt et al., 2010) eventually led to a randomised phase III trial, OlympiAD (NCT02000622), comprising patients with *gBRCA1m*, HER2-negative, metastatic breast cancer (Robson et al., 2017). Olaparib demonstrated superior

Table 1 FDA labels for approved PARPi with clinical trial data (2022).

Drug	Site	Indication	Relevant trial NCT	Relevant trial name	Relevant publication
Olaparib (Lynparza)	Breast	Germline BRCA-mutant, HER2-negative, with prior chemotherapy	NCT02000622; NCT02032823	OlympiAD; OlympiA	(Robson et al., 2017) (Tutt et al., 2021)
	Ovarian	Maintenance: first line BRCA-mutant advanced cancer (platinum sensitive)	NCT01078662	N/A	(Kaufman et al., 2015)
		Maintenance: recurrent platinum sensitive	NCT01874353	SOLO-2	(Pujade-Lauraine et al., 2017).
		Maintenance: in combination with VEGF inhibitor (bevacizumab) for first line platinum sensitive HRD-positive advanced cancer	NCT02477644	PAOLA-1	(Ray-Coquard et al., 2019)
		Treatment: Germline BRCA-mutant advanced cancer, 3+ lines of chemotherapy	NCT01844986	SOLO-1	(Moore et al., 2018)
	Pancreatic	"Maintenance" treatment of germline BRCA-mutant metastatic PDAC with no progression after at least 16-weeks of platinum	NCT02184195	POLO	(Golan et al., 2019)
	Prostate	Germline or somatic HRR gene mutant (e.g. ATM, CDK12, CHEK1/2) mCRPC, after enzalutamide or abiraterone	NCT02987543	PROfound	(de Bono et al, 2020)
Talazoparib (Talzenna)	Breast	Germline BRCA-mutant, HER2-negative, locally advanced or metastatic	NCT01945775	EMBRACA	(Litton et al., 2018)
Rucaparib (Rubraca)	Ovarian	Maintenance: recurrent platinum sensitive	NCT01968213	ARIEL3	(Coleman et al., 2017)
		Treatment: Germline BRCA-mutant advanced cancer, 2+ lines of chemotherapy	NCT01891344	ARIEL2	(Oza et al., 2017)
	Prostate	Germline or somatic BRCA-mutant mCRPC, prior androgen-receptor and taxane therapy (Accelerated approval)	NCT02952534	TRITON2	(Abida et al., 2020)
Niraparib (Zejula)	Ovarian	Maintenance: recurrent platinum sensitive	NCT01847274	ENGOT-OV16/NOVA	(Mirza et al., 2016)
		Maintenance: first line platinum sensitive advanced cancer	NCT02655016	PRIMA	(Gonzalez-Martin et al., 2019)
		Treatment: HRD-positive, 3+ lines of chemotherapy	NCT02354586	QUADRA	(Moore et al. 2019)
Veliparib	NSCLC	Orphan drug status	NCT01560104; NCT02106546		(Ramalingam et al., 2017) (Ramalingam et al., 2021

Abbreviations: BRCA breast and ovarian cancer associated; HER2 human epidermal growth factor receptor 2; VEGF vascular endothelial growth factor, HRD homologous recombination deficient; PDAC pancreatic ductal adenocarcinoma; HRR homologous recombination repair; ATM Ataxia Telangiectasia mutated; CDK12 cyclin dependent kinase 12; CHEK1/2 checkpoint kinase 1/2; mCRPC, metastatic castration-resistant prostate cancer; NSCLC non-small cell lung cancer.

median PFS compared to standard chemotherapy in these patients (7.0 vs 4.2 months, hazard ratio 0.58 (95% confidence interval (CI) 0.43-0.80)) (Robson et al., 2017). In addition, a delayed quality of life deterioration was apparent with olaparib (hazard ratio 0.44; 95% CI 0.25-0.77) (Robson et al., 2017). The FDA also approved talazoparib for *BRCA1/2*-mutant advanced breast cancer in 2018 following results from a phase III trial, EMBRACA (NCT01945775); median PFS was significantly longer in the talazoparib-treated patients than the patients treated with standard-of-care chemotherapy (8.6 vs. 5.6 months) (Litton et al., 2018).

In early breast cancer, the recently reported OlympiA phase III trial (NCT02032823) demonstrated significantly longer survival free of invasive or distant disease in the olaparib group compared to placebo in *BRCA1*/2-mutant, HER2-negative patients with breast cancer, as an adjuvant treatment subsequent to standard-of-care chemotherapy (Tutt et al., 2021). The three-year invasive disease-free survival was 85.9% in the olaparib group and 77.1% in the placebo group. Three-year distant disease-free survival was 87.5% in the olaparib group and 80.4% in the placebo group (Tutt et al., 2021). As a result of the OlympiA trial, olaparib has been granted approval for use in high risk, early-stage breast cancers with germline *BRCA1* or *BRCA2* mutation; initially by the FDA then European Medicines Agency (EMA) and subsequently the UK regulator Medicines and Healthcare products Regulatory Agency (MHRA) in September 2022.

1.9.3. Extending the utility of PARPi to other HR-defective tumour types

Beyond gynaecological and breast cancers, clinical trials have demonstrated that other HR-defective tumours could be suitable for PARPi treatment. Initially, a basket trial in *gBRCA1/2m* patients reported 21.7% and 50% response rates in pancreatic and prostate cancers, respectively (Kaufman et al., 2015). In the randomised, double-blind POLO phase III trial (NCT02184195) (Golan et al., 2019), eligibility criteria comprised gBRCAm metastatic pancreatic cancer patients who had not progressed following at least 16 weeks of platinum-based chemotherapy. Subjects were randomised 3:2 to olaparib (300 mg) or placebo. The olaparib group were reported to have significantly longer median PFS than the placebo group (7.4 months vs. 3.8 months) (Golan et al., 2019). As a result of this trial, olaparib was approved for clinical use according to the eligibility criteria for the POLO trial; *BRCA1/2*-mutant metastatic pancreatic cancer which has not progressed following at least 16 weeks of platinum treatment. Due to the PROFOUND trial (NCT02987543), olaparib has been approved for germline or somatic HR-mutant prostate cancer following enzalutamide or abiraterone treatment (de Bono et al., 2020). In the case of mCRPC with germline or somatic *BRCA1/2* mutation, rucaparib has been approved following prior androgen-receptor and taxane therapy, as assessed in the TRITON2 trial (NCT02952534) (Abida et al., 2020).

1.9.4. Understanding clinical PARPi response

The aforementioned clinical trials have been successful in providing clinical evidence for the preclinical observation of PARP-BRCA synthetic lethality (Bryant

et al., 2005; Farmer et al., 2005) in multiple histologies, including ovarian, breast, prostate, and pancreatic cancers. As a result, PARPi represent the first DDR-targeting agents approved as anti-cancer therapies, and the first targeted agents used in an inherited disorder. Further preclinical work is ongoing to identify further genes responsible for altering PARPi response, for various reasons as set out below.

In the HR-deficient setting, identification of genes whose perturbation mediates PARPi sensitivity or resistance could provide further refinement of PARPi mechanism of action in the clinically relevant contexts for which PARPi are already approved. Since most patients with advanced disease eventually progress on PARPi, resistance to PARPi also needs to be better understood. Despite the progress made for patients with *BRCA1* or *BRCA2* mutations, the possible reasons for the PARPi efficacy observed in *BRCA1/2* wild-type patients (for example, Figure 1.5C) have not been fully worked out. Further pre-clinical studies will help to optimise the current use of PARPi in the clinic by informing future trials, and potentially extend the utility of PARPi beyond BRCA-PARP synthetic lethality. The question of what determines PARPi sensitivity beyond *BRCA1*, *BRCA2* and other HR gene mutations, is what I sought to answer through the work described in this thesis.

1.10. Determinants of PARPi sensitivity

Early studies used a candidate-based approach to identify determinants of PARPi response. Building on the work of Farmer et al. and Bryant et al., demonstrating BRCA/PARP1 synthetic lethality, a later publication identified mediators of PARPi

sensitivity beyond *BRCA1/2* for the first time (McCabe et al., 2006). Compared to scrambled control-transfected cells, *RAD51* siRNA-depleted cells demonstrated >1000-fold enhanced olaparib sensitivity, an effect which was even more profound than upon siRNA-mediated depletion of *BRCA1* or *BRCA2* (McCabe et al., 2006). Similarly, McCabe et al. observed increased olaparib sensitivity with siRNA-mediated depletion of *DSS1*, *RPA1*, *CHK1*, *CHK2*, *ATM*, *ATR* in *BRCA1/2* wild-type HeLa cells compared to scrambled control-transfected cells (McCabe et al., 2006). These findings were strengthened by comparison of PARPi sensitivity in isogenic models. *Rad54*-deficient ES cells demonstrated 9-fold increased PARPi sensitivity compared to wild-type (McCabe et al., 2006). McCabe et al. also demonstrated that the olaparib sensitivity of human fibroblasts deficient in *NBS1* was more profound than the same cells complemented with NBS1 cDNA (McCabe et al., 2006).

1.10.1. Early genetic perturbation screens for identifying determinants of PARPi sensitivity

Genetic perturbation screening approaches, which have historically been used to identify genetic elements which are important for a specific biological process, were subsequently established to identify genes responsible for altering PARPi response. The earliest examples utilised RNAi technology as a method of genetic perturbation. RNAi screening using a library of siRNA targeting the kinome identified *CDK5*, *MAPK12*, *PLK3*, *PNKP*, *STK22c* and *STK36* as modifiers of PARPi sensitivity, in addition to known HR mediators (Turner et al., 2008). A parallel RNAi screen using a library of DDR genes identified *DDB1* and *XAB2* as novel drivers of PARPi sensitivity (Lord et al., 2008). Later, a genome-wide RNAi

screen identified genes involved in replication and cell cycle progression (MCM proteins, *TOP3A*, *POLB*, *CDK7),* as well as genes involved in the DDR (*BRCA1*, *NBN*, *FANCD*, *FANCC*, *RAD51*, *LIG3*, *RAD51C*, *RAD51D*, *RAD21*, *ESCO1*, and *SMC3)* (Bajrami et al., 2014). This latter screen also identified *CDK12* defects as a cause of PARPi sensitivity. Post-screen validation confirmed short hairpin RNA (shRNA)-mediated *CDK12* depletion sensitised a panel of different ovarian cancer models, including profoundly olaparib-resistant OV90. Suppression of HR was demonstrated in these *CDK12*-depleted cells via observation of decreased RAD51 foci upon IR and decreased green fluorescent protein (GFP)-positive cells with DR-GFP assay. A correlation between PARPi sensitivity and CDK12 expression in ovarian tumour cell lines was also reported. These *in vitro* results were confirmed *in vivo*; improved PARPi efficacy was demonstrated in *CDK12*-depleted tumour cells compared to cells expressing control shRNA in mouse experiments. Given that *CDK12* is one of a small number of highly recurrently mutated driver genes in HGSOC, this observation provided the rationale for assessing *CDK12* as a clinically relevant biomarker of PARPi sensitivity in subsequent clinical trials (Bajrami et al., 2014). Although these RNAi screens proved informative, the off-target effects of RNAi suggested refined technologies could be used for the identification of synthetic lethal effects (Jackson et al., 2003). As such, clustered regularly interspaced short palindromic repeats (CRISPR)/Cas9 technology has more recently been used to identify synthetic lethal effects.

1.10.2. Overview of CRISPR/Cas9

CRISPR/Cas9 exploits a nuclease (Cas9) first identified in bacteria and archaea for adaptive immune protection against exogenous, and potentially deleterious

DNA, such as those introduced by viruses (Barrangou et al., 2007). The components of this system have been adapted for genome engineering in eukaryotes (Cong et al., 2013). A 20 nucleotide single-guide RNA (sgRNA) is designed to guide the Cas9 to its 2- to 5- bp recognition site, protospacer adjacent motif (PAM) sequence (NGG) 3' of the target DNA (Jinek et al., 2012), where it induces a DSB (Ran et al., 2013). The DDR present within cells attempts to repair these lesions to restore the native DNA sequence. Occasionally, however, mutations can be introduced. This potential mutagenic consequence is exploited to disrupt the endogenous DNA sequence, resulting in perturbed or even complete loss of protein translation; in the case of frameshift insertion/deletion (indel) mutations, loss-of-function alleles are generated (Cong et al., 2013). The aforementioned iteration of CRISPR-Cas9 mutagenesis is referred to as CRISPRn (Figure 1.6). Development of a catalytically-inactive Cas9 mutant (dCas9) fused to effector proteins for effective transcriptional enhancement or repression, allows adaptation of conventional CRISPRn to CRISPR technologies referred to as CRISPR activation (CRISPRa) (Mali et al., 2013) or CRISPR inference (CRISPRi) (Gilbert et al., 2013), respectively. Similarly to CRISPRn, CRISPRi/a mediated targeting involves the sgRNA guiding the dCas9 to the promoter region of the gene of interest. Given the catalytically-inactive nature of dCas9, no DSBs are generated, and there is no modification of the DNA sequence with CRISPRi/a, (unlike CRISPRn). Instead, dCas9-bound effectors proteins, VP64-p65-Rta (VPR) in the case of CRISPRa (Gossen & Bujard, 1992) or Krüppel associated box (KRAB) domain of Kox1 in the case of CRISPRi, promote or repress gene expression (Chavez et al., 2015; Gilbert et al., 2013), respectively (Figure 1.7).

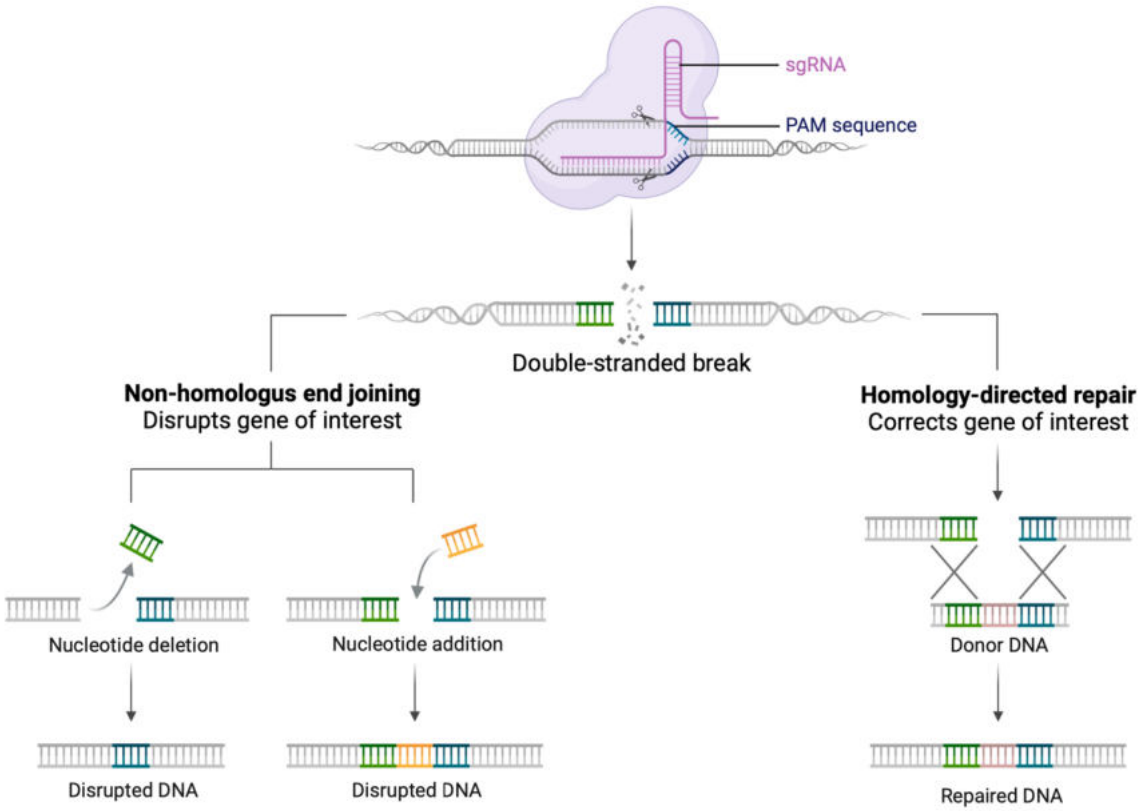

Figure 1.6 Schematic diagram of CRISPR-Cas9 gene editing system.
20 nucleotide single-guide RNA (sgRNA) directs Cas9 to its 2- to 5- bp recognition site, protospacer adjacent motif (PAM) sequence (NGG) 3' of the target DNA, where it induces a double strand break (DSB). Non-homologous end joining (NHEJ)-mediated repair of the Cas9-generated DSB leads to insertion/deletion mutations due to its inherent error-prone nature. As such, loss-of-function alleles are generated via complete loss of protein translation. Upon introduction of a DNA template, homologous recombination (HR)-mediated repair allows incorporation of the desired sequence into the genome. Figure modified from (Ran et al., 2013).

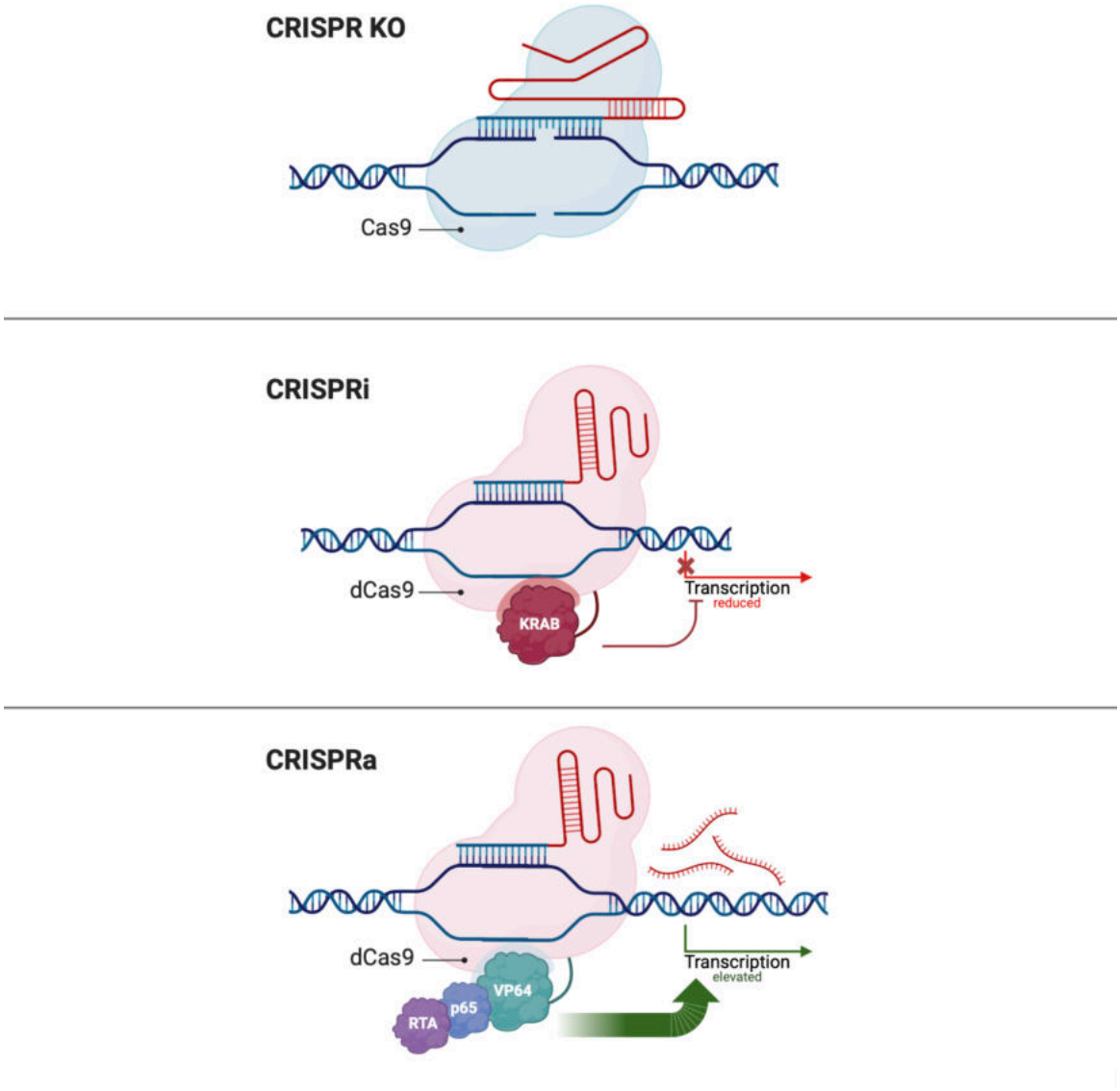

Figure 1.7 Schematic of modified CRISPR/Cas9 systems (CRISPRi/a).
A catalytically inactivated Cas9 (dCas9) is guided to the region of interest via single-guide RNA (sgRNA) but does not generate a double-strand break (DSB). Instead, effector proteins fused to dCas9 alters expression. Fusion to transcription repressor Krüppel associated box (KRAB) domain of Kox1 allows silencing of a target gene at the transcriptional level via CRISPRi. Fusion of dCas9 with transcription activators (VPR – RTA, p65, VP64) (VPR) allows upregulation of gene transcription (CRISPRa). Figure adapted from (Gebre et al., 2018).

Given that Cas9 targeting specificity is determined by sgRNA, which can be easily generated at high-throughput, thousands of genes can be systematically modified by sgRNA-directed loss-of-function. Consequently, the role of thousands of genes to a phenotype of interest can be simultaneously determined in a single experiment, referred to as a screen. The entire coding genome can be targeted in genome-wide screens using such sgRNA libraries, which can consist of more than 200,000 sgRNAs. In order to minimise off-target effects, 5-10 sgRNAs are designed to target each gene. In a pooled format, libraries of sgRNA expression constructs are stably integrated into mammalian cell genomes via lentiviral transduction of a large population of cells, either Cas9- or dCas9-expressing cells, depending on the desired type of CRISPR screen (CRISPRn or CRISPRi/a, respectively). In order to ensure that each cell only contains a single sgRNA, a very low multiplicity of infection (MOI) is required.

CRISPR screens can be designed to examine many different biological questions. In order to study sensitivity to a particular drug, the Cas9/dCas9-sgRNA expressing cells can also be exposed to a low dose of the drug of interest. Deep sequencing of genomic DNA extracted from the surviving population allows for the estimation of relative decreases in sgRNA frequency, compared to dimethyl sulphoxide (DMSO) control, following drug exposure (Hartenian & Doench, 2015; Wang et al., 2014). Theoretically, the genes targeted by these sgRNAs cause drug sensitivity, upon their loss. In contrast, the Cas9/dCas9-sgRNA expressing cells can also be exposed to a high dose of the drug of interest to study drug resistance. Deep sequencing of genomic DNA extracted from the surviving population allows for the estimation of relative increases in sgRNA frequency (compared to DMSO control)

following drug exposure (Hartenian & Doench, 2015; Wang et al., 2014). Theoretically, the genes targeted by these sgRNAs cause drug resistance, upon their loss. Using the aforementioned approaches, CRISPR screens were pioneered by Shalem et al. to identify genes whose loss is involved in BRAF inhibitor (vemurafenib) resistance (Shalem et al., 2014). The remaining sections of this introductory Chapter will outline examples in which CRISPR screens were used to specifically identify mediators of PARPi sensitivity and resistance.

1.11. Genetic determinants of PARPi resistance

The development of resistance, which is typical of targeted therapeutic strategies, negates the initial PARPi-induced anti-tumour activity in patients with *BRCA1/2*-mutated tumours (Lord & Ashworth, 2017). *De novo* PARPi resistance is also possible. CRISPR screens have validated previously identified mechanisms of PARPi resistance and further refined the responsible pathway mechanisms. As summarised in Figure 1.8, these include restoration of HR function, including secondary mutations which restore the open reading frame of HR repair genes, or via removal of barriers to DNA end resection; protection of the RF; PARP1 mutations; and pharmacological alteration. In the preceding sections, I will provide more details into each of these PARPi resistance mechanisms, in context of their recent confirmation with CRISPR screens.

1.11.1. Restoration of HR capacity

"Reversion mutation" and restoration of HR repair gene reading frame.

The reversion of *BRCA*-truncating mutations was initially observed *in vitro* with

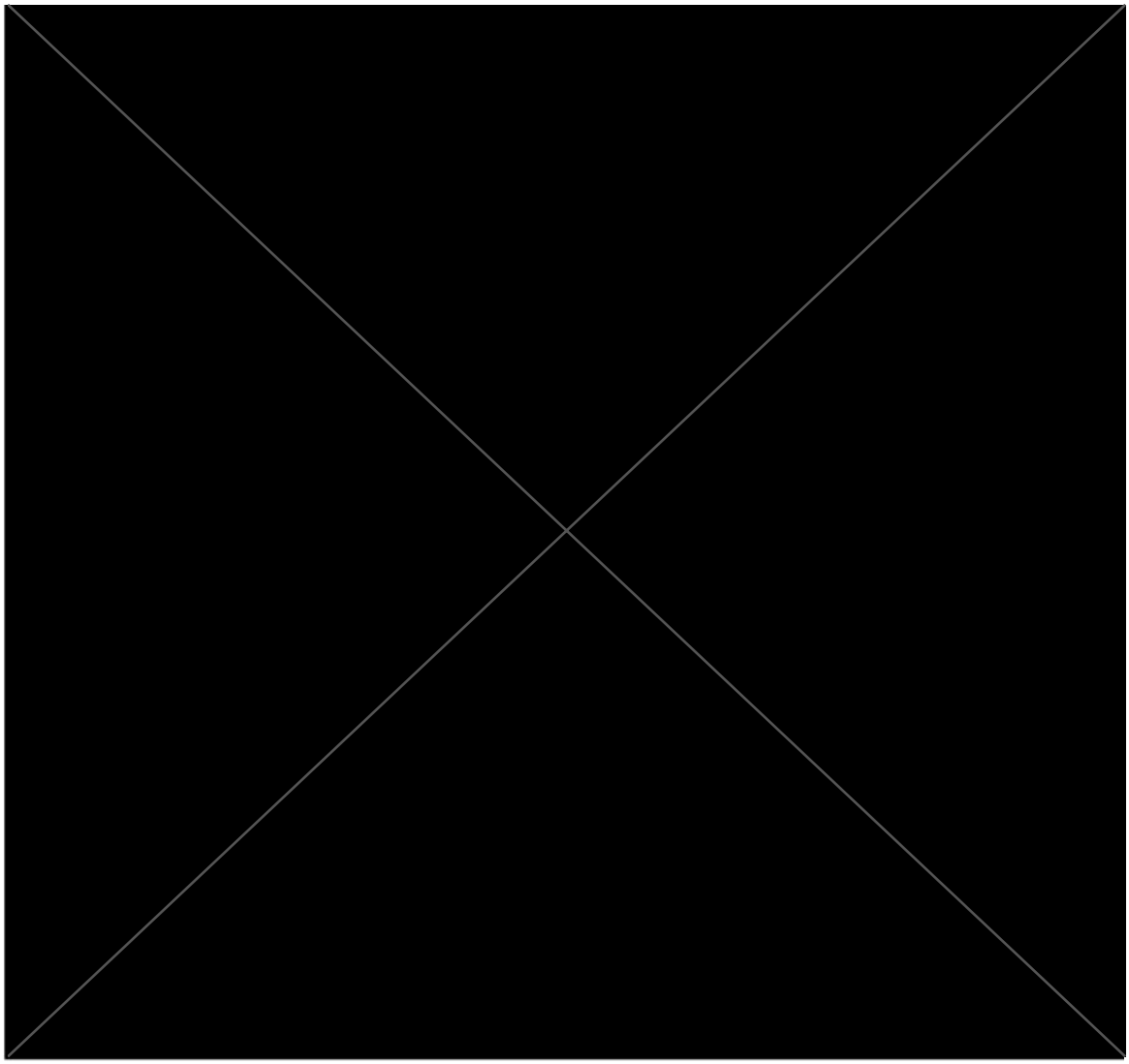

Figure 1.8 Summary of mechanisms of PARPi resistance.
Schematic summarising mechanisms of PARPi resistance. These comprise restoration of homologous recombination (HR) function, including secondary mutations which restore the open reading frame of HR repair genes, or via removal of barriers to DNA end resection; protection of the RF; mutations in the DNA-binding domains of PARP1 and mechanisms rewiring the DNA damage response (DDR). Figure from Kim et al. (2021).

BRCA2-mutated pancreatic and ovarian cancer cell lines (Edwards et al., 2008; Sakai et al., 2009; Sakai et al., 2008). Resistant clones were generated with long-term exposure with PARPi or platinum salt, in which the majority of clones acquired secondary *BRCA2* mutations; these constituted restoration of full-length BRCA2, or BRCA2 protein with intact C-terminal domains required for HR function. HR competency was confirmed in these cells, as well as resistance to both PARPi and platinum salts. Similar observations in patient-derived xenograft (PDX) models of *BRCA1*-mutated and *BRCA*-methylated triple-negative breast cancer have been made (Sakai et al., 2008). BRCA1 re-expression was demonstrated in 31 out of 42 resistant cases after chemotherapy or PARPi exposure. In a *BRCA1*-mutated PDX model, acquired secondary mutations restored the reading frame, while those with *BRCA1* epigenetic silencing demonstrated demethylation of the promoter region (Ter Brugge et al., 2016). Intriguingly, BRCA1 re-expression in four resistant cases was attributed to *de novo* gene fusions, resulting in BRCA1 being positioned under the transcriptional control of a heterologous promoter, while *BRCA1* promoter methylation was conserved. As such, it was determined that the mechanism of BRCA1 restoration was dependent on the type of *BRCA1* inactivation (Sakai et al., 2008). Clements et al. further refined this mechanism of PARPi resistance, with a genome-wide CRISPRn screen demonstrating that loss of ubiquitin ligase *HUWE1* caused PARPi resistance in *BRCA2*-deficient cells by increasing RAD51 levels to partially restore HR (Clements et al., 2020).

Multiple clinical cases have been reported where PARPi exposure has resulted in selective pressure for functional BRCA1/2 restoration in resistant breast (Barber et al., 2013), ovarian (Barber et al., 2013; Edwards et al., 2008; Goodall et al., 2017;

Lheureux et al., 2017) and pancreatic (Pishvaian et al., 2017) cancers. Similarly, in patients with breast (Afghahi et al., 2017), ovarian (Norquist et al., 2011; Patch et al., 2015; Sakai et al., 2009; Sakai et al., 2008) and pancreatic (Pishvaian et al., 2017) cancers, somatic BRCA recovery has been evidenced in patients with acquired resistance to platinum-based drugs. Several independent reversion events have been observed in some patients. Notably, Patch et al. (2015) detected 12 independent reversions from a chemoresistant *BRCA2*-mutated ovarian cancer patient. This suggests intra-patient heterogeneity and multiclonal evolution of resistant disease. Reversion mutations in genes beyond *BRCA1/2* genes have also been detected. In PARPi-resistant ovarian cancer patients, reversion mutations in *RAD51C* (Kondrashova et al., 2017) and *PALB2* (Goodall et al., 2017) have been identified in ovarian cancer patients. Despite the fact that reversions are the only clinically-demonstrated resistance mechanism thus far, they only explain a fraction (up to 40% in ARIEL2 trial) of PARPi resistance cases (Pettitt et al., 2020), while the resistance mechanisms of remaining cases remain unaccounted for.

Restoration of DNA end resection

Studies from Bouwman et al., Bunting et al. and Jaspers et al. (Bouwman et al., 2010; Bunting et al., 2010; Jaspers et al., 2013) found that restoration of DNA end resection, via loss of *53BP1*, mediates PARPi resistance in *BRCA1*-deficient cells. As such, restoration of DNA end resection restores HR, which impedes synthetic lethality. Bouwman and colleagues utilised the piggyBac transposon system to carry out an insertional mutagenesis screen for factors that could restore the defective proliferation associated with loss of *Brca1*. *Trp53bp1* loss-of-function mutation was reported to rescue *Brca1*-null cell clonal outgrowth. Correspondingly,

shRNA-mediated Trp53bp1 depletion rescued the enhanced cisplatin sensitivity of *Brca1*-deficient ES cells (Bouwman et al., 2010). More relatedly, in the presence of PARPi, *Brca1*-mutant cells with *Trp53bp1* deletion (*Brca1*$^{\Delta 11/\Delta 11;}$ *Trp53bp1*$^{-/-}$) demonstrated increased cell viability compared to cells with only *Brca1* mutation (*Brca1*$^{\Delta 11/\Delta 11}$) (Bunting et al., 2010). Loss of *Trp53bp1* was shown to partially restore defective HR associated with *Brca1*-mutant cells. In the *Brca1*$^{\Delta 11/\Delta 11;}$ *Trp53bp1*$^{-/-}$ *cell model,* RAD51 foci were induced upon damage and GFP-positive cells were observed via DR-GFP assay, both of which are indicative of HR, which were not observed in *Brca1*$^{\Delta 11/\Delta 11}$ cells. Ultimately, Bunting and colleagues demonstrated that loss of *Trp53bp1* resulted in increased DSB end resection (Bunting et al., 2010). Given that NHEJ-mediated ligation can occur with unresected DNA ends, while 5'-3' end resection is obligatory for HR, DNA end protection mediated by 53BP1 (Trp53bp1*)* stimulates NHEJ. During S phase, this is inhibited by BRCA1. Given the inability to process DSB ends, *BRCA1*-deficient cells are unable to initiate HR (Shibata, 2017). *In vivo* mouse models have supported *Trp53bp1*-mediated PARPi resistance in *Brca1*-defective tumours, whereby acquired PARPi resistance was linked to de novo protein-truncating mutations in *Trp53Bp1* (Jaspers et al., 2013).

Noordermeer et al. further refined this model to demonstrate that loss of components of a 53BP1-effector complex, referred to as Shieldin, mediates PARPi resistance in *BRCA1*-deficient setting (Noordermeer et al., 2018). Comprised of C20orf196 (SHLD1), FAM35A (SHLD2), CTC-534A2.2 (SHLD3) and REV7, Shieldin's role in mediating PARPi response was emphasised in an independent publication, which confirmed that loss of *SHLD1* induced PARPi resistance in

BRCA1-deficient cells (Noordermeer et al., 2018). SHLD2 binding to ssDNA via three predicted OB (oligonucleotide/oligosaccharide-binding) fold domains (Noordermeer et al., 2018) has been proposed as the mechanism by which Shieldin inhibits DNA end resection (Noordermeer et al., 2018). Several other studies also identified the role of Shieldin in suppressing resection (Dev et al., 2018; Ghezraoui et al., 2018; Gupta et al., 2018; Mirman et al., 2022).

An additional contributory factor involved in the observed maintenance of Shieldin-mediated DSB resection was identified by Barazas et al., who carried out several CRISPR screens (Barazas et al., 2018). In *Brca1*-deficient mouse cells, Barazas et al. performed genome-wide and focused screens with an sgRNA library containing DDR-associated genes. They also performed a genome-wide screen in the human *BRCA1*-mutant SUM149 cell model. They identified that loss of *CTC1* drives PARPi resistance to a similar degree as a known mediator of PARPi resistance, *53BP1*. Post-screen validation demonstrated that in addition to *CTC1*, loss of *STN1* and *TEN1*, which collectively comprise the CST complex, mediate PARPi resistance in *BRCA1*-deficient cells. By visualising RPA loading with immunofluorescence, they attributed the observed PARPi resistance to restoration of DNA end processing (Barazas et al., 2018). The POLA-dependent fill-in DNA synthesis, in which the CST complex mediates its well-established function at the telomere, could also explain the mechanism behind CST-mediated inhibition of end resection at non-telomeric DSBs. An independent manuscript confirmed these observations (Mirman et al., 2022).

Another CRISPR screen demonstrated a similar mechanism of PARPi resistance of restoration of DNA end resection, but independent of 53BP1. In *BRCA1*-deficient cells, loss of *Dynein light chain 1* protein (*DYNLL1*) has been attributed with olaparib or cisplatin resistance in *BRCA*-deficient ovarian cancer cell lines (He et al., 2018). As detailed in an earlier section of this thesis, MRE11 catalyses short-range resection, limited to the vicinity of the DSB, as part of the MRN complex (Yun & Hiom, 2009), which is an essential step to initiate HR. Post-screen mechanistic experiments determined that DYNLL1 binds directly with MRE11 to inhibit its end resection activity (He et al., 2018). As such, loss of DYNLL1 restores HR in *BRCA*-deficient cells (He et al., 2018).

1.11.2. Protection of the replication fork

The results from the genome-wide CRISPRn screen performed in *BRCA*-mutant background by Clements et al. validated earlier observations of PARPi resistance resulting from protection of the RF via reduced MRE11 recruitment to stalled RFs (Ray Chaudhuri et al., 2016). Given that *BRCA1* and *BRCA2*, independent of their HR function, impart vital protective functions for stalled RFs (Berti et al., 2013; Lomonosov et al., 2003; Schlacher et al., 2012), their absence leads to extensive degradation of protected forks. Independent of its function in 53BP1-mediated DSB repair, *PTIP* or *MLL3/4* in *BRCA2*-mutant cells restored RF protection by preventing MRE11 recruitment to stalled RFs (Ray Chaudhuri et al., 2016). *Ptip* loss not only rescued the viability of *Brca2*-deficient murine ES cells, it also maintained genome stability with exposure to PARPi, as well as other replication poisons such as HU and cisplatin (Ray Chaudhuri et al., 2016). Similarly, downregulation of nucleosome remodelling factor *CDH4* in *BRCA2*-mutant PEO1

cells rewired RF protection via decreased MRE11-RF association, resulting in partial PARPi and cisplatin resistance (Guillemette et al., 2015; Ray Chaudhuri et al., 2016).

Upon their inactivation, further factors have been identified to contribute to RF progression in the absence of functional *BRCA1/2.* Inhibition of the methyltransferase *EZH2* has been shown to stabilise RFs independently of MRE11, via restricted recruitment of *MUS81*, in partially PARPi- and cisplatin-resistant *BRCA2*-deficient cells (Rondinelli et al., 2017). MRE11- and EXO1 nuclease-mediated RF degradation may be initiated by fork reversal, which results from replication stress (Lemacon et al., 2017; Mijic et al., 2017). Correspondingly, ZRANB3, SMARCAL1 and HLTF are fork remodellers which have been shown to stimulate MRE11-dependent RF degradation (Kolinjivadi et al., 2017; Taglialatela et al., 2017; Vujanovic et al., 2017). Loss of the aforementioned factors restored RF integrity in *BRCA1/2*-deficient cells. *SMARCAL1* depletion has also been shown to decrease the sensitivity of *BRCA1*-deficient tumour cells to PARPi and chemotherapy agents (Kolinjivadi et al., 2017; Taglialatela et al., 2017).

Although all these factors mediate partial PARPi resistance in *BRCA*-deficient cells via protection of reversed RFs from nucleolytic degradation, further work is required to establish the coordination of all these processes to promote fork stability in the absence of *BRCA1/2*. Given that genomic instability is prevented, rather than reverted, with RF rewiring, the partial therapy resistance conferred by these factors is justified. The evasion of cisplatin toxicity by restoration of RF

protection seems conceivable, while the mechanism underlying PARPi resistance seems more complex. Increased premature, RECQ1-dependent restart of reversed RFs has been demonstrated upon PARPi exposure. As such, RF stabilisation is abrogated, which is required for subsequent RF degradation (Berti et al., 2013; Mijic et al., 2017; Ray Chaudhuri et al., 2012). The genome-wide CRISPRn screen performed by Clements et al. further refined this model to demonstrate that loss of acetyl-transferase *KAT5* mediates PARPi resistance via rescue of fork degradation defect in *BRCA2*-deficient cells. They demonstrated this via DNA fibre assay; as expected, RF progression was slower in *BRCA2*-deficient cells than in wild-type cells. siRNA-mediated *KAT5* depletion rescued the speed of RF progression in BRCA2-deficient cells, to a similar rate observed in the wild-type cells (Clements et al., 2020).

1.11.3. Pharmacological alteration

The genome-wide CRISPRa screen performed in a *BRCA2*-deficient background by Clements et al. (Clements et al., 2020) validated earlier findings from Rottenberg et al. that overexpression of ABCB1 results in PARPi resistance (Rottenberg et al., 2008). Increased drug efflux is a well-established phenomenon of pharmacological resistance in cancer therapy (Borst et al., 2000), resulting in insufficient accumulation of compound. Correspondingly, PARPi resistance became evident in mammary tumours arising from genetically engineered mouse models for *Brca1*-mutated breast cancer, which was attributed to upregulation of *Abcb1a/b* genes, which encode the drug efflux transporter P-glycoprotein (P-gp) (Rottenberg et al., 2008). Simultaneous administration of olaparib and P-gp inhibitor (tariquidar) restored PARPi sensitivity (Rottenberg et al., 2008). In the

clinic, the extent of P-gp-mediated PARPi resistance remains unclear. P-gp upregulation, resulting from *ABCB1* gene fusions and translocations, was identified in 8% of chemoresistant ovarian cancers in a large-scale whole-genome sequencing study (Patch et al., 2015). Given that PARPi have been approved for ovarian cancers on the condition of previous exposure to chemotherapy, further efforts are required to evaluate the significance of P-gp as a biomarker.

1.11.4. PARP1 mutations

The genome-wide CRISPRn screen performed by Pettitt et al. in 2018 (Pettitt et al., 2018) corroborated prior observations by Murai et al.; *PARP1*-deficient cells were more resistant to PARPi than wild-type cells in a HR-proficient setting (Murai et al., 2012). This was also corroborated by a prior genome-wide shRNA screen (Bajrami et al., 2014) in *BRCA1/2*-proficient MCF7 cells, and in a genetic perturbation screen utilising the piggyBac transposon system in *BRCA1/2*-proficient haploid ES cells (Pettitt et al., 2013). In a panel of 30 isogenic mutant avian DT40 cell lines with a variety of different DNA repair deficiencies, Murai et al. assessed PARPi response (Murai et al., 2012). Compared to wild-type cells, DT40 cells with *PARP1* deletion were more resistant to all PARPi assessed; olaparib, MK-4827, and to a lesser extent, veliparib. They utilised a fluorescence anisotropy binding assay whereby DNA substrate is labelled with Alexa Fluor488. PARP1 binding to DNA substrate results in slow rotation with a high fluorescence anisotropy readout whereas unbound DNA substrate rotates fast with a low fluorescence anisotropy readout. Murai and colleagues demonstrated dose-dependent increased fluorescence anisotropy readout with the PARP inhibitors MK-4827 and olaparib. As such, PARPi-induced cytotoxicity was

attributed, at least partly, to trapping of PARP1/2 onto DNA. As a result of this preclinical study, *PARP1* has been established as a key mediator of PARPi response (Murai et al., 2012). PARPi binding to the catalytic pocket of PARP1 was hypothesised to enhance interaction between PARP1 N-terminal DNA-binding domain and DNA (Murai, Huang, et al., 2014). Consistent with this hypothesis, Pettitt et al. demonstrated that point mutations in the *PARP1* DNA-binding ZnF domains abrogated PARP1 trapping, with observed decreased PARPi (talazoparib) sensitivity (Pettitt et al., 2018). Beyond the DNA-binding domain of PARP1, further candidate residues have been identified as important for PARPi cytotoxicity via CRISPR-mediated PARP1 mutagenesis (Pettitt et al., 2018). Other intramolecular interactions were reported to manipulate PARP1 binding and activation, and consequently affect PARPi-mediated PARP1 trapping. In this study, a *PARP1* mutation was identified in a PARPi-resistant patient, which resulted in failure to trap to DNA upon PARPi exposure (Pettitt et al., 2018).

1.11.5. CRISPR screens identify determinants of PARPi sensitivity

From the compendium of the aforementioned preclinical work, including CRISPR screens, various candidate genes and mechanisms have been suggested to contribute to PARPi resistance; these include reversion mutations, which have even been demonstrated in the clinic. In comparison, preclinical work regarding mechanisms for PARPi sensitivity is reported less frequently; most likely due to the more technically challenging ability to detect genes which mediate PARPi sensitivity with CRISPR screens – up until recently, CRISPR screens had primarily been used to screen only for resistance mechanisms. Recently, a few groups have

reported several candidate genes, beyond *BRCA1* and *BRCA2*, responsible for altering PARPi response by CRISPR screening.

Zimmerman and colleagues performed multiple CRISPR screens to identify genetic determinants of PARPi sensitivity (Zimmermann et al., 2018). Following genomic DNA extraction and sequencing of the olaparib-selected and control DMSO-selected cell populations, use of the DrugZ algorithm (Colic et al., 2019) revealed genes whose inactivation might mediate olaparib sensitivity. 73 such genes were identified, including three *RNASEH2*-family genes, *RNASEH2A, RNASEH2B, RNASEH2C.* In post-screen validation experiments, RNase H2 deficiency was demonstrated to cause defective RER and consequently accumulation of topoisomerase 1 (TOP1)-cleaved ribonucleotides. Ribonucleotide processing results in nicks, covalent TOP1-DNA adducts, as well as ssDNA gaps. These can act as PARP1-trapping lesions so impart PARPi efficacy (Zimmermann et al., 2018). As with the PARPi olaparib, similar phenotypes were reported with the PARPi talazoparib, which imparts enhanced ability to trap PARP1 onto DNA (Krastev et al., 2021; Murai et al., 2012). This screen was performed in multiple cell line models, each of which are representative of a different type of cancer: HeLa derived from a human papilloma virus-induced cervical adenocarcinoma; RPE1-hTERT, a telomerase-immortalised retinal pigment epithelium cell line; and SUM149PT, originating from a triple-negative breast cancer with a hemizygous BRCA1 mutation (Elstrodt et al., 2006). Therefore, the findings from this screen are likely highly penetrant and have furthered our understanding of the PARP1-trapping model for PARPi cytotoxicity.

Another group aimed to identify genes responsible for altering PARPi response, specifically in a HR-proficient context, via CRISPR screening. *C12orf5* was identified as a mediator of olaparib sensitivity upon its CRISPRn-mediated dysfunction. *C12orf5* encodes a metabolic regulator, *TP53*-induced glycolysis and apoptosis regulator (TIGAR). In post-screen mechanistic dissection, elevated ROS were reported upon siRNA-mediated *TIGAR* depletion, which in turn enhances DNA damage (Fang et al., 2019). In addition, the downregulation of BRCA1 was observed upon *TIGAR* KD, inducing "BRCAness" (Fang et al., 2019). The A2780 ovarian cancer cell line was used for the initial CRISPR screen, and two other ovarian cell lines for validation. Given the limited range of cancer cell models used to demonstrate the reported phenotypes, the penetrance of the identified PARPi-*C12orf5* synthetic lethality remains to be evaluated.

Several groups have also performed genome-wide screens in HR-deficient cell lines, with the aim to identify genes which potentiate PARPi therapy to overcome resistance. In HR-deficient MUS81$^{-/-}$ cells, PARPi sensitivity was observed upon loss of *DNPH1* (2′-deoxynucleoside 5′-monophosphate N-glycosidase), which is involved in nucleotide salvage pathways (Fugger et al., 2021). Interestingly, *inosine triphosphatase (ITPA)*, another nucleotide sanitiser, was also identified. Post-screen validation demonstrated that the PARPi-DNPH1 synthetic lethality is also applicable to *BRCA1*-mutant and *BRCA2*-defective cells. Although *DNPH1* was known to hydrolyse deoxyribonucleoside monophosphates (dNMPs) *in vitro*, Fugger et al. identified that *DNPH1* specifically acts upon cytotoxic hydroxymethyl-deoxyuridine (hmdU) monophosphate (hmdUMP) in the nucleotide pool to limit genomic DNA incorporation. As such, loss of *DNPH1* was found to

increase hmdU levels, which they attributed to PARPi sensitivity. Cotreatment with hmdU and olaparib induced strong synthetic lethality in various *BRCA1*- and *BRCA2*-deficient cells, increasing the therapeutic window by up to three-fold (Fugger et al., 2021).

Aiming to elucidate loss-of-function mutations in chromatin regulators which mediate PARPi sensitivity, Verma et al. (Verma et al., 2021) performed a focused CRISPR screen using an sgRNA library targeting chromatin regulators in three different *BRCA*-mutant cell lines. *ALC1* loss resulted in olaparib sensitivity in all assessed cell lines; *BRCA1* exon 11 mutant ovarian UWB1.289 and breast SUM149 cell lines, as well as *BRCA2*-mutant pancreatic cell line CAPAN1. Follow-up mechanistic experiments with ATAC-seq were used to assess global accessibility of chromatin. Compared to *ALC1* loss alone, or talazoparib treatment alone, *ALC1* depletion in combination with talazoparib resulted in greater reduction of chromatin accessibility. As such, the association of base damage repair proteins on the chromatin is decreased, leading to increased replication-associated DNA damage and reliance on HR. *ALC1* loss as a driver of olaparib sensitivity in HR-deficient cells was also confirmed with genome-wide CRISPR screens in an independent publication (Hewitt et al., 2021), whereby depletion of HR factors (*BRCA1, RAD51*, *RAD51C*, *CHD4*) reduced the viability of *ALC1*-defective cells upon olaparib treatment. Additionally, depletion of factors involved in DSB resection (*RAD50*, *UBE2N/UBC13*, and *DNA2*), or the DSB-sensing kinase *ATM* confer PARPi sensitivity when combined with *ALC1* loss (Hewitt et al., 2021).

Although the cancer cell line models used in the aforementioned CRISPR screens (e.g. HeLa, U2OS etc.) represent a practical choice to facilitate the experimental execution of CRISPR screens, given their high proliferation rate which allows quick generation of the large cell numbers required for a genome-wide CRISPR screen (typical 1000X representation requires approximately 100 million cells with sgRNA libraries e.g. Yusa), they may not represent the most suitable cell line model choice for CRISPRn screens. Cancer cells are inherently heterogenous and frequently demonstrate varying levels of aneuploidy (Cohen-Sharir et al., 2021). Therefore, cancer cell lines may not represent the most suitable cell lines to assess the effects of altering gene expression on drug response (Soule et al., 1990), and also pose problems of copy number dependent toxicity of sgRNAs observed with CRISPRn; a phenomenon which can lead to false positives (Aguirre et al., 2016). In addition, the utilised cell line models may not be clinically relevant, and the penetrance of the identified synthetic lethal effects has not been fully explored. The aforementioned factors may provide an explanation as to why none of the candidate genes identified from the CRISPR screens for PARPi sensitivity have been demonstrated clinically.

All the published CRISPR screens reporting determinants of PARPi sensitivity utilise CRISPR mutagenesis (CRISPRn). While CRISPRn-mediated mutagenesis results in gene “knockout”, whereby expression of the target gene is completely ablated, CRISPRi-mediated transcriptional repression reduces expression of the target gene. Determinants of PARPi sensitivity upon transcriptional repression (CRISPRi) remains to be explored.

1.12. Aims and approaches

Despite the progress made for patients with *BRCA1* or *BRCA2* mutations, the possible reasons for the PARPi efficacy observed in *BRCA1/2* wild-type patients (for example, Figure 1.5C) have not been fully worked out. Further pre-clinical studies will help to optimise the current use of PARPi in the clinic by informing future trials, and potentially extend the utility of PARPi beyond BRCA-PARP synthetic lethality. Therefore, the aim of my project was to identify novel determinants of PARPi sensitivity to potentially address the question of what determines PARPi sensitivity beyond *BRCA1*, *BRCA2* and other HR gene mutations. Overall, this thesis aims to contribute to the mechanistic insight of our understanding of how PARPi response is controlled in mitotic cells in order to potentially overcome the current limitations of PARPi in the clinic.

In order to achieve this, I decided to use an unbiased genetic screening approach. By performing two parallel CRISPR screening approaches of parallel CRISPR mutagenesis and interference screens, I aimed to minimise the issue of off-target effects that have been reported with CRISPR screens. I also aimed to use two different clinical PARPi to minimise drug-specific effects. In order to ensure that the findings of my CRISPR screen could be potentially translated into the clinic, I used a p53 mutant breast cell line which more accurately reflects the disease context in which clinical PARPi are typically used. Using this approach, CRISPR mutagenesis and interference screens identified the meiotic recombination heterodimer PSMC3IP-MND1 as controlling PARPi response in mitotic cells.

Since *MND1* and *PSMC3IP* are conventionally thought to be involved in meiosis, I aimed to establish whether these proteins are commonly expressed in mitotic tumour cells and human tumours. Once I had confirmed that this was indeed the case, I validated the findings of my screen using CRISPR-Cas9 gene editing technology to generate *MND1*- or *PSMC3IP*-defective cell lines.

I aimed to assess the effect of *MND1* and *PSMC3IP* dysfunction on a common readout for HR-mediated DNA repair, RAD51 foci formation. Using this approach, I found that *MND1*- or *PSMC3IP*-deficient cells accumulate RAD51 foci in response to DNA damage, which is in direct contrast to the findings in other genotypes that confer PARPi sensitivity such as *BRCA1* or *BRCA2* mutant cells. Finally, I aimed to deduce the functions which MND1 and PSMC3IP contribute to in the context of PARPi sensitivity. To this end, I demonstrated that PSMC3IP-MND1 heterodimer may support RAD51-mediated D-loop formation, which mediates PARPi response. This is corroborated by the fact that a *PSMC3IP* p.Glu201del D-loop formation mutant associated with ovarian dysgenesis fails to reverse PARPi sensitivity. The hypothesis of impaired D-loop formation being responsible for the HR defect and toxic RAD51 foci formation in *MND1* or *PSMC3IP* defective cells are strengthened with our experiments demonstrating rescue of PARPi sensitivity of *MND1*- and *PSMC3IP*-defective cells using small molecule RAD51 inhibitor, B02, which specifically inhibits ssDNA and dsDNA binding, as well as strand exchange activity of RAD51.

Chapter 2. Materials and Methods

Reagents

2.1. General chemicals and solutions

PBS: 137 nM NaCl, 2 mM KCl, 8 mM Na_2HPO_4, 1.5 mM KH_2PO_4 in H_2O, pH adjusted to 7.4 with HCl.

10x TBS: 200 mL 1M Tris pH 7.5, 300 mL 5M NaCl made up to 1L with H_2O.

Sulphorhodamine B (SRB): 0.057% sulphorhodamine B (w/v) in 1% acetic acid.

TCA: 10% trichloroacetic acid (TCA) in H_2O.

PFA: 4% (w/v) paraformaldehyde in PBS.

Transfer buffer: 14.4 g glycine, 3.03 g Tris, 200 mL methanol, made up to a final volume of 1 L with H_2O.

Permeablisation solution: 20 mM TRIS-HCl, 50 mM NaCl, 3 mM $MgCl_2$, 1M sucrose, 0.5% Triton X-100 made up to a final volume of 50 mL with H_2O.

Blasticidin: (A1113903, Thermo Fisher Scientific, Thermo).

Puromycin: (A1113803, Thermo).

EDTA 0.5M: di-sodium salt of ethylenediaminetetraacetate in H_2O, pH adjusted to 8.0 with NaOH.

MOPS: 3-(N-morpholino)propanesulfonic acid (Thermo).

TRIS: tris(hydroxymethyl)aminomethane (Thermo).

10X TAE: 48.4 g Trizma base, 20 mL 0.5 M EDTA pH 8.0, 11.43 mL glacial acetic acid made up to a final volume of 1 L with H_2O.

2.2. Cell lines and growth media

Table 2.1 Cell lines and corresponding growth medium used in this thesis.

Cell line	Origin	Source	Media	Media additives
MCF10A *TP53*$^{-/-}$ MCF10A *TP53*$^{-/-}$ *RB1*$^{-/-}$	Breast (human)	ATCC	DMEM/Ham's F-12 (Gibco, 11330-032)	5% horse serum (Thermo, 16050-122); EGF (20 ng/mL); hydrocortisone (0.5 mg/mL); cholera toxin (100 ng/mL); insulin (10 µg/mL)
CAL51		DSMZ	DMEM (Gibco, 11960)	10 % FBS (Thermo, 10437028)
MDAMB-231		ATCC	DMEM (Gibco, 11960)	10 % FBS (Thermo, 10437028)
SUM149		Asterand Bioscience	Ham's F-12 medium (11765054)	5 % FBS (Thermo, 10437028); 10 µg/mL insulin; 1 µg/mL hydrocortisone
KB1P-G3 KB1P-G3B1	Mammary (mouse)	Barazas et al., 2019	DMEM/Ham's F-12 (Gibco, 11330-032)	10% foetal calf serum (FCS, Sigma); 50 units/mL penicillin-streptomycin (Gibco); 5 µg/mL Insulin (Sigma, #I0516); 5 ng/mL cholera toxin (Sigma, #C8052); 5 ng/mL murine epidermal growth-factor (EGF, Sigma, #E4127).
U2OS DR-GFP	Bone (human)	Gift from Jeremy Stark	DMEM (Gibco, 11960)	10 % FBS (Thermo Fisher Scientific, 10437028)
HAP1	Chronic myelogenous leukaemia (CML) (human)	Horizon	Iscove's Modified Dulbecco's Medium (IMDM, 12440053)	10 % FBS (Thermo Fisher Scientific, 10437028)

HEK293T	Kidney (human)	ATCC	DMEM (Gibco, 11960)	10 % FBS (Thermo Fisher Scientific, 10437028)
Phoenix-ECO		ATCC	DMEM (Gibco, 11960)	10% foetal calf serum (FCS, Sigma) and 50 units/mL penicillin-streptomycin (Gibco).

Abbreviations: ATCC American Type Culture Collection; CML Chronic myelogenous leukaemia; DMEM FBS Foetal bovine serum; EGF epidermal growth-factor; FCS Foetal calf serum; IMDM Iscove's Modified Dulbecco's Medium.

2.3. Antibodies

Table 2.2 Details of antibodies used in this thesis.

Antibody	Application	Dilution	Manufacturer	Product code
Rabbit polyclonal anti-RAD51	Immunofluorescence	1:2,000	Santa Cruz	sc-8349
Mouse monoclonal Anti-phospho-H2AX (Ser139), clone JBW301			Millipore	05-636
Goat anti-mouse IgG (H+L) cross-adsorbed secondary antibody, Alexa Fluor 555		1:1,000	Thermo Fisher Scientific	A-21422
Goat anti-rabbit IgG (H+L) cross-adsorbed secondary antibody, Alexa Fluor 488				A-11034
Mouse monoclonal CRISPR-Cas9	Immunoblotting	1:1,000	Novus	NBP2-36440
Rabbit polyclonal anti-PSMC3IP			Atlas	HPA044439
Rabbit polyclonal anti-MND1			Atlas	HPA043499
Monoclonal rabbit anti-V5-Tag			Cell Signaling Technology	13202

Rabbit monoclonal anti-RAD51			Abcam	ab133534
Monoclonal rabbit anti-HA-Tag (C29F4)			Cell Signaling Technology	3724
Mouse monoclonal anti-β-Actin			Sigma	A2228
Anti-rabbit IgG, HRP-linked secondary			Cell Signaling Technology	7074
Anti-mouse IgG, HRP-linked secondary			Cell Signaling Technology	7076
IRDye 800CW anti-rabbit IgG donkey secondary		1:10,000	LI-COR	926-32213
IRDye 800CW anti-Mouse IgG goat secondary			LI-COR	925-32210
IRDye 680RD anti-mouse IgG Goat secondary			LI-COR	926-68070
Mouse monoclonal anti-BrdU/IdU	DNA fibre assay	30 µM	BD Biosciences	347580
Rat monoclonal Anti-BrdU/CldU		150 µM	Abcam	ab6326
Goat Anti-Mouse IgG (H+L) highly cross-adsorbed secondary, Alexa Fluor 488		1:300	Thermo Fisher Scientific	A-11029
Donkey anti-Rat IgG (H+L) Cy3 AffiniPure $F(ab')_2$ Fragment		1:150	Jackson ImmunoResearch	712-165-513

Abbreviations: BrdU Bromodeoxyuridine; CIdU 5-chloro-2'-deoxyuridine; HRP Horseradish peroxidase; IdU 5-iodo-2′-deoxyuridine.

2.4. Oligonucleotides

Table 2.3 Details of oligonucleotides used in this thesis.

Oligonucleotide type	Application	Oligonucleotide sequence (5'-3') or Cat #
CRISPR RNA (crRNA)	MCF10A *TP53*$^{-/-}$ *MND1* CRISPR-targeting.	CTTGCATGAAGAGCTTTACT CGGAACTTCTAATTATTATT
	MCF10A *TP53*$^{-/-}$ *PSMC3IP* CRISPR-targeting.	GCTGACCTTCAAGTCCTAGA GTGAGGTTGAACACTTACTT
	MCF10A *TP53*$^{-/-}$ CRISPR non-targeting control	GATACGTCGGTACCGGACCG
sgRNA	MCF10A *TP53*$^{-/-}$ *MND1* CRISPRi targeting (sgMND1-1)	GCGGCGAAGCCCACACACTA
	MCF10A *TP53*$^{-/-}$ *MND1* CRISPRi targeting (sgMND1-2)	GGTAGCCTCAGTCCTTACCA
	MCF10A *TP53*$^{-/-}$ PSMC3IP CRISPRi targeting (sgPSMC3IP-1)	GCGGGAAAGGCGATGAGTAA
	MCF10A *TP53*$^{-/-}$ PSMC3IP CRISPRi targeting (sgPSMC3IP-2)	GAAGCTGCGGCGGGAGGTAA
	KB1P-G3B1 *MND1* CRISPR-targeting (sgMnd1-1)	GACAAACATACCGTCTCTTGC
	KB1P-G3B1 *MND1* CRISPR-targeting (sgMnd1-2)	GTCATGCCAGGAAGCGCAAGT
	KB1P-G3B1 CRISPR non-targeting control	TGATTGGGGGTCGTTCGCCA
TIDE analysis primer	Forward primer for KB1P-G3B1 *MND1* CRISPR-targeting (sgMnd1-1)	AACACAAGCTAAGCCAACAGTC
	Reverse primer for KB1P-G3B1 *MND1* CRISPR-targeting (sgMnd1-1)	TCCCCATGTAACAACTGAGAAA
	Forward primer for KB1P-G3B1 *MND1* CRISPR-targeting (sgMnd1-2)	GCTGCTTAACTTAGCGTCTGTG
	Reverse primer for KB1P-G3B1 *MND1* CRISPR-targeting (sgMnd1-2)	GCGTTGAGCCCAAATAAGAA

PCR primer	Forward primer for *PSMC3IP* site-directed mutagenesis (PSMC3IP p.Glu201del)	GCAAGAAGCAGTTCTTTGAGGTTG GGATAGAGACGGATGAAG
	Reverse primer for *PSMC3IP* site-directed mutagenesis (PSMC3IP p.Glu201del)	CTCAAAGAACTGCTTCTTGCTCTTG
siRNA	MND1 silencing	Horizon, D-014779-01 Horizon, D-014779-02 Horizon, D-014779-03 Horizon, D-014779-04 Horizon, M-014779-00
	PSMC3IP silencing	Horizon, D-018726-01 Horizon, D-018726-02 Horizon, D-018726-03 Horizon, D-018726-04 Horizon, M-018726-01
	PLK1 silencing	Horizon, M-003290
	BRCA1 silencing	Horizon, M-003461
	BRCA1 silencing	Horizon, M-003462
DNA Sanger sequencing primer	Forward primer for *PSMC3IP*	GAAATCCAGGAGTTAAAGAAG
	Reverse primer for *PSMC3IP*	GGCCAGAGCTGCCAGGAAAC
	Forward M13 primer	GTAAAACGACGGCCAG-
	Forward primer U6	GGCCTATTTCCCATGATTCCTTC
HiSeq PCR CRISPRi primer	Forward primer for 1st HiSeq PCR CRISPRi	GACTTGTGGGAGAAGCTCGG
	Reverse primer for 1st HiSeq PCR CRISPRi	TGCATGGCGGTAATACGGTT
	Primer for 2nd HiSeq PCR CRISPRi	CAAGCAGAAGACGGCATACGAGAT CGACTCGGTGCCACTTTTTC
	Barcode primer sequence for 2nd HiSeq PCR CRISPRi iPCRtag1	aatgatacggcgaccaccgagatctacacgatcg gaagagcacacgtctgaactccagtcacCTTG TAgcacaaaaggaaact caccct
	Barcode primer sequence for 2nd HiSeq PCR CRISPRi iPCRtag2	aatgatacggcgaccaccgagatctacacgatcg gaagagcacacgtctgaactccagtcacGCCA ATgcacaaaaggaaact caccct
	Barcode primer sequence for 2nd HiSeq PCR CRISPRi iPCRtag3	aatgatacggcgaccaccgagatctacacgatcg gaagagcacacgtctgaactccagtcacAGTT CCgcacaaaaggaaact caccct
	Barcode primer sequence for 2nd HiSeq PCR CRISPRi iPCRtag4	aatgatacggcgaccaccgagatctacacgatcg gaagagcacacgtctgaactccagtcacTAGC TTgcacaaaaggaaact caccct
	Barcode primer sequence for 2nd HiSeq PCR CRISPRi iPCRtag5	aatgatacggcgaccaccgagatctacacgatcg gaagagcacacgtctgaactccagtcacTTAG GCgcacaaaaggaaact caccct
	Barcode primer sequence for 2nd HiSeq PCR CRISPRi iPCRtag6	aatgatacggcgaccaccgagatctacacgatcg gaagagcacacgtctgaactccagtcacATCA CGgcacaaaaggaaact caccct

Barcode primer sequence for 2nd HiSeq PCR CRISPRi iPCRtag7	aatgatacggcgaccaccgagatctacacgatcg gaagagcacacgtctgaactccagtcacGAGT GGgcacaaaaggaaact caccct
Barcode primer sequence for 2nd HiSeq PCR CRISPRi iPCRtag8	aatgatacggcgaccaccgagatctacacgatcg gaagagcacacgtctgaactccagtcacAGTC AAgcacaaaaggaaact caccct
Barcode primer sequence for 2nd HiSeq PCR CRISPRi iPCRtag9	aatgatacggcgaccaccgagatctacacgatcg gaagagcacacgtctgaactccagtcacACAG TGgcacaaaaggaaact caccct
Barcode primer sequence for 2nd HiSeq PCR CRISPRi iPCRtag10	aatgatacggcgaccaccgagatctacacgatcg gaagagcacacgtctgaactccagtcacTGAC CAgcacaaaaggaaact caccct
Barcode primer sequence for 2nd HiSeq PCR CRISPRi iPCRtag11	aatgatacggcgaccaccgagatctacacgatcg gaagagcacacgtctgaactccagtcacCAGA TCgcacaaaaggaaact caccct
Barcode primer sequence for 2nd HiSeq PCR CRISPRi iPCRtag12	aatgatacggcgaccaccgagatctacacgatcg gaagagcacacgtctgaactccagtcacGGCT ACgcacaaaaggaaact caccct
Barcode primer sequence for 2nd HiSeq PCR CRISPRi iPCRtag13	aatgatacggcgaccaccgagatctacacgatcg gaagagcacacgtctgaactccagtcacGATC AGgcacaaaaggaaact caccct
Barcode primer sequence for 2nd HiSeq PCR CRISPRi iPCRtag14	aatgatacggcgaccaccgagatctacacgatcg gaagagcacacgtctgaactccagtcacCGAT GTgcacaaaaggaaact caccct
Barcode primer sequence for 2nd HiSeq PCR CRISPRi iPCRtag15	aatgatacggcgaccaccgagatctacacgatcg gaagagcacacgtctgaactccagtcacCCGT CCgcacaaaaggaaact caccct
Barcode primer sequence for 2nd HiSeq PCR CRISPRi iPCRtag16	aatgatacggcgaccaccgagatctacacgatcg gaagagcacacgtctgaactccagtcacGTCC GCgcacaaaaggaaact caccct
Barcode primer sequence for 2nd HiSeq PCR CRISPRi iPCRtag17	aatgatacggcgaccaccgagatctacacgatcg gaagagcacacgtctgaactccagtcacACTT GAgcacaaaaggaaact caccct
Barcode primer sequence for 2nd HiSeq PCR CRISPRi iPCRtag18	aatgatacggcgaccaccgagatctacacgatcg gaagagcacacgtctgaactccagtcacCGTA CGgcacaaaaggaaact caccct
Barcode primer sequence for 2nd HiSeq PCR CRISPRi iPCRtag19	aatgatacggcgaccaccgagatctacacgatcg gaagagcacacgtctgaactccagtcacATTC CTgcacaaaaggaaact caccct
Barcode primer sequence for 2nd HiSeq PCR CRISPRi iPCRtag20	aatgatacggcgaccaccgagatctacacgatcg gaagagcacacgtctgaactccagtcacATGT CAgcacaaaaggaaact caccct

	Barcode primer sequence for 2nd HiSeq PCR CRISPRi iPCRtag21	aatgatacggcgaccaccgagatctacacgatcg gaagagcacacgtctgaactccagtcacGTGA AAgcacaaaaggaaact caccct
	Barcode primer sequence for 2nd HiSeq PCR CRISPRi iPCRtag22	aatgatacggcgaccaccgagatctacacgatcg gaagagcacacgtctgaactccagtcacGTGG CCgcacaaaaggaaact caccct
	Barcode primer sequence for 2nd HiSeq PCR CRISPRi iPCRtag23	aatgatacggcgaccaccgagatctacacgatcg gaagagcacacgtctgaactccagtcacGTTT CGgcacaaaaggaaact caccct
	Barcode primer sequence for 2nd HiSeq PCR CRISPRi iPCRtag24	aatgatacggcgaccaccgagatctacacgatcg gaagagcacacgtctgaactccagtcacACTG ATgcacaaaaggaaact caccct
	Index reading primer for HiSeq CRISPRi	GTGTGTTTTGAGACTATAAGTATCCCT TGGAGAACCACCTTGTTGG
HiSeq PCR CRISPRn primer	Forward primer for 1st HiSeq PCR CRISPRn	ACACTCTTTCCCTACACGACGCTCT TCCGATCTCTTGTGGAAAGGACGA AACA
	Reverse primer for 1st HiSeq PCR CRISPRn	TCGGCATTCCTGCTGAACCGCTCT TCCGATCTCTAAAGCGCATGCTCC AGAC
	Forward primer for 2nd HiSeq PCR CRISPRn	AATGATACGGCGACCACCGAGATC TACACTCTTTCCCTACACGACGCTC TTCCGATCT
	Barcode primer sequence for 2nd HiSeq PCR CRISPRn iPCRtag1	CAAGCAGAAGACGGCATACGAGAT AACGTGATCGGTCTCGGCATTCCT GCTGAACCGCTCTTCCGATCT
	Barcode primer sequence for 2nd HiSeq PCR CRISPRn iPCRtag2	CAAGCAGAAGACGGCATACGAGAT cctcctgaCGGTCTCGGCATTCCTGCT GAACCGCTCTTCCGATCT
	Barcode primer sequence for 2nd HiSeq PCR CRISPRn iPCRtag3	CAAGCAGAAGACGGCATACGAGAT ggtagcacCGGTCTCGGCATTCCTGC TGAACCGCTCTTCCGATCT
	Barcode primer sequence for 2nd HiSeq PCR CRISPRn iPCRtag4	CAAGCAGAAGACGGCATACGAGAT cagatctgCGGTCTCGGCATTCCTGCT GAACCGCTCTTCCGATCT
	Barcode primer sequence for 2nd HiSeq PCR CRISPRn iPCRtag5	CAAGCAGAAGACGGCATACGAGAT tagcttgtCGGTCTCGGCATTCCTGCT GAACCGCTCTTCCGATCT
	Barcode primer sequence for 2nd HiSeq PCR CRISPRn iPCRtag6	CAAGCAGAAGACGGCATACGAGAT cgatgtttCGGTCTCGGCATTCCTGCT GAACCGCTCTTCCGATCT

	Barcode primer sequence for 2nd HiSeq PCR CRISPRn iPCRtag7	CAAGCAGAAGACGGCATACGAGAT gccaatgtCGGTCTCGGCATTCCTGCT GAACCGCTCTTCCGATCT
	Barcode primer sequence for 2nd HiSeq PCR CRISPRn iPCRtag8	CAAGCAGAAGACGGCATACGAGAT acagtggtCGGTCTCGGCATTCCTGCT GAACCGCTCTTCCGATCT
	Barcode primer sequence for 2nd HiSeq PCR CRISPRn iPCRtag9	CAAGCAGAAGACGGCATACGAGAT gatcagcgCGGTCTCGGCATTCCTGC TGAACCGCTCTTCCGATCT
	Barcode primer sequence for 2nd HiSeq PCR CRISPRn iPCRtag10	CAAGCAGAAGACGGCATACGAGAT tagtgactCGGTCTCGGCATTCCTGCT GAACCGCTCTTCCGATCT
	Barcode primer sequence for 2nd HiSeq PCR CRISPRn iPCRtag11	CAAGCAGAAGACGGCATACGAGAT ttaggcatCGGTCTCGGCATTCCTGCT GAACCGCTCTTCCGATCT
	Barcode primer sequence for 2nd HiSeq PCR CRISPRn iPCRtag12	CAAGCAGAAGACGGCATACGAGAT ggctacagCGGTCTCGGCATTCCTGC TGAACCGCTCTTCCGATCT
	Barcode primer sequence for 2nd HiSeq PCR CRISPRn iPCRtag13	CAAGCAGAAGACGGCATACGAGAT cttgtactCGGTCTCGGCATTCCTGCT GAACCGCTCTTCCGATCT
	Barcode primer sequence for 2nd HiSeq PCR CRISPRn iPCRtag14	CAAGCAGAAGACGGCATACGAGAT acttgatgCGGTCTCGGCATTCCTGCT GAACCGCTCTTCCGATCT
	Barcode primer sequence for 2nd HiSeq PCR CRISPRn iPCRtag15	CAAGCAGAAGACGGCATACGAGAT tgaccactCGGTCTCGGCATTCCTGCT GAACCGCTCTTCCGATCT
	Barcode primer sequence for 2nd HiSeq PCR CRISPRn iPCRtag16	CAAGCAGAAGACGGCATACGAGAT tggttgttCGGTCTCGGCATTCCTGCTG AACCGCTCTTCCGATCT
	Barcode primer sequence for 2nd HiSeq PCR CRISPRn iPCRtag17	CAAGCAGAAGACGGCATACGAGAT gatctcttCGGTCTCGGCATTCCTGCT GAACCGCTCTTCCGATCT
	Barcode primer sequence for 2nd HiSeq PCR CRISPRn iPCRtag18	CAAGCAGAAGACGGCATACGAGAT ggtcgtgtCGGTCTCGGCATTCCTGCT GAACCGCTCTTCCGATCT
	Barcode primer sequence for 2nd HiSeq PCR CRISPRn iPCRtag19	CAAGCAGAAGACGGCATACGAGAT gaatctgtCGGTCTCGGCATTCCTGCT GAACCGCTCTTCCGATCT

	Barcode primer sequence for 2nd HiSeq PCR CRISPRn iPCRtag20	CAAGCAGAAGACGGCATACGAGAT gtacatctCGGTCTCGGCATTCCTGCT GAACCGCTCTTCCGATCT
	Index reading primer for HiSeq CRISPRn	AGATCGGAAGAGCGGTTCAGCAGGAA TGCCGAGACCG
	U6-Illumina-seq2 SE	TCTTCCGATCTCTTGTGGAAAGGACGA AACACCG

Abbreviations: CRISPR Clustered Regularly Interspaced Short Palindromic Repeats; crRNA CRISPR RNA; PCR Polymerase Chain Reaction; sgRNA single-guide RNA; siRNA Small interfering RNA; TIDE Tracking of Indels by Decomposition; tracrRNA Trans-activating CRISPR RNA.

2.5. Plasmids

Table 2.4 Details of plasmids used in this thesis.

Plasmid	Source	Product code
plentiCRISPR v2	Addgene	52961
pOZ_MND1	This thesis	N/A
Edit-R Inducible Lentiviral hEF1α-Blast-Cas9 Nuclease Plasmid DNA	Horizon	CAS11229
Human genome-wide lentiviral CRISPR gRNA library version 1	Addgene	67989
Lenti-dCas9-KRAB-blast	Addgene	89567
Human genome-wide CRISPRi-V2 library	Addgene	83969
CRISPRi sgRNA backbone	Addgene	50946
psPAX2	Addgene	12260
pMD2.G	Addgene	12259
pLX302	Addgene	25896
pCBASceI	Addgene	26477

Abbreviations: CRISPRi CRISPR interference; gRNA guide RNA; N/A Not available

2.6. Drugs

Talazoparib was purchased from Selleckchem and RAD51i B02 was purchased from Sigma. Olaparib was provided by AstraZeneca. Drug stock solutions were prepared in 100% DMSO and aliquots stored in -20°C.

Protocols

2.7. General tissue culture conditions

All tissue culture was performed under sterile conditions in a laminar flow cabinet. Tissue culture was carried out under standard conditions (37°C, 5% CO_2), except for KB1P-G3 cells lines, which were cultured under low oxygen (3%) conditions. Cells were maintained at sub-80% confluency before passaging according to the following procedure: (i) growth media was aspirated from the cells; (ii) cells were washed once with 1X PBS; (iii) cells were detached via incubation at 37°C with a covering volume of trypsin-EDTA (Sigma); (iv) cells were resuspended in foetal bovine serum (FBS)-containing growth media and seeded at an appropriate density in a new flask. Cells were counted for cell viability and clonogenic assays using a Countess automated cell counter (Thermo Fisher Scientific). Cell lines were resuspended in freezing media (90% FBS, 10% DMSO) and stored in liquid nitrogen for long-term storage. Testing for mycoplasma contamination was performed using the MycoAlert kit (Lonza) fortnightly.

2.8. Cell lines

MCF10A *TP53*$^{-/-}$ cells and MCF10A *TP53*$^{-/-}$ *RB1*$^{-/-}$ daughter cells generated by CRISPR-Cas9 mutagenesis were purchased from Horizon. MCF10A cells were cultured in Dulbecco's Modified Eagle Medium/Nutrient Mixture F-12 (DMEM/F12, Gibco) supplemented with 5% horse serum; epidermal growth factor (EGF, 20 ng/mL); hydrocortisone (0.5 mg/mL); cholera toxin (100 ng/mL); insulin (10 µg/mL). DR-GFP U2OS (kindly gifted by Jeremy Stark (City of Hope, USA)), HEK293T (ATCC), CAL51 (DSMZ) and MDAMB-231 (ATCC) were maintained in Dulbecco's Modified Eagle Medium (DMEM, Gibco) supplemented with 10% FBS.

SUM149 cells (Asterand Bioscience) were maintained in Ham's F-12 medium supplemented with 5% FBS, 10 µg/mL insulin and 1 µg/mL hydrocortisone. The KB1P-G3 cell line was previously established from a *K14cre;Brca1$^{F/F}$;Trp53$^{F/F}$* (KB1P) mouse mammary tumour and cultured as previously described (Jaspers et al., 2013). The KB1P-G3B1 cell line was derived from the KB1P-G3 cell line which was reconstituted with human *BRCA1* by (Barazas et al., 2019). KB-derived cell lines were grown in DMEM/F12, supplemented with 10% foetal calf serum (FCS), 5 µg/mL insulin, 5 ng/mL cholera toxin and 5 ng/mL murine EGF (Sigma, #E4127). The HEK293T cell line, as well as the Phoenix-ECO cell line, were cultured in DMEM (Gibco). The DMEM media for the HEK29T and Phoenix-ECO cell lines was supplemented with 10% FBS or 10% FCS, respectively. HAP1 cells were purchased from Horizon and were cultured in Iscove's Modified Dulbecco's Medium (IMDM) containing 10% FBS (Gibco).

2.9. CRISPR mutagenesis

MCF10A *MND1* and *PSMC3IP* mutant cell lines were generated using the Edit-R Gene Engineering System (Horizon). Cells were seeded at a density of 1x10^6 cells/well in 6-well plates. After 24 hours, cells were transfected with 40 µM Edit-R Cas9 nuclease protein NLS (CAS11729) mixed with 20 µM 2X CRISPR RNA (crRNA) and 10 µM trans-activating CRISPR RNA (tracrRNA) using Lipofectamine CRISPRMAX transfection reagent (Thermo Fisher Scientific), according to manufacturer's instructions. Target sequences for crRNA used: 5'-GCTGACCTTCAAGTCCTAGA-3' and 5'-GTGAGGTTGAACACTTACTT-3' to target *PSMC3IP*, 5'-CTTGCATGAAGAGCTTTACT-3' and 5'-CGGAACTTCTAATTATTATT-3' for

MND1 targeting, 5-GATACGTCGGTACCGGACCG-3' for non-targeting control. Four days after transfection, cells were FACS-sorted into 96-well plates at one cell per well. Targeted genome modifications were analysed by Sanger sequencing (Forward M13 primer, 5'-GTAAAACGACGGCCAG-3') of PCR products cloned into pCR-TOPO-blunt (Thermo Fisher Scientific). Constructs were introduced into MCF10A TP53$^{-/-}$ cells expressing inducible Cas9, which was generated by lentiviral transduction with hEF1a-Cas9 (#CAS11229, Dharmacon). The procedure for lentiviral transduction is described in 2.12. Cas9 expression was induced with 1 μg/mL doxycycline.

MCF10A *MND1* and *PSMC3IP* CRISPRi cell lines were generated by cloning sgRNAs into the BbsI site of the pKLV5-U6sgRNA5-PGKPuroBFP (Addgene, #50946), as previously described (Tzelepis et al., 2016). sgRNA sequences are as follows: sgMND1-1: 5'-GCGGCGAAGCCCACACACTA-3'; sgMND1-2: 5'-GGTAGCCTCAGTCCTTACCA-3'; sgPSMC3IP-1: 5'-GCGGGAAAGGCGATGAGTAA-3'; sgPSMC3IP-2: 5'GAAGCTGCGGCGGGAGGTAA-3'. These constructs were introduced into cells generated by lentiviral transduction of MCF10A TP53$^{-/-}$ cells with lenti-BLAST-dCas9-KRAB (Addgene, #89567), followed by selection with 10 μg/mL blasticidin. The procedure for lentiviral transduction is described in Section 2.12.

In order to generate cells expressing a *PSMC3IP* mutant associated with D-loop defect (*PSMC3IP p.Glu201del),* a human PSMC3IP ORF (Dharmacon) was PCR-amplified using primers designed to result in a deletion of glutamic acid (E)

at amino acid position 201

Fw-GCAAGAAGCAGTTCTTTGAGGTTGGGATAGAGACGGATGAAG;

Rev-CTCAAAGAACTGCTTCTTGCTCTTG. In-fusion reaction was performed to re-circularise the vector. *PSMC3IP* p.Glu201del or wild-type *PSMC3IP* cDNA was cloned into pLX302 (Addgene, #25896) expression vector. These constructs were introduced into wild-type MCF10A *TP53*$^{-/-}$ cells or MCF10A *TP53*$^{-/-}$ *PSMC3IP* CRISPRi cell lines via lentiviral transduction, the procedure for which is described in Section 2.12.

CRISPR/SpCas9 plasmids for *MND1* targeting in KB1P-G3 and KB1P-G3B1 cell lines were generated using a modified version of the lentiCRISPR v2 backbone (Addgene, #52961), in which a puromycin resistance ORF was cloned under the hPGK promoter. sgRNA sequences were cloned into the modified lentiCRISPR v2 backbone using custom DNA oligos (Microsynth), which were melted at 95°C for 5 minutes, annealed at room temperature for 2 hours and subsequently ligated with quick-ligase (NEB) into BsmBI-digested (Fermantas) lentiCRISPR v2 backbone. sgRNA sequences are as follows for KB1P-G3 and KB1P-G3B1 cell lines.

Non-targeting control: 5'-TGATTGGGGGTCGTTCGCCA-3';

sgMnd1-1: 5'-GACAAACATACCGTCTCTTGC-3';

sgMnd1-2: 5'-GTCATGCCAGGAAGCGCAAGT-3'. The target site modifications of the polyclonal cell pools were analysed by Tracking of Indels by Decomposition (TIDE) analysis, as described in Section 2.10. All construct sequences were verified by Sanger sequencing using primers outlined in Table 2.3.

2.10. TIDE analysis

In order to assess the modification rate in CRISPR-mutagenised polyclonal murine KB1P-G3 cell lines, cells were pelleted and genomic DNA was extracted using the QIAmp DNA mini kit (Qiagen), according to the manufacturer's protocol. Target loci were PCR-amplified using Phusion High Fidelity Polymerase (Thermo Fisher Scientific) using a 3-step protocol: (1) 98°C for 30 seconds, (2) 30 cycles at 98°C for 5 seconds, 63.3°C for 10 seconds and 72°C for 15 seconds, (3) 72°C for 5 minutes. Reaction mix consisted of 10 µL of 2X Phusion Mastermix (Thermo Fisher Scientific), 1 µL of 20 µM forward and reverse primer and 100 ng of DNA in 20 µL total volume. Primers are detailed in Section 2.4. PCR products were purified using the QIAquick PCR purification kit (Qiagen), according to the manufacturer's protocol, and submitted with corresponding forward primers for Sanger sequencing to confirm target modifications using the TIDE algorithm (Brinkman et al., 2014).

2.11. CRISPR screen

In order to perform the CRISPR screen, cell lines were generated in the desired MCF10A background to achieve knockout (CRISPRn) or knockdown (CRISPRi), by initial transduction with a CRISPR plasmid with a low MOI to minimise the risk of multiple integrations of the CRISPR construct into a single cell, which can lead to genotoxicity or clonal selection bias. The MOI was titrated to ensure that a sufficient number of cells were infected with the CRISPR construct to achieve effective gene knockout, while avoiding excessive toxicity or off-target effects; MOI 0.3 was used. For the CRISPRn screen, inducible Cas9 MCF10A *TP53*$^{-/-}$ cells were generated by lentiviral transduction of MCF10A *TP53*$^{-/-}$ cells with Inducible Lentiviral hEF1α-Blast-Cas9 Nuclease Plasmid DNA (Horizon, #CAS11229). In

order to assess Cas9 function, the Cellecta CRISPRtest™ assay was utilised. This assay involves sequential transduction of the Cas9-expressing cells with two lentivirus mixes; one lentivirus construct expresses an sgRNA targeting an essential gene and GFP fluorescent protein. A second non-targeting sgRNA construct expresses red fluorescent protein (RFP) marker. Upon transduction, cells expressing the sgRNA with the GFP marker undergo knockout of the essential target gene, leading to cell death. The difference in depletion between GFP-positive cells with the lethal sgRNA and non-targeting sgRNA expressing cells with the RFP marker provides a quantitative measurement of Cas9 activity. GFP and RFP fluorescence of the cells was measured using a flow cytometer. Following antibiotic selection with 10 µg/mL blasticidin, Cas9-expressing cells were infected at MOI 0.3, with a previously published genome-wide human lentiviral CRISPR library (Addgene, #67989) (Tzelepis et al., 2016). The library contains 90,709 sgRNAs targeting 18,010 genes. Following 2 µg/mL puromycin selection for 72 hours, doxycycline was added for 72 hours to induce Cas9 expression. The cell line used for CRISPRi screen was generated by lentiviral transduction of MCF10A *TP53*$^{-/-}$ cells with lenti-BLAST-dCas9-KRAB plasmid DNA (Addgene, #89567). In order to assess dCas9-KRAB function, Cellecta CRISPRiTest™ was utilised. The assay involves sequential transduction of both dCas9-KRAB and parental cells with two lentivirus mixes. One lentivirus construct expresses an sgRNA targeting the CMV-GFP transcription start site and GFP fluorescent protein, while the second non-targeting sgRNA construct expresses an RFP fluorescent marker. Upon transduction, parental cells should express high levels of both RFP and GFP, while dCas9-KRAB expressing cells should exhibit low levels of GFP (due to CRISPRi-mediated depletion of GFP), but high levels of RFP.

Transcriptional repression efficiency in the dCas9-KRAB cell line is calculated as the ratio between the normalised GFP intensity of parental cells and the normalised GFP intensity of dCas9-KRAB cells (normalisation to RFP-transduced cells). GFP and RFP fluorescence of the cells was measured using a flow cytometer. Following antibiotic selection with 10 μg/mL blasticidin. dCas9-KRAB expressing cells were infected at MOI 0.3 with a previously published genome-wide human lentiviral CRISPRi library (Horlbeck et al., 2016). The library contains 104,535 sgRNAs targeting 18,905 protein coding genes. In both CRISPRn and CRISPRi screens, cells were collected for an early time point sample of initial library representation (T_0) following selection. 100 million CRISPR-mutagenised cells were exposed to concentrations that caused a 20% reduction in cell survival (Surviving Fraction 80, SF_{80}) of either olaparib or talazoparib. In total, cells were exposed to drug or DMSO for 14 days (10 population doublings), after which the cells were recovered (T_1). The olaparib and talazoparib arms of the CRISPRn screens were performed simultaneously, so the same T_0 sample was used for comparison with the T_1 samples, whereas the olaparib and talazoparib arms of the CRISPRi screens were performed at different times, so different T_0 samples were used for comparison with the respective T_1 sample. In order to identify genes, i.e., CRISPR sgRNAs, that increased the sensitivity of cells to PARP inhibition, sgRNA depletion was identified in cells that survived PARPi or DMSO exposure using massively parallel sequencing. In brief, genomic DNA was extracted from T_0 and T_1 cells using the DNeasy blood and tissue kit (Qiagen), according to the manufacturer's protocol. sgRNA sequences were PCR amplified for Illumina sequencing (HiSeq 2500) in a two-step process; the first PCR reactions involve amplifying sgRNA region, which is then barcoded in the second PCR step. PCR primer sequences are detailed in

Section 2.4. In order to maintain 1000X representation during the first PCR step, a specific amount of genomic DNA requires amplification. Given both Yusa and Weissman sgRNA libraries contain approximately 100,000 sgRNAs, and that a diploid human genome is approximately 6.6 pg, 1000X representation required 660 µg genomic DNA for these PCR amplifications. For each PCR reaction, 1.5 µg DNA was amplified with Q5 polymerase (New England Biolabs) in 5X buffer, with 10 µM forward and 10 µM reverse primer and dNTPs in excess. Thermocycler settings were as follows, (1) 98°C for 1 minute, (2) 25 cycles at 98°C for 30 seconds, 62°C for 30 seconds and 72°C for 20 seconds, (3) 72°C for 5 minutes. ~600 individual PCR reactions were required per genome-wide CRISPR screen, and these PCR reactions were pooled together for the second PCR reaction to maintain 1000X representation. Following PCR purification with SPRI beads (AMPure XP, Beckman Coulter), according to the manufacturer's instructions, a second PCR step involved PCR primers with unique index sequences for barcoding. 250 ng genomic DNA was amplified with Q5 polymerase (New England Biolabs) in 5X buffer, with 10 µM primer, 10 µM barcode primer, and dNTPs in excess. In order to maintain representation in this second PCR step, a number of precautionary steps were taken. Equimolar amounts of each sample were used to ensure that all samples were represented equally in the final sequencing library and was accomplished by normalising the concentration of each sample prior to pooling for the barcoding step. In addition, optimised PCR conditions were used, including annealing temperature, extension time, and primer concentration. Specifically, limiting the number of PCR cycles avoids overamplification and ensured efficient and unbiased amplification of the target DNA sequences. Appropriate no template and positive controls were used during this PCR step, to

help detect and correct for potential sources of bias, such as primer dimers or PCR artefacts. Thermocycler settings were as follows, (1) 98°C for 30 seconds, (2) 8 cycles at 98°C for 10 seconds, 65°C for 30s and 72°C for 30 seconds, (3) 72°C for 5 minutes. Next-generation sequencing (NGS) was performed from the resulting PCR amplicons on an Illumina (HiSeq 2500) platform, which generated >1,000 short-reads for each sgRNA in the library. Analysis of the CRISPR screen is described in the Section 2.28.

2.12. Lentiviral transduction

Lentiviral stocks for stable cell lines in human MCF10A were generated by transient transfection of HEK293T cells. On day 0, $3x10^6$ HEK293T cells were seeded in a 6-well plate and on the next day transiently transfected with lentiviral packaging plasmids psPAX2 (Addgene, #12260) and pMD2.G (Addgene, #12259) with plasmid DNA. For instance, the CRISPRi cell lines in the MCF10A $TP53^{-/-}$ background were generated by using viral particles expressing pKLV-U6gRNA(BbsI)-PGKpuro2ABFP vector containing the respective sgRNA or a non-targeting sgRNA with Lipofectamine 2000 transfection reagent (Thermo Fisher Scientific), according to the manufacturer's protocol. After 30 hours, virus-containing supernatant was harvested and filtered (0.45 µm). For lentiviral transduction, 150,000 cells were seeded in 6-well plates. 24 hours later, lentivirus was applied. Virus-containing medium was replaced with medium containing puromycin (2 µg/mL, Gibco) 24 hours later. Puromycin selection was performed for three days; cells were subsequently expanded and frozen down at early passage.

Lentiviral stocks for stable cell lines in murine KB1P-G3/KB1P-G3B1 were generated by transient transfection of HEK293T cells. On day 0, $8x10^6$ HEK293T cells were seeded in 150 cm cell culture dishes. The next day, the HEK293T cells were transiently transfected with lentiviral packaging plasmids psPAX2 (Addgene, #12260) and pMD2.G (Addgene, #12259), with the plentiCRSIPRv2 (Addgene, #52961) vector containing the respective sgRNA or a non-targeting sgRNA using 2xHBS (280nM NaCl, 100mM HEPES, 1.5mM Na_2HPO_4, pH 7.22), 2.5M $CaCl_2$ and 0.1x TE buffer (10 mM Tris pH 8.0, 1 mM EDTA pH 8.0, diluted 1:10 with dH_2O). After 30 hours, virus-containing supernatant was concentrated by ultracentrifugation at 20,000 RPM for 2 hours in a SW40 rotor and the virus was finally resuspended in 100 µL PBS. The virus titre was determined using a RT-qPCR Lentivirus Titration Kit (Applied Biological Materials). For lentiviral transduction, 150,000 target cells from both cell lines were seeded in 6-well plates. 24h later, virus at a MOI of 25 was applied with 8 µg/mL Polybrene (Merck Millipore). Virus-containing medium was replaced with medium containing puromycin (3.5 µg/mL, Gibco) 24 hours later. Puromycin selection was performed for three days; cells were subsequently expanded and frozen down at an early passage. The target site modifications of the polyclonal cell pools were analysed by TIDE analysis, which in Section 2.10.

In order to achieve Mnd1 reconstitution in the murine KB1P-G3/KB1P-G3B1 cells, lentiviral stocks were generated using the Phoenix-ECO cells. On day 0, $1x10^6$ cells were seeded in 10 cm cell culture dishes. The next day, the Phoenix-ECO cells were transiently transfected with MND1-pOZ plasmid (expressing interleukin-2 receptor α chain (IL2Rα/ CD25) as selection marker) using

Turbofectin transfection reagent. On days 2 and 3, virus-containing supernatant was harvested and filtered (0.45 µm). Transduction of the target cells was performed on last day of harvest by adding 7 µg/mL Polybrene (Merck Milipore) to the retroviral supernatant, which was applied to the target cells (9 mL/10 cm cell culture dish). Selection of the target cells was performed using the Dynabeads® CD25 (Invitrogen) according to the manufacturer's protocol. In order to generate the Mnd1-pOZ plasmid, the *Mnd1* coding sequence was cloned into pOZ-N-FH plasmid (Nakatani & Ogryzko, 2003)) using the in-fusion HD cloning kit (Takara).

2.13. Retroviral mutagenesis screen

The retroviral mutagenesis screen was performed and analysed as described in (Francica et al., 2020) and (Blomen et al., 2015). Briefly, wild-type HAP1 cells were mutagenised using a retroviral gene-trap cassette. $1x10^8$ mutagenised HAP1 cells were seeded in 14X T175 cell culture flasks. Cells were exposed to IR after 24 hours (day 1), 72 hours (day 3) and 120 hours (day 5) with 1.5 Gy each time, which led to a confluency of 70-80% on day 10. Cells were subsequently harvested and fixed, then stained for FACS-mediated 1n DNA content sorting. Sequencing data processing, insertion site mapping to GRCh37 human genome assembly, and subsequent analysis of sense and antisense integrations was performed, following Linear Amplification Mediated (LAM)-PCR of isolated genomic DNA, as described in (Blomen et al., 2015). Four independent wild-type control datasets were used for normalisation (Blomen et al., 2015). The retroviral mutagenesis screens were performed twice with individual mutagenised HAP1 batches.

2.14. Site-directed mutagenesis

The *PSMC3IP* coding sequence was ordered from Eurofins. Yeast p.Glu201del was mapped to GRCh37 human genome assembly to design the primers for amplification of the linear construct. In order to generate PSMC3IP p.Glu201del DNA, 10 ng wild-type PSMC3IP cDNA was amplified with the generated forward and reverse primers and Q5 polymerase (New England Biolabs) using a 3-step protocol: (1) 98°C for 30 seconds, (2) 30 cycles at 98°C for 10 seconds, 60°C for 10 seconds and 72°C for 90 seconds, (3) 72°C for 5 minutes. Sequences for primers used are provided in Table 2.3. PCR products were purified using the QIAquick PCR purification kit (Qiagen) according to manufacturer's protocol; PCR amplification was confirmed via gel electrophoresis. The PCR amplified DNA was incubated with *DpnI* restriction enzyme (NEB, R0176S). Following In-fusion reaction, using the in-fusion HD cloning kit (#12141, Takara), DNA was transformed in Stellar Competent cells (Takara, t# 636763), according to manufacturer's protocol. DNA was isolated and purified (Qiagen) before gateway cloning (using Gateway™ LR Clonase™ II Enzyme mix (Thermo Fisher Scientific, 11791020) to introduce either PSMC3IP or PSMC3IP p.Glu201del into pLX302 expression vector (Addgene, #25896). The reaction mixture was transformed into competent cells for antibiotic selection on agar plates. Plasmid DNA was isolated from bacterial colonies with miniprep (QIAprep Spin Miniprep Kit), and subsequently maxiprep (HiSpeed Plasmid Maxi Kit). PSMC3IP-pLX302 or PSMC3IP p.Glu201del-pLX302 DNA was introduced into MCF10A $TP53^{-/-}$ cells via lentiviral transduction, as detailed in 2.12.

2.15. Drug survival assays

Cells were seeded into 384-well plates at a concentration of 300 cells per well in 50 µL growth medium. After 24 hours, drug or vehicle (DMSO) dilutions in growth media were added to the cells using an Echo liquid handler (Beckman). In 384-well format, cells were continuously exposed to drug for a total of 5 days. MCF10A or HAP1 cells were also plated in 96-well plates at a density of 1,500 cells/well in 100 µL medium and treated with the indicated drug at the indicated dosages after 24 hours. In 96-well format, cells were continuously exposed to drug for a total of ten days. Cell viability was assessed using CellTiter-Glo luminescent cell viability assay (Promega). Media was removed from the plate and 20 µL of CellTiter-Glo (diluted 1:4 with 1X PBS) was added to each well. Plates were continuously shaken and incubated in the dark for 10 minutes at room temperature. Luminescence was measured using the Victor X5 Multilabel plate reader (Perkin Elmer). Cell viability (surviving fraction, SF) was calculated as a fraction of luminescence in vehicle-treated (DMSO) cells. Dose/response curves plotted using GraphPad Prism graphing software.

2.16. Clonogenic drug survival assays

MCF10A or HAP1 cells were seeded into 6-well plates at a concentration of 500 cells per well in 2 mL growth medium. After 24 hours, media was replaced with media containing drug or vehicle (DMSO) at the indicated concentrations. Drug was replenished every three days for up to 14 days, at which point colonies were fixed with 10% TCA for 1 hour at 4°C and stained with SRB for 1 hour at room temperature. Excess dye was removed by washing plates with 1% acetic acid. Colonies counting was automated with the “analyze particles” command in Fiji.

KB1P-G3B1 cells were seeded in 10 cm dishes at a density of 100 cells/dish. Cells were exposed to PARPi 24 hours later. Cells were selected in PARPi for 15 days in total, and PARPi was replenished every three days. At day 15, colonies were fixed with 4% formalin and stained with 0.1% crystal violet. All colonies were counted in an automated manner using the colony counter tool with Image J.

2.17. DR-GFP assay

$1.5x10^5$ U2OS cells expressing a synthetic HR reporter substrate (DR-GFP; (Gunn & Stark, 2012)) were reverse transfected with 200 nM indicated siRNA using Lipofectamine RNAiMAX (Thermo Fisher Scientific) in Opti-MEM (Gibco). Details for siRNA reagents used are provided in 2.4, which include non-targeting control siRNAs to serve as transfection controls; for baseline comparison to evaluate the effects of gene silencing to help distinguish the specific effects of the target siRNA from any non-specific or unintended consequences arising from the siRNA transfection process itself. In order to serve as a positive control, a population of cells were transfected with a DNA construct known to result in a reduction of HR upon gene silencing (siRNA targeting either *BRCA1* or *BRCA2*) to validate the sensitivity and functionality of the assay, as well as providing a reference for comparing HR activity in experimental conditions. A population of cells also remained untransfected. After 24 hours, cells were forward transfected with 2.5 µg pCBASceI plasmid (Addgene, # 26477) using Lipofectamine 3000 (Thermo Fisher Scientific) in Opti-MEM (Gibco). In order to serve as controls, cell populations remained untransfected with pCBASceI plasmid. After 5 days from initial cell seeding, the cells were fixed in 4% PFA. Flow cytometry was performed with BD LSR II Flow Cytometer (BD Biosciences) with at least 10,000 events measured.

Single-cell gating strategy was established using untransfected cell sample as follows: during acquisition of the sample, the forward scatter and side scatter voltages were adjusted to visualise the cell population of interest, and a gate was applied to exclude debris and aggregates. Fluorescence gating strategy was established by overlaying the GFP histogram plot of the positive control cell samples (cells transfected with siRNA targeting *BRCA1* or *BRCA2*) with negative control cell sample (cells transfected with non-targeting control siRNA); the events in the positive control sample represent background fluorescence level, so the gate was set to include events present in the negative control sample, but absent in the positive control sample, to capture the GFP-positive population. The GFP fluorescence of the target siRNA was normalised to that of the non-targeting control, in order to differentiate specific gene silencing effects from non-specific or unintended consequences. As such, the reduction in GFP fluorescence could be calculated.

2.18. Immunofluorescence

75,000 cells were plated onto coverslips pre-coated with 50 µg/mL poly-L-lysine (Sigma Aldrich) in 24-well plates. The following day, cells were fixed either 16 hours post 10 µM olaparib treatment or 3 hours post IR (10 Gy) exposure. Control cells were either exposed to DMSO or no IR. Prior to fixation, cells were permeabilised for 5 minutes at room temperature in permeablisation buffer (20 mM TRIS-HCl, 50 mM NaCl, 3 mM $MgCl_2$, 1M sucrose, 0.5% Triton X-100) following a PBS wash step. Cells were fixed in 4% PFA (Sigma Aldrich) for 20 minutes at room temperature. Fixed cells were washed with PBS and then permeabilised for 20 minutes in permeablisation buffer (20 mM TRIS-HCl, 50 mM NaCl, 3 mM $MgCl_2$,

1M sucrose, 0.5% Triton X-100). For staining of micronuclei only, coverslips were mounted onto glass slides using ProLong™ Diamond Antifade Mountant with DAPI (Thermo Fisher Scientific). RAD51 and γH2AX staining was performed as follows. Following the final aforementioned permeabilisation step, cells were washed three times in PBS and blocked with 5% BSA in PBS with 0.2% Tween for 30 minutes at room temperature, incubated with the primary antibodies overnight at 4°C; rabbit anti-RAD51 (Santa Cruz, 8349 (H-92) and mouse-anti-phospho-H2AX (Milipore, 05-636) at 1:2,000 dilution. Coverslips were washed 3 times, then incubated with the secondary antibodies for 1 hour at room temperature; Goat polyclonal anti-Rabbit IgG (H+L) Highly Cross-Adsorbed Alexa Fluor 488 (Thermo Fisher Scientific, A-11034) and Goat Anti-Mouse IgG (H+L), Alexa Fluor 555 (Thermo Fisher Scientific, A-21422) at 1:1,000 dilution. Coverslips were washed 3 times in PBS before mounting onto glass slides using ProLong™ Diamond Antifade Mountant with DAPI (Thermo Fisher Scientific). Z-stack images were acquired using the Marianas advanced spinning disk confocal microscope (3i) and multiple different fields were imaged per sample (63x objective). Integrated density per nucleus was determined using the Fiji image processing package of ImageJ (1.8.0). Data was checked to ensure signal saturation has not occurred.

2.19. Protein extraction and quantification

Cells were cultured and pelleted at 1500 RPM for 5 minutes following harvest via trypsinisation. Cells were lysed for 30 minutes on ice using RIPA lysis buffer (ab156034, Abcam) with protease and phosphatase inhibitors (Roche) and sonicated for 5 seconds at 5 amps. Lysates were centrifuged at 4°C and supernatants collected for storage at -80°C and used for Western blotting. Protein

concentration was determined using the Pierce BCA Protein Assay Kit (Thermo Fisher Scientific, 23225) according to manufacturer's instructions.

2.20. Western blotting

50-100 µg of whole cell lysate was electrophoresed on NuPage Novex 4-12% gradient precast gel (Invitrogen, NP0321BOX) using NuPage MOPS SDS Running Buffer (Invitrogen, NP0001). All gels were run with full range rainbow molecular weight protein marker (NEB, p7712) as a size reference. Proteins were transferred at 100 volts (V) for 1 hour at room temperature (on ice) onto nitrocellulose membranes (GE Healthcare). Membranes were blocked with 5% milk and probed with primary antibody diluted 1:1,000 in 5% milk overnight at 4°C (Table 2.2). Fluorescent secondary antibodies were diluted 1:10,000 in 5% milk and incubated at room temperature for 1 hour (Table 2.2). Protein bands were visualised using the Li-cor Odyssey Fc imaging system.

2.21. DNA/RNA extraction and quantification

RNA was isolated using the Qiagen RNAeasy kit and genomic DNA was extracted using QIAGEN DNeasy cell and tissue kit, according to the manufacturer's instructions. DNA and RNA was quantified at 260 nm using a spectrophotometer (NanoDrop, Thermo Fisher Scientific).

2.22. Polymerase chain reaction (PCR) and gel electrophoresis

10-100 ng DNA was typically used for PCR reactions. PCR was performed using Q5 polymerase (New England Biolabs) according to manufacturer's protocol using the primers described in Table 2.3. PCR was carried out on a thermocycler as

follows, unless otherwise detailed: 98°C for 30 seconds, followed by 30 cycles of 98°C for 10 seconds (melting), 60°C for 10 seconds (annealing) and 72°C 20-30 seconds per kb (elongation), followed by a final step at 72°C for 5 minutes. The annealing temperature and elongation times were adjusted for each reaction, according to primer requirements and length of product, respectively. All primers were ordered from Integrated DNA Technologies as lipolysed powder, which was resuspended in DEPC-treated H_2O (Ambion) to a concentration of 100 µM and stored at -20°C. Primers were then diluted to 10 µM for use in PCR reactions. PCR products were analysed by agarose gel electrophoresis by mixing with 6X gel loading dye (New England Biolabs) and separation by gel electrophoresis. Agarose gels were made as follows: 1% ultra-pure agarose (Life Technologies) dissolved in 1x TAE buffer with GelRed nucleic acid stain (Biotium). Hyperladder 1 (Bioline) was used to estimate length of PCR products. DNA was visualised using an ultraviolet transilluminator (Syngene).

2.23. TOPO cloning and Sanger sequencing of mutant clones

100 ng purified PCR product was cloned into the pCR-Blunt II-TOPO vector using the Zero Blunt TOPO PCR Cloning kit (Thermo Fisher Scientific), following the manufacturer's protocol. The final mix was incubated for 1 hour at room temperature and transformed according to the following protocol (i) 150 µL of competent cells (DH5α) were mixed gently with 5 µL of cloned product; (ii) after 30 minutes of incubation on ice, tubes were heated at 42ºC for 45 seconds and cooled back on ice; (iii) 300 µL of outgrowth SOC media (Thermo Fisher Scientific) was added and the tubes were placed in a shaking incubator for 1 hour at 37ºC; (iv) bacteria were streaked out on kanamycin-containing Petri dishes and

incubated overnight at 37ºC; (v) single colonies were picked and expanded in kanamycin selective media overnight at 37°C. DNA was extracted using the Qiaprep Spin Miniprep/Midiprep kit (Qiagen). TOPO vectors were sequenced using M13 forward primer (2 µL 10 µM) with 15 µL 10 ng/µL purified DNA (Table 2.3). Sequencing with an appropriate forward primer was performed to confirm CRISPR-mediated modifications via Sanger sequencing methodology outsourced to Eurofins.

2.24. Quantitative reverse transcription polymerase chain reaction (RT-qPCR)

Total RNA was isolated (Qiagen RNAeasy) and 1000 ng RNA was reverse transcribed with High Capacity cDNA Reverse Transcription Kit (#4368814, Thermo Fisher Scientific), as per kit instructions. 25 ng cDNA was amplified with 125 nM Hs01552130_g1 MND1 TaqMan probe human (Thermo Fisher Scientific, 4351372) or Hs00917175_g1 PSMC3IP TaqMan probe human (Thermo Fisher Scientific, 4351372) and Hs02786624_g1 GAPDH TaqMan probe human (Thermo Fisher Scientific, 4448489) with TaqMan master mix (Thermo Fisher Scientific). QuantStudio 6 Flex Real-Time PCR System (Thermo Fisher Scientific) used for quantification. Fold depletion for CRISPR-mutagenised cells or each siRNA treatment was determined as $2^{\Delta\Delta Ct}$, for which the cycle threshold (Ct) value for the target mRNA was subtracted by Ct value for GAPDH (mean of duplicate amplifications from the same RT-qPCR reaction) to calculate the ΔCt value, which was then subtracted from the corresponding ΔCt from wild-type or siCTRL treated cells to calculate ΔΔCt.

2.25. DNA fibre assay

Fork progression was measured as described previously in (Schmid et al., 2018) with a few modifications. Briefly, asynchronously growing sub-confluent cells were labelled with 30 μM thymidine analogue 5-chloro-2'-deoxyuridine (CldU) (Sigma) for 20 minutes, washed three times with warm PBS and subsequently exposed to 250 μM of 5-iodo-2′-deoxyuridine (IdU) for 20 minutes. In the experiment assessing RF stability, IdU pulse was followed by adding medium containing 8 mM hydroxyurea (HU) for 6 hours for KB1P-G3B1 cells or 4 mM HU for 3 hours for *Brca1*-deficient KB1P-G3 cells. In order to assess RF reversal in KB1P-G3 cells, 600 nM Mitomycin C (MMC) was used ahead of pulse labelling with CldU and IdU, as previously described. MMC treatment was maintained during labelling. All cells were then collected and resuspended in cold PBS at $3.5x10^5$ cells/mL cell density. The labelled cells were mixed 1:5 with unlabelled cells, then resuspended in cold PBS at 2.5×10^5 cells/mL cell density. Cells were then resuspended in lysis buffer (200 mM Tris-HCl, pH 7.4, 50 mM EDTA, and 0.5% (v/v) SDS) on a positively-charged microscope slide. After nine minutes incubation at room temperature, the DNA fibres were stretched, air-dried, fixed in 3:1 methanol/acetic acid, and stored at 4°C overnight. The following day, the DNA fibres were denatured by incubation in 2.5 M HCl for 1 hour at room temperature, washed five times with PBS and blocked with 2% (w/v) BSA in 0.1% (v/v) PBST (PBS and 0.1% Tween 20) for 40 minutes at room temperature while gently shaking. The newly replicated CldU and IdU tracks were stained for 2.5 hours at room temperature using two different anti-bromodeoxyuridine (BrdU) antibodies recognising CldU (Abcam, ab6326) and IdU (Becton Dickinson, 347580), respectively. After washing five times with PBST, the slides were stained with secondary antibodies;

goat-anti-mouse IgG (H+L) Cross-Adsorbed, Alexa Fluor 488 (Thermo Fisher Scientific, A-11029) diluted 1:300 and Cy3 AffiniPure F(ab')$_2$ Fragment Donkey Anti-Rat IgG (H+L) (Jackson ImmunoResearch, 712-165-513) diluted 1:150. Incubation with secondary antibodies was carried out for 1 hour at room temperature in the dark. The slides were washed five times for 3 minutes in PBST, air-dried and mounted in fluorescence mounting medium (Dako). Fluorescent images were acquired using the DeltaVision Elite widefield microscope (GE Healthcare Life Sciences). To assess RF progression CldU + IdU track lengths of at least 120 fibres per sample were measured using the line tool in ImageJ software. RF stability was analysed by measuring the track lengths of CldU and IdU separately and by calculating IdU/CldU ratio.

Statistical analysis

2.26. General statistical analysis

Statistical tests were performed using GraphPad Prism version 9.4.1 or using RStudio software. Statistical tests performed depended on whether parametric or non-parametric data was used; details of the chosen statistical test are provided in the legend of each figure. Statistical significance was set at p-value <0.05.

2.27. Dose/response curves

The effect of each drug concentration was determined using survival fraction calculations, as described in the equation below:

$$Survival\ fraction = \frac{x}{\mu_{DMSO}}$$

Where x = raw luminescence for the drug and μ_{DMSO}= median luminescence for the DMSO-exposed control wells. The SFs for all replica wells, for each drug concentration, were used to calculate the median SF and standard deviation (SD). In dose/response survival curves, error bars represent SD from typically n=3 replicates.

Dose/response curves were plotted using GraphPad Prism version 9.4.1 using the SFs, calculated as described above. Curves were fitted using the four-parameter logistic regression function. In order to determine the significance of difference between dose/response curves, *P*-values were calculated via two-way ANOVA function with Tukey's post-test. As such, the median effect of drug exposure could be compared to the control.

2.28. CRISPR screen analysis

The short-read sequences were aligned to the known sgRNA sequences present in each pool by colleagues in the Bioinformatics department at the ICR, Aditi Gulati and John Alexander. As such, they were able to compare the relative enrichment or depletion of sgRNAs from T_0 vs. T_1 samples in both DMSO and PARPi-exposed samples; ultimately calculating a normalised drug-effect (DE) Z-score (normZ (Colic et al., 2019)) for each sgRNA targeting a specific gene. MAGeCK (Model-based Analysis of Genome-wide CRISPR/Cas9 Knockout) analysis was used to generate sgRNA counts according to the sequences present in the genome-wide CRISPR library (Li et al., 2014). Using normalised read count data from MAGeCK, quality checks were performed (distribution of read counts, clustering of samples), to confirm the robustness of the data. For downstream

analysis of sgRNA read count data, three approaches were used for comparative analysis: (1) MAGeCK (2) Z-score and (3) DE Z-score. From MAGeCK workflow, we extracted a ranked list of positively selected hits generated using its robust ranking aggregation algorithm (RRA) approach (Li et al., 2014). For the Z-score approach, the low abundant guides with a read count of zero in the T_0 sample were first identified and removed from the analysis. In order to account for variation in the amounts of DNA sequenced, the read counts were converted to parts per ten million (pptm), and then $\log_2$-transformed after adding a pseudo count of 0.5. For each screen, Z-scores were calculated for each individual sgRNA, corrected for viability and drug effects, as follows. The DE* Z-score was elucidated by calculating the difference in abundance of each sgRNA between the drug-treated (Drug (T)) and DMSO-treated samples (DMSO(T)) at a matched timepoint. VE**, the rate of decrease of sgRNA abundance in the population over time in the absence of drug treatment, were taken into account by calculating a Z-score between the T_0 (DMSO (T0)) and T_1 DMSO-treated (DMSO (T1)) sample. Both DE and VE Z-scores were normalised by median absolute deviation*** (MAD). In order to remove variation in drug effect that can be attributed to VE, a linear model of DE vs VE is plotted, which is used to adjust DE, so is referred to as Corrected DE****. In order to assess the overall effect size of each gene, the corrected DE Z-score was normalised to generate a gene-level DE Z-score*****.

$$^{*}\boldsymbol{Drug\ Effect\ (DE)} = \frac{(Drug\ (T) - DMSO(T)) - median(Drug\ (T) - DMSO(T))}{MAD(Drug\ (T) - DMSO(T))}$$

$$^{**}\boldsymbol{Viability\ Effect\ (VE)} = \frac{(DMSO\ (T1) - DMSO\ (T0)) - median(DMSO\ (T1) - DMSO\ (T0))}{MAD(DMSO\ (T1) - DMSO\ (T0))}$$

I.e. Z = (x – median)/median absolute deviation

*** $\boldsymbol{MAD} = median\ |x_i - \tilde{x}|$

**** $\boldsymbol{Corrected\ DE} = \dfrac{(\boldsymbol{DE} - \boldsymbol{c})}{(\boldsymbol{VE} \times \boldsymbol{m})}$

***** $\boldsymbol{Gene\ drug\ effect\ Zscore} = \dfrac{(\sum sgRNA\ Zscores)}{(\sqrt{n\ of\ gRNAs})}$

In this case, CRISPR mutagenesis of genes resulting in negative gene-level DE Z-score are determined to enhance PARPi sensitivity. I defined genes as "hits" with a gene-level DE Z-score threshold of ≤-3, for at least two independent significant (p = 0.05) sgRNAs, to capture the top ~2% and identify the most profound effects. Ranks for negative selection were generated by sorting results based on their Z-score in ascending order. A final list of "hits" was consolidated from the three approaches, (1) MAGeCK (2) Z-score and (3) DE Z-score, by taking the rank product of their ranks.

2.29. Retroviral mutagenesis screen analysis

The identified candidates were required to pass an FDR-corrected binominal test with p<0.05, an FDR-corrected Fisher's exact test with p <0.05 comparing the IR screens with the four wild-type control screens, and had to be either depleted or enriched for sense integrations in both replicates.

Chapter 3. Parallel CRISPR mutagenesis and interference screens identify *MND1* and *PSMC3IP* as highly penetrant determinants of PARPi sensitivity

3.1. Introduction

My thesis work aimed to identify genetic determinants of PARPi sensitivity. At the end of the thesis, I demonstrate that this work ultimately led to the direct association of meiosis genes *MND1*/*PSMC3IP* with HR, thereby influencing the response of HR-inducing agents, such as PARPi and IR.

As I described in Chapter 1, CRISPR screening has been utilised as a high-throughput approach to identify genetic determinants of drug sensitivity. I performed genome-wide CRISPR screens for PARP inhibitor sensitivity, the results of which will be presented in this Chapter. I worked together with colleagues in the ICR Gene Function Lab, Joe Baxter and Feifei Song, to execute this work, which involved: (i) designing suitable parallel CRISPR mutagenesis (CRISPRn) and CRISPR interference (CRISPRi) screens; (ii) generating and characterising the Cas9 and dCas9-KRAB expressing cell lines for the CRISPRn and CRISPRi screens, respectively; (iii) executing the experimental work involved for CRISPRn and CRISPRi screens, and processing the resulting samples; (iv) assessing the quality of the CRISPR screen data; (v) analysing the CRISPR screen data; (vi) identifying CRISPR-mediated determinants of PARPi sensitivity to shortlist gene candidates for further investigation. In addition to recognising genes classically associated with HR in mitotic cells as determinants of PARP inhibitor

sensitivity, these screens identified *MND1* and *PSMC3IP* whose canonical function is in meiotic recombination. This finding was subsequently strengthened by an orthogonal genetic perturbation screen carried out by our collaborators, which indicates that PSMC3IP-MND1 also controls the response to IR in mitotic cells. Finally, I assessed the penetrance of the role of *MND1* and *PSMC3IP* in PARPi sensitivity by re-analysing published CRISPR screens performed in various backgrounds.

3.2. Results

3.2.1. Design of CRISPR screens

Careful CRISPR screen design is crucial to ensuring good quality data output by minimising any potentially confounding artefacts. Prior to performing any experimental work, the CRISPR screens were designed to specifically address the aims I had in mind. As such, I will initially present the rationale for the design of the CRISPR screens in this Chapter.

Schematics demonstrating the workflow for the CRISPRn and CRISPRi screens are shown in Figure 3.1A and Figure 3.1B, respectively. The choice of the model system that is representative of the desired genetic background is crucial. In these screens, I decided to use a PARPi-resistant, HR-proficient, non-tumour epithelial cell line, MCF10A. This immortalised breast cell line has a stable diploid genome (Soule et al., 1990), so is suitable to assess the effects of altering gene expression on drug response (Soule et al., 1990), and also avoids the problem of copy number dependent toxicity of sgRNAs observed with CRISPRn; a phenomenon which can lead to false positives (Aguirre et al., 2016). In addition, this cell line is amenable

for high-efficiency lentiviral infection, which is required for introduction of the sgRNA library into the cells. I used *TP53* mutant MCF10A (MCF10A *TP53*$^{-/-}$), as many cancer-associated mutations (such as *BRCA1)* (Hakem et al., 1997; Hakem et al., 1996; Ludwig et al., 1997) impair cellular fitness by invoking *TP53*-mediated cell cycle checkpoints, and are thus better tolerated when *TP53* is inactivated. In addition, loss of functional *TP53* is clinically relevant; *TP53* mutations are reported in 50% of triple-negative breast cancer (TNBC) cases (Curtis et al., 2012), for example. To facilitate screening, utilised cell lines require expression of Cas9 for CRISPRn (Figure 3.1A) or catalytically-inactive Cas9 (dCas9) fused to KRAB transcriptional repressor (Gossen & Bujard, 1992) for CRISPRi (Figure 3.1B), details of which will be presented in the subsequent chapter.

The plan for the CRISPRn screens (Figure 3.1A) involved mutagenising Cas9-expressing cells with the previously described Yusa genome-wide sgRNA library (Tzelepis et al., 2016). The Yusa library has been designed to target 18,010 protein coding genes, with at least 5 sgRNAs per gene, for a total of 90,706 sgRNAs. The genome-wide Weissman sgRNA library was chosen for the CRISPRi screens (Figure 3.1B), and as such required expression in the dCas9-KRAB expressing cells. The Weissman library was designed to silence 18,905 protein coding genes (104,535 sgRNAs in total) (Horlbeck et al., 2016)).

As described above, the expression of each respective library into the appropriate MCF01A cell line (either Cas9-expressing, or dCas9-expressing) was achieved with lentiviral transduction. In order to ensure that each cell only contains a single

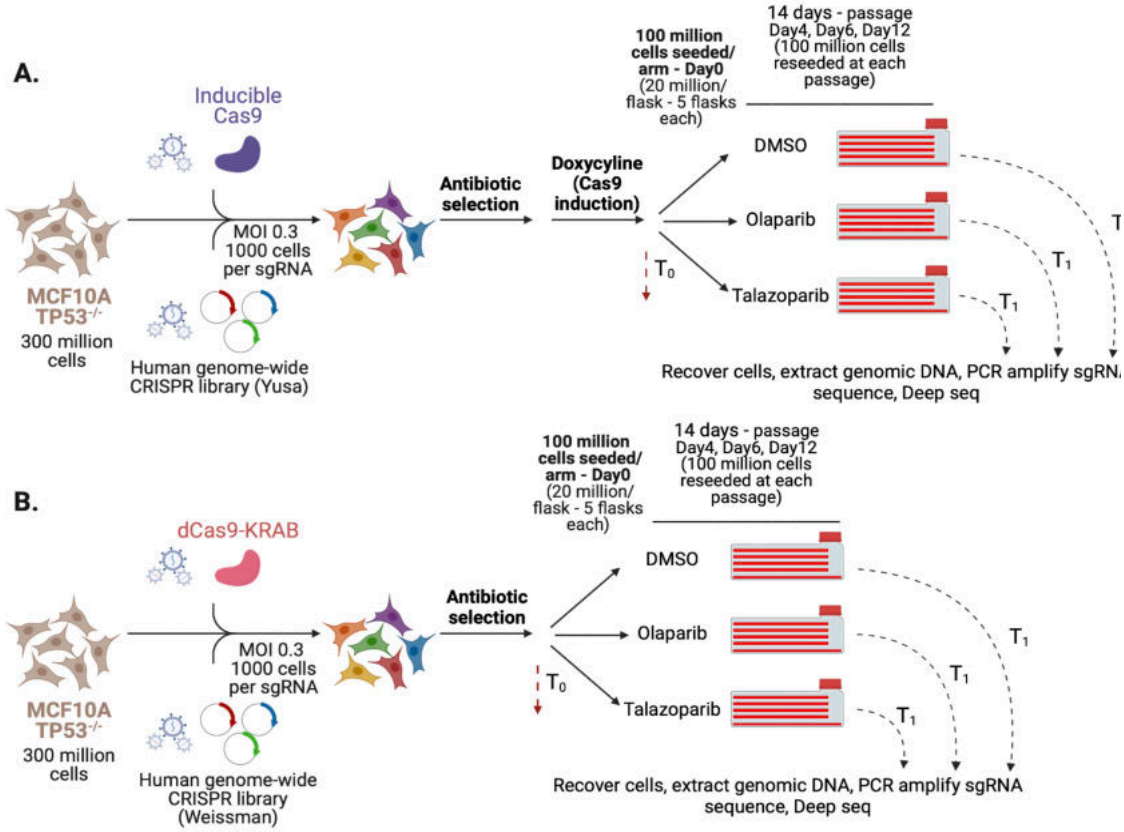

Figure 3.1 Workflow for the CRISPR screens.
A. Workflow for the CRISPRn screens. The cell model for the CRISPRn screen, MCF10A *TP53*$^{-/-}$ iCas9, is generated by infection with lentiviral particles expressing doxycycline-inducible Cas9 transgene (Cas9) into MCF10A *TP53*$^{-/-}$. Blasticidin antibiotic selection eliminates uninfected cells not expressing the Cas9 construct. The human genome-wide Yusa sgRNA library is introduced via lentiviral infection (with MOI 0.3) into MCF10A *TP53*$^{-/-}$ iCas9 cells (100 million cells for 1000X representation). Subsequent puromycin antibiotic selection eliminates uninfected cells not expressing the sgRNA library construct. Cas9 expression is induced with doxycycline. An initial fraction of the cell population (T_0 sample) needs to be taken prior to division of the cell population into three cohorts; those to be cultured in either: (i) drug vehicle (DMSO); (ii) olaparib; or (iii) talazoparib for two weeks. SF_{80} drug concentrations were chosen to allow for identification of sensitising effects. **B.** Workflow for the CRISPRi screens. The cell model for the CRISPRi screen, MCF10A *TP53*$^{-/-}$ dCas9-KRAB, is generated by infection with lentiviral particles expressing catalytically-inactive Cas9 (dCas9) fused to the KRAB transcriptional repressor into MCF10A *TP53*$^{-/-}$. Blasticidin antibiotic selection eliminates uninfected cells not expressing the dCas9-KRAB construct. The human genome-wide Weissman sgRNA library is introduced via lentiviral infection (with MOI 0.3) into stable MCF10A *TP53*$^{-/-}$ dCas9-KRAB cells (100 million cells for 1000X representation). Subsequent puromycin antibiotic selection eliminates uninfected cells not expressing the sgRNA library construct. An initial fraction of the cell population (T_0 sample) would be taken prior to division of the cell population into three cohorts; those to be cultured in either: (i) drug vehicle (DMSO); (ii) olaparib; or (iii) talazoparib for two weeks. SF_{80} drug concentrations were chosen to allow for identification of sensitising effects. Figure adapted from (Zimmermann et al., 2018).

sgRNA, a very low MOI is required ~0.3. Following packaging of the libraries, I titrated the volume of lentivirus mix (and thus the quantity of viral particles) applied to the MCF10A cell line to be used for the CRISPR screen. By counting the number of surviving colonies, and normalising this to the volume of lentivirus mix added, I calculated the volume of lentivirus mix required to generate the desired MOI. In order to adhere to the standard 1000X representation used in published CRISPR screens, whereby 1000 cells express each sgRNA construct, I calculated that approximately 300 million cells would require transduction with the respective library.

Given that the Yusa and Weissman sgRNA library was cloned into the pKLV lentiviral vector with a puromycin resistance gene, exposure to puromycin would allow selection of positively-infected cells. A kill curve determined that exposure to 2 μg/mL puromycin for 7 days was required for the selection of positively-infected cells in MCF10A model.

An initial fraction of the CRISPR-mutagenised cell population (T_0 sample) needs to be reserved for later analysis, prior to division of the cell population into three cohorts; those to be cultured in either: (i) drug vehicle (DMSO); (ii) olaparib; or (iii) talazoparib. For the CRISPRn screen, this T_0 sample needs to be reserved following doxycycline exposure, given the inducible nature of the Cas9-expression vector. Given that the aim of the CRISPR screens was to identify sensitising effects, sublethal drug concentrations which result in 20% reduction in cell survival (Surviving Fraction 80, SF_{80}) would maintain long-term cell viability and drug effectiveness.

In order to maximise the cytotoxic effect of PARPi, a high level of PARPi exposure needs to be maintained over a number of cell cycles (Bryant et al., 2005; Farmer et al., 2005), an effect which has translated clinically (Fong et al., 2009). As such, we planned to expose the cells to PARPi or DMSO for 14 days (10 population doublings) in order to model chronic exposure (T_1 sample).

3.2.2. Cell line generation and characterisation for the CRISPR screens

Prior to commencing the experimental work required for the CRISPR screens, I generated the cell line models to be used, and subsequently characterised these. In brief, I achieved this via lentiviral transduction into the cell line model of choice, MCF10A *TP53*$^{-/-}$. As described in the previous section outlining the strategy for the CRISPR screens, establishing the model for the CRISPRn screen required introduction of a doxycycline-inducible Cas9 transgene (Cas9), to generate a cell line which I will refer to as MCF10A *TP53*$^{-/-}$ iCas9. In addition to the FACs-based functional assay used to confirm Cas9 activity of the cell line to mediate gene knockout, described in 2.11, I confirmed inducible Cas9 expression upon addition of doxycycline with immunoblotting, as shown in Figure 3.2. For the CRISPRi screen model, I introduced into MCF10A *TP53*$^{-/-}$ a transgene expressing catalytically-inactive Cas9 (dCas9) fused to the KRAB transcriptional repressor (Gossen & Bujard, 1992), to generate a cell model which I will refer to as MCF10A *TP53*$^{-/-}$ dCas9-KRAB. In addition to the FACs-based functional assay used to confirm dCas9-KRAB activity of the cell line to mediate gene knockdown, described in 2.11, immunoblotting was used to confirm constitutive dCas9-KRAB expression in MCF10A *TP53*$^{-/-}$ dCas9-KRAB cell line (Figure 3.2).

The PARPi response of the MCF10A *TP53*$^{-/-}$ cell model was determined experimentally by Rachel Brough, a colleague in the Gene Function lab, ICR. Upon analysing the data, I determined that the SF_{80} for olaparib and talazoparib in MCF10A *TP53*$^{-/-}$ cell model is 2.5 μM and 25 nM, respectively (Figure 3.3). As such, these PARPi doses were used in the CRISPRn and CRISPRi screens. In addition, I found that the MCF10A *TP53*$^{-/-}$ cells were significantly more resistant to PARPi than *BRCA1* mutant SUM149 triple-negative breast tumour cells, but had a similar PARPi sensitivity profile to the PARPi-resistant SUM149 cell line with a *BRCA1* reversion mutation (Drean, et al., 2017). This was the case for both clinical PARPi tested, olaparib (Figure 3.3A) and talazoparib (Figure 3.3B).

3.2.3. CRISPR screen sample preparation

After two weeks continuous culture of the Yusa sgRNA library-expressing MCF10A *TP53*$^{-/-}$ iCas9 cells or the Weissman sgRNA library-expressing MCF10A *TP53*$^{-/-}$ dCas9-KRAB cells in PARPi- or DMSO-containing medium, the surviving cells were recovered (T_1). The olaparib and talazoparib arms of the CRISPRn screens were performed simultaneously, so the same T_0 sample could be used for comparison with the T_1 samples. For the CRISPRi screens, the olaparib and talazoparib arms were performed at different times, so different T_0 samples were used for comparison with the respective T_1 sample. In order to identify genes, i.e. CRISPR sgRNAs, that enhanced the sensitivity of cells to PARPi, sgRNA depletion was identified in cells that survived drug or DMSO exposure using massively parallel sequencing. With the help of Gene Function laboratory colleague, Feifei Song, the sequencing samples were prepared from the T_0 and T_1 cell suspensions.

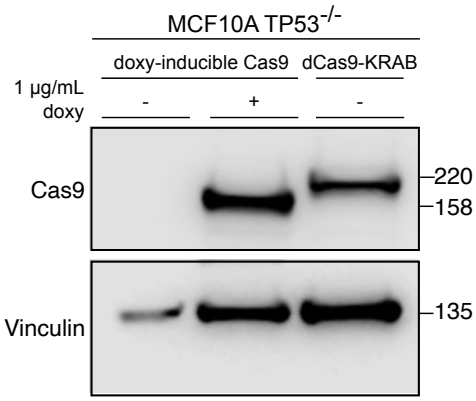

Figure 3.2 Cas9 immunoblotting of MCF10A TP53$^{-/-}$ cell lines used in CRISPR screens.
Western blot image of MCF10A TP53$^{-/-}$ cell lysates illustrating expression of either doxycycline-inducible Cas9 or catalytically-inactive Cas9 (dCas9) fused to a KRAB transcriptional repressor (dCas9-KRAB). Vinculin was used as a loading control.

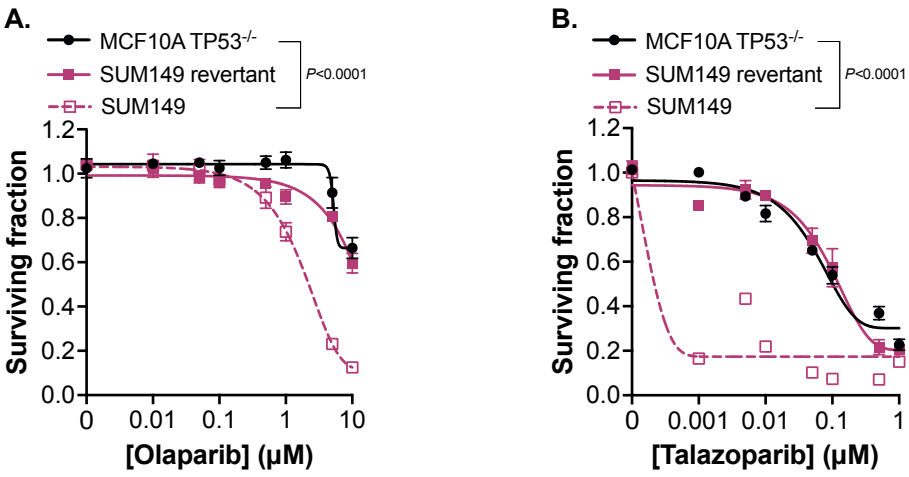

Figure 3.3 Characterisation of PARPi response for MCF10A TP53$^{-/-}$ model used in CRISPR screens.
Dose/response survival curves are shown with surviving fractions at the indicated doses of olaparib (A) or talazoparib (B). Cells were plated in 384-well plates and exposed to the specified PARPi for five continuous days, after which cell viability was quantified by CellTiter-Glo®. Surviving fraction was calculated for each drug dose relative to DMSO-exposed cells. PARPi sensitive *BRCA1* mutant SUM149 and PARPi-resistant *BRCA1* revertant SUM149 cells are shown as controls. Error bars represent SD from n=3 replicates. *P*-values were calculated via ANOVA with Tukey's post-test.

Sample preparation required extraction of genomic DNA, followed by two separate PCR reactions. The first PCR reactions involve the amplification of the sgRNA region, which is then barcoded in the second PCR step, as outlined in Figure 3.4. In order to maintain 1000X representation during the first PCR step, PCR amplification of certain amount of genomic DNA is required. Given both the Yusa and Weissman sgRNA libraries contain approximately 100,000 sgRNAs, and that a diploid human genome is approximately 6.6 pg, 1000X representation required 660 µg genomic DNA for these PCR amplifications. Following PCR purification, I barcoded the PCR products from the first PCR reaction, with multiple PCR reactions using PCR primers with unique index sequences. The ICR Tumour Profiling Unit carried out NGS from the resulting PCR amplicons on an Illumina (HiSeq 2500) platform, to generate >1,000 reads for each sgRNA in the library.

3.2.4. CRISPR screen data analysis

The short-read sequences were aligned to the known sgRNA sequences present in each pool by colleagues in the ICR Bioinformatics department, Aditi Gulati and John Alexander. The relative enrichment or depletion of sgRNAs from T_0 vs. T_1 samples in both DMSO and PARPi-exposed samples was compared, as follows, to ultimately calculate a normalised DE Z-score (normZ (Colic et al., 2019)) for each sgRNA targeting a specific gene. MAGeCK analysis was used to generate sgRNA counts, according to the sequences present in the genome-wide CRISPR library (Li et al., 2014). Using normalised read count data from MAGeCK, quality checks were performed (distribution of read counts, clustering of samples), to confirm the robustness of the data. For downstream analysis of sgRNA read count data, three approaches were used for comparative analysis: (1) MAGeCK

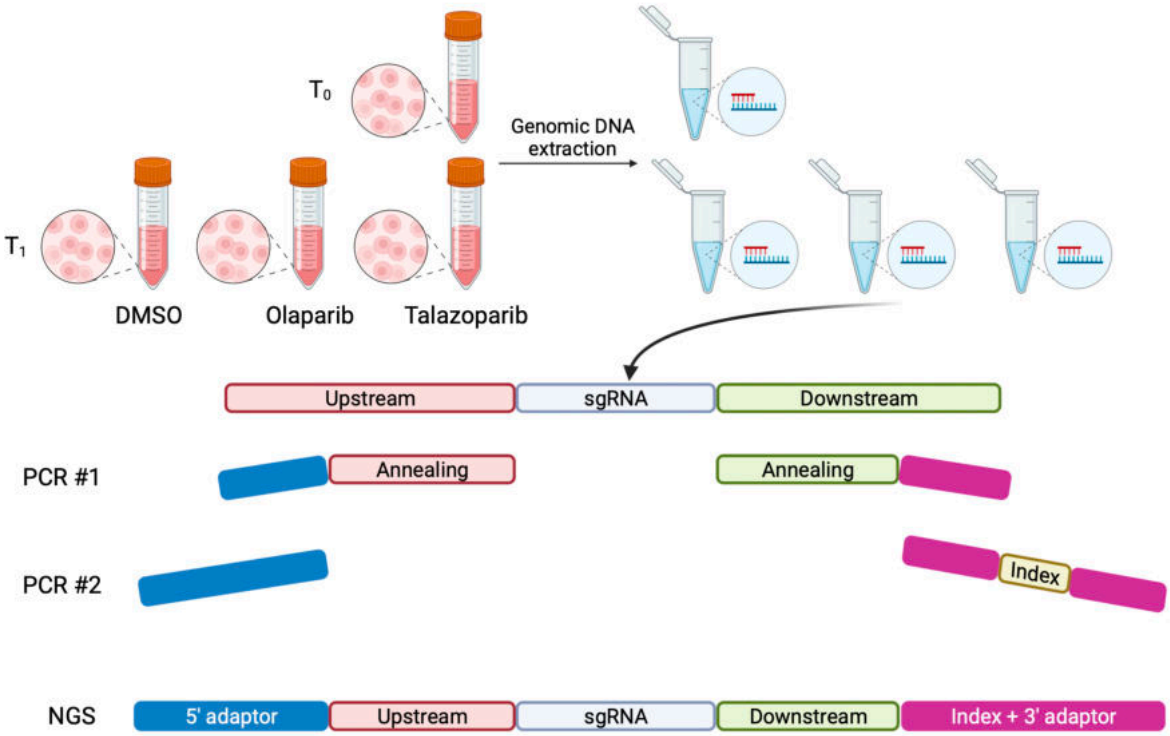

Figure 3.4 Schematic of CRISPR screen sample preparation.
Sample preparation of CRISPR screen samples for Illumina sequencing initially involved extraction of genomic DNA from T_0 and T_1 cell suspensions, which were cultured in DMSO, olaparib or talazoparib for two weeks. PCR #1 involves amplifying the sgRNA region, which is then barcoded in PCR #2 following PCR purification. The primers utilised in PCR #2 have unique index sequences. The resulting PCR amplicons were sequenced via next-generation sequencing (NGS). Figure adapted from (Holm et al., 2019).

(2) Z-score and (3) DE Z-score. From the MAGeCK workflow, we extracted a ranked list of positively selected hits generated using a RRA approach (Li et al., 2014). For the Z-score approach, the low abundant guides, with a read count of 0 in the T_0 sample, were initially identified and removed from the analysis. In order to account for variation in the amounts of DNA sequenced, the read counts were converted to parts per ten million (pptm), and then $\log_2$-transformed after adding a pseudo count of 0.5. For each screen, Z-scores were calculated for each individual sgRNA, corrected for viability and drug effects, as follows. The DE* Z-score was calculated from the difference in abundance of each sgRNA between the drug-treated (Drug (T)) and DMSO-treated samples (DMSO(T)) at a matched timepoint. Viability effects (VE)**, the rate of decreased sgRNA abundance in the population over time in the absence of drug treatment, were taken into account by calculating a Z-score between the T_0 (DMSO (T0)) and T_1 DMSO-treated (DMSO (T1)) sample. Both DE and VE Z-scores were normalised by MAD***. The variability in DE, that can be attributed to VE, was taken in account by adjusting DE according to a plotted linear model of DE vs VE, referred to as Corrected DE****. In order to assess the overall effect size of each gene, the corrected DE Z-score was normalised to generate a gene-level DE Z-score*****.

$$^{*}\boldsymbol{Drug\ Effect\ (DE)} = \frac{(Drug\ (T) - DMSO(T)) - median(Drug\ (T) - DMSO(T))}{MAD(Drug\ (T) - DMSO(T))}$$

$$^{**}\boldsymbol{Viability\ Effect\ (VE)} = \frac{(DMSO\ (T1) - DMSO\ (T0)) - median(DMSO\ (T1) - DMSO\ (T0))}{MAD(DMSO\ (T1) - DMSO\ (T0))}$$

I.e. Z = (x – median)/median absolute deviation

*** $\boldsymbol{MAD} = median\ |x_i - \tilde{x}|$

**** $\boldsymbol{Corrected\ DE} = \dfrac{(\boldsymbol{DE} - \boldsymbol{c})}{(\boldsymbol{VE} \times \boldsymbol{m})}$

***** $\boldsymbol{Gene\ drug\ effect\ Zscore} = \dfrac{(\sum sgRNA\ Zscores)}{(\sqrt{n\ of\ gRNAs})}$

In this case, CRISPR mutagenesis of genes resulting in negative gene-level DE Z-score are determined to enhance PARPi sensitivity. I defined genes as "hits" with a gene-level DE Z-score threshold of ≤ -3, for at least two independent significant (p = 0.05) sgRNAs, to capture the top ~2% and identify the most profound effects. Ranks for negative selection were generated by sorting results based on their Z-score in ascending order. A final list of "hits" was consolidated from the three approaches, (1) MAGeCK (2) Z-score and (3) DE Z-score, by taking the rank product of their ranks. Such a "hit-list" of genes with the top 50 most profound effects from the CRISPRn and CRISPRi screens is provided in Table 5 and Table 6, respectively.

3.2.5. CRISPR screen data quality control

Building on the quality checks performed by the Bioinformatics department, I plotted the density of VE Z-scores for sgRNAs targeting core essential genes and non-essential genes (Hart et al., 2014) during the course of the screen in the absence of drug (DMSO) (i.e. T_1 vs T_0). The olaparib and talazoparib arms of the CRISPRn screens were performed simultaneously, so the VE Z-scores are the

Table 5 Top 50 CRISPRn screen data for MCF10A *TP53*$^{-/-}$ cells.

GeneID	CRISPRn Viability Z score (olap and talaz screen)	CRISPRn Drug Effect Z score (olap screen)	CRISPRn Olaparib sgRNA Drug Effect Zcount	CRISPRn Olaparib Gene Rank	CRISPRn Drug Effect Z score (talaz screen)	CRISPRn Talazoparib sgRNA Drug Effect Zcount	CRISPRn Talazoparib Gene Rank
RAD54L	0.693	-13.121	4	9.691	-16.779	5	1.000
RAD51B	-2.255	-8.480	4	15.461	-15.953	4	2.714
PSMC3IP	-0.979	-11.689	4	7.862	-13.193	4	4.481
RNASEH2A	-3.640	-16.917	5	1.442	-12.572	5	4.380
MND1	0.067	-10.841	4	8.896	-11.947	4	9.166
POLB	0.615	-3.438	1	820.249	-11.882	4	11.972
LIG3	-2.648	-4.037	2	296.977	-11.587	5	10.027
SRP68	-6.486	-0.214	0	7058.487	-11.053	3	34.554
LIG1	-1.671	-13.249	5	7.489	-11.049	5	9.356
XRCC1	-0.476	-6.840	4	57.117	-10.734	5	6.840
C19orf40	0.948	-5.572	2	170.480	-10.453	5	25.339
HMGCS1	-9.959	-3.359	1	3060.480	-10.280	3	94.103
RNASEH2B	-0.065	-14.791	4	5.828	-10.119	3	30.187
DAD1	-7.026	-9.587	3	66.748	-10.069	2	274.008
MAPK1	-6.636	-4.168	2	1529.996	-10.026	4	121.743
HIGD1A	1.587	2.492	0	16650.668	-10.001	2	99.465
RNMT	-11.401	-6.613	3	187.752	-9.581	4	74.858
ATM	-0.405	-9.081	5	14.518	-9.489	4	16.812
NBN	-0.960	-9.073	4	15.724	-9.423	3	21.277
TARDBP	-5.164	-0.548	1	4737.602	-9.389	2	131.985
HIST1H2BN	-5.207	0.680	0	13648.090	-9.303	2	52.269
RTTN	-3.379	-2.321	1	2882.636	-9.261	3	50.746
DSCC1	-2.087	-8.600	4	34.778	-9.192	3	21.498
MUS81	-1.568	-8.398	3	27.447	-9.170	3	20.856
ACTR10	-10.304	-4.129	2	1447.761	-9.163	3	78.077
CHTF8	-4.210	-6.601	3	86.474	-9.135	4	54.224
YARS	-10.015	-3.414	2	2056.473	-9.112	4	64.538
KIAA1524	-1.132	-3.332	1	291.472	-8.946	4	23.096
RAD51AP1	0.604	-4.564	2	232.666	-8.780	4	56.414
PPA2	-2.506	-1.672	1	3208.510	-8.756	2	474.519
LSM4	-10.296	-7.858	4	72.665	-8.738	4	33.929
IDI1	-2.901	-7.227	2	961.500	-8.636	2	722.276
C8orf59	2.582	-6.177	2	161.804	-8.579	2	53.236
USP9X	-6.962	-2.621	1	2512.901	-8.559	3	157.375
FANCM	-1.273	-5.430	2	329.069	-8.427	4	50.684
UFD1L	-9.186	-4.369	4	384.749	-8.359	2	290.660
WRN	-0.456	-3.100	2	1167.539	-8.229	2	234.188
RAD1	-4.378	-8.300	4	89.447	-8.226	2	259.382
EIF3B	-10.129	-5.263	3	525.351	-8.207	3	128.148
L2HGDH	-0.611	0.902	0	14739.068	-8.175	2	333.497
ZNF429	2.160	-2.055	2	4750.975	-8.165	3	62.721
SIVA1	-2.832	-3.221	1	393.167	-8.156	6	19.626
MZT1	-5.273	-5.067	2	543.023	-8.130	2	72.308
ITGB1	-9.433	-4.192	2	1521.944	-8.107	4	136.996
GBAS	0.241	-1.392	0	2992.235	-8.076	3	196.391
RMI1	-7.453	-3.782	2	1130.896	-8.037	3	100.461
CDK1	-8.208	-1.562	2	5858.678	-8.028	3	64.925

Table 6 Top 50 CRISPRi screen data for MCF10A TP53$^{-/-}$ cells

GeneID	CRISPRi Viability Z score (olap screen)	CRISPRi Drug Effect Z score (olap screen)	CRISPRi Olaparib sgRNA Drug Effect Zcount	CRISPRi Olaparib Gene Rank	CRISPRi Viability Z score (talaz screen)	CRISPRi Drug Effect Z score (talaz screen)	CRISPRi Talazoparib sgRNA Drug Effect Zcount	CRISPRi Talazoparib Gene Rank
EME1	-1.042	-5.672	4	69.243	-1.558	-28.459	0	1.260
PSMC3IP	-5.780	-9.875	5	7.731	-7.776	-28.314	3	1.817
MUS81	-4.318	-9.812	5	12.254	-5.068	-24.466	1	3.302
XRCC1	0.125	-3.954	1	270.776	-0.167	-22.513	0	6.000
LIG1	-1.623	-12.574	4	3.302	-1.193	-18.740	0	6.840
MND1	-0.679	-6.083	4	30.825	-0.690	-18.683	0	3.915
ATM	-0.140	-7.877	4	33.238	-1.661	-18.598	5	11.855
DDX11	-3.014	-5.846	3	101.985	-3.141	-18.298	1	15.810
POLB	-0.002	-2.868	2	637.384	0.029	-17.818	0	8.963
TRAIP	-8.397	-12.417	5	5.192	-10.609	-17.483	0	13.389
AUNIP	0.161	-4.021	3	90.445	-0.440	-16.409	0	12.557
CHTF18	-3.471	-2.728	1	1011.837	-2.978	-15.887	2	22.490
RAD51B	-2.062	-6.631	4	61.806	-3.277	-15.564	5	11.788
RAD54L	-1.321	-4.616	4	166.958	-1.735	-15.495	0	10.492
RNASEH2C	-4.435	-5.372	3	308.384	-4.731	-15.209	2	23.382
BARD1	-7.241	-9.910	4	17.287	-8.240	-15.020	4	16.980
PALB2	-7.276	-13.633	5	5.518	-9.701	-14.776	5	22.561
BRCA2	-11.466	-17.378	5	2.000	-15.896	-13.928	2	36.022
H2AFX	-0.493	-4.966	3	101.712	-1.521	-13.340	5	16.485
FAM178A	-5.073	-1.977	0	1905.895	-7.536	-13.335	1	25.990
ATR	-18.732	-2.797	3	1303.653	-19.822	-12.432	5	61.525
RAD51D	-10.716	-5.773	3	317.168	-11.819	-12.425	4	38.234
CAD	-17.197	-5.863	2	528.666	-16.666	-11.991	5	43.912
ATAD5	-7.395	-2.932	1	815.720	-6.892	-11.061	1	56.853
SOCS4	-2.490	-6.853	3	34.002	-3.744	-11.061	3	25.303
XRCC2	-7.862	-7.402	3	67.853	-11.388	-11.038	4	39.398
SKA1	-11.363	-4.716	1	786.158	-12.067	-10.528	2	190.020
DSN1	-30.627	-8.954	4	252.655	-28.773	-10.219	3	167.321
PNKP	-4.404	-3.049	2	519.412	-6.351	-10.088	1	47.069
PRDX1	0.951	-2.530	1	492.703	0.534	-10.011	0	15.212
SPON2	2.441	-0.684	1	9163.836	2.079	-9.962	1	44.944
MRPL27	-6.161	-9.114	4	25.133	-6.823	-9.716	0	63.666
NAE1	-12.375	-1.191	2	1821.364	-11.558	-9.587	1	38.653
AURKB	-24.830	-1.091	0	4059.444	-21.750	-9.500	3	150.208
RIBC1	-14.834	-7.473	3	155.439	-15.042	-9.484	4	117.236
CWC22	-12.669	-3.613	2	1075.167	-10.107	-9.459	2	157.532
TTC1	-30.766	-5.395	2	1105.126	-26.177	-9.392	2	77.544
RNF8	-3.231	-3.629	3	148.102	-4.711	-9.295	1	22.104
RFC2	-13.727	-5.079	3	346.044	-11.422	-9.247	5	36.885
NFRKB	-11.276	-4.646	3	567.454	-11.269	-8.964	2	91.900
RAD50	-1.391	-3.597	2	368.063	-2.819	-8.960	2	37.588
SF3B2	-17.647	-4.855	3	640.381	-16.669	-8.830	4	196.410
FANCM	-0.836	-0.713	0	4768.108	-1.226	-8.795	4	32.559
SIVA1	0.997	-1.972	1	1076.028	0.601	-8.747	0	34.974
BCS1L	-10.787	-6.015	3	235.658	-12.832	-8.615	0	60.257
RMI1	-5.552	0.720	0	15742.654	-3.627	-8.613	4	68.321
CDC23	-25.264	-8.538	3	334.576	-20.707	-8.528	1	252.996

same, whereas the olaparib and talazoparib arms of the CRISPRi screens were performed at different times. For both the CRISPRn and CRISPRi screens, the VE Z-scores for essential genes are reduced in comparison to those of the non-essential genes (Figure 3.5), highlighting the efficiency of the CRISPRn-mediated mutagenesis or CRISPRi-mediated transcriptional repression in the respective screens. While the VE Z-scores for the non-essential genes are similar between the CRISPRn and CRISPRi screens, the VE Z-scores for the essential genes are reduced to a greater extent in the CRISPRn screens. While CRISPRn-mediated mutagenesis results in gene “knockout”, whereby expression of the target gene is completely ablated, CRISPRi-mediated transcriptional repression reduces expression of the target gene. Compared to those for CRISPRn, CRISPRi sgRNAs may also not be as effective; they are designed in proximity to the target gene’s promoter region or transcriptional start site (TSS), which can be inaccessible due to the presence of other protein factors, or TSS are not accurately annotated. Overall, this QC approach indicated that each of the screens was of sufficient quality to warrant further analysis.

I analysed the CRISPRn and CRISPRi screens simultaneously, in which PARPi sensitivity-causing effects are represented with negative Z-scores, whereas genes with positive Z-scores represent PARPi resistance-causing effects. By comparing data from olaparib *vs.* talazoparib screens, I found both CRISPRi and CRISPRn screens to be highly reproducible (Figure 3.6), providing confidence in their fidelity. As detailed in Chapter 1, the cytotoxic effect of clinical PARPi, such as olaparib and talazoparib, is at least partially caused by trapping PARP1 on DNA (Krastev et al., 2021). Given that talazoparib is a more potent PARP1 trapping inhibitor

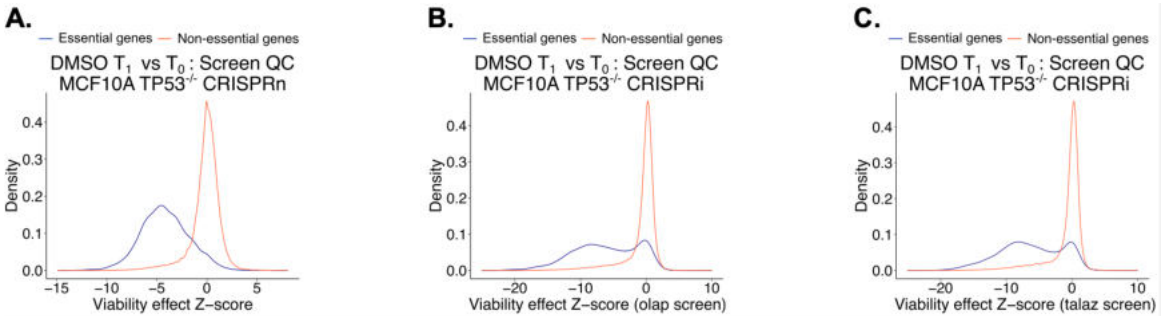

Figure 3.5 Depletion of sgRNAs targeting core essential genes assures CRISPR screen data quality.
Density plots are shown of viability effect Z-scores from genome-wide CRISPRn (A) and CRISPRi (B, C) screens. Viability effect Z-scores, the rate of decrease of sgRNA abundance in the population over time in the absence of drug treatment, were calculated from the difference in Z-score between the T_0 (DMSO (T0)) and T_1 DMSO-treated (DMSO (T1)) sample. The olaparib and talazoparib arms of the CRISPRn (A) screens were performed simultaneously, so the viability effect Z-scores are the same, whereas the olaparib and talazoparib arms of the CRISPRi screens (B, C) were performed at different times.

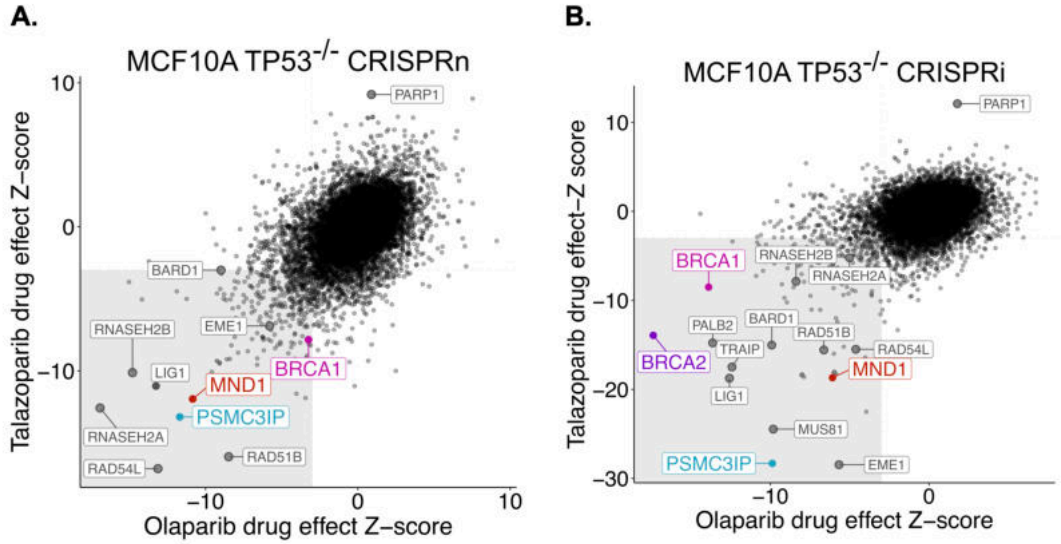

Figure 3.6 PARPi drug-effect Z-scores for CRISPRn and CRISPRi screens.
Scatter plots are shown of olaparib vs. talazoparib drug-effect Z-scores for CRISPRn (A) and CRISPRi (B) screens. Genes with negative Z-scores represent PARPi sensitivity-causing effects (as shown by named HR/DNA repair genes), whereas genes with positive Z-scores represent PARPi resistance-causing effects (e.g. PARP1). Genes annotated in grey are known HR mediators. Grey shaded area captures drug-effect Z-scores ≤ -3. CRISPR screens described in Figure 3.1.

compared to olaparib, the more negative DE Z-scores reported in the talazoparib CRISPRn and CRISPRi screens was expected. PARPi-mediated cytotoxicity via PARP1 trapping also indicates that prevention of PARP1 trapping by deletion of *PARP1* or *PARP1* mutations cause PARPi resistance, in both *BRCA1* wild-type and most *BRCA1*-mutant cells (Pettitt et al., 2018). I noted that sgRNA designed to target *PARP1* gave one of the most profound PARPi resistance-causing effects in both CRISPRn and CRISPRi screens (Figure 3.6).

Previous focused shRNA screens (McCabe et al., 2006), genome-wide shRNA screens (Bajrami et al., 2014) and genome-wide CRISPRn screens for PARPi sensitivity (Clements et al., 2020; DeWeirdt et al., 2020; Jamal et al., 2022; Olivieri et al., 2020) indicated that a number of different genes involved in HR enhance PARPi sensitivity when inactivated. This was also the case in the CRISPRn and CRISPRi screens reported in this thesis. Some of the most profound PARPi sensitivity-causing effects were due to CRISPRi or CRISPRn targeting of the HR-associated genes *RAD51B, RAD54L, EME1, MUS81, PALB2, BRCA1, BARD1* and *BRCA2* (Figure 3.6). Unbiased pathway annotation of “hits” in CRISPRn and CRISPRi screens, revealed that in both olaparib and talazoparib screens, HR was identified as an enriched pathway. In fact, HR represents one of the top 20 most enriched pathways, when ranking pathways according to statistical significance (Figure 3.7).

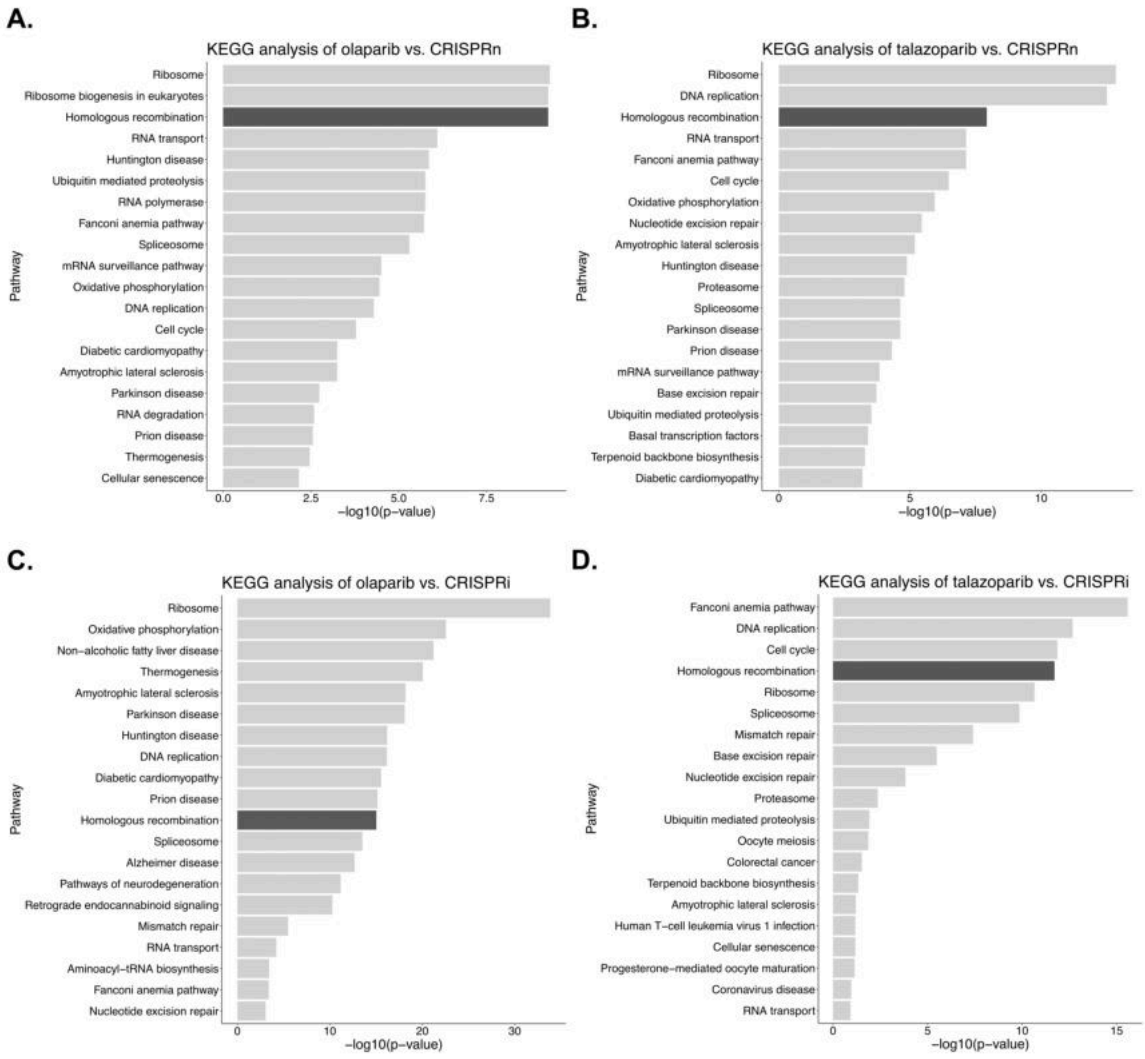

Figure 3.7 Unbiased pathway annotation of CRISPR screen data.
Bar plots are shown from unbiased pathway annotation of "hits" in CRISPR screens, ranked according to statistical significance (-$\log_{10}$(p-value)). Screen "hits" are included in the analysis from cells exposed to PARPi olaparib (A) or talazoparib (B) following CRISPRn-mutagenesis. Identical analysis was performed including screen "hits" from CRISPRi-expressing cells exposed to PARPi olaparib (C) or talazoparib (D) following CRISPRn-mutagenesis. Pathways were ranked according to statistical significance (*p*-value) to identify those most highly enriched. *P*-values were -$\log_{10}$transformed to facilitate data visualisation. HR pathway is highlighted in dark grey. CRISPR screens described in Figure 3.1.

3.2.6. CRISPR-mediated identification of determinants of PARPi sensitivity

In addition to the genes detailed above, additional genes involved in HR and DSBR also scored as “hits” in the screens (*ACTR5, ATM, ATRIP, AUNIP, CHAF1B, FAAP24 (C19orf40), FANCA, FANCD2, FANCE, FANCI, FANCL, FANCM, INO80, KIAA1524 (CIP2A), MCM8, MCM9, MRE11A, NBN, NSMCE1, NDNL2, PNKP, RAD50, RAD51, RAD51C, RAD51AP1, RBBP8 (CtIP), RMI1, RNF8, RNF168, SHFM1 (DSS1), SLX4, SMC4, SMC6, SFR1, STRA13 (CENPX), SLX4, SWI5, TELO, TONSL, TRAIP, USP1, WDR48, WRN, XRCC2, XRCC3*), recruitment and activity of the 9-1-1 complex (*ATAD5, RAD1, RAD9A, RAD17*), control of the DNA damage-induced S/G_2 and G_2/M checkpoints (*FOXM1*, *CCNB2*), chromatin remodelling complex components (*ACTL6A, BRD2, RBBP7, SMARCB1*), chromosome cohesion factors (*CHTF18, CHTF8, ESCO2, DSCC1*), BER (*LIG1, LIG3, FEN1, UNG, APEX2, MUTYH*), NER (*CUL4A, GTF2H2C, RFC4, LIG1, RPA3, POLD2, ERCC2, GTF2H3, RFC5, PCNA, RFC1, CCNH, CETN2, GTF2H4, DDB1, POLE4, CDK7, ERCC3*), the PARP1 co-factor *C4orf27* (*HPF1*) and three *RNASEH2*-family genes known to control PARPi sensitivity by modulating levels of genomic uracil (*RNASEH2A, RNASEH2B, RNASEH2C* (Zimmermann et al., 2018)).

The combinatorial approaches of both CRISPRn and CRISPRi, as well as the use of two different clinical PARPi, allowed the identification of the most profound effects that were independent of the mode of gene perturbation or the PARPi used. As expected, I identified a number of HR-associated genes (as detailed above), but also two genes that encode a heterodimer classically involved in meiotic recombination, MND1 (Meiotic Nuclear Division Protein 1 Homolog) and PSMC3IP (PSMC3 Interacting Protein, HOP2, (Figure 3.6). Examination of each individual PARPi CRISPRi screen revealed that the effect of targeting *MND1* or *PSMC3IP* on PARPi sensitivity was comparable, or more profound, than that achieved by CRISPRi-mediated targeting of either *BRCA1* or *BRCA2* (Figure 3.8). While CRISPRi-mediated transcriptional repression reduces expression of the target gene, CRISPRn-mediated mutagenesis results in gene “knockout”, whereby expression of the target gene is completely ablated. As such, the DE Z-scores for *MND1* and *PSMC3IP* are even more negative than those for *BRCA1* and *BRCA2*. *BRCA1* and *BRCA2* are known essential genes, whereby CRISPRn-mediated knockout of *BRCA1* or *BRCA2* is known to cause a viability effect even in the absence of drug. As described in 3.2.4, viability effects were taken into account for final calculation of the DE Z-scores. This suggests that *MND1* or *PSMC3IP* are not essential genes and are amenable to knockout. The advantages of using CRISPRi-mediated transcriptional repression as a method of genetic perturbation instead of CRISPRn-mediated knockout in CRISPR screens are evidenced here; CRISPRn screens used in isolation can mask profound drug sensitivity effects from essential genes.

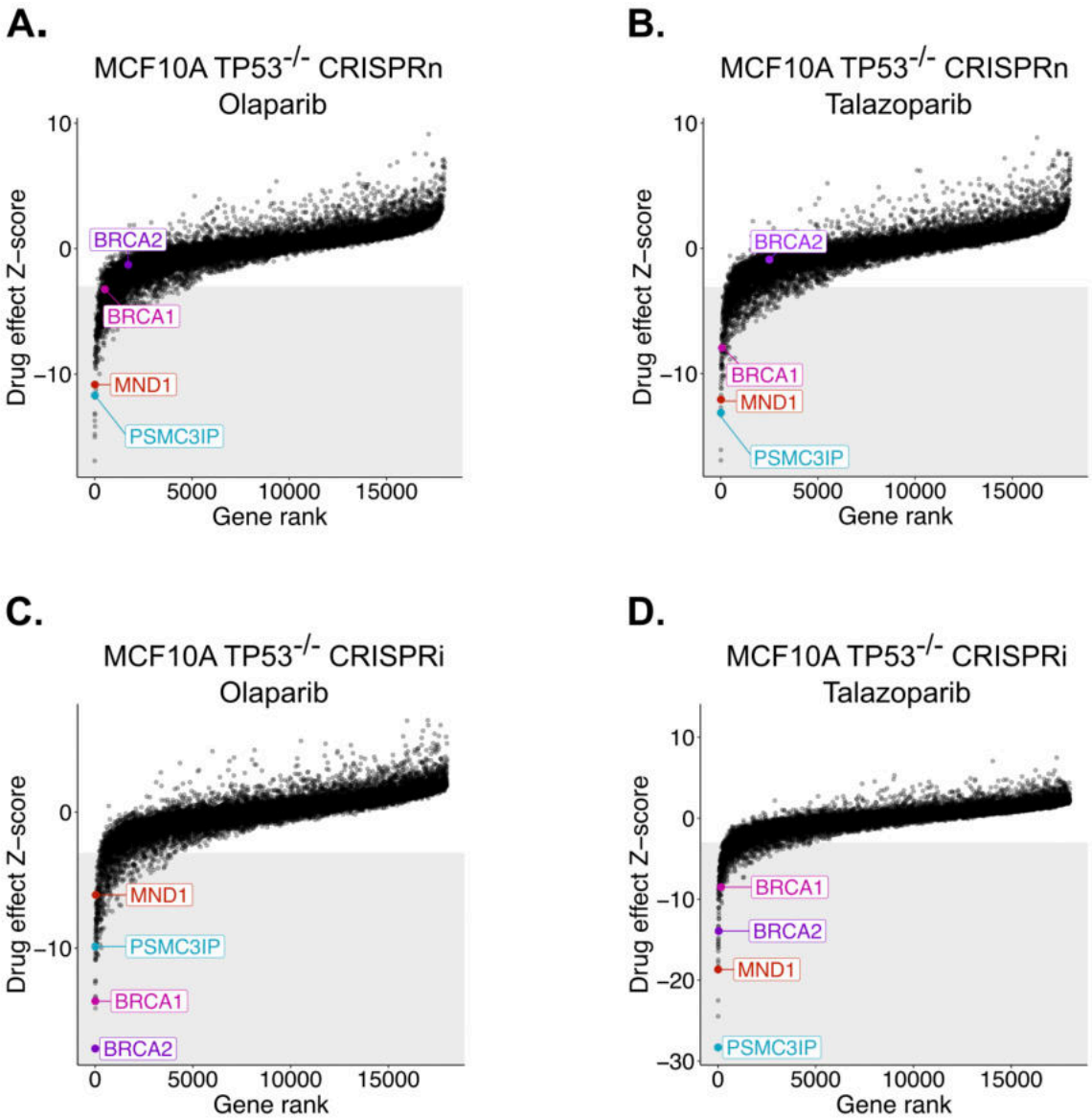

Figure 3.8 CRISPR-targeting of *MND1* or *PSMC3IP* in comparison to CRISPR-targeting of *BRCA1* or *BRCA2*, known HR mediators.
Scatter plots are shown from screens described in Figure 3.1. Drug-effect Z-scores are demonstrated from cells exposed to PARPi olaparib (A) or talazoparib (B) following CRISPRn-mutagenesis. Drug-effect Z-scores are shown from CRISPRi-expressing cells exposed to PARPi olaparib (C) or talazoparib (D). In each of the scatter plots, the drug-effect Z-scores are compared to gene rank. Ranks for negative selection were generated by sorting results based on their Z-score in ascending order and consolidating scores from the three approaches, (1) MAGeCK (2) Z-score and (3) drug-effect Z-score, by taking the rank product of their ranks (see methods). Genes with negative Z-scores represent PARPi sensitivity-causing effect, as demonstrated with BRCA1 and BRCA2 labelled in pink and purple, respectively. Grey shaded area captures drug-effect Z-scores ≤ -3.

The profound effect of targeting *MND1* or *PSMC3IP* on PARPi sensitivity was also evident when comparing DE Z-scores of each individual sgRNA targeting *BRCA1* and *BRCA2* with those for *MND1* and *PSMC3IP* (Figure 3.9). Given that the drug-effect Z-scores were relatively consistent between individual sgRNAs targeting *MND1* and *PSMC3IP*, I deduced that the reported gene-level DE Z-scores were reliable and not skewed by outlier DE Z-scores from sgRNAs targeting a particular gene region which results loss of cell fitness (Figure 3.9).

3.2.7. Penetrance of PSMC3IP and MND1 as determinants of sensitivity to DNA damage agents

In parallel, our collaborators, Sven Rottenberg and colleagues (University of Bern) also identified *MND1* and *PSMC3IP* depletion in a retroviral mutagenesis screen selecting HAP1 cells by IR (Figure 3.10) (Francica et al., 2020). Paola Francica performed the initial screen as previously described (Francica et al., 2020), and then I replotted and analysed the data so that it could be compared with the CRISPRn and CRISPRi screen data. Together, the results from the CRISPR and retroviral mutagenesis screens suggested that the effect of *PSMC3IP-MND1* inhibition was not specific to PARPi, but also caused sensitivity to other forms of DNA damage.

A major issue that has limited the utility of synthetic lethal interactions in cancer treatment in general is incomplete penetrance, whereby the reported synthetic lethality is restricted to the specific genetic background in which it was identified (Ryan et al., 2018). In order to assess the generality of the identified synthetic lethality relationship with *MND1*/*PSMC3IP* for numerous genetic backgrounds,

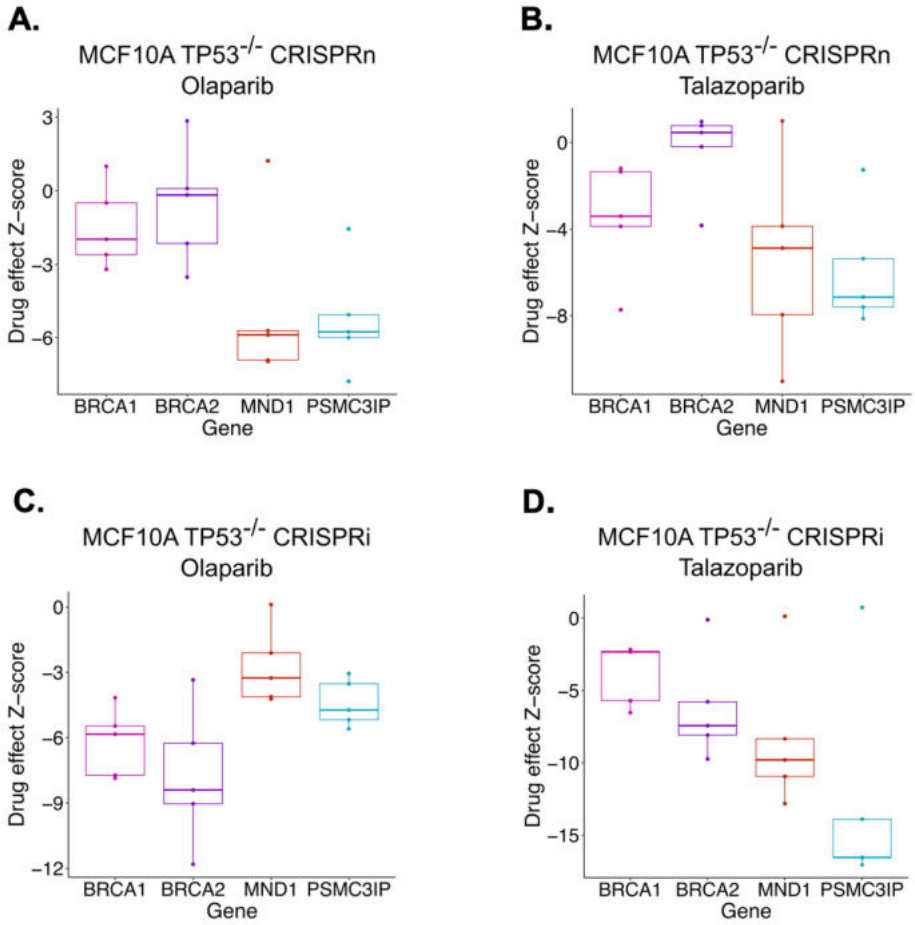

Figure 3.9 CRISPR-targeting of *MND1* or *PSMC3IP* in comparison to CRISPR-targeting of *BRCA1* or *BRCA2*, known HR mediators at sgRNA-level. Box plots are shown of drug-effect Z-scores for each sgRNA targeting the specified gene from screens described in Figure 3.1. sgRNA-level drug-effect Z-scores are demonstrated from cells exposed to PARPi olaparib (A) or talazoparib (B) following CRISPRn-mutagenesis. sgRNA-level drug-effect Z-scores are shown from CRISPRi-expressing cells exposed to PARPi olaparib (C) or talazoparib (D). sgRNAs targeting specified genes with negative Z-scores represent PARPi sensitivity-causing effect, as demonstrated with sgRNAs targeting BRCA1 and BRCA2, which are labelled in pink and purple, respectively.

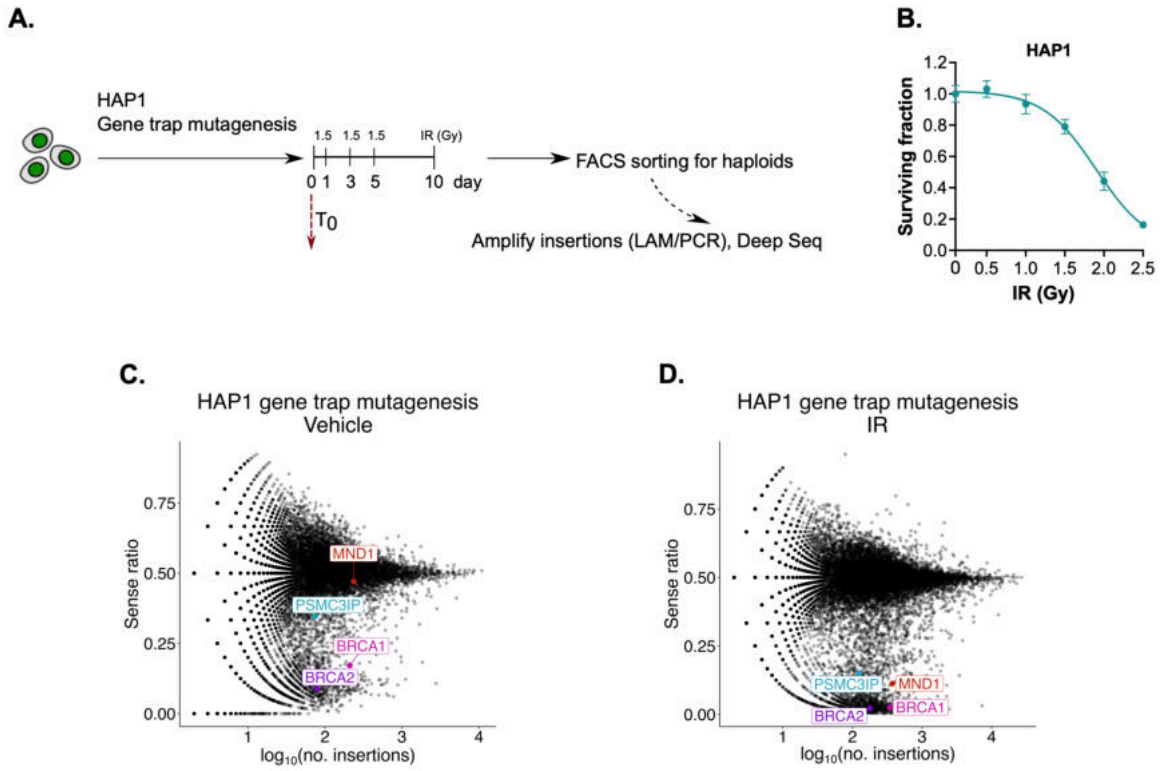

Figure 3.10 HAP1 retroviral mutagenesis screen identified *PSMC3IP* and *MND1* as determinants of IR sensitivity.
A. Workflow for retroviral mutagenesis screen. **B**. Ionising radiation (IR) response of the HAP1 cell line used in the retroviral mutagenesis screen was characterised prior to commencement of the screen. Dose/response survival curve is shown with surviving fractions at the indicated doses of IR. Cells were plated in 24-well plates and exposed to indicated dose of IR, after which cell viability was quantified via CellTiter-Blue®. Surviving fraction was calculated for each IR dose relative to cells which remained unexposed to IR. Error bars represent SD from n=6 replicates. **C, D.** Fishtail plots are shown from retroviral mutagenesis screens comparing control (C) to IR-treated (D). Genes with low sense ratio and high $\log_{10}$(no. insertions) represent IR sensitivity-causing effects (as shown by named HR/DNA repair genes). Data generated by Paola Francica.

I assessed the penetrance of this effect by re-analysing published CRISPR screens in numerous cell lines of various tumour types. Quantile normalisation of the CRISPR screen data was required to account for technical variation across samples, since these CRISPR screens were performed and analysed by different investigators. Specifically, quantile normalisation equalises the data distributions of the CRISPR data, so that they became statistically identical to each other. I also analysed an olaparib CRISPRn screen in another MCF10A derivative with an *RB1* tumour suppressor defect in addition to the *TP53* mutation, which was executed by colleagues in the Gene Function team, Rachel Brough, Sandhya Sridhar and Feifei Song. Prior to commencement of this CRISPR screen, the workflow of which is shown in Figure 3.11A, the MCF10A *TP53*$^{-/-}$ *RB1*$^{-/-}$ cell model to be utilised was characterised. As expected, Cas9 expression was shown to be induced upon doxycycline treatment Figure 3.11B. The PARPi response of MCF10A *TP53*$^{-/-}$ *RB1*$^{-/-}$ cell line was similar to MCF10A *TP53*$^{-/-}$ cells without *RB1* defect (Figure 3.3), as demonstrated in Figure 3.11C and Figure 3.11D for olaparib and talazoparib, respectively. Comparison of this additional olaparib CRISPRn screen in MCF10A *TP53*$^{-/-}$ *RB1*$^{-/-}$ (Figure 3.11E) to the CRISPRn screen results presented earlier in this thesis (Figure 3.8A) revealed that the olaparib sensitivity mediated by loss of MND1 and PSMC3IP is independent of *RB1* defect. These findings suggest that the identified PARPi-MND1/PSMC3IP synthetic lethality may be applicable to a wider genetic background. In order to rigorously assess the penetrance of the PARPi-MND1/PSMC3IP synthetic lethality, I extended my analysis to published CRISPR datasets which includes numerous somatic cancer cell lines of various tumour types (Figure 3.12). Given the lack of published data available for PARPi CRISPRi screens, only published CRISPRn screens were

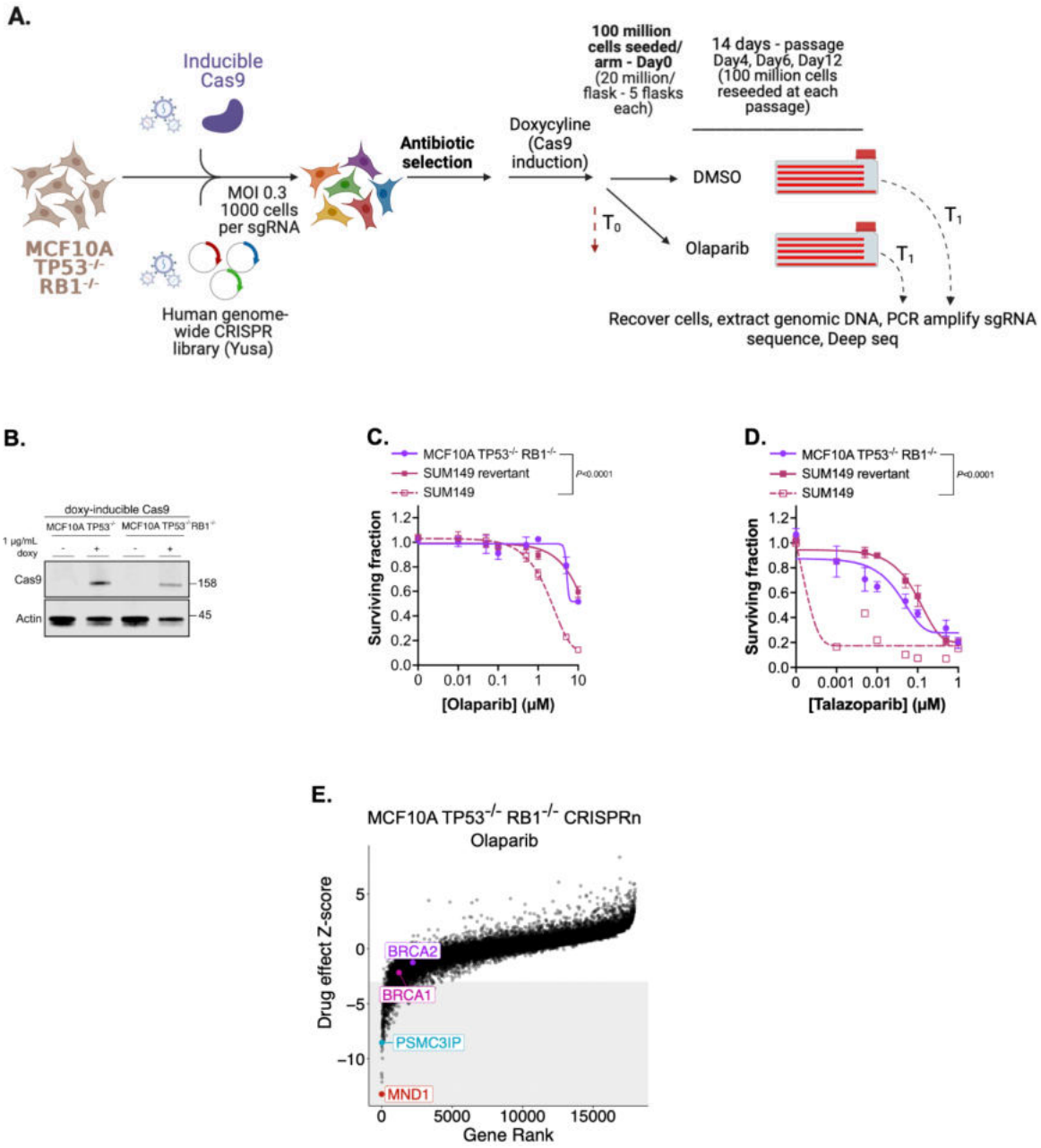

Figure 3.11 MND1 and PSMC3IP are also determinants of PARPi sensitivity with an additional *RB1* defect in MCF10A TP53$^{-/-}$ model.

A. Workflow for the CRISPRn screen with MCF10A TP53$^{-/-}$ RB1$^{-/-}$ cell model. The CRISPR screening procedure was identical to the CRISPRn screen in Figure 3.1. The MCF10A cell model used has a *RB1* defect, in addition to the *TP53* defect. **B**. Western blot image of MCF10A TP53$^{-/-}$ cell lysates with or without *RB1* defect illustrating expression of doxycycline-inducible Cas9. **C**, **D**. Dose/response survival curves are shown with surviving fractions at the indicated doses of olaparib (C) or talazoparib (D). **E.** Scatter plots are shown of drug-effect Z-scores from MCF10A TP53$^{-/-}$ RB1$^{-/-}$ cells exposed to olaparib following CRISPRn-mutagenesis. Identical analysis was used as in Figure 3.8. Genes with negative Z-scores represent PARPi sensitivity-causing effect. Grey shaded area captures drug-effect Z-scores ≤ -3.

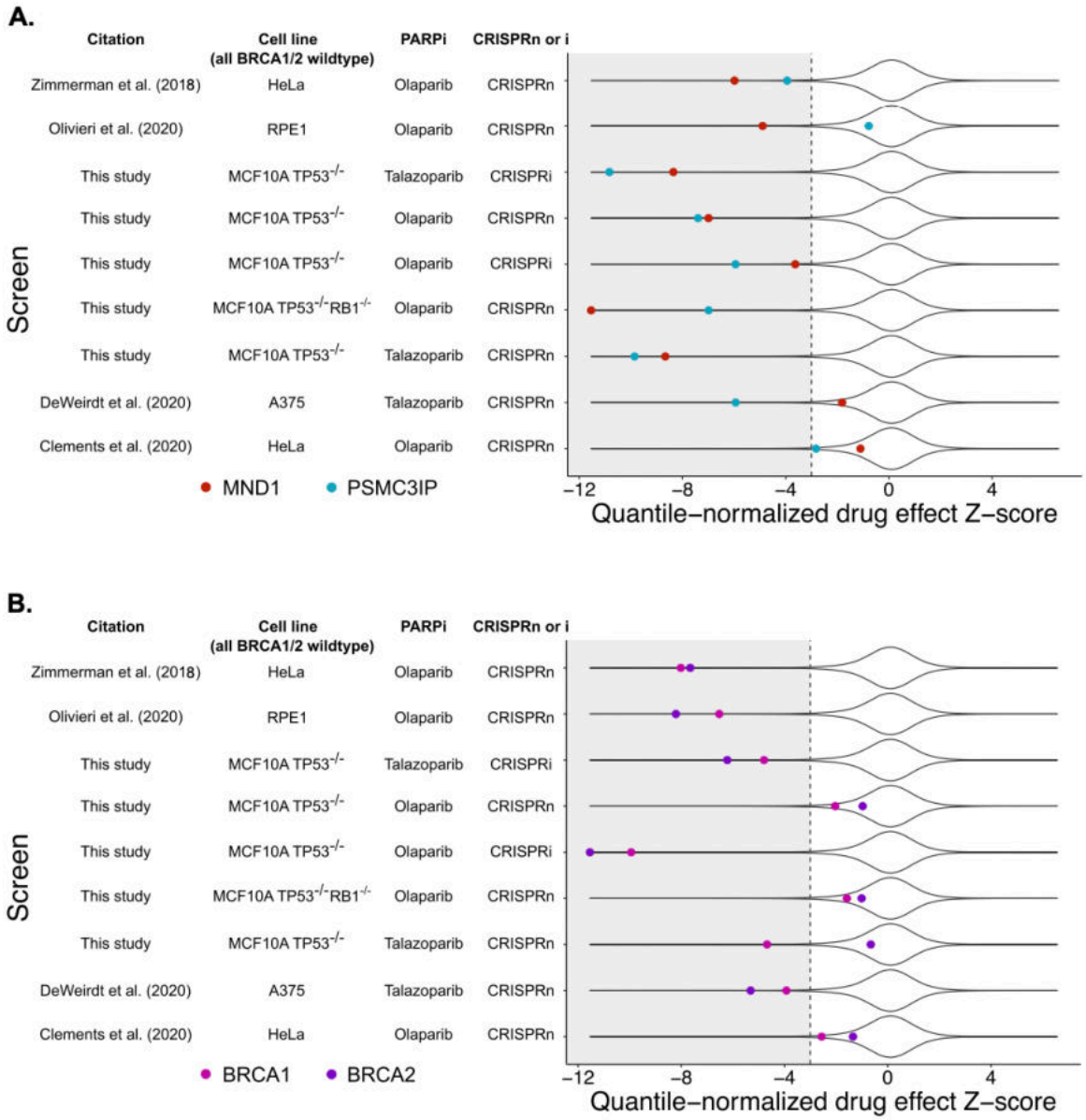

Figure 3.12 *MND1* and *PSMC3IP* are highly penetrant determinants of PARPi sensitivity.
Violin plots are shown of quantile normalised Z-score data (see methods) from nine different CRISPRn or CRISPRi screens for PARPi sensitivity, described either in this study or elsewhere Clements et al., 2020; DeWeirdt et al., 2020; Jamal et al., 2022; Olivieri et al., 2020). Data was reanalysed using a consistent pipeline format (see methods) by Aditi Gulati in the Bioinformatics team, to allow cross comparison. Quantile normalised Z-scores for MND1 and PSMC3IP (A) or BRCA1 and BRCA2 (B) are highlighted in the indicated colour in the legend. Each of the cell lines shown is a mitotic hTERT-positive/ALT-negative cell line. Genes with negative Z-scores represent PARPi sensitivity-causing effect. Grey shaded area captures drug-effect Z-scores ≤ -3.

included in my analysis (Clements et al., 2020; DeWeirdt et al., 2020; Jamal et al., 2022; Olivieri et al., 2020). hTERT-positive/ALT-negative, HR-proficient mitotic cell lines were included in this analysis from a range of different tumour types. In addition to the MCF10A breast model, I analysed CRISPR screens using HeLa, which are derived from human papilloma virus-induced cervical adenocarcinoma, RPE1-hTERT, a telomerase-immortalised retinal pigment epithelial cell line, and A375, a melanoma line. Interestingly, this analysis suggests that the relationship between CRISPR-targeting of *MND1* or *PSMC3IP* and PARPi sensitivity is of comparable penetrance (if not more so) than the effect of targeting either *BRCA1* or *BRCA2*, (Figure 3.12). As detailed in a previous section, CRISPRn-mediated mutagenesis results in gene "knockout". As such, direct comparison of penetrance of *MND1* and *PSMC3IP* to essential genes *BRCA1* or *BRCA2* from CRISPRn screens is not ideal. My screen is the only published investigation of PARPi sensitivity using CRISPRi to date, so I was unable to compare it with other CRISPRi screens. Despite quantile normalisation of all the CRISPR data, *MND1* or *PSMC3IP* loss was associated with PARPi sensitivity in the HeLa cell line used for the CRISPRn screen reported by Zimmerman et al., but not in the HeLa cell line used for the CRISPRn screen from Clements et al. (Figure 3.12A). The observed differences in PARPi sensitivity, associated with *MND1* or *PSMC3IP* loss-of-function, in theoretically the same HeLa cell line from different investigators, could be due to the differences in drug doses that were used by the different investigators. Zimmerman et al. (Zimmermann et al., 2018) decided to use 2 μM olaparib for SF_{80}, as in our CRISPR screens, whereas Clements et al. (Clements et al., 2020) used 5 μM, which was more appropriate for their intended aim to identify determinants of PARPi resistance. In totality, my analysis (Figure 3.12A)

suggests that the MND1/PSMC3IP heterodimer might be involved in the response to PARPi in mitotic cells, in general, regardless of genetic background.

3.3. Discussion

In Chapter 3, I described the design, performance and analysis of a series of CRISPR mutagenesis and CRISPR interference screens designed to identify genetic determinants of PARPi sensitivity. These screens identified *MND1* and *PSMC3IP* as determinants of PARP inhibitor sensitivity in mitotic cells, in addition to genes classically associated with somatic HR. *MND1* and *PSMC3IP* encode the two components of a heterodimer whose canonical role is in meiotic recombination (Chen et al., 2004; Tsubouchi & Roeder, 2002), but for which a general function in the DDR in somatic cells has yet to be described.

Bioinformatic analyses of PARPi CRISPR screens from independent investigators, published during the course of my PhD, revealed *MND1* and/or *PSMC3IP* as statistically significant “hits” (Clements et al., 2020; DeWeirdt et al., 2020; Jamal et al., 2022; Olivieri et al., 2020). Although *MND1* and *PSMC3IP* have indeed been previously identified to contribute to PARPi response in large-scale screens, none of these investigators validated the effect of *MND1*/*PSMC3IP* perturbation on PARPi response in follow-up studies, or even flagged up *MND1* and *PSMC3IP* as candidate genes of interest. By identifying *MND1* and *PSMC3IP* in multiple PARPi CRISPR screens performed in various backgrounds, we have been the first to appreciate the penetrance of their role in PARPi response and validate this effect. As such, the scope of this identified PARP-MND1/PSMC3IP synthetic lethal interaction is very wide, which is in contrast with some recently identified synthetic

lethal interactions, that appear to be restricted to the specific genetic background in which they were identified (Ryan et al., 2018). Given their identification as “hits” in so many CRISPR screens, it could be argued that *MND1* and *PSMC3IP* are artefacts associated with CRISPR screening. Despite being regarded as a highly specific method of genetic perturbation, with the sgRNA guiding Cas9 to a PAM sequence adjacent to the target DNA (Jinek et al., 2012), off-target effects have been reported with Cas9 binding to unintended genomic site for cleavage (Alkan et al., 2018). Sequence homology of the target loci has been implicated for off-target effects. As such, the sgRNAs designed to target a gene of interest (such as *MND1*/*PSMC3IP*) could in fact target a genomic region that results in loss of cell fitness, which would be mis-interpreted as sensitivity to the drug used in the screen (such as PARPi).

However, an orthogonal genetic perturbation screen carried out by our collaborators identified that loss of *MND1* resulted in a marked increase in IR sensitivity. In a recent preprint, this finding has been corroborated with an identical screening approach (Koob et al., 2023). Given the profound effect demonstrated in the screen, Koob et al. proceeded to pursue the *MND1* “hit” with further experimental work (Koob et al., 2023). Taking into account all the available data from various screening approaches, the role for *PSMC3IP-MND1* in response to PARPi, or even IR, seems to not be private to a singular mitotic cell line, being seen in a variety of mitotic cells.

In order to verify whether *MND1* and *PSMC3IP* really are determinants of PARPi and IR response in mitotic cells, validation is required. Given the canonical function

of MND1 and PSMC3IP in meiotic recombination, the relevance and importance of these findings is highly dependent on whether MND1/PSMC3IP expression can actually be evidenced in mitotic cells, including cancer cells. This matter will be explored in the next chapter.

Chapter 4. MND1 and PSMC3IP control PARPi sensitivity in mitotic cells

4.1. Introduction

4.1.1. MND1/PSMC3IP canonical function in meiosis

Classically, MND1 and PSMC3IP are involved in the DNA recombination that occurs during meiosis (Henry et al., 2006). Meiotic HR aims to recombine homologous regions of DNA on paternal and maternal homologous chromosomes, as part of crossing over and the generation of genetic variation during gametogenesis (Baudat et al., 2013). MND1 and PSMC3IP proteins form a DNA binding heterodimer whose canonical function is within meiotic RAD51- or DMC1-mediated meiotic recombination (Chen et al., 2004; Tsubouchi & Roeder, 2002), as outlined in Figure 1.2. As part of the meiotic recombination process, DSBs are formed by SPO11 (Keeney et al., 1997). The DNA ends at the DSB are resected to release SPO11 and generate a DSB with ssDNA overhangs, which are in turn bound by either RAD51 (Sharan et al., 1997) or meiosis-specific DMC1 (Bugreev et al., 2011), forming a helical presynaptic nucleoprotein filament. DMC1 functions as the predominant strand exchange protein during meiosis (Cloud et al., 2012) to promote strand invasion, recombination between homologous chromosomes and crossing over (Hong et al., 2013; Schwacha & Kleckner, 1997). RAD51 also functions to repair residual DSBs after recombination between homologous chromosomes and synapsis are complete (Cloud et al., 2012; Da Ines et al., 2013). In contrast to somatic HR, accessory proteins MND1 and PSMC3IP support RAD51 and DMC1 function in meiotic HR. Early studies regarding *Hop2*

and *Mnd1* genes (orthologs of the human *PSMC3IP* and *MND1*) were performed in yeast. In the study which reported the initial identification of the budding yeast *Hop2* gene, *Hop2 was reported* to be meiosis-specific (Leu et al., 1998). Later, co-purification of Hop2 with affinity-tagged Mnd1 was observed, suggesting that Hop2 forms a stable heterodimer with Mnd1 (Hop2-Mnd1) independent of other proteins (Chen et al., 2004). Work carried out by Pezza et al. demonstrating physical interaction between Hop2-Mnd1 heterodimer and Dmc1 (Pezza et al., 2007), were later confirmed by Zhao et al*.,* who also reported Hop2-Mnd1 interaction with Rad51 via affinity pulldown experiments (Zhao et al., 2015). Building on this work, Zhao et al. was able to specifically identify the Hop2 and Mnd1 domains responsible for Rad51/Dmc1 interaction (Zhao et al., 2015). The authors demonstrated that mutants deleted for the C-terminal region in either *Hop2* or *Mnd1* resulted in impaired interaction with Rad51 or Dmc1 (Zhao et al., 2015). N-terminal deleted mutants did not affect Rad51/Dmc1 interactions (Zhao et al., 2015). Other studies used DNA binding assays to reveal that Hop2 and Mnd1 also bind DNA; Hop2 was found to bind ssDNA with another C-terminus domain (Zhao et al., 2014), while Hop2-Mnd1 directly binds dsDNA (Chen et al., 2004) specifically at the N-terminus (Zhao et al., 2014). In totality, these *in vitro* studies provide a functional model of PSMC3IP-MND1 function in meiotic recombination (Figure 4.1); C-terminus PSMC3IP-MND1 interacts with RAD51/DMC1 and PSMC3IP binds ssDNA to orchestrate the localisation of DMC1 on the ssDNA (Zhao et al., 2015), while the N-terminus of PSMC3IP-MND1 binds dsDNA to bring the chromosome homologs in close juxtaposition together (Chen et al., 2004; Pezza et al., 2007). As such, PSMC3IP-MND1 promotes recombination between homologous chromosomes, rather than sister chromatids, which is desired for

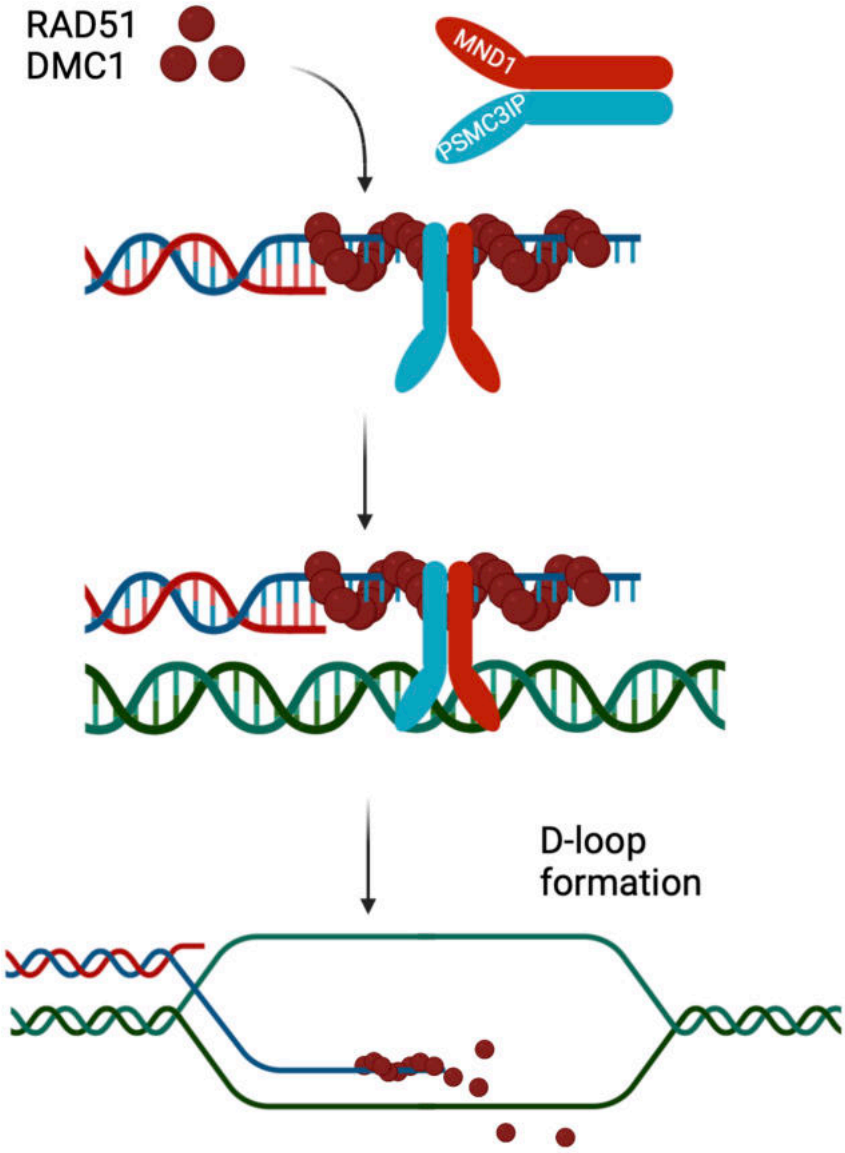

Figure 4.1 Simplified schematic of MND1 and PSMC3IP function in meiotic recombination.
Following DNA end resection, C-terminus PSMC3IP-MND1 interacts with RAD51/DMC1 and another C-terminal domain of PSMC3IP binds ssDNA to orchestrate the localisation of DMC1 onto the ssDNA, while the N-terminus of PSMC3IP-MND1 binds dsDNA to bring the chromosome homologs in close juxtaposition together. PSMC3IP-MND1 complex functions to support downstream RAD51 and DMC1 functions to facilitate the homology search process and strand invasion. Figure adapted from (Zhao & Sung, 2015).

meiotic recombination (Leu et al., 1998). PSMC3IP-MND1 also condenses dsDNA surrounding the filament to enhance the homology search (Pezza et al. 2010). Overall, PSMC3IP-MND1 complex functions to support RAD51 and DMC1 functions to facilitate the homology search process and strand invasion (Chen et al., 2004; Tsubouchi & Roeder, 2002).Given that the well-established canonical role of MND1/PSMC3IP is within meiotic recombination, I was interested to understand why these genes might also control response to DNA damaging agents, such as PARPi, in mitotic cells; as suggested by genetic perturbation screen data outlined in the previous Chapter.

4.1.2. MND1/PSMC3IP mitotic function

In addition to its roles within meiotic recombination, there is some evidence that the MND1/PSMC3IP heterodimer also functions in miotic cells, which predominantly carry out DNA recombination between sister chromatids, as opposed to homologous chromosomes. MND1/PSMC3IP function in mitotic cells was evidenced with identification of their expression in tumour cell lines by investigators in Roger Greenberg's group (Cho et al., 2014). They claimed that MND1/PSMC3IP are expressed exclusively in tumour cell lines that maintain telomeres via the alternative lengthening of telomeres (ALT) pathway, a form of HR. They hypothesised that PSMC3IP-MND1 functions in mitotic cells to contribute to ALT (Figure 4.2) by promoting telomere clustering and RAD51-mediated recombination between otherwise geographically distant telomeres on different chromosomes, a process which is supposedly dependent on MND1/PSMC3IP-mediated non-sister chromosome interactions (Cho et al., 2014; Dilley et al., 2016). However, the MCF10A cell line that I conducted my screen in

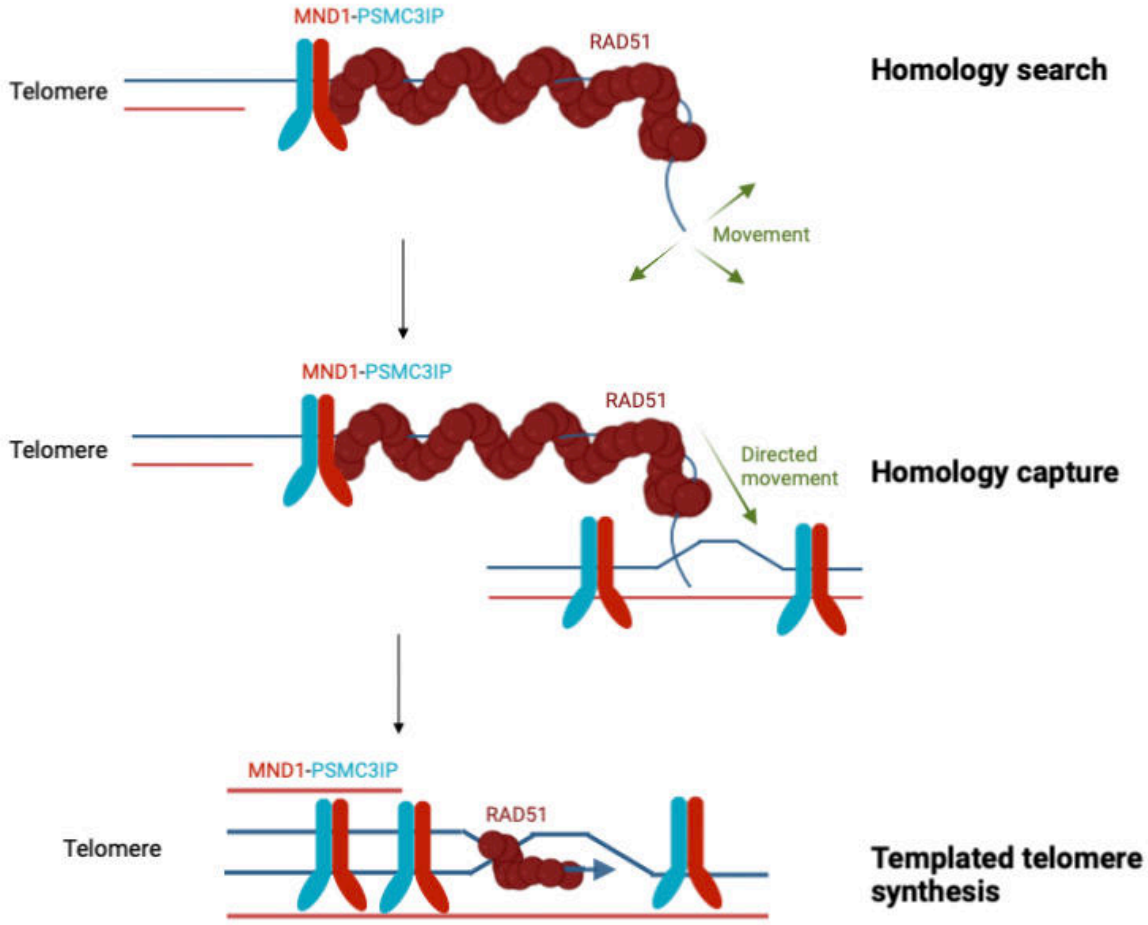

Figure 4.2 Hypothesised involvement of MND1 and PSMC3IP in ALT.
Following DNA damage response (DDR), end resection at telomeres triggers RAD51-mediated homology search, including accessory factors MND1-PSMC3IP, a mechanism which enables synapsis between distant telomeres. Directional movement occurs via homology capture, followed by synapsis of homologous non-sister telomeres. Figure adapted from (Cho et al., 2014).

is ALT-negative (Hu et al., 2021), and the observations of a PARPi sensitivity phenotype caused by sgRNA targeting MND1/PSMC3IP implies that they are expressed and functional. This suggested that MND1 and PSMC3IP expression is not limited to ALT-positive mitotic cells. In this chapter I describe further evidence for this hypothesis.

4.2. Results

4.2.1. MND1/PSMC3IP are commonly expressed in normal human tissue, mitotic tumour cells and human tumours

I was initially interested to establish normal MND1 and PSMC3IP expression levels in human tissue. As such, I plotted MND1 and PSMC3IP mRNA expression according to organ sub-type from the Genotype-Tissue Expression (GTEx) Project (Figure 4.3). As expected, this analysis revealed that MND1 and PSMC3IP mRNA expression (transcripts per million, TPM) is very high in the testis. Surprisingly, MND1 and PSMC3IP mRNA expression was also observed in all other analysed tissue types, albeit at rather low levels in comparison to testis. Interestingly, median PSMC3IP mRNA expression seems to be elevated compared to MND1 mRNA expression. In summary, MND1 and PSMC3IP seem to be ubiquitously expressed in normal tissues.

In order to assess the generality of MND1/PSMC3IP expression in mitotic cells, gene expression and mass spectrometry proteomic data from human tumour cell lines was analysed by Chris Lord (https://depmap.org) (Ghandi et al., 2019). Data within the proteomics dataset are normalised to the total protein amount, rather than cell numbers; approximately equal amounts of total protein from lysate

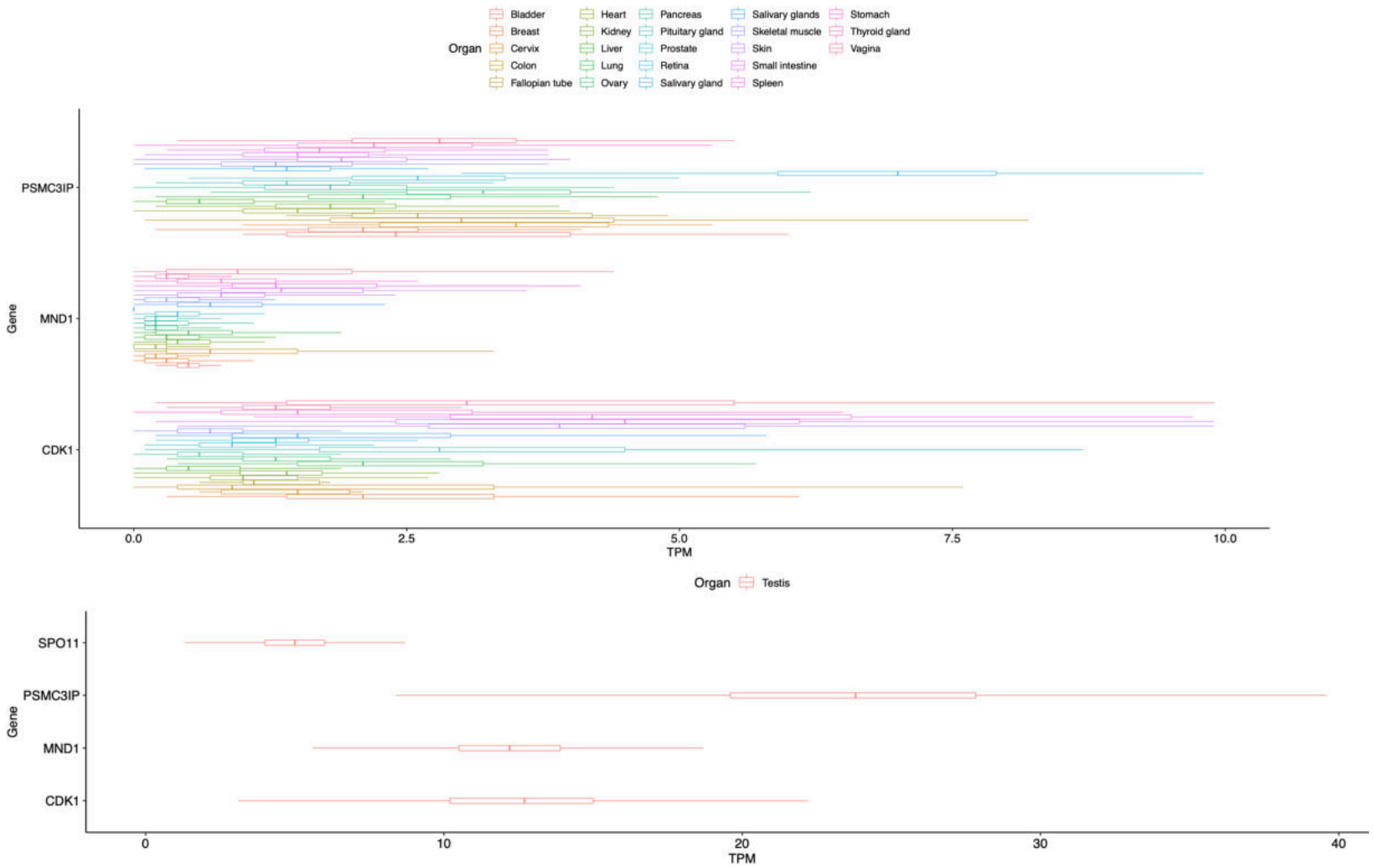

Figure 4.3 MND1 and PSMC3IP are ubiquitously expressed in normal tissue.
Normalised mRNA transcription expression in various organs represented as transcripts per million (TPM). CDK1 and SPO11 are shown as somatic and meiotic controls, respectively. Expression levels in testis on separate plot (lower panel). Data source: GTEx.

were processed for each sample, which may represent different cell numbers depending on the cell line. Normalisation of this data involves median normalisation, batch effect correction, control sample normalisation, and quality control filters. Median normalisation adjusts protein expression levels based on the median value across all samples, helping to equalise distributions and correct for systematic variations. Batch effect correction addresses technical variations introduced by different processing conditions, ensuring consistency across experimental runs. Control sample normalisation aligns protein expression levels to reference points provided by control samples, accounting for processing and measurement variations. Finally, quality control filters remove outliers and low-quality data points. I plotted the mRNA and protein expression of MND1 and PSMC3IP from tumour cell lines according to their cancer origin. I also plotted these for BRCA1 and BRCA2 for reference. mRNA expression data was available for 1407 tumour cell lines, while proteomics data was limited to 352 tumour cell lines. This analysis revealed that mRNA and protein expression of MND1 and PSMC3IP was relatively common in human tumour cell lines (Figure 4.4). I conducted further in silico analysis (Figure 4.5) using the datasets from Figure 4.4. For both MND1 and PSMC3IP, a moderate correlation of mRNA expression was observed with protein expression, as shown in Figure 4.5A and Figure 4.5B, respectively. By plotting MND1 *vs.* PSMC3IP expression data of tumour cell lines, I observed that the degree of correlation MND1 and PSMC3IP expression is moderate at the mRNA level (Figure 4.5C, r=0.4), which was to a much higher degree of correlation at the protein level (Figure 4.5D, r=0.8). The overall findings from this *in silico* analysis of MND1 and PSMC3IP expression data (Figure 4.5) is consistent with the hypothesis that these two heterodimer components have a

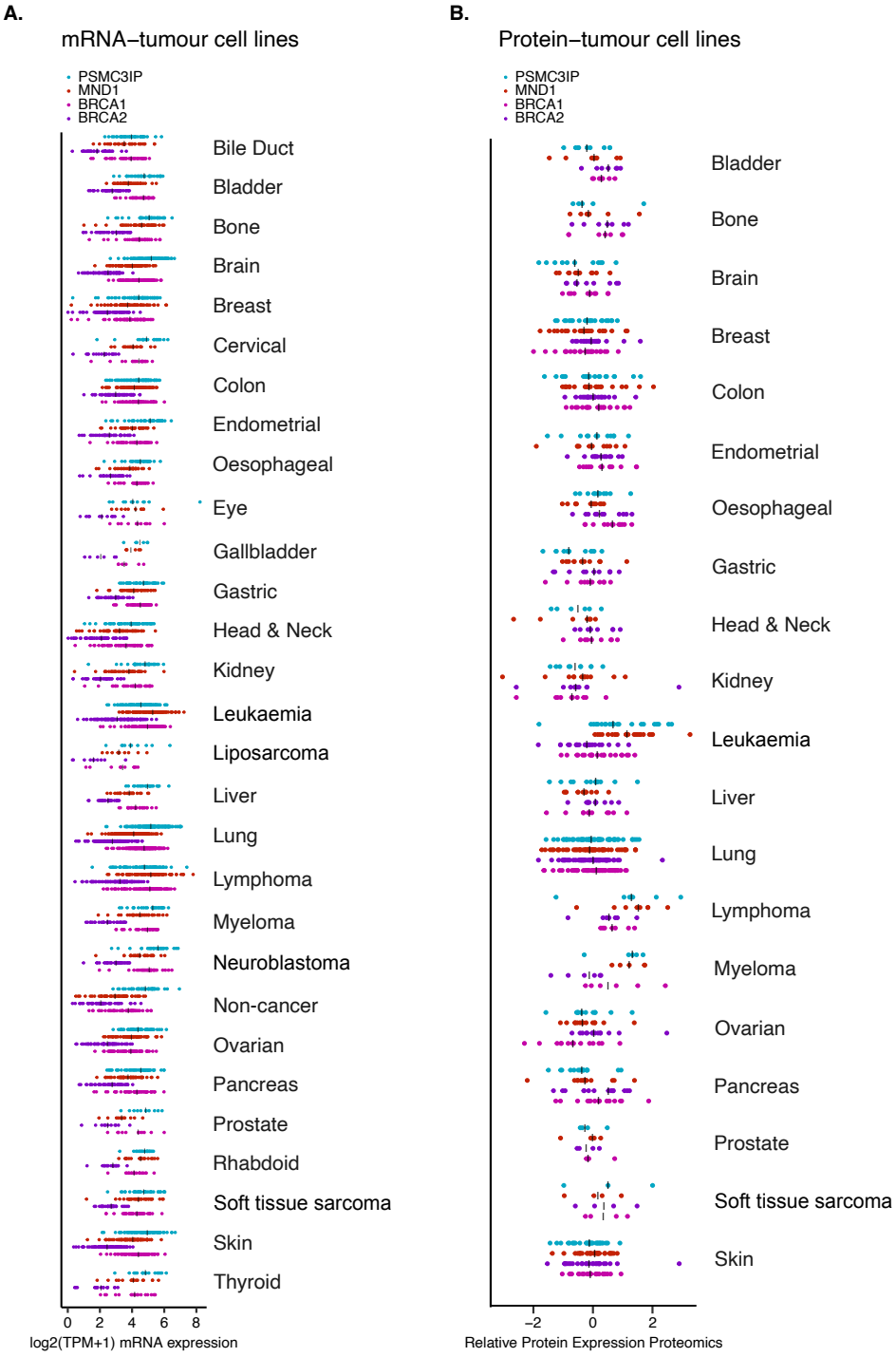

Figure 4.4 MND1 and PSMC3IP mRNA and protein expression is relatively common in human tumour cell lines.
Scatter plot shown of normalised mRNA (A) or protein (B) expression for *MND1* and *PSMC3IP* in 1407 tumour cell lines (A) or 352 tumour cell lines (B) profiled as part of the DepMap project (Ghandi et al., 2019). Data for *BRCA1* and *BRCA2* is also shown for comparison. Black line represents median expression value of the specified gene for each cancer origin. Raw data for plot retrieved from https://depmap.org/portal/ on 1st July 2022. Analysis performed by Chris Lord. mRNA data normalised as transcripts per million (TPM).

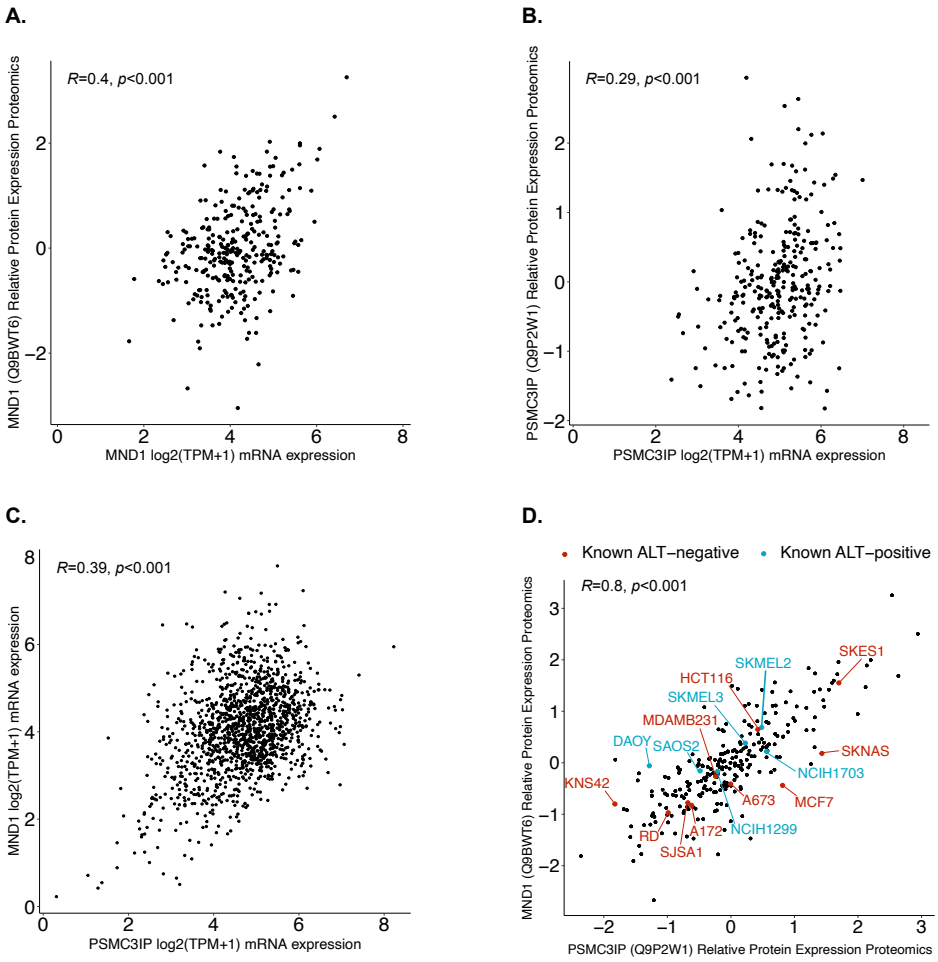

Figure 4.5 Correlation of MND1 and PSMC3IP mRNA and/or protein expression in human tumour cell lines.

Scatter plot shown of mRNA vs. protein levels for MND1 (A) and PSMC3IP (B) in tumour cell line data from Figure 4.4. Scatter plot shown of MND1 vs. PSMC3IP mRNA (C) or protein (D) expression in tumour cell line data from Figure 4.4. Examples of known ALT-positive and ALT-negative cell lines are highlighted in blue and red, respectively (D). Data is adapted from protein expression data but also includes ALT status of cell lines, if known (Hu et al., 2021). Pearson's correlation coefficient was used. Tumour cell lines included in this analysis were profiled as part of the DepMap project (Ghandi et al., 2019). Raw data for plot retrieved from https://depmap.org/portal/ on 1st July 2022. Analysis performed by Chris Lord. mRNA data normalised as transcripts per million (TPM).

shared function in mitotic cells, as in meiotic cells. In order to assess whether the protein expression of PSMC3IP or MND1 was linked to the ALT status of the tumour cell line, I annotated the ALT status of the tumour cell lines, if known, in the plot demonstrating PSMC3IP vs. MND1 protein expression data (Figure 4.5D). This analysis revealed that MND1 or PSMC3IP protein expression is not solely restricted to tumour cell lines that carry out telomere maintenance by ALT. The conclusions derived from the *in silico* analysis was confirmed experimentally by Western blotting; irrespective of PARPi exposure, PSMC3IP protein expression was observed in multiple ALT-negative tumour cell lines of multiple cancer origin (Figure 4.6)

In order to assess the generality of MND1/PSMC3IP expression in a more clinically relevant setting, similar analysis was performed with gene expression data from human tumours (Figure 4.7) by Chris Lord. Data included in this analysis is part of the TCGA project described on the CBio portal (Cerami et al., 2012; Gao et al., 2013). I plotted the mRNA expression of MND1 and PSMC3IP of tumours according to their cancer origin. I also plotted these for BRCA1 and BRCA2 for reference. mRNA expression data was available for 10,882 tumours. Interestingly, tumour expression of MND1 and PSMC3IP was also relatively common, as demonstrated in Figure 4.7. Further *in silico* analysis was performed by Chris Lord (Figure 4.8) using the datasets from Figure 4.7. By plotting MND1 *vs.* PSMC3IP mRNA expression data from human tumours of various types, I observed that MND1 correlates with PSMC3IP mRNA in tumour types where PARPi are used clinically (breast, serous ovarian, pancreatic adenocarcinoma and prostate adenocarcinoma), as shown in Figure 4.8. As demonstrated with the tumour cell

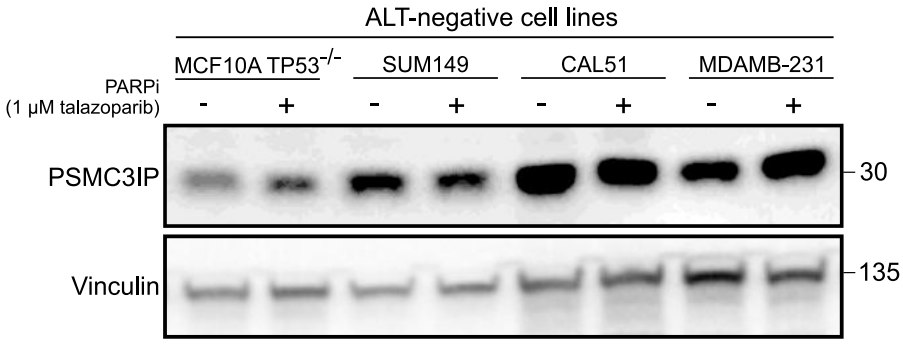

Figure 4.6 PSMC3IP expression was observed in multiple ALT-negative tumour cell lines of multiple cancer origin.
Western blot image of cell lysates from multiple cancer origins, illustrating PSMC3IP expression. All cell lines included in the panel are ALT-negative cell lines (Hu et al., 2021). Cell lysate samples loaded in (+) lanes were derived from cells pre-treated with 1 μM talazoparib PARPi for 24 hours prior to harvesting and lysis. Cell lysate samples loaded in (-) lanes were derived from cells which remained unexposed to PARPi (DMSO) for 24 hours prior to harvesting and lysis.

Figure 4.7 MND1 and PSMC3IP mRNA expression is relatively common in human tumours.

Scatter plot shown of normalised mRNA expression for MND1 and PSMC3IP in 10,882 human tumours as part of the TCGA project described on the CBio portal (Cerami et al., 2012; Gao et al., 2013). Data for BRCA1 and BRCA2 is also shown for comparison. Raw data for plot retrieved from https://www.cbioportal.org/ on 1st July 2022. Black line represents median expression value of the specified gene for each cancer origin. Analysis performed by Chris Lord. mRNA data is normalised as RNA-Seq by Expectation-Maximisation (RSEM).

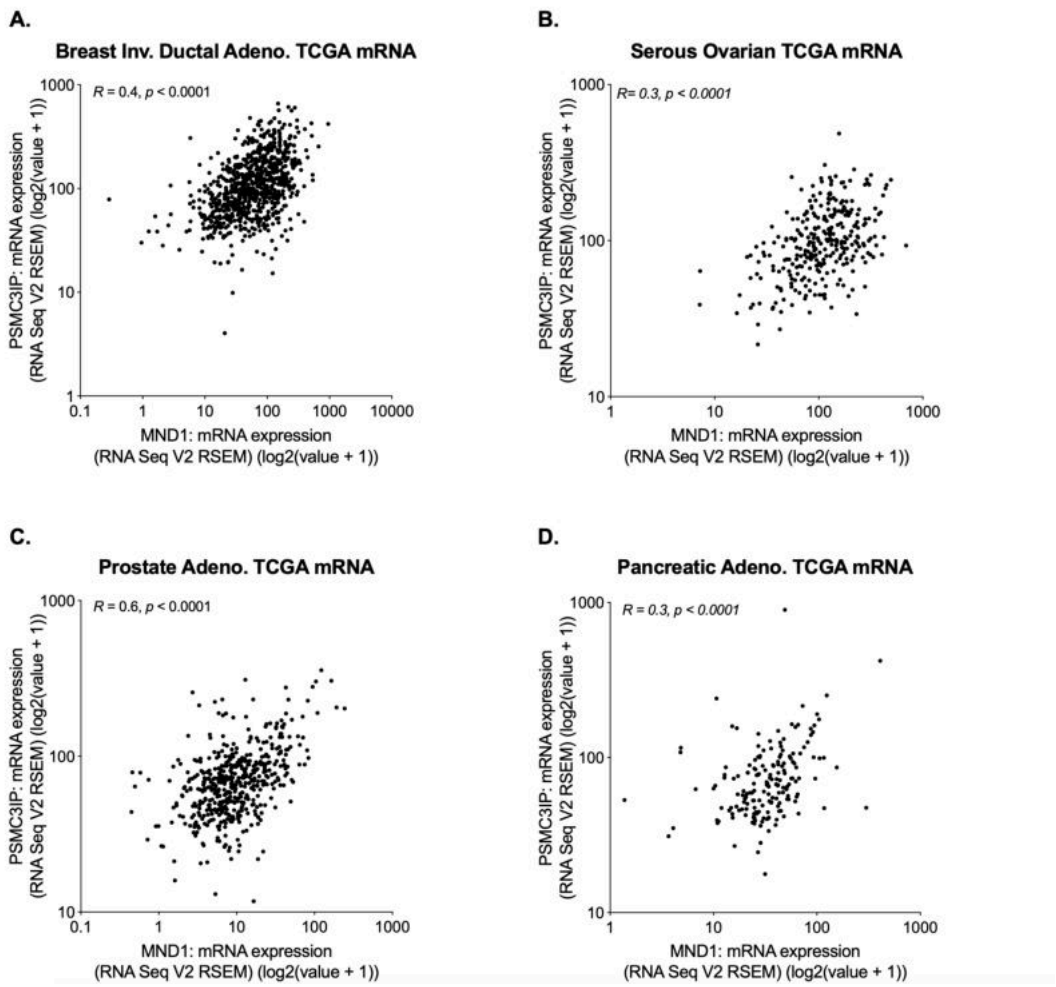

Figure 4.8 Correlation of MND1 and PSMC3IP mRNA protein expression in human tumours.

Scatterplot of MND1 vs. PSMC3IP mRNA expression in tumours from four histologies where PARPi are clinically used; breast (A), serous ovarian (B), pancreatic adenocarcinoma (C) and prostate adenocarcinoma (D). Pearson's correlation coefficient was used. Raw data for plot retrieved from https://www.cbioportal.org/ on 1st July 2022. Data derived from Figure 4.7. Analysis performed by Chris Lord. mRNA data is normalised as RNA-Seq by Expectation-Maximisation (RSEM).

line expression data, the overall findings from the *in silico* analysis of MND1 and PSMC3IP expression data in patient tumours (Figure 4.8) is consistent with the hypothesis that these two heterodimer components have a shared function in not just tumour cell lines, but also in tumours derived from patients.

4.2.2. MND1 and PSMC3IP dysfunction causes PARPi sensitivity in mitotic cells

On the basis of the data presented in the previous section indicating that MND1 and PSMC3IP are commonly expressed in mitotic tumours, and the genetic perturbation screen results from Chapter 2, I subsequently sought to formally assess whether *MND1* or *PSMC3IP* defects caused PARPi sensitivity. In order to evaluate this, I initially generated CRISPRi cell models in the same MCF10A *TP53*$^{-/-}$ cell line used for my CRISPR screens. I verified that transduction of MCF10A *TP53*$^{-/-}$ cells expressing dCas9-KRAB with lentiviral constructs encoding sgRNA targeting *MND1* or *PSMC3IP* caused a significant reduction in MND1 or PSMC3IP mRNA levels, respectively, as shown in Figure 4.9. Dose/response experiments, whereby the fraction of surviving cells (surviving fraction, SF) is determined for the PARPi dose to which the cells were exposed, were performed with the generated CRISPRi cell models. As expected, MCF10A *TP53*$^{-/-}$ CRISPRi cells expressing a non-targeting control sgRNA (sgNT) were relatively resistant to the PARPi, whereas CRISPRi-mediated depletion of MND1 or PSMC3IP enhanced sensitivity to olaparib or talazoparib (Figure 4.10). These observations validated the results from my CRISPR screens with the same model.

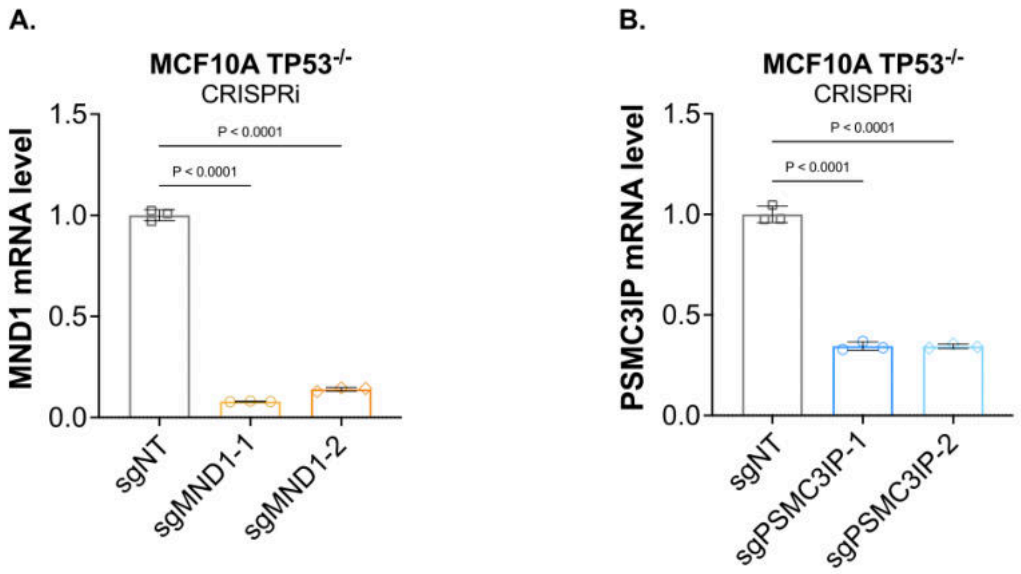

Figure 4.9 sgRNA-mediated targeting of *MND1* and *PSMC3IP* with CRISPRi caused significant depletion of MND1 or PSMC3IP mRNA.
Barplots are shown of mRNA expression levels in MCF10A *TP53*$^{-/-}$ cells expressing dCas9-KRAB transduced with lentiviral constructs encoding non-targeting sgRNA (sgNT), or sgRNA targeting *MND1* (sgMND1-1 or sgMND1-2), or *PSMC3IP* (sgPSMC3IP1-1 or sgPSMC3IP-2). Two independent sgRNAs were used to target *MND1* and *PSMC3IP*. mRNA expression levels were determined with RT-qPCR. Error bars represent SD from n=3 replicates, for which individual data points are shown. *P*-values were calculated via ANOVA with Tukey's post-test.

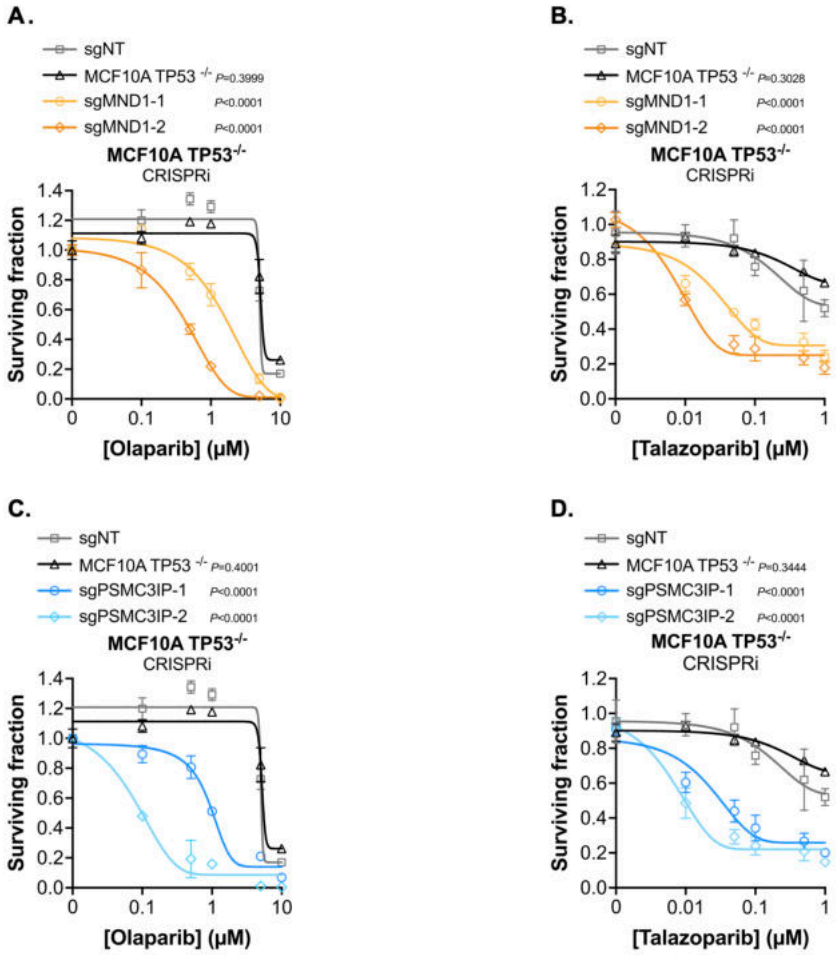

Figure 4.10 CRISPRi-mediated depletion of MND1 or PSMC3IP enhanced sensitivity to PARP inhibitors olaparib or talazoparib.
Dose/response survival curves are shown with surviving fractions at the indicated doses of PARPi. MCF10A *TP53*$^{-/-}$ cells expressing dCas9-KRAB transduced with lentiviral constructs encoding non-targeting sgRNA (sgNT), or sgRNA targeting *MND1* (sgMND1-1 or sgMND1-2), or *PSMC3IP* (sgPSMC3IP1-1 or sgPSMC3IP-2) were included. Two independent sgRNAs were used to target *MND1* and *PSMC3IP*. Cells were plated in 6-well plates (A, C) or 384-well plates (B, D) and exposed to PARPi for 14 continuous days (6-well plates) or five continuous days (384-well plates). Cell viability was quantified by CellTiter-Glo® and surviving fraction was calculated for each drug dose relative to DMSO-exposed cells. Error bars represent SD. *P*-values were calculated via ANOVA with Tukey's post-test.

To further corroborate these results, I generated further models in the MCF10A *TP53*$^{-/-}$ cell line. I transfected MCF10A *TP53*$^{-/-}$ cells with Cas9-crRNA ribonucleoproteins targeting *MND1* or *PSMC3IP*, as shown in the schematic in Figure 4.11, to generate daughter clones with different *MND1* or *PSMC3IP* mutations. I subsequently performed genotyping on these clones to determine the exact mutations that had been generated. For *MND1*-mutant clones (Figure 4.12), I determined that clones A1 and B1 had a large genomic deletion g.153,358,406-153,358,600 spanning *MND1* exon 4 and intron in one allele. In addition, clone A1 had 3 bp and 1 bp deletions, while clone B1 had 35 bp deletion, on the second allele (MND1$^{p.Y71del,K77Kfs*45}$ and MND1$^{p.N69Sfs*4}$, respectively). Genotyping of *PSMC3IP* mutant clones (Figure 4.13), termed C3 and C4, confirmed the presence of a 9 bp deletion p.89L_91G in the second allele. In allele 1, clone C3 had a 362 bp deletion g.42,573,812-42,574,174 and C4 had a 401 bp deletion g.42,573,773-42,574,174 spanning PSMC3IP exon 4 and intron (Figure 4.13). I did not identify any PSMC3IP-mutant clones with biallelic frameshift deletions, despite numerous attempts to generate this. In order to predict the functional consequences of the PSMC3IP in-frame deletions, I deduced that the p.89L_91Gdel mutation is within the leucine zipper region (84-124/126) (Figure 4.14A), which is responsible for homolog pairing & recombination. In addition, the AlphaFold artificial intelligence system (Jumper et al., 2021) was utilised by a colleague in the Gene Function lab, Dragomir Krastev, with the genotyping results to predict the consequences of the *PSMC3IP* p.89L_91Gdel mutation on the three-dimensional protein structure. This predicted model demonstrated that the PSMC3IP glutamate residue at position 90 (D90) forms a hydrogen bond with the MND1 arginine residue at position 82 (R82), as shown in Figure 4.14B.

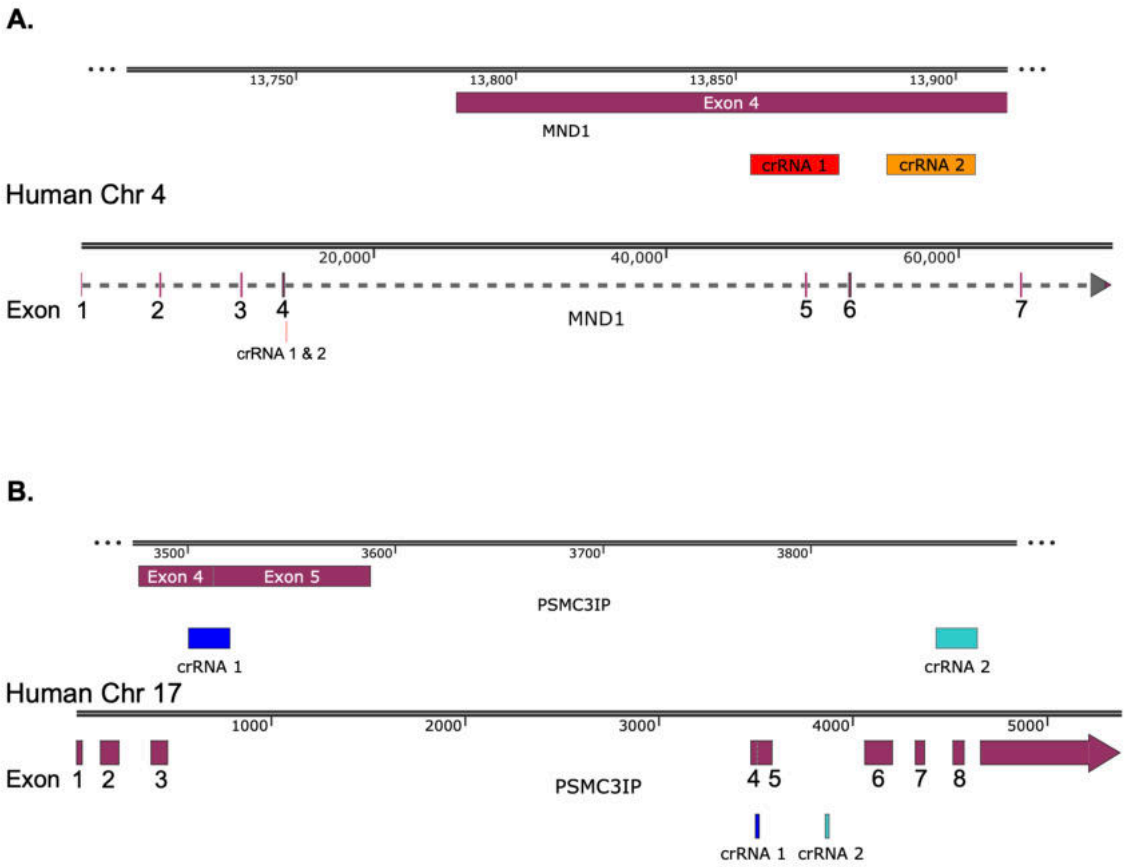

Figure 4.11 Schematic of Cas9-crRNA ribonucleoproteins targeting *MND1* or *PSMC3IP* to generate cell models with *MND1* or *PSMC3IP* mutations.
A. Cas9-crRNA ribonucleoproteins (crRNA 1 & crRNA 2) were designed to target exon 4 of *MND1* on chromosome 4. A global overview of *MND1* is shown on the lower panel, with a blown-up view of *MND1* exon 4 demonstrated on the upper panel. **B.** Cas9-crRNA ribonucleoproteins (crRNA 1 & crRNA 2) were designed to target between exon 4 and exon 6 of *PSMC3IP* on chromosome 17. A global overview of *PSMC3IP* is shown on the lower panel, with a blown-up view of *PSMC3IP* exon 17 demonstrated on the upper panel.

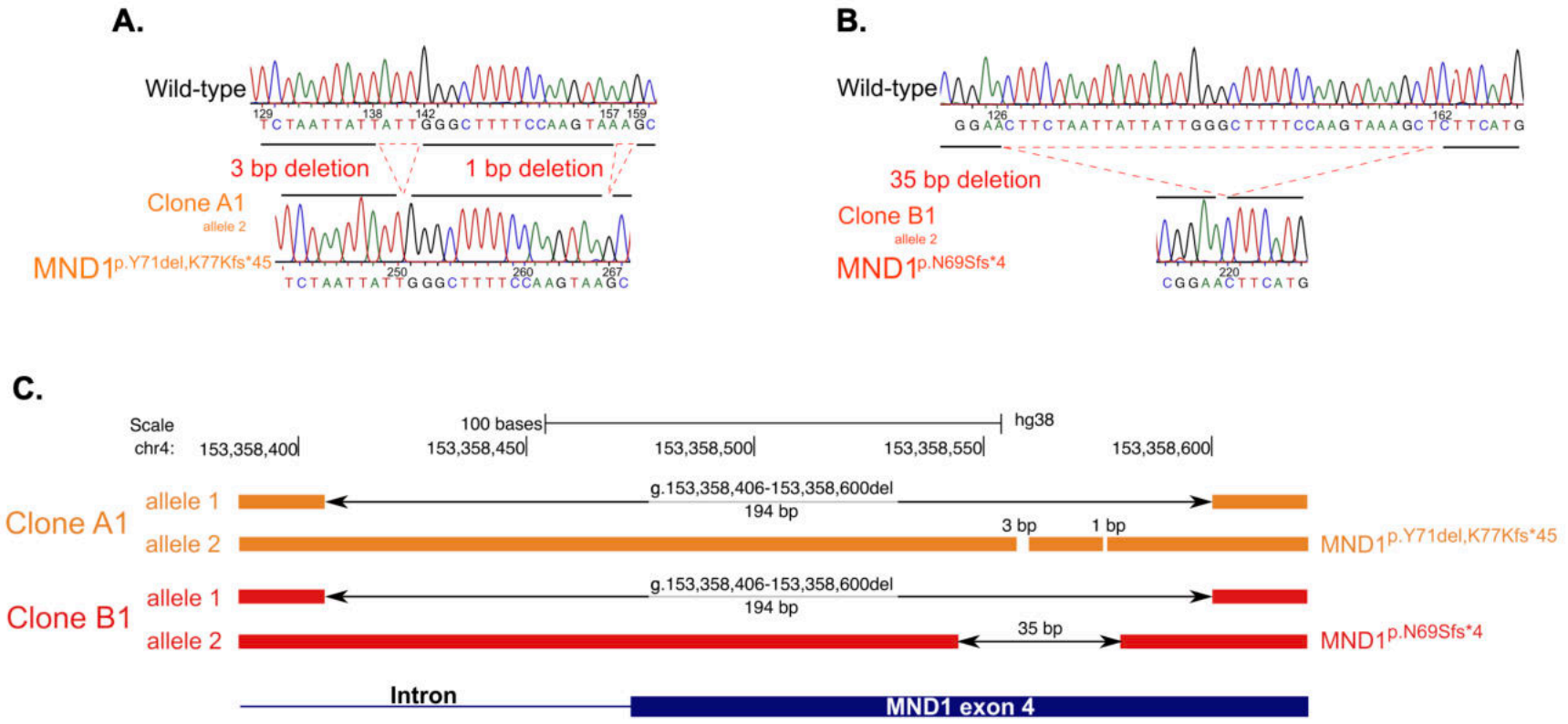

Figure 4.12 Genotyping of *MND1*-mutant MCF10A *TP53*$^{-/-}$ cell lines.
A, B. Sanger sequencing traces of topoclones from *MND1*-mutant clones A1 (A) and B1 (B). **C.** The results from Sanger sequencing of topoclones from both *MND1*-mutant clones A1 and B1 were mapped to the human genome (hg38). A1 and B1 had a large genomic deletion g.153,358,406-153,358,600 spanning *MND1* exon 4 and intron in one allele. In addition, A1 had 3 bp and 1 bp deletions, while clone B1 had 35 bp deletion, on the second allele (MND1$^{p.Y71del,K77Kfs*45}$ and MND1$^{p.N69Sfs*4}$, respectively).

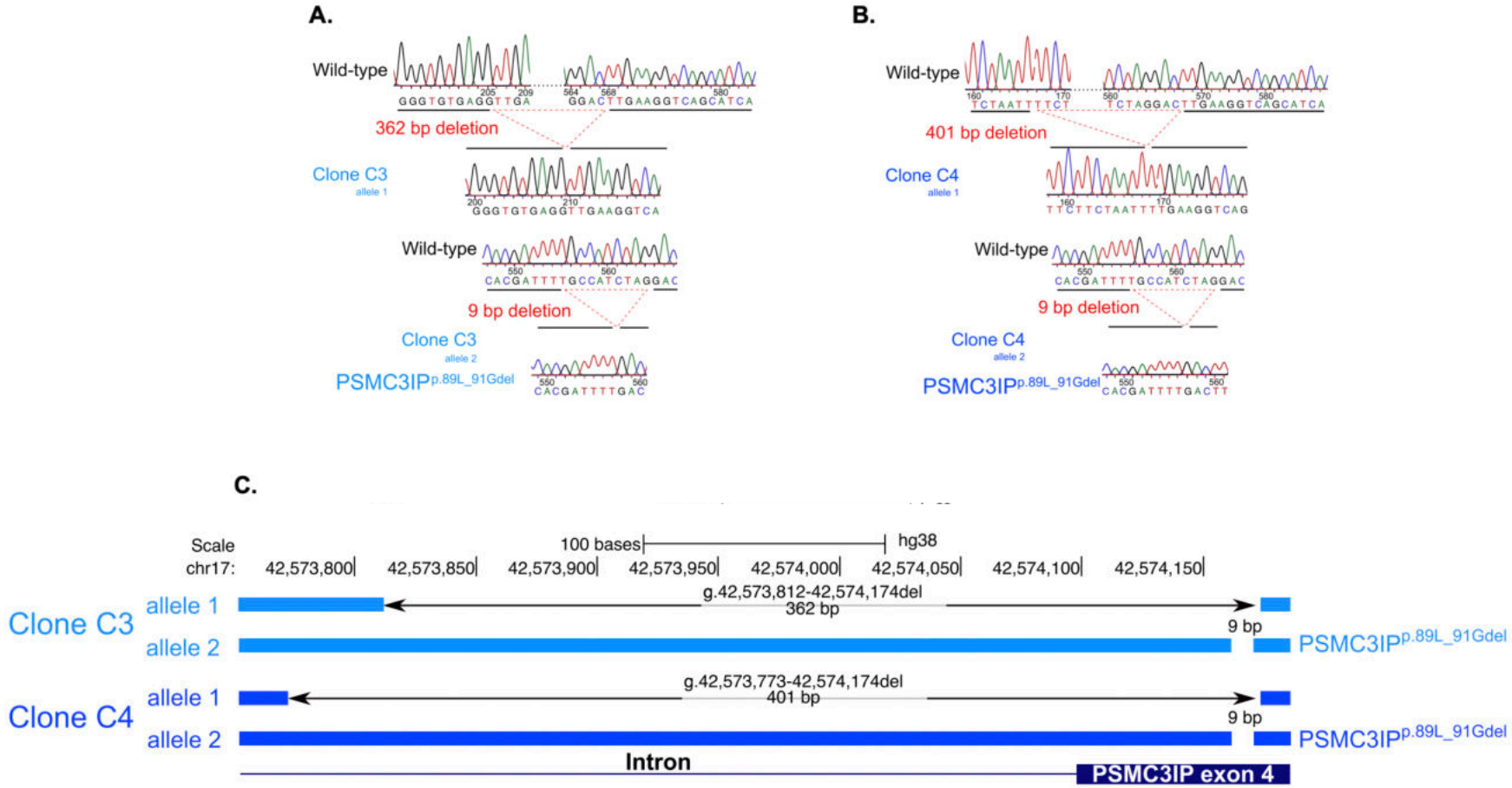

Figure 4.13 Genotyping of *PSMC3IP*-mutant MCF10A *TP53*$^{-/-}$ cell lines.
A, B. Sanger sequencing traces of topoclones from *PSMC3IP*-mutant clones C3 (A) and C4 (B). **C.** The results from Sanger sequencing of topoclones from both *PSMC3IP*-mutant clones C3 and C4 were mapped to the human genome (hg38). Both *PSMC3IP* clones C3 and C4 had a 9 bp deletion p.89L_91G in the second allele. In allele 1, clone C3 had a 362 bp deletion g.42,573,812-42,574,174 and C4 had a 401 bp deletion g.42,573,773-42,574,174 spanning *PSMC3IP* exon 4 and intron.

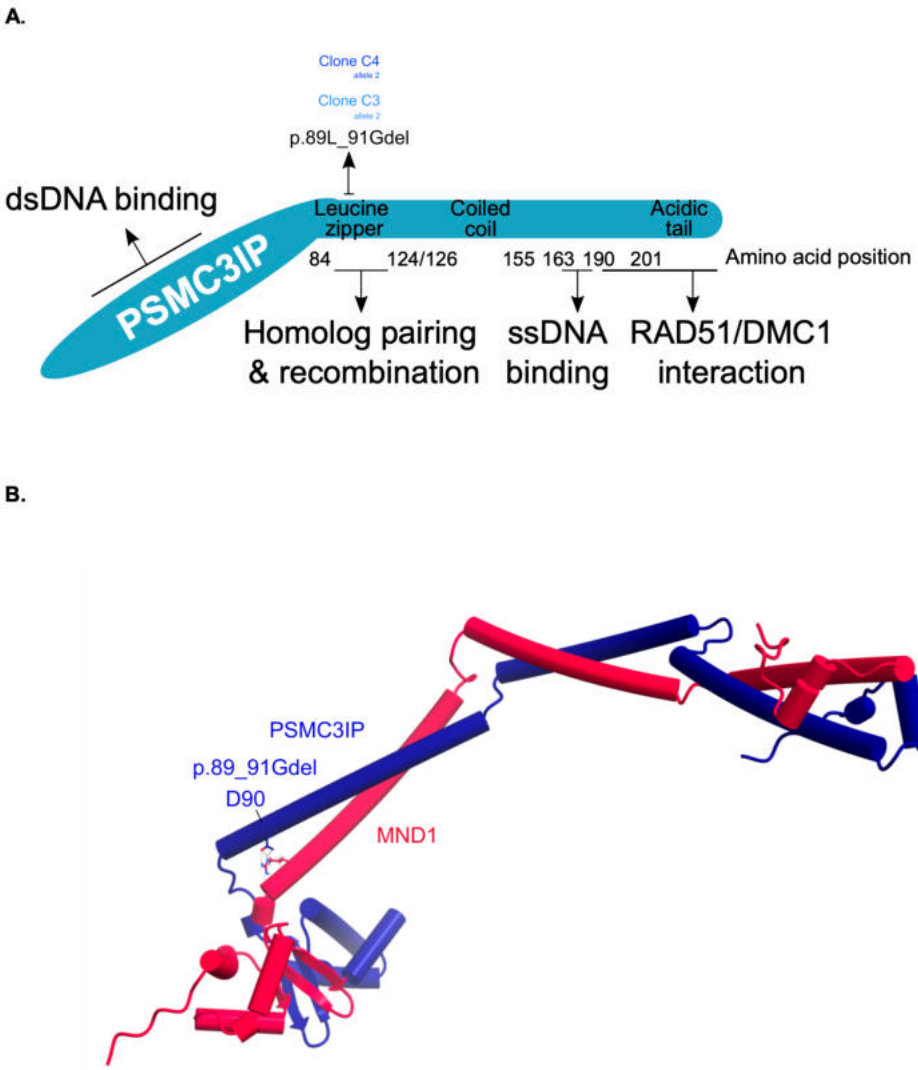

Figure 4.14 Predicted model of generated *PSMC3IP*-mutant clones on structure and function.

A. PSMC3IP structure and function. Double-stranded DNA (dsDNA) binding occurs within region 1-84.The leucine zipper region (84-124/126) is responsible for homolog pairing & recombination; the p.89L_91Gdel mutation from allele 2 of PSMC3IP-mutant clones C3 and C4 is within this region. Coiled-coil is contained within amino acids 124/126-155. Amino acid position 163-190 function involves single-stranded DNA (ssDNA) binding. 190-201 amino acid position, which comprises the acidic tail, is responsible for RAD51/DMC1 interaction. **B.** AlphaFold-predicted model of the p.89L_91Gdel mutation in human PSMC3IP (blue) in its heterodimer configuration with MND1 (red). This predicted model demonstrated that the PSMC3IP glutamate residue at position 90 (D90) forms a hydrogen bond with the MND1 arginine residue at position 82 (R82).

Despite the generated *PSMC3IP*-mutant clones still possessing a wild-type allele, I verified these mutations resulted in loss of function (Figure 4.15). In clones C3 and C4, I observed an almost complete absence of PSMC3IP compared to wild-type with Western blotting. Similarly, I observed an almost complete absence of MND1 in clones A1 and B1 compared to wild-type. For both *PSMC3IP* and *MND1* mutant clones, the mRNA expression level of the corresponding gene was decreased compared to wild-type (Figure 4.15).

The generated models of *MND1* and *PSMC3IP* dysfunction were used to carry out dose/response experiments to assess their sensitivity to PARPi, as with the CRISPRi models. Similarly to *MND1* or *PSMC3IP* CRISPRi, I found that *MND1*-defective clones (A1 and B1) or *PSMC3IP*-defective clones (C3 and C4) were also sensitive to talazoparib (Figure 4.16), a clinical PARPi known to effectively "trap" PARP1 on chromatin (Krastev et al., 2021; Murai, Huang, et al., 2014). I found that this was not the case for the poor PARP1-trapper, but effective PARP1 catalytic inhibitor, veliparib (Figure 4.17), suggesting that like PARPi *vs.* BRCA1/2 synthetic lethality (Shen et al., 2013), PARPi/MND1 or PARPi/PSMC3IP synthetic lethality might be more dependent upon PARP1 trapping than catalytic inhibition. In order to mitigate possible confounding effects from possible incomplete knockout, I confirmed that PARPi sensitivity was not restricted to MCF10A *TP53*$^{-/-}$ cells, with a commercially-generated MND1 knockout cell line in HAP1 haploid model (Figure 4.18).

Our collaborators, Sven Rottenberg and colleagues (University of Bern) were able to independently validate PARPi sensitivity of *MND1*-defective cells. Their chosen

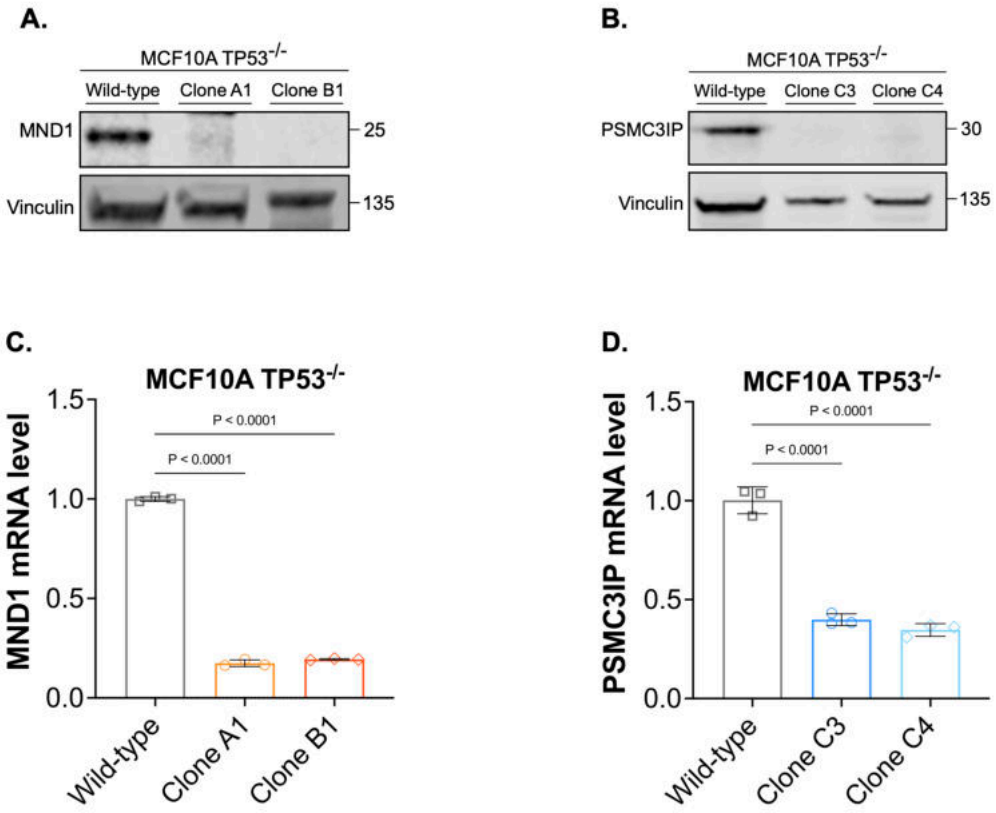

Figure 4.15 Validation of loss of function in generated *MND1* or *PSMC3IP* mutant clones.
MCF10A *TP53*$^{-/-}$ cells were transfected with non-targeting control or Cas9-crRNA ribonucleoproteins targeting *MND1* to generate daughter clones A1 and B1 (A, C) or *PSMC3IP* to generate daughter clones C3 and C4 (B, D). **A, B.** Western blot images are shown demonstrating an almost complete absence of either MND1 (A) or PSMC3IP (B) in lysates extracted from mutant clones. The antibodies used detect epitopes in the p.R82-E142 and p.P156-D216 regions of *MND1* and *PSMC3IP*, respectively. The targeted epitopes are C-terminal to MND1 or PSMC3IP mutations generated. Vinculin was used as a loading control. **C, D.** Barplots are shown of mRNA expression levels in MND1-mutant (C) or PSMC3IP-mutant (D) clones compared to unedited wild-type cells. mRNA expression levels were determined with RT-qPCR. Error bars represent SD from n=3 replicates, for which individual data points are shown. *P*-values were calculated via ANOVA with Tukey's post-test.

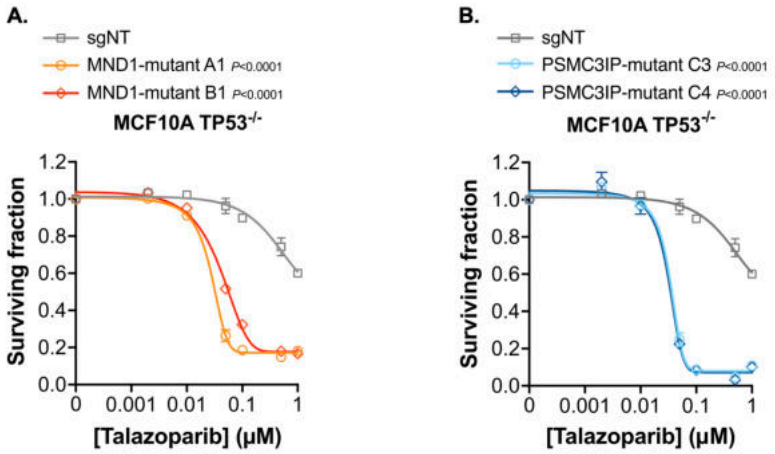

Figure 4.16 *MND1* and *PSMC3IP* defects enhanced PARPi sensitivity in mitotic cells.
Dose/response survival curves are shown with surviving fractions at the indicated doses of PARPi talazoparib. *MND1* (A) or *PSMC3IP* (B) mutant clones were more sensitive to talazoparib than wild-type cells. Two independent clones were used to represent *MND1* and *PSMC3IP* dysfunction. Cells were plated in 384-well plates and exposed to talazoparib for five continuous days, after which cell viability was quantified by CellTiter-Glo® and surviving fraction was calculated for each drug dose relative to DMSO-exposed cells. Error bars represent SD. *P*-values were calculated via ANOVA with Tukey's post-test.

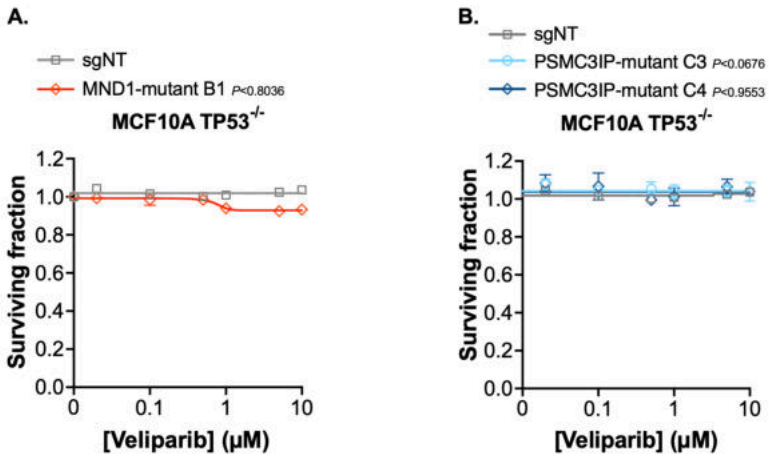

Figure 4.17 PARPi/MND1 or PARPi/PSCM3IP synthetic lethality may be dependent on PARP1 trapping.
Dose/response survival curves are shown with surviving fractions at the indicated doses of PARPi veliparib. *MND1* (A) or *PSMC3IP* (B) mutant clones were equally resistant to veliparib compared wild-type cells. Cells were plated in 384-well plates and exposed to veliparib for five continuous days, after which cell viability was quantified by CellTiter-Glo® and surviving fraction was calculated for each drug dose relative to DMSO-exposed cells. Error bars represent SD. *P*-values were calculated via ANOVA with Tukey's post-test.

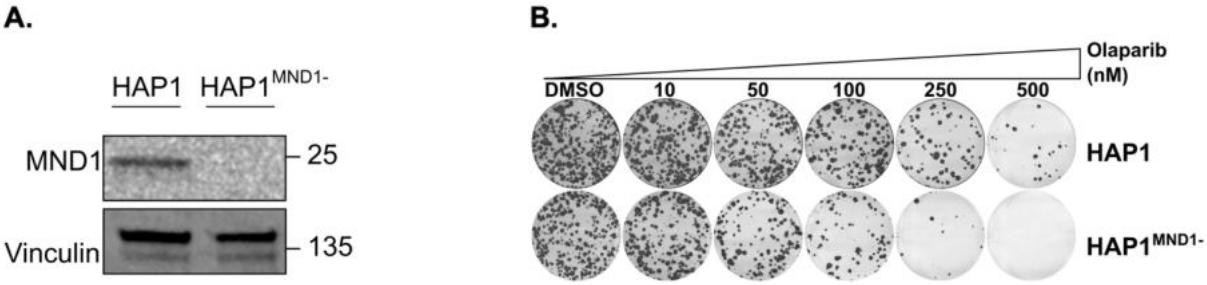

Figure 4.18 *MND1* knockout enhanced PARPi sensitivity in mitotic HAP1 cells. **A.** Western blot image demonstrating absence of MND1 in cell lysates extracted from *MND1*-knockout, but not wild-type, HAP1 cells. Vinculin was used as a loading control. **B.** HAP1 cells with *MND1* knockout were more sensitive to olaparib than wild-type cells. Images of clonogenic assay are shown. Cells were plated in 6-well plates and exposed to olaparib for 14 continuous days, after which colonies were stained with sulphorhodamine B (SRB).

model of KB1P-G3B1 comprises BRCA1 reconstituted KB1P-G3 tumour derived cell line, which was previously established from a *K14cre;Brca1$^{F/F}$;Trp53$^{F/F}$* (KB1P) mouse mammary tumour (Barazas et al., 2019). As such, KB1P-G3B1 was HR-proficient, which was also the case with the MCF10A TP53$^{-/-}$ model that I used in my validation experiments. KB1P-G3B1 were grown *ex vivo* and CRISPR-Cas9 mutagenised by Mnd1 sgRNA, the efficiency of which was determined with the TIDE algorithm (Brinkman et al., 2014); high *Mnd1* frameshift mutation rate was apparent in cells targeted with two different sgRNA against *Mnd1* (sgMnd1-1 or sgMnd1-2) compared to non-targeting control cells (sgNT) (Figure 4.19). Mnd1 targeting efficacy was validated via RT-qPCR analysis, which demonstrates significant reduction in Mnd1 mRNA in KB1P-G3B1 cells expressing sgRNA targeting *Mnd1*, compared to KB1P-G3B1 cells expressing non-targeting control. Mnd1-resconstituted cells were also generated by transfecting *Mnd1*-deficient KB1P-G3B1 cells with HA-tagged mouse *Mnd1* cDNA expression construct, which was validated via Western blotting in comparison to KB1P-G3B1 cells transfected with empty-vector and via RT-qPCR analysis; Mnd1 mRNA level of KB1P-G3B1 cells expressing sgRNA targeting Mnd1 expressing vector containing Mnd1 cDNA is much greater than KB1P-G3B1 cells expressing non-targeting control (Figure 4.19). Using these characterised cell models, our collaborators demonstrated that *Mnd1* defective KB1P-G3B1 cells are more sensitive to the PARP inhibitor olaparib than cells expressing non-targeting control (Figure 4.20). PARPi dose/response experiments performed by our collaborators in KB1P-G3B1 cells corroborated the results from analogous experiments I carried out with the models I generated in MCF10A *TP53*$^{-/-}$ background. Mnd1 overexpression only partially rescued the PARPi sensitivity of the *Mnd1* defective KB1P-G3B1 cells (Figure 4.20); Mnd1

expression may be inappropriately high in these cells, as demonstrated in the RT-qPCR. Perhaps upregulated Mnd1 expression may impart a similar PARPi and IR sensitivity phenotype to cells deficient in *Mnd1*. Although beyond the scope of this thesis, it would be interesting to formally assess whether *MND1*, and perhaps *PSMC3IP*, are "Goldilocks" genes whereby inappropriate expression (too little or too much) drives PARPi sensitivity.

After establishing the importance of *MND1* and *PSMC3IP* in PARPi response of mitotic cells, I sought to assess whether this could be extended to other sources of DNA damage, such IR, as indicated from our collaborators' gene-trap mutagenesis screen results. I confirmed sensitivity to IR in *MND1* or *PSMC3IP* mutant MCF10A *TP53*$^{-/-}$ cells, as demonstrated in Figure 4.21A and Figure 4.21B, respectively. Our collaborators were also able to validate the IR sensitivity of *Mnd1* defective KB1P-G3B1 cells (Figure 4.21C and Figure 4.21D). Restoration of Mnd1 expression in *Mnd1* defective KB1P-G3B1 cells also partially reversed radiosensitivity in KB1P-G3B1 cells (Figure 4.21C and Figure 4.21D). Contrastingly, I found that *MND1* or *PSMC3IP* mutant clones were equally sensitive to a small molecule ATR inhibitor (VX970) as wild-type cells (Figure 4.22), suggesting that the effect of PARPi did not necessarily extend to any agent that causes RF stress.

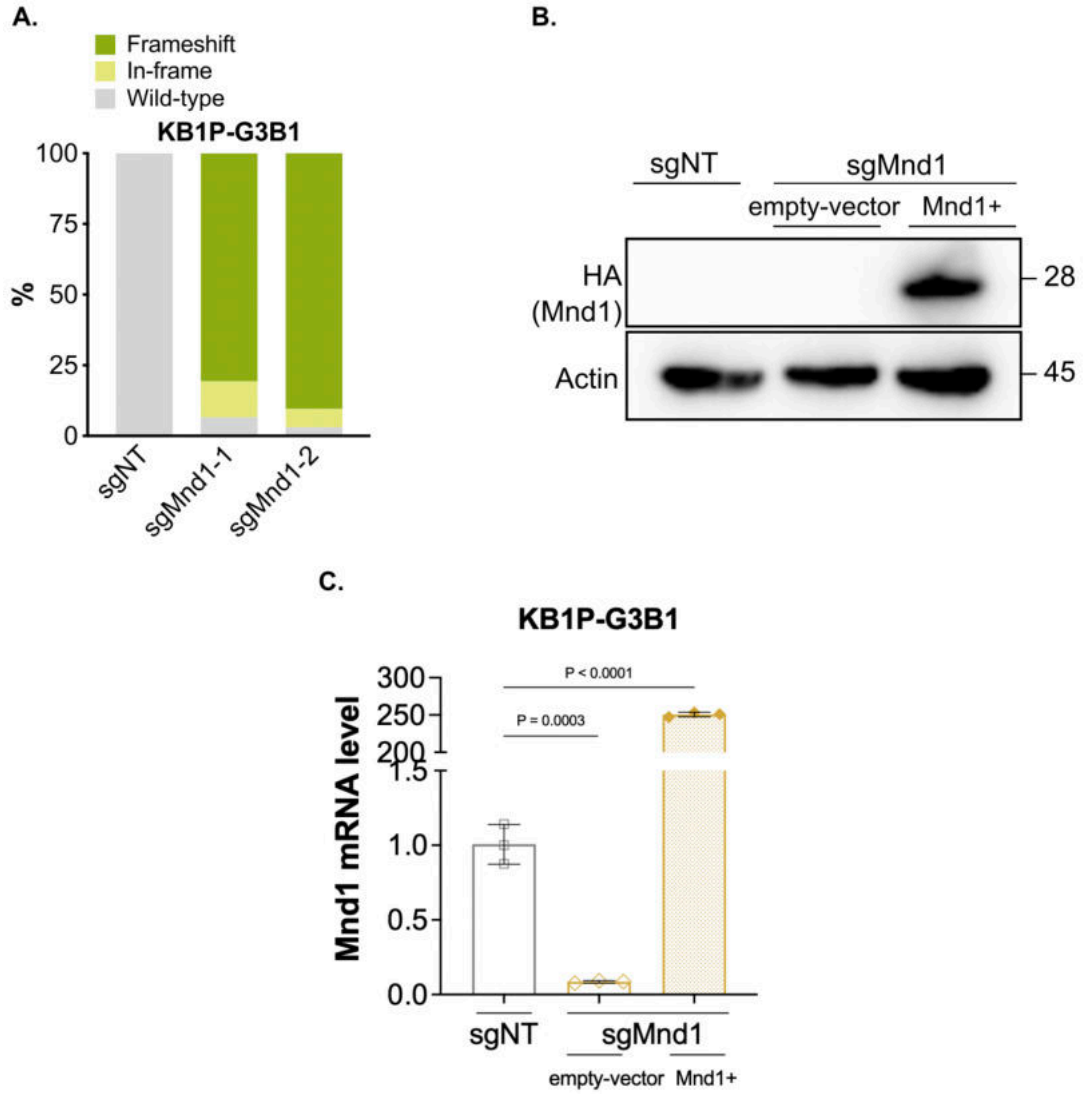

Figure 4.19 Characterisation of *Mnd1* sgRNA-mediated targeting and reconstitution in KB1P-G3B1 background.

A. Barplot is shown demonstrating the efficiency of sgRNA-mediated *Mnd1* targeting. High *Mnd1* frameshift mutation rate was apparent in cells targeted with two different sgRNA against *Mnd1* (sgMnd1-1 or sgMnd1-2) compared to non-targeting control cells (sgNT). Proportion of cells in grey were determined to be wild-type, those in yellow were determined to have in-frame deletions and those in green were determined to have frameshift mutations. DNA extracted from cells were sequenced via Sanger sequencing and target modifications were confirmed using the TIDE algorithm (Brinkman et al., 2014). **B.** Western blot image is shown of KB1P-G3B1 cell lysates illustrating restoration of Mnd1 expression via HA-tag in cells expressing a vector containing Mnd1 cDNA (Mnd1+), but not in cells expressing empty-vector. As indicated, KB1P-G3B1 cells express sgRNA targeting *Mnd1* (sgMnd1) or non-targeting control (sgNtc). Actin was used as a loading control. **C.** RT-qPCR analysis demonstrates significant reduction in Mnd1 mRNA in KB1P-G3B1 cells expressing sgRNA targeting Mnd1 compared to KB1P-G3B1 cells expressing non-targeting control (sgNT). Mnd1 mRNA level of KB1P-G3B1 cells expressing sgRNA targeting Mnd1 expressing vector containing Mnd1 cDNA (Mnd1+) is much greater than KB1P-G3B1 cells expressing non-targeting control (sgNT). Data normalised to sgNT (grey). Error bars represent SD from n=3 replicates. P-values calculated via unpaired t-test. Data generated by Paola Francica.

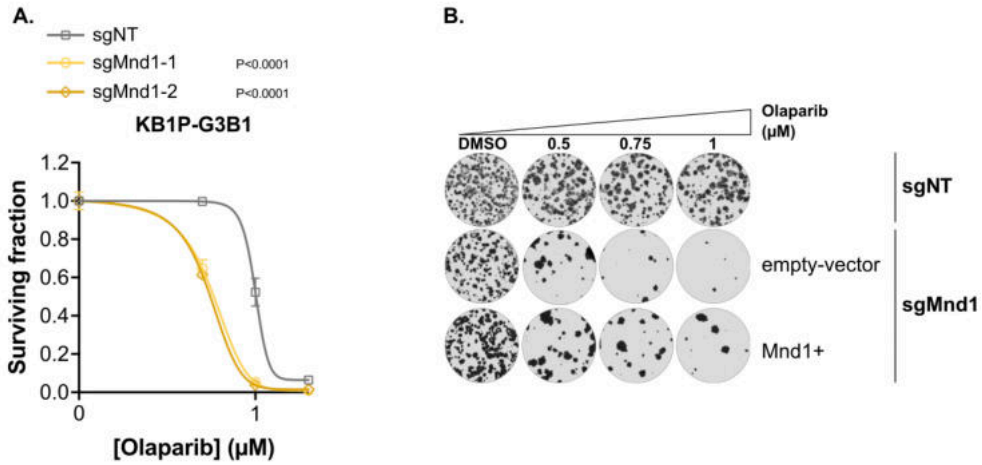

Figure 4.20 *MND1* defective KB1P-G3B1 cells demonstrated enhanced PARPi sensitivity, which was partially rescued by Mnd1 overexpression.
Mnd1-defective KB1P-G3B1 cells were more sensitive to olaparib than wild-type cells, which was partially restored with Mnd1 overexpression. Two independent clones were used to represent *MND1* dysfunction. KB1P-G3B1 cells were transduced with lentiviral constructs encoding sgRNA targeting *Mnd1* (either sgMnd1-1 or sgMnd1-2) or non-targeting control (sgNT). Cells were plated in 6-well plates and exposed to olaparib for 11 continuous days, after which colonies were stained with crystal violet; colonies were quantified in an automated manner with macros using ImageJ. **A.** Dose/response survival curves are shown with surviving fractions at the indicated doses of PARPi olaparib. Surviving fraction was calculated for each drug dose relative to DMSO-exposed cells. Error bars represent SD. *P*-values were calculated via ANOVA with Tukey's post-test. **B.** Representative images of growth assays are shown of KB1P-G3B1 cells transduced with lentiviral constructs encoding sgRNA targeting *Mnd1* (sgMnd1) expressing either empty-vector or Mnd1 cDNA expression vector (Mnd1+). Restoration of Mnd1 expression (Mnd1+) in *Mnd1* defective (sgMnd1) KB1P-G3B1 cells partially reversed PARPi sensitivity. Data generated by Paola Francica.

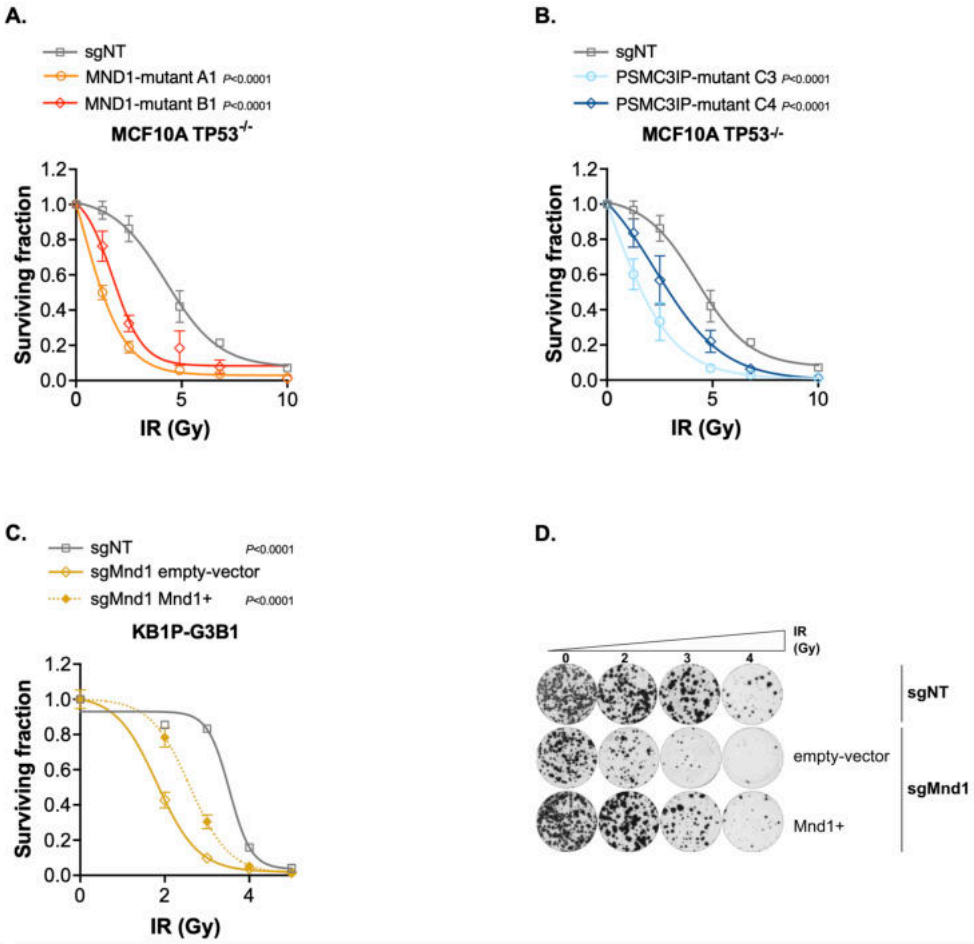

Figure 4.21 *MND1* and *PSMC3IP* defects enhanced IR sensitivity in mitotic cells. Generated *MND1* (A) or *PSMC3IP* (B) mutant clones were more sensitive to ionising radiation (IR) compared to non-targeting control cells (sgNT). Dose/response survival curves are shown with surviving fractions at the indicated doses of IR. Cells were plated in 96-well plates and exposed to indicated dose of IR. After 7 days, cell viability was quantified by CellTiter-Glo® and surviving fraction was calculated for each drug dose relative to DMSO-exposed cells. Error bars represent SD from n=8 replicates. *P*-values were calculated via ANOVA with Tukey's post-test. **C.** *Mnd1*-defective KB1P-G3B1 cells (sgMnd1) were more sensitive to IR compared to non-targeting control cells (sgNT), which was partially reversed with reconstitution of Mnd1 (Mnd1+). Cells were plated in 6-well plates and exposed to indicated dose of IR, after which colony formation was estimated by crystal violet staining. **D.** Representative image from C. Data in C and D generated by Paola Francica.

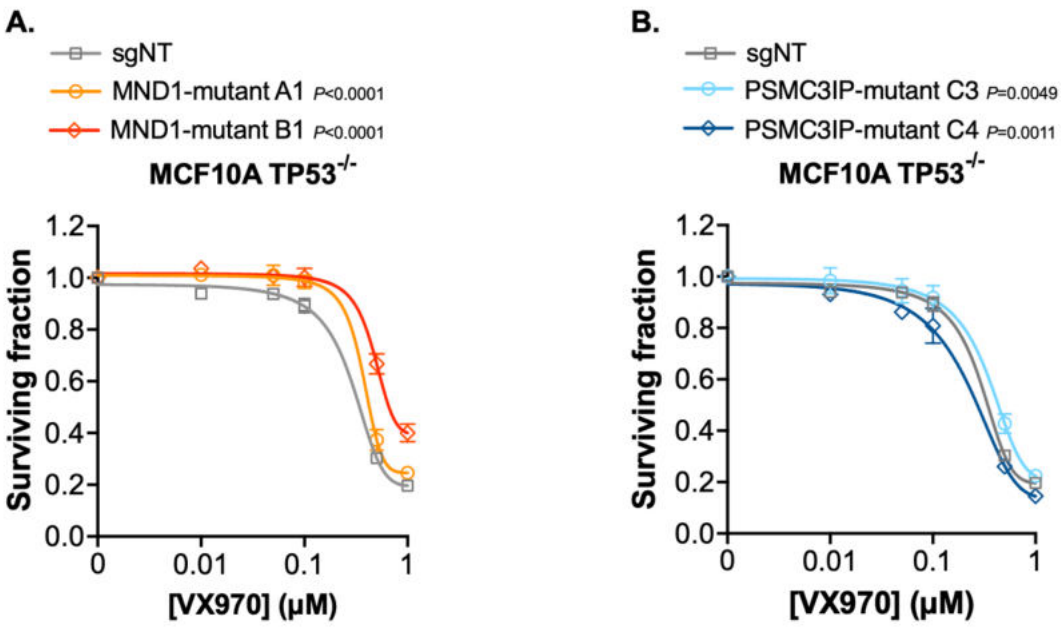

Figure 4.22 *MND1* and *PSMC3IP* defective cells were equally sensitive as wild-type cells to ATR inhibitor in mitotic cells.
Dose/response survival curves are shown with surviving fractions at the indicated doses of ATR inhibitor VX970. *MND1* (A) or *PSMC3IP* (B) mutant clones were equally resistant to VX970 compared to wild-type cells. Cells were plated in 384-well plates and exposed to VX970 for five continuous days, after which cell viability was quantified by CellTiter-Glo® and surviving fraction was calculated for each drug dose relative to DMSO-exposed cells. Error bars represent SD. *P*-values were calculated via ANOVA with Tukey's post-test.

4.3. Discussion

In this Chapter, I described the common PSMC3IP-MND1 expression in mitotic tumour cells. This frequent expression of PSMC3IP-MND1 was also evident in human tumours, including those in which PARPi are used clinically. The expression data from both mitotic tumour cell lines and human tumours revealed a correlation between MND1 and PSMC3IP expression, which is consistent with the hypothesis that these two heterodimer components may have a shared function in mitotic cells and tumours, as is presently demonstrated in meiotic cells, in which their canonical function has been well described. Together with our collaborators, I also validated that *MND1*- and *PSMC3IP*-defective cells were more sensitive to PARPi and IR in various cell lines.

A potential caveat of my *in vitro* interpretation that *MND1*- and *PSMC3IP*-defective cells are more sensitive to PARPi and IR is that this may not be applicable *in vivo*, and could potentially be an *in vitro* artefact. It may not necessarily be the case that a *MND1* or *PSMC3IP* defect renders a human patient more amenable to PARPi or IR therapy. As such, further work is required to assess this; initially PARPi or IR response in a mouse model upon *MND1* or *PSMC3IP* defect could be compared to wild-type. Experimental validation of the *in silico* analysis to assess MND1 or PSMC3IP expression in human tumours could be verified with immunohistochemistry analysis on patient samples with a variety of tumour types.

In agreement with our findings, Domenichini et al. (2006) observed MND1 expression (Atmnd1 in plants) in somatic cells, as well as meiotic cells, in Arabidopsis model (Domenichini et al., 2006). Similarly, Cho et al. observed

PSMC3IP expression in somatic cells (Cho et al., 2014). More recently, work conducted by Koob et al. demonstrated that MND1 and PSMC3IP are widely expressed in mitotic cell lines and tissues from proteomics data, as well as Western blotting (Koob et al., 2023). Notably, they demonstrated MND1 and PSMC3IP protein expression seems to be independent of ALT in cancer cell lines. Following their gene-trap mutagenesis screen, Koob et al. validated that *MND1*-defective HAP1 cells are more sensitive to IR compared to wild-type (Koob et al., 2023). A similar phenotype was also observed with PSMC3IP depletion. To a lesser extent, they observed that *MND1*-defective cells are more sensitive to olaparib than wild-type cells.

After establishing the importance of *MND1* and *PSMC3IP* in PARPi and IR response of mitotic cells, it would be interesting to assess whether this could be extended to further sources of DNA damage. I identified that *MND1*- or *PSMC3IP*-defective cells were equally resistant to a small molecule ATR inhibitor (VX970) as wild-type cells, so the effect of PARPi did not necessarily extend to any agent that causes RF stress, but it would be interesting to assess sensitivity to other agents which cause replication stress, such as HU, aphidocolin, camptothecin, cisplatin and MMC. In addition, these agents impair the progression of RFs via varying mechanisms, which could allow further refinement of a potential mechanism of action for PSMC3IP-MND1. For example, HU stalls RFs by limiting the synthesis of deoxyribonucleotides (Fong et al., 2009), which is distinct from platinum salt-mediated mechanism of RF function impairment via cross-linking DNA (Faivre et al., 2003). The trapping of PARP1 on DNA, the main source of

PARPi-induced cytotoxicity, results in DNA damage associated with the RF, including impairment of nascent DNA strand maturation (Vaitsiankova et al., 2022).

The DNA lesions caused by PARP inhibitors and IR often activate HR and Ser-139 phosphorylation of histone variant H2AX (γH2AX), as well as the localisation of the recombinase RAD51 to the site of DNA damage (Bryant et al., 2005; Farmer et al., 2005). RAD51 foci formation is used as a surrogate marker for HR deficiency and PARPi response, whereby the inability to localise the DNA recombinase RAD51 to site of damage has classically been used to determine defective HR and predict PARPi sensitivity (Cruz et al., 2018; Llop-Guevara et al., 2021; van Wijk et al., 2020). This matter of MND1 and PSMC3IP potential influence on HR-mediated repair will be assessed in the following chapter.

Chapter 5. PARPi sensitivity in MND1/PSMC3IP defective cells is characterised by an increase in RAD51 foci and suppression of HR

5.1. Introduction

After establishing the importance of *MND1* and *PSMC3IP* in PARPi and IR response of mitotic cells, functional experiments were required to identify the specific mode of action of MND1 and PSM3CIP.

The PSMC3IP-MND1 heterodimer has been shown to facilitate meiotic RAD51 function in yeast (Tsubouchi & Roeder, 2002) and in cell-free *in vitro* assays, PSMC3IP-MND1 catalyses the binding of mouse and human RAD51 to nucleotides and DNA (Bugreev et al., 2014). Therefore, I initially sought to investigate whether MND1/PSMC3IP may share similar functions in miotic mammalian cells.

The DNA lesions caused by PARP inhibitors and IR often activate HR and γH2AX, as well as the localisation of the recombinase RAD51 to the site of DNA damage (Bryant et al., 2005; Farmer et al., 2005). As such, RAD51 foci formation is used as a surrogate marker for HR deficiency and PARPi response, whereby the inability to localise the DNA recombinase RAD51 to site of damage has classically been used to determine defective HR and predict PARPi sensitivity (Cruz et al., 2018; Llop-Guevara et al., 2021; van Wijk et al., 2020). As such, I planned to assess HR proficiency in *MND1* and *PSMC3IP* dysfunctional cells, using RAD51 foci as a surrogate marker.

In the context of altered RF progression in response to DNA damage, RAD51 has been identified to mediate RF reversal in a BRCA1/2-independent fashion, a mechanism which processes stalled RFs and appears to protect cells against genotoxic stress (Mijic et al., 2017; Zellweger et al., 2015). Moreover, in a BRCA1/2-dependent manner, RAD51 filament formation is required for its protective effect on the regressed arm, allowing PARP1/RECQ1-regulated restart of reversed RFs (Mijic et al., 2017; Schlacher et al., 2012; Zellweger et al., 2015). High concentrations of PARPi accelerate RF progression (Maya-Mendoza et al., 2018). Based on these findings, we wanted to test the hypothesis that the PSMC3IP-MND1 heterodimer contributes to RAD51 function at RFs.

5.2. Results

5.2.1. MND1/PSMCIP defective cells are characterised by an increase in RAD51 foci

Given that the PSMC3IP-MND1 heterodimer has been shown to facilitate RAD51 function in yeast (Tsubouchi & Roeder, 2002; Bugreev et al., 2014), I initially sought to investigate whether MND1/PSMC3IP may share similar functions in miotic mammalian cells. I initially wanted to assess the ability of RAD51 to localise to the site of DNA damage in *MND1* mutant MCF10A *TP53*$^{-/-}$ cells, for which I characterised the PARPi response in Chapter 4. Rather than seeing reduction in nuclear RAD51 foci (a phenotype normally associated with a HR defect, and radio- or PARPi sensitivity (van Wijk et al., 2020), I observed significantly higher levels of RAD51 foci in *MND1*-defective cells (Figure 5.1A) upon PARPi- or IR-exposure. This phenotype was upon exposure to either olaparib or IR. As demonstrated in Figure 5.1B, a corresponding increase in γH2AX was observed. I also observed a

PARPi- or IR-induced increase of RAD51 and γH2AX foci in *PSMC3IP* mutant MCF10A *TP53*$^{-/-}$ cells (Figure 5.2).

5.2.2. MND1/PSMCIP defective cells are characterised by defective HR

In order to assess the impact of this increase in RAD51 foci on DNA repair by HR, I used a cell line with a synthetic HR reporter substrate (DR-GFP; (Gunn & Stark, 2012)). As demonstrated in the schematic in Figure 5.3A, a DSB is introduced with I-*Sce*I in a mutated, inactive, GFP. HR-mediated repair of this DSB restores GFP fluorescence. As such, GFP is a readout of HR efficiency. U2OS DR-GFP cells were transfected with siRNAs targeting *MND1, PSMC3IP* or non-targeting control, prior to expression of I-*Sce*I. A proportion of cells remained untransfected (mock) and another proportion of cells transfected with indicated siRNAs were not transfected with I-*Sce*I for controls of background GFP positivity. I found that either siRNA-mediated silencing of *MND1* or *PSMC3IP* (Figure 5.4) caused a reduction of HR-mediated repair, as demonstrated in Figure 5.3B and Figure 5.3C. siRNA-mediated silencing of *BRCA1* or *BRCA2* were used as positive controls for HR deficiency in this assay. As such the results from the DR-GFP assay indicate that *MND1* and *PSMC3IP* indeed facilitates HR in somatic cells, but perhaps not to as great an extent as *BRCA1* or *BRCA2.* The crucial role for *MND1* in HR in mitotic cells was corroborated by our collaborators, whereby increased micronuclei formation was observed in *Mnd1*-deficient KB1P-G3B1 cells exposed to olaparib or IR (Figure 5.5), which is indicative of genomic instability.

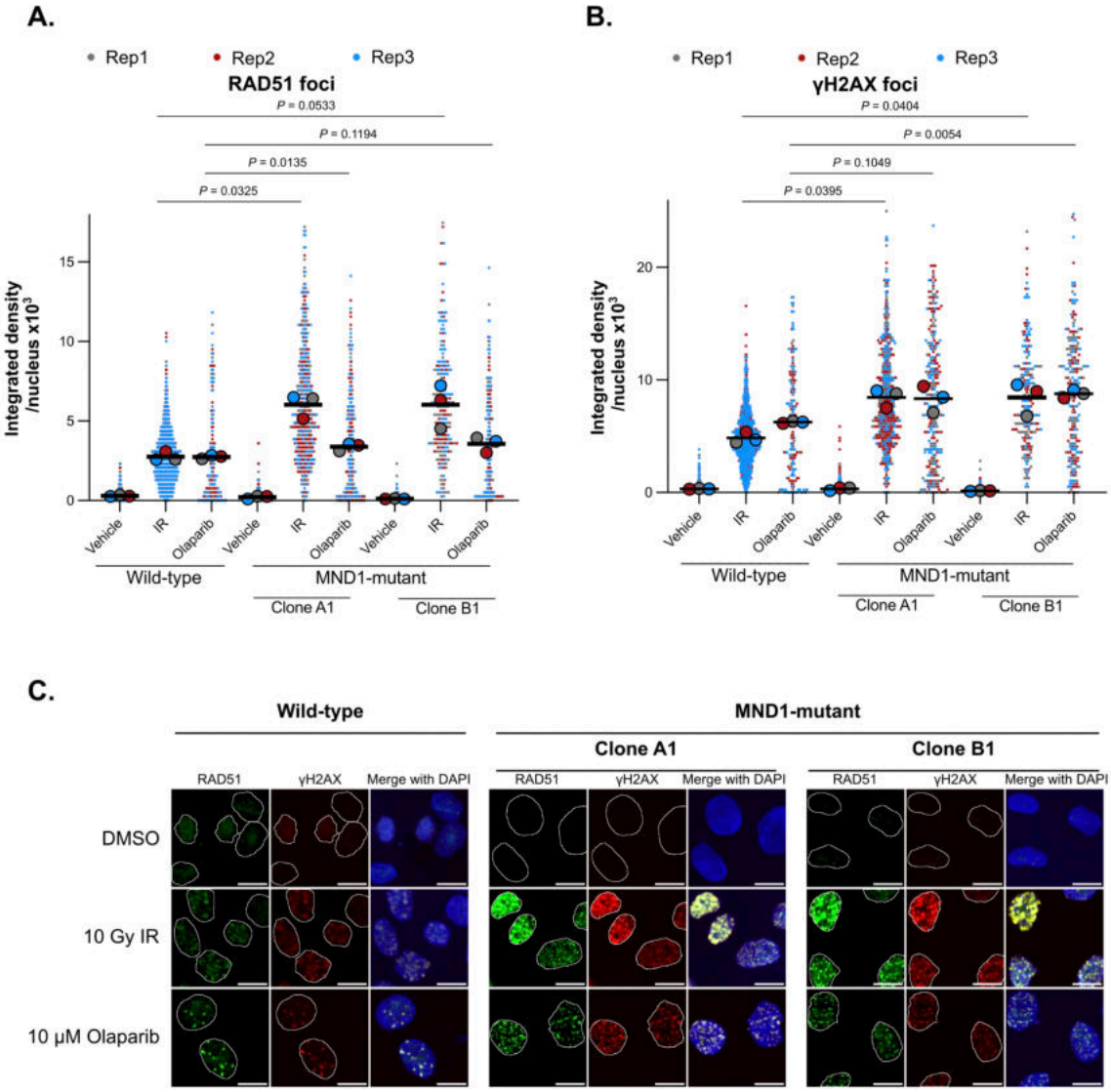

Figure 5.1 PARPi- or IR-induced increase of RAD51 and γH2AX foci in *MND1* mutant MCF10A *TP53*$^{-/-}$ cells.

A, B. Superplot of RAD51 (A) or γH2AX (B) integrated density in each indicated cell line is shown. Small dots represent data from each nuclei with the colour corresponding to the biological replicate. Horizontal black line represents the mean of all the data, while large dots represent the mean of each biological replicate. *P*-values were calculated via two-tailed t-test using mean of each biological replicate (n=3). Min. 48 nuclei were quantified per each biological replicate. **C.** Representative images of RAD51 or γH2AX foci upon exposure to either 10 Gy IR or 10 μM olaparib or DMSO. Nuclei are shown in blue, while RAD51 and foci are represented in green and red, respectively. MCF10A *TP53*$^{-/-}$ cells, either wild-type or with *MND1* defect (clones A1 and B1) were plated onto coverslips. Cells were either exposed to 10 μM olaparib and then fixed after 16 hours or 10 Gy IR and then fixed after 4 hours. Vehicle cells remained untreated and were fixed simultaneously with the olaparib- or IR-exposed samples. Cells were co-stained with anti-RAD51 and anti-γH2AX antibodies.

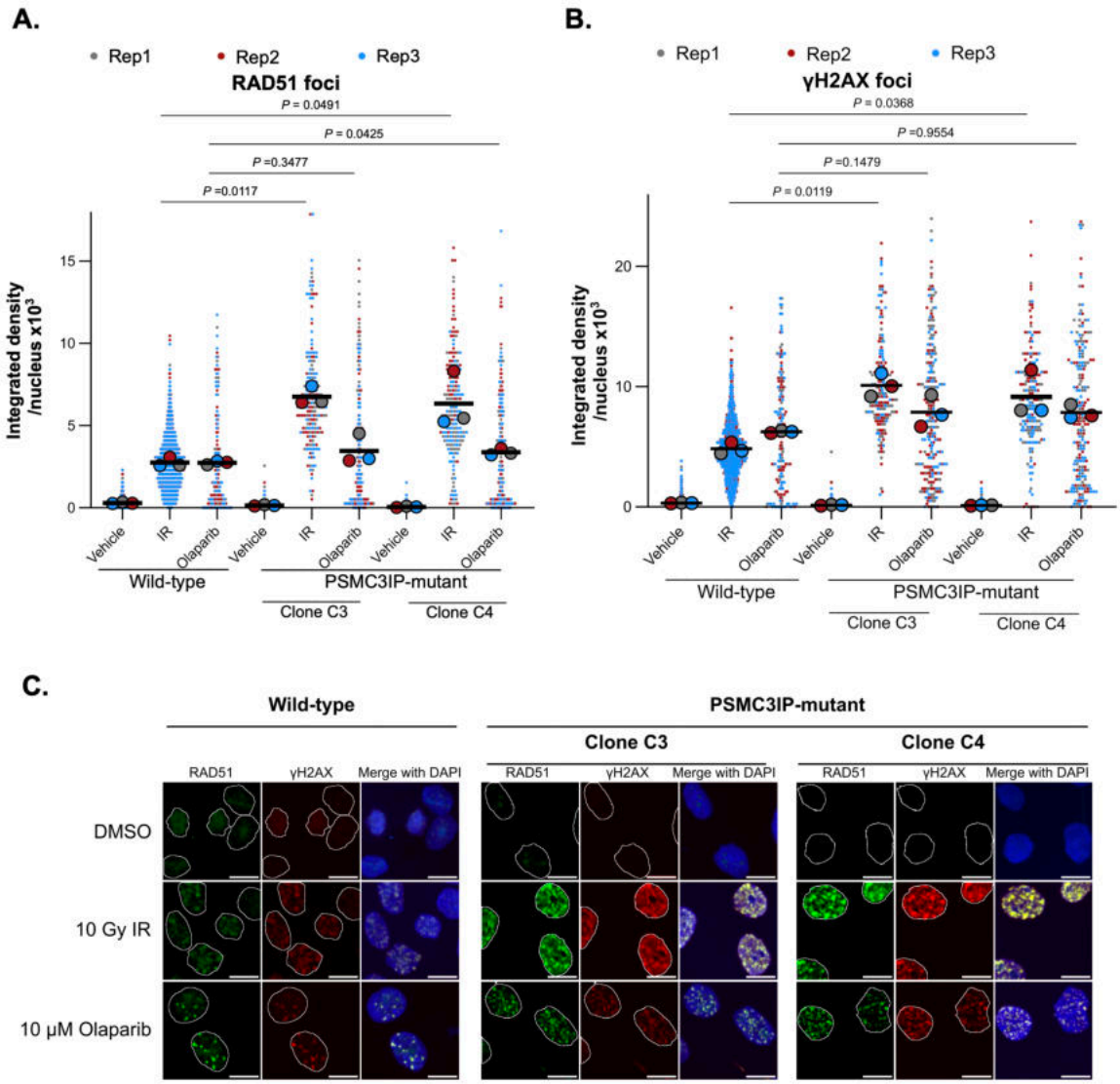

Figure 5.2 PARPi- or IR-induced increase of RAD51 and γH2AX foci in *PSMC3IP* mutant MCF10A *TP53*$^{-/-}$ cells.

A, B. Superplot of RAD51 (A) or γH2AX (B) integrated density in each indicated cell line is shown. Small dots represent data from each nuclei with the colour corresponding to the biological replicate. Horizontal black line represents the mean of all the data, while large dots represent the mean of each biological replicate. *P*-values were calculated via two-tailed t-test using mean of each biological replicate (n=3). Min. 48 nuclei were quantified per each biological replicate. **C.** Representative images of RAD51 or γH2AX foci upon exposure to either 10 Gy IR or 10 μM olaparib or DMSO. Nuclei are shown in blue, while RAD51 and foci are represented in green and red, respectively. MCF10A *TP53*$^{-/-}$ cells, either wild-type or with *PSMC3IP* defect (clones C3 and C4) were plated onto coverslips. Cells were either exposed to 10 μM olaparib and then fixed after 16 hours or 10 Gy IR and then fixed after 4 hours. Vehicle cells remained untreated and were fixed simultaneously with the olaparib- or IR-exposed samples. Cells were co-stained with anti-RAD51 and anti-γH2AX antibodies.

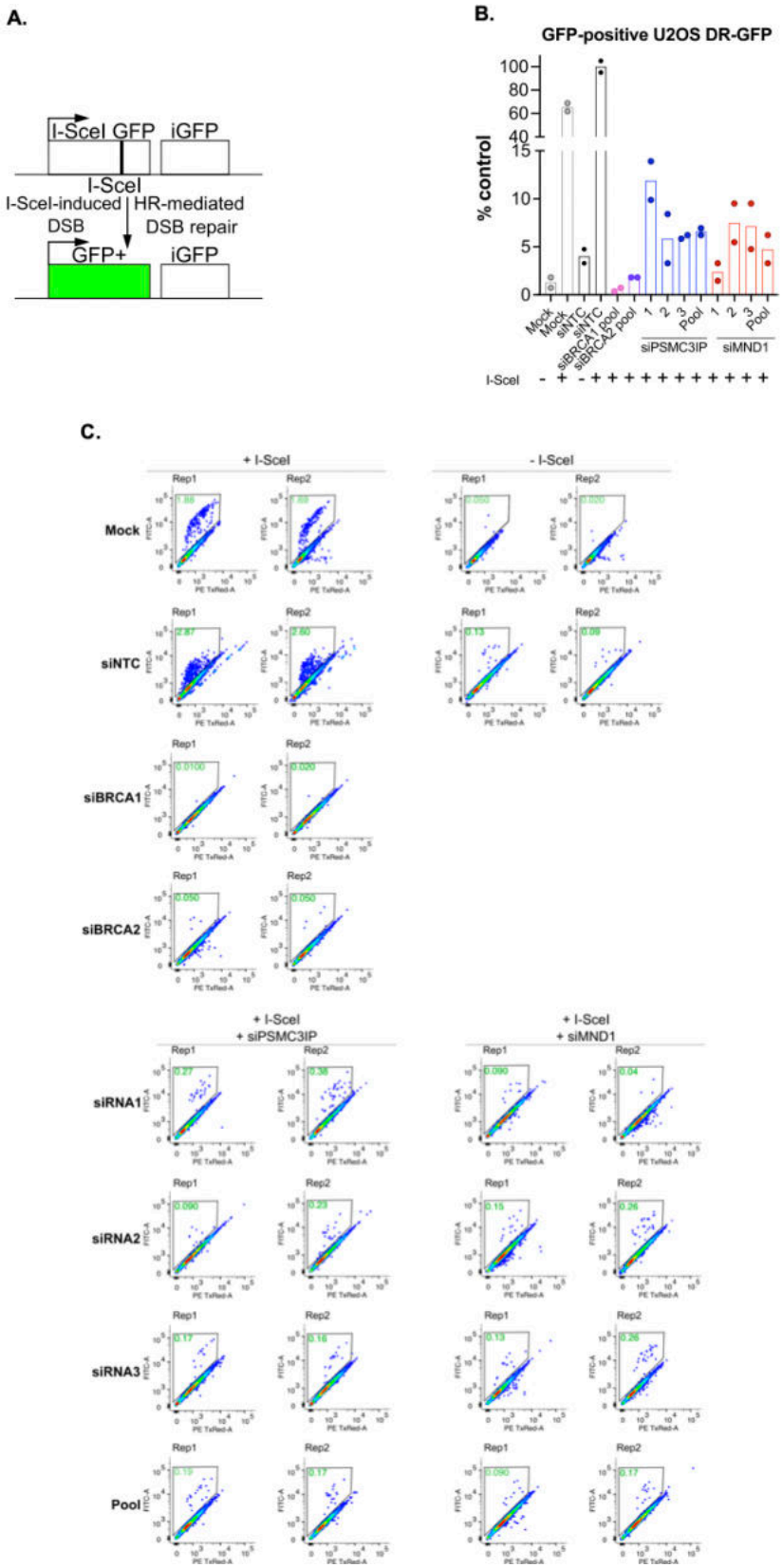

Figure 5.3 *MND1* or *PSMC3IP* silencing reduced HR-mediated repair.
A. Schematic of DR-GFP reporter. **B**. Bar plot of % GFP+ cells relative to cells transfected with both non-targeting control siRNA (siNTC) and I-*Sce*I is shown. *BRCA1* or *BRCA2* were used as positive controls for HR deficiency. GFP+ cells were analysed by flow cytometry. **C**. Representative FACS scatterplots from (B).

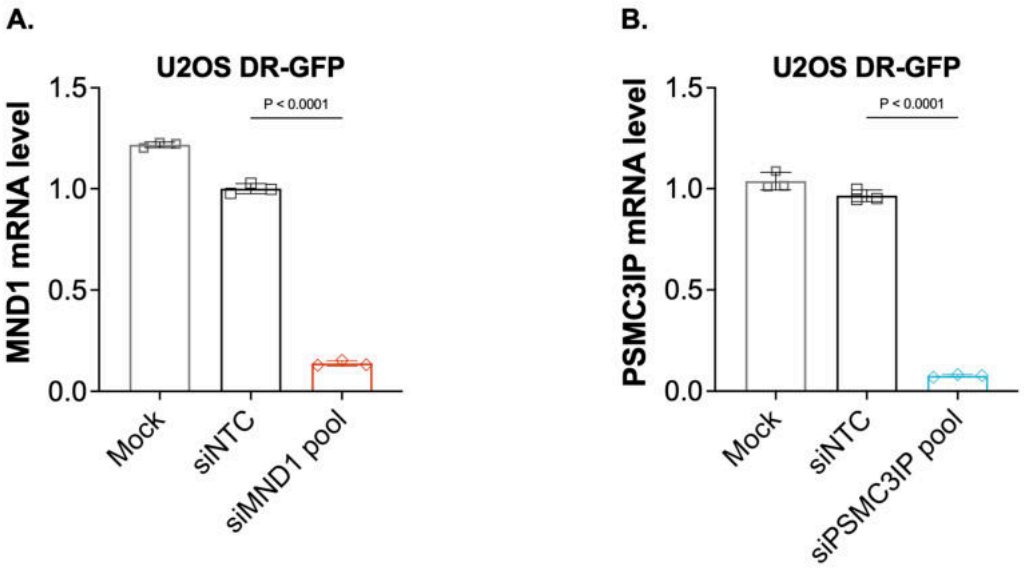

Figure 5.4 siRNA-mediated depletion reduced mRNA expression in U2OS DR-GFP cells,

Barplots are shown of mRNA expression levels with siRNA-mediated depletion of *MND1* (A) *PSMC3IP* (B) compared to cells transfected with non-targeting siRNA (siNTC). Data normalised to siNTC. mRNA expression levels were determined with RT-qPCR. Error bars represent SD from n=3 replicates, for which individual data points are shown. *P*-values were calculated via ANOVA with Sidak's post-test.

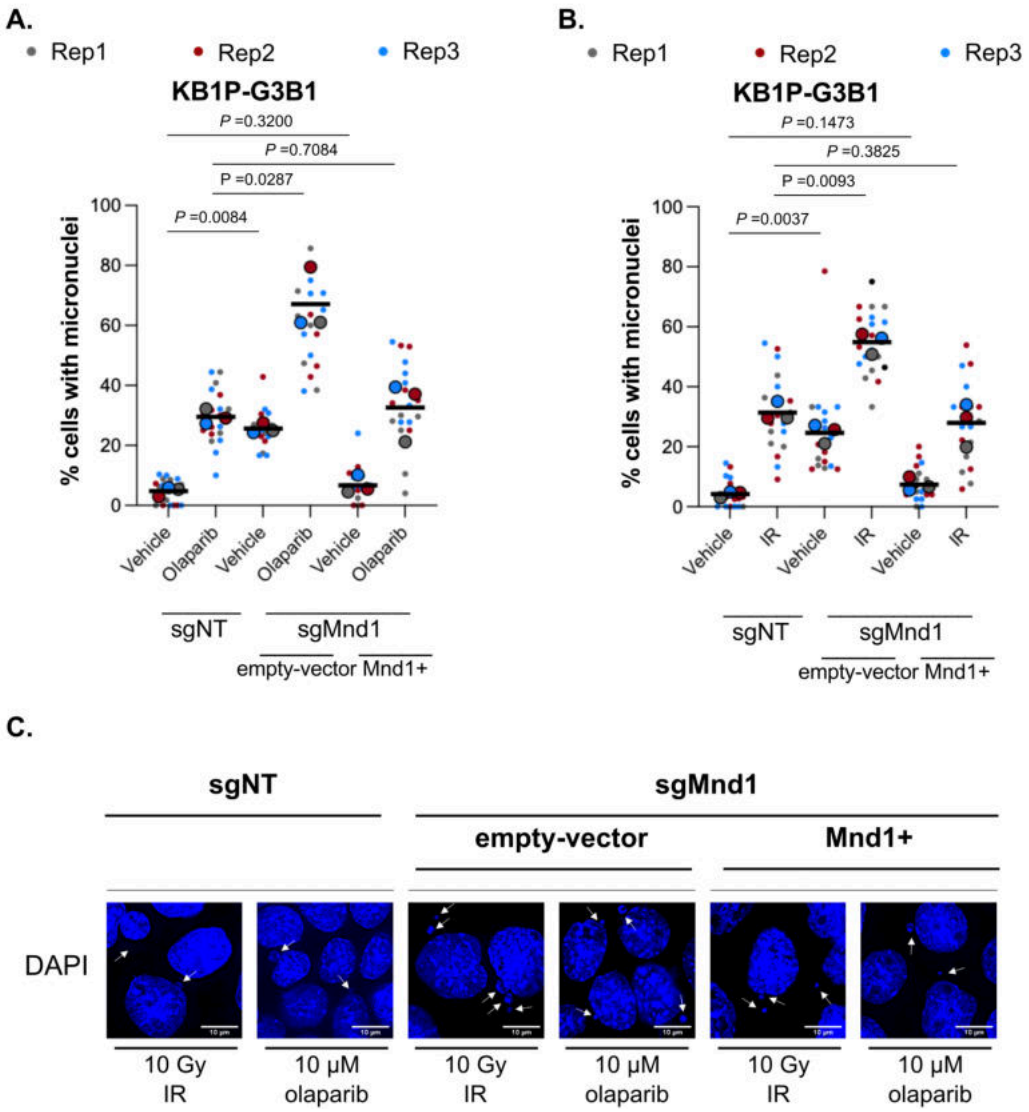

Figure 5.5 MND1 or PSMC3IP dysfunction increases micronuclei formation upon exposure to olaparib or IR.

A, B. Superplot of % cells with micronuclei in each indicated sample are shown (n=20). KB1P-G3B1 expressing either non-targeting control (sgNT) sgRNA or sgRNA targeting *Mnd1* (sgMnd1) were plated onto coverslips. *Mnd1*-deficient cells either express an empty-vector or a vector containing *Mnd1* cDNA (Mnd1+). Cells were either exposed to 8 Gy IR, 10 μM olaparib for 16 hours or remained untreated. Small dots represent data from each field of view, with the colour corresponding to the biological replicate. *P*-values were calculated via two-tailed t-test using mean of each biological replicate (n=3). **C.** Representative images shown of quantified micronuclei with sgMnd1 (C). Data generated by Paola Francica.

5.2.3. MND1/PSMC3IP contributes to RAD51 function at RFs.

After establishing the influence of MND1 or PSMC3IP expression on RAD51-mediated HR in mitotic mammalian cells, I wanted to further identify the specific mode of action of MND1 and PSMC3IP on RAD51. Given that RAD51 has been shown to mediate RF reversal, in a BRCA1/2-independent fashion, to protect cells against genotoxic stress (Mijic et al., 2017; Zellweger et al., 2015), I sought to assess whether MND1/PSMC3IP contributes to RAD51 function at RFs. Indications that this might be the case originated from *in situ* analysis of protein interactions at DNA RF (SIRF) assay (Roy & Schlacher, 2019), whereby Mnd1 was demonstrated to co-localise with EdU-labelled nascent DNA in KB1P-G3B1 cells, an interaction further increased by HU-induced RF stalling (Figure 5.6A and Figure 5.6B). After establishing that MND1 is at the RF, our collaborators subsequently assessed whether defective *Mnd1* affects the stability of stalled RFs via DNA fibre assay. Initially, *Brca1*- and *Tp53*-deficient KB1P-G3 cells were used (Barazas et al., 2019). As expected, pulse-labelling with CldU and IdU followed by RF stalling using 4 mM HU resulted in a significant reduction in the IdU/CldU track length ratio, indicating nucleolytic degradation of the nascent DNA of reversed RFs (Figure 5.6C). This was consistent with previous findings that BRCA1 stabilises stalled forks (Schlacher et al., 2012). Interestingly, this fork degradation phenotype was reversed in *Mnd1*-mutant cells (Figure 5.6C). We then investigated the effect of Mnd1 on RF stability in isogenic *Brca1* proficient KB1P-G3B1 cells. Due to the presence of Brca1, a high concentration of 8 mM HU was needed to generate the RF intermediates that eventually become degraded (Figure 5.6D). In these cells, RF degradation was rescued by loss of Mnd1; an effect that was reversed by reconstitution of the *Mnd1* cDNA (Figure 5.6D). These data from our collaborators

suggested that the effect of MND1 on RF stalling was BRCA1-independent. A reason for the lack of HU-mediated degradation in *MND1* defective cells may be a defect in RF reversal, a BRCA1/2-independent effect previously described in RAD51-deficient cells (Mijic et al., 2017; Qiu et al., 2021). Potent RAD51-dependent slowing of RF and their reversal is achieved by MMC treatment (Zellweger et al., 2015). Indeed, when exposed KB1P-G3 cells were exposed to 600 nM MMC for 2 hours, a clear slowing of RF progression was observed (Figure 5.6E). Interestingly, *Mnd1* loss counteracted this fork slowing, consistent with a defect in RF reversal (Figure 5.6E). In fact, RF progression in *Mnd1*-mutant cells was slightly higher than in the non-targeting control cells, even in the absence of drug (vehicle) (Figure 5.6E). These data suggested that MND1 is important for RF slowing upon replication-blocking DNA damage. In its absence, unrestrained RF progression may result in accumulation of toxic DNA damage.

5.2.4. PSMC3IP-MND1 heterodimer may support RAD51-mediated D-loop formation, which mediates PARPi response.

To build on the work carried out by our collaborators, I functionally assessed the relevance of a D-loop defect in PARPi response, making use of a previously described p.Glu201del mutant of PSMC3IP (Zhao & Sung, 2015). Human PSMC3IP has eight exons, which span approximately 5.5 kb. *PSMC3IP* encodes a 217-amino acid protein containing an N-terminus which binds dsDNA; a leucine zipper domain required for homolog pairing and recombination; a coiled-coil domain, which contains a region that binds ssDNA; and an acidic tail at the C-terminus, which allows RAD51/DMC1 interaction (Figure 5.7).

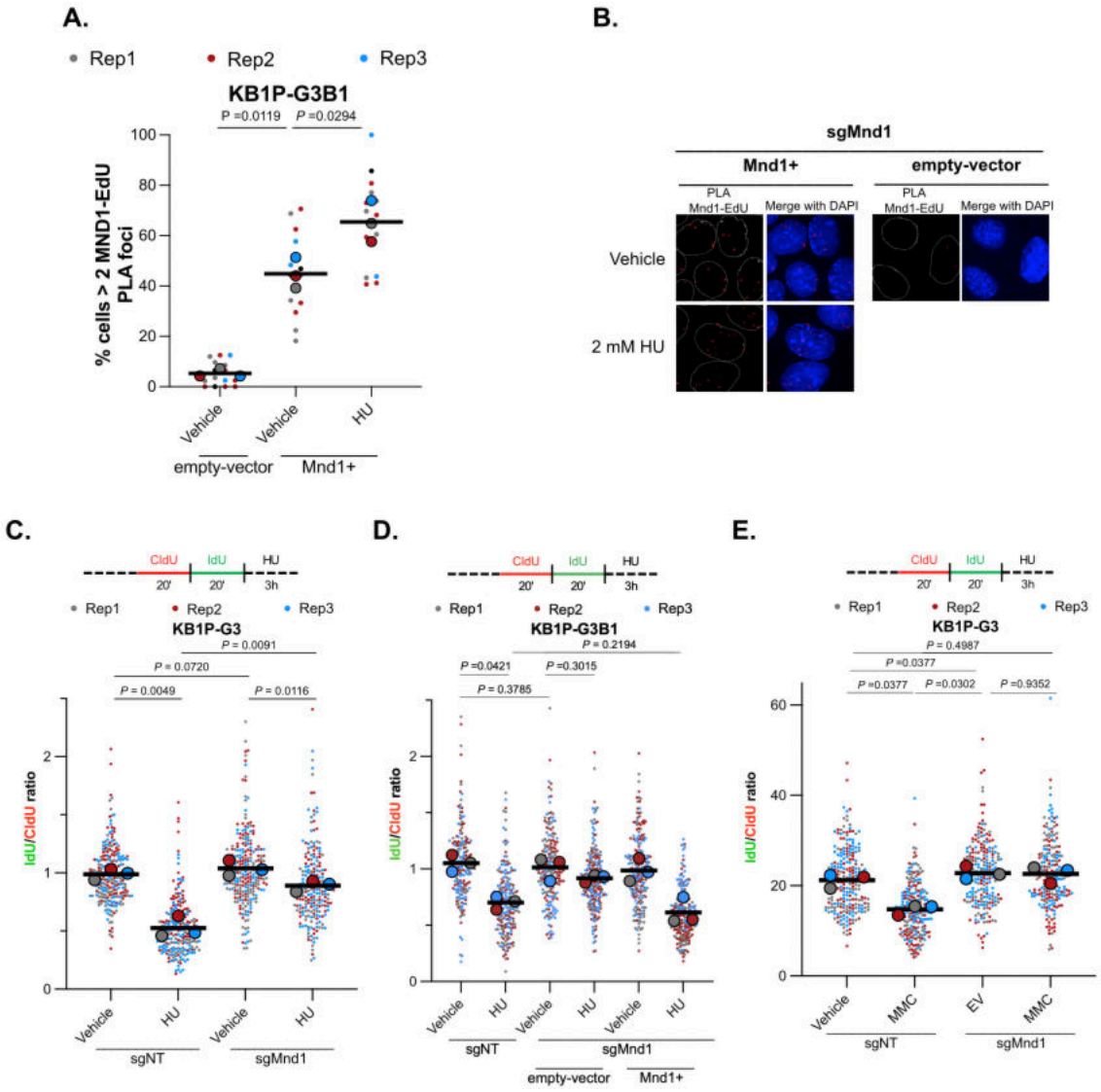

Figure 5.6 MND1/PSMC3IP contributes to RAD51 function at replication forks. **A, B.** Superplot of SIRF assay are shown of cells with >2 PLA foci, normalised to the total number of cells. Data generated by Paola Francica (A). Small dots represent data from each field of view with the colour corresponding to the biological replicate. Horizontal black line represents the mean of all the data, while large dots represent the mean of each biological replicate. *P*-values were calculated via two-tailed t-test using mean of each biological replicate (n=3). Representative images are shown (B) from quantification in (A). **C, D, E.** Schematic of DNA fibre assay, as described in (Schmid et al., 2018) with a few modifications (detailed in upper panels). Superplot showing quantification of IdU/CldU ratio of at least n=120 fibres per sample (lower panels). Small dots represent data from each fibre with the colour corresponding to the biological replicate. Horizontal black line represents the mean of all the data, while large dots represent the mean of each biological replicate. *P*-values were calculated via two-tailed t-test using mean of each biological replicate (n=3).

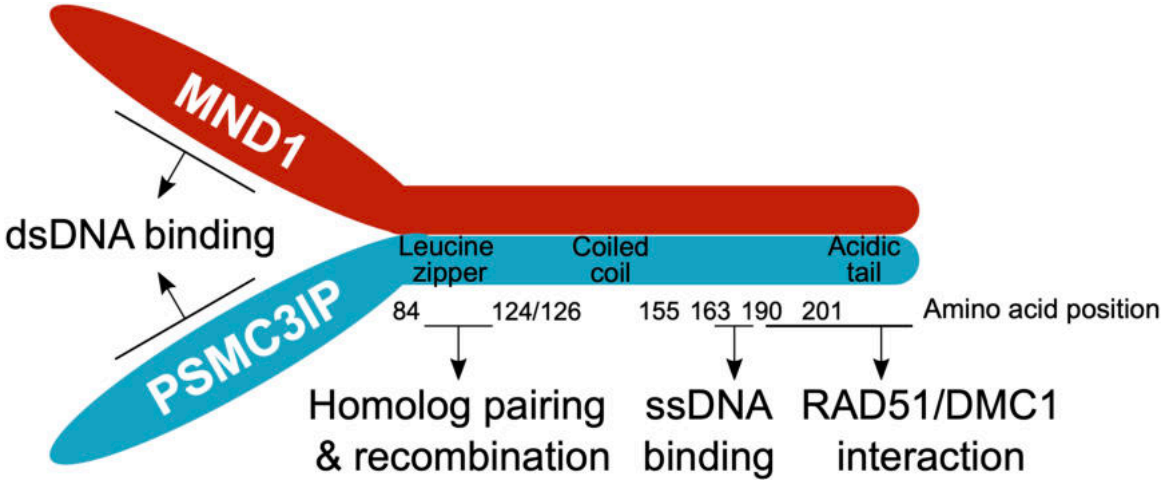

Figure 5.7 PSMC3IP-MND1 structure and function.
Amino acid position annotated with its respective function. dsDNA binding occurs within region 1-84. The leucine zipper region (84-124/126) is responsible for homolog pairing & recombination. Coiled-coil is contained within amino acids 124/126-155. Amino acid position 163-190 function involves ssDNA binding. 190-201 amino acid position, which comprises the acidic tail, is responsible for RAD51/DMC1 interaction; the PSMC3IP p.Glu201del mutation is within this region.

A specific mutation in *PSMC3IP* acidic tail (*PSMC3IP* p.Glu201del) has also been directly attributed to XX ovarian dysgenesis cases (Zhao et al., 2015), a condition characterised by the lack of spontaneous pubertal development, primary amenorrhea, uterine hypoplasia, and hypergonadotropic hypogonadism. By directly studying the effect of this *PSMC3IP* mutant in yeast, investigators from Patrick Sung's group were able to determine that the mutation resulted in abrogated RAD51/DMC1 interaction of PSMC3IP along with its heterodimer partner MND1. Given the clinical relevance of this mutation, I generated the model of this *PSMC3IP* mutant in a human model. Although the p.Glu201del mutation (in the C-terminus of *PSMC3IP*) does not diminish the interaction of the MND1/PSMC3IP heterodimer with DNA, the interaction with RAD51 is impaired, as is the ability to promote D-loop formation (Zhao & Sung, 2015). I found that re-expression of wild-type *PSMC3IP* reversed PARPi sensitivity in *PSMC3IP*-depleted cells, establishing causality of *PSMC3IP* in PARPi response (Figure 5.8). Interestingly, expression of a p.Glu201del mutant version of *PSMC3IP* did not demonstrate this phenotype, but rather further sensitised the cells to PARPi (Figure 5.8). Expression of the PSMC3IP p.Glu201del mutant also sensitised MCF10A *TP53*$^{-/-}$ cells with wild-type *PSMC3IP* to PARPi (Figure 5.8), which supports the conclusion that this mutation acting as a dominant negative (Zhao & Sung, 2015). Consistent with our aforementioned observation that PARPi sensitivity in *PSMC3IP*-mutant cells is associated with an increase in RAD51 foci, expression of *PSMC3IP* p.Glu201del resulted in increased RAD5 foci formation upon IR or PARPi treatment (Figure 5.9A, Figure 5.9C and Figure 5.10). A similar phenotype was observed with expression of PSMC3IP p.Glu201del in wild-type cells upon DNA damage (Figure 5.9A, Figure 5.9C and Figure 5.10), strengthening

our observations from the PARPi sensitivity assays that *PSMC3IP* p.Glu201del may be acting as a dominant negative mutation. The observed increase in RAD51 foci upon IR- or PARPi- exposure can be directly attributed to PSMC3IP, given that RAD51 return to wild-type levels with PSMC3IP reconstitution (Figure 5.9A, Figure 5.9C and Figure 5.10). As demonstrated in Figure 5.9B, Figure 5.9D and Figure 5.10, a corresponding increase in γH2AX foci was observed. Interestingly, we did not observe any difference in γH2AX foci between MND1/PSMC3IP defective cells and wild-type. Therefore, the *MND1* or *PSMC3IP* deficiency itself does not result in increased DNA lesions, rather deficiencies of these proteins result in failure to remove "toxic" RAD51 resulting from PARPi- or IR-exposure.

We hypothesised that the increased RAD51 nucleoprotein formation in *MND1* and *PSMC3IP* mutant cells exposed to PARPi might be the key cytotoxic event. Consistent with this, inhibition of RAD51 with the previously described RAD51 inhibitor B02, which inhibits the ssDNA and dsDNA binding and strand exchange activity of RAD51 (Huang et al., 2012; Huang et al., 2011), partially reversed the PARPi sensitivity phenotype in both *MND1* and *PSMC3IP* mutant cells (

Figure 5.11). Together, these data strongly suggest that the main control of PARPi response of the PSMC3IP-MND1 heterodimer in mitotic cells is due to its role in supporting RAD51-mediated D-loop formation.

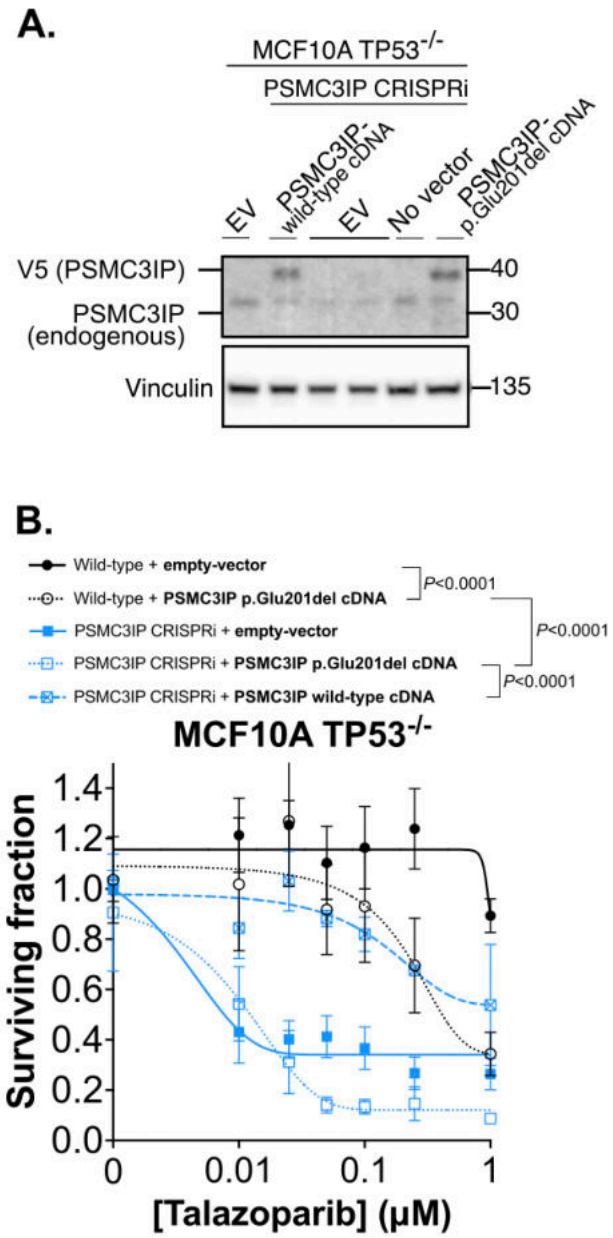

Figure 5.8 PARPi sensitivity observed in PSMC3IP-depleted cells is reversed by wild-type PSMC3IP, but not a p.Glu201del mutant.
A. Western blot image of MCF10A *TP53*$^{-/-}$ dCas9-KRAB cells (with or without sgRNA targeting *PSMC3IP*) with ectopic expression of either wild-type or p.Glu201del (D-loop mutant) PSMC3IP. Vinculin was used as a loading control. **B.** Dose/response survival curves are shown with surviving fractions at the indicated doses of talazoparib. MCF10A *TP53*$^{-/-}$ dCas9-KRAB cells expressing non-targeting control (wild-type) or sgRNA targeting *PSMC3IP* (PSMC3IP CRISPRi) were transduced with lentiviral constructs encoding expression vector containing *PSMC3IP* cDNA, either wild-type *PSMC3IP* (*PSMC3IP* wild-type cDNA) or *PSMC3IP* p.Glu201del (PSMC3IP D-loop mutant cDNA). Wild-type or PSMC3IP CRISPRi cells expressing empty-vector were used as controls. Cells were plated in 96-well plates and exposed to talazoparib for ten continuous days. Cell viability was quantified by CellTiter-Glo® and surviving fraction was calculated for each drug dose relative to DMSO-exposed cells. Error bars represent SD from n=3 replicates. *P*-values were calculated via ANOVA with Tukey's post-test.

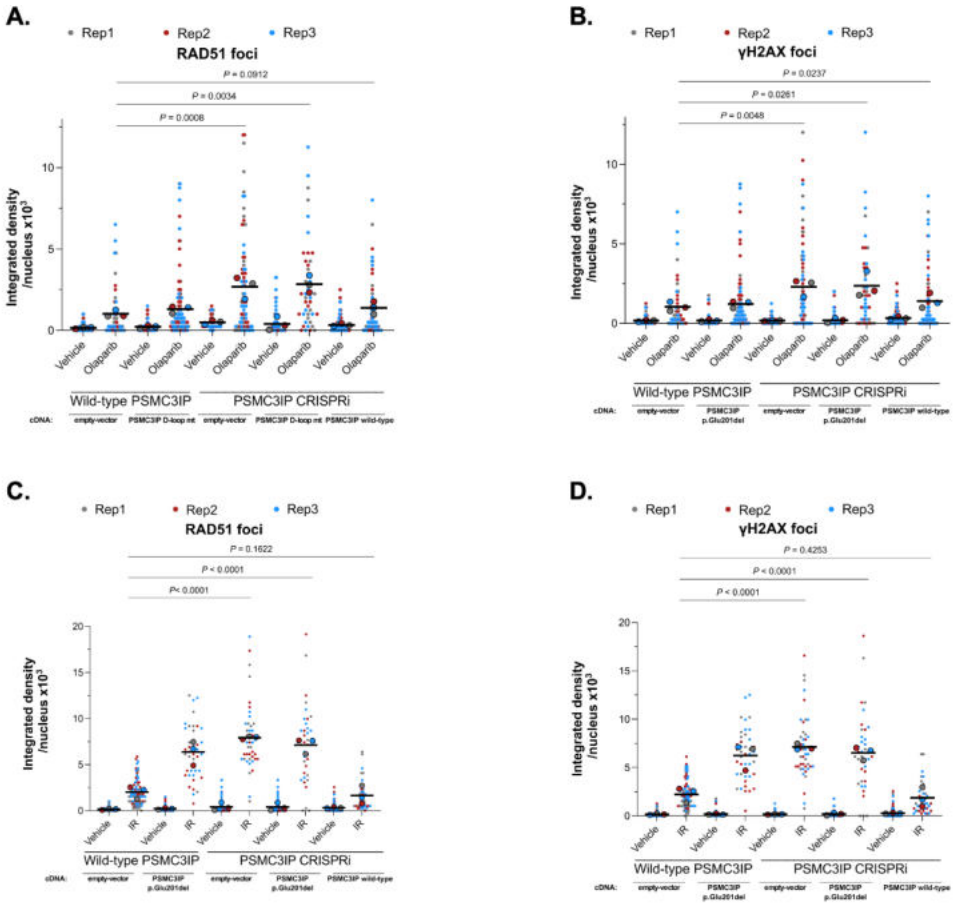

Figure 5.9 Elevated RAD51 foci observed in PSMC3IP-depleted cells was reversed by wild-type PSMC3IP but not a p.Glu201del mutant.

Superplot of RAD51 integrated density in each indicated cell line is shown. Cells were plated onto coverslips and either exposed to 10 μM olaparib and then fixed after 16 hours or 10 Gy IR and then fixed after 4 hours or remained untreated. Cells were co-stained with anti-RAD51 and anti-gH2AX antibodies. Small dots represent data from each nuclei with the colour corresponding to the biological replicate. Horizontal black line represents the mean of all the data, while large dots represent the mean of each biological replicate. Min. 13 nuclei were quantified per each biological replicate for olaparib and 11 for IR. *P*-values were calculated via two-tailed t-test using mean of each biological replicate (n=3).

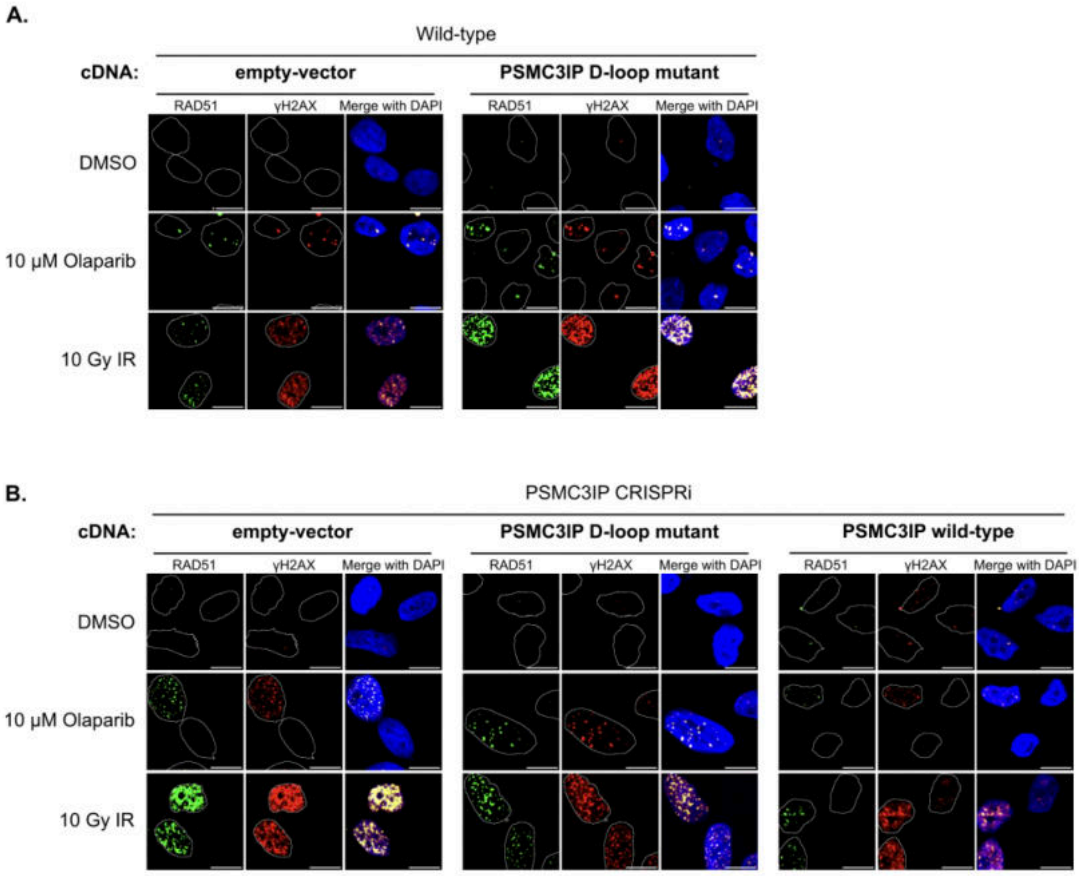

Figure 5.10 Elevated RAD51 foci observed in PSMC3IP-depleted cells was reversed by wild-type PSMC3IP but not a p.Glu201del mutant.
A, B. Representative images are shown of foci quantified in Figure 5.9 compared to wild-type cells (A), elevated RAD51 and γH2AX foci levels were observed in PSMC3IP CRISPRi cells (B) upon olaparib- or IR-exposure, which was partially reversed with expression of wild-type *PSMC3IP*, but not *PSMC3IP* p.Glu201del D-loop mutant. Cells were plated onto coverslips and either exposed to 10 μM olaparib and then fixed after 16 hours or 10 Gy IR and then fixed after 4 hours or remained untreated. Cells were co-stained with anti-RAD51 and anti-γH2AX antibodies.

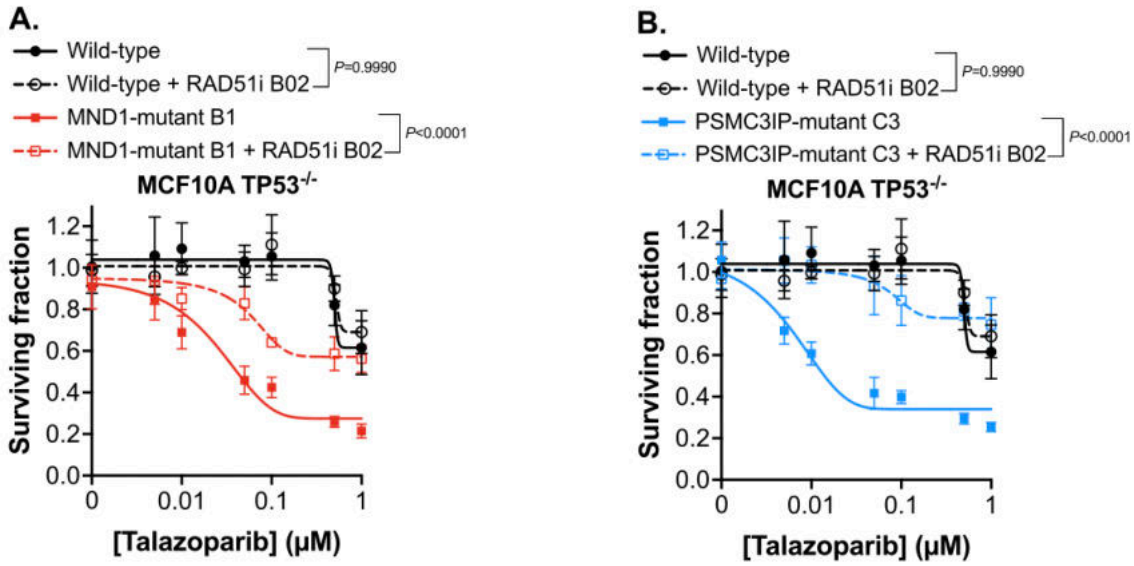

Figure 5.11 RAD51 inhibition reverses the PARPi sensitivity phenotype in MND1 and PSMC3IP defective cells.
RAD51 inhibition reverses the PARPi sensitivity phenotype in both *MND1* (A) and *PSMC3IP* (B) mutant cells. Dose/response survival curves are shown with surviving fractions at the indicated doses of talazoparib. Cells were plated in 384-well plates and exposed to 25 μM small molecule RAD51 inhibitor B02 for one hour prior to talazoparib addition. Cells were exposed to PARPi for five continuous days. Cell viability was quantified by CellTiter-Glo® and surviving fraction was calculated for each drug dose relative to DMSO-exposed cells. Error bars represent SD from n=3 replicates. *P*-values were calculated via ANOVA with Tukey's post-test.

5.3. Discussion

In this Chapter, I described functional experiments to identify the specific mode of action of MND1 and PSMC3IP on DNA repair. Although PSMC3IP-MND1 depleted cells were shown to accumulate toxic RAD51 foci in response to DNA damage, impaired homology-directed DNA repair was demonstrated via DR-GFP reporter assay and increased micronuclei formation. Identified interaction of MND1 at the RF led to DNA fibre experiments in which MND1 was demonstrated to contribute to RAD51 function at the replication. Subsequently, I observed that impaired D-loop formation may be responsible for the HR defect and toxic RAD51 foci formation in *MND1* or *PSMC3IP* defective cells. In totality, our experiments support the conclusion that PSMC3IP-MND1 may support RAD51-mediated D-loop formation in HR.

In a recent preprint, Koob et al. also observed increased RAD51 foci in *MND1*-defective cells compared to wild-type (Koob et al., 2023). Given that RAD51 foci formation is used as a surrogate marker for HR deficiency and PARPi response, whereby the inability to localise the DNA recombinase RAD51 to site of damage has classically been used to determine defective HR and predict PARPi sensitivity (Cruz et al., 2018; Llop-Guevara et al., 2021; van Wijk et al., 2020), our common observations are surprising. Our findings are reminiscent of the persistence of nuclear RAD51 foci in *PSMC3IP*-defective meiotic cells (Petukhova et al., 2003). As such, it would have been interesting to quantify the RAD51 foci over time following PARPi or IR-exposure, in order to assess the resolution of the RAD51 foci between the *MND1*- and *PSMC3IP*-defective cells compared to wild-type. This experiment could provide further evidence of defective HR

associated with *MND1* and *PSMC3IP* deficiency, if associated with slower RAD51 foci resolution. Given that the PSMC3IP-MND1 heterodimer provides support to both DNA recombinases, RAD51 and DMC1, to facilitate the homology search process and strand invasion (Chen et al., 2004; Tsubouchi & Roeder, 2002), it would have also been interesting to use an anti-DMC1 primary antibody. It has been suggested that DMC1 functions as the predominant strand exchange protein during meiosis (Cloud et al., 2012) to promote strand invasion, recombination between homologous chromosomes and crossing over (Hong et al., 2013; Schwacha & Kleckner, 1997). RAD51 has been shown to repair residual DSBs after recombination between homologous chromosomes and synapsis are complete in meiotic recombination (Cloud et al., 2012; Da Ines et al., 2013). After establishing whether DMC1 is indeed expressed in miotic cells, anti-DMC1 staining could have been applied to compare the number of DMC1 foci between wild-type and *MND1*- or *PSMC3IP*-mutant cells upon IR or PARPi.

The observed increase in γH2AX foci upon exposure to PARPi or IR in *MND1*- or *PSMC3IP*-defective cells in comparison to wild-type cells could be indicative of *MND1* or *PSMC3IP* deficiency, resulting in increased DNA lesions that require repair. Alternatively, it could be argued that this phenotype might be due to failure to remove RAD51 with *MND1*- or *PSMCIP*-deficiency. The distinction between these two possibilities is difficult to resolve. However, we have settled on a model where *MND1*/*PSMC3IP* defects do not themselves cause a profound increase in DNA lesions that require RAD51 for repair but, in cells exposed to PARPi, the lack of *MND1/PSMC3IP* causes the formation of “toxic” RAD51 (i.e., failure to remove RAD51). This is for a number of reasons, including: no detectable increase in

RAD51 or γH2AX foci were observed in the absence of PARPi or IR in the *PSMC3IP*- or *MND1*-defective cells; we were able to partially reverse the MND1/PSMC3IP *vs.* PARPi synthetic lethality by use of a small molecule that disrupts the interface between individual RAD51 monomers when arranged on a nucleoprotein filament. However, further experiments could be performed in attempt to address this point by staining for an additional marker of DNA damage, 53BP1 foci, using anti-53BP1 primary antibodies.

Within the HR pathway, I observed that that an impaired D-loop formation may be responsible for the HR defect and toxic RAD51 foci formation in *MND1*- or *PSMC3IP*-defective cells. This is based on experiments using the p.Glu201del mutant of *PSMC3IP*, a mutation that does not alter the interaction of the PSMC3IP-MND1 heterodimer with DNA but which does impair the interaction with RAD51 and its ability to promote D-loop formation (Zhao & Sung, 2015). In contrast to wild-type *PSMC3IP*, the p.Glu201del mutant does not recue PARPi-induced prolonged RAD51 foci formation and PARPi sensitivity. These conclusions are strengthened with our experiments demonstrating rescue of PARPi sensitivity of *PSMC3IP*-defective cells using small molecule RAD51 inhibitor, B02, which specifically inhibits ssDNA and dsDNA binding and strand exchange activity of RAD51. PARPi sensitivity of *MND1*-defective cells was also rescued with B02. Interestingly, this RAD51 inhibitor has been previously shown to increase PARPi sensitivity of HR-proficient TNBC cell lines, but not HR-proficient non-TNBC cell lines, such as MCF10A which is the main breast model used in this study (Shkundina et al., 2021). Zhao and Sung's publication regarding PSMC3IP p.Glu201del mutation is one of several studies to have described germline

PSMC3IP mutations in familial breast and ovarian cancers (Peng, Bakker, et al., 2013; Peng, Yang, et al., 2013; Yang et al., 2016). In fallopian tube cancer, Yang et al. identified *PSMC3IP* mutations resulting in defective alternative splicing, truncating the *PSMC3IP* open reading frame. Yang et al. also demonstrated that these identified *PSMC3IP* mutants act as a dominant negative to counteract wild-type *PSMC3IP* activity. In all splice variants identified, the open reading frame at the 3' half of *PSMC3IP* was undisrupted to permit the expression of the coiled-coil and acidic tail at the C-terminus by utilising an internal start codon ATG in exon 5, but the expression of N-terminal leucine zipper domain of *PSMC3IP* was not permissible. As demonstrated in a previous section of this thesis, this *PSMC3IP* leucine zipper domain is required for homolog pairing and recombination. Interestingly, RAD51 foci formation in these PSMC3IP splice variants was not induced upon IR, compared to wild-type cells (Peng, Yang, et al., 2013). Unlike the *PSMC3IP* mutant utilised in Yang et al.'s publication, the *PSMC3IP* leucine zipper domain, required for homolog pairing and recombination, was retained in the *PSMC3IP* p.Glu201del mutant utilised in this thesis, potentially explaining the reported differences in RAD51 foci induction between the two *PSMC3IP* mutants. As with Yang et al.'s *PSMC3IP* mutant, we found *PSMC3IP* p.Glu201del mutation to be dominant negative with regards to PARPi response; I observed that the *PSMC3IP* p.Glu201del mutant was also a lot more sensitive to PARPi compared to wild-type cells. In both these described mutants, *PSMC3IP* p.Glu201del used in this thesis and the *PSMC3IP* mutant utilised in Yang et al., the *PSMC3IP* N-terminus and coiled-coil domain is unaffected, which contain the regions which bind dsDNA and ssDNA, respectively. It would be interesting to assess the PARPi sensitivity of the clinically relevant *PSMC3IP* mutants identified by Yang et al. given

their lack of RAD51 foci upon exposure to DNA damage. The hypothesis that loss of either the RAD51 interaction and/or the inability to promote D-loop formation is the cause of PARPi sensitivity in PSMC3IP defective cells from experiments using the *PSMC3IP* p.Glu201del mutant is by inference (i.e., implied by *in vitro* assays described by Zhao and Sung), and not directly assessed in this thesis. Future experiments are required to specifically assay D-loop formation in *MND1*- or *PSMC3IP*-defective cells would be required in order to test this hypothesis. For instance, D-loop formation can be visualised using electron microscopy.

Although our experiments have established that PSMC3IP-MND1 may support RAD51-mediated D-loop formation in HR, the specific mechanism is yet to be determined.

Chapter 6. General Discussion

6.1. Summary of the work presented in this thesis

In summary, using CRISPR mutagenesis and interference screens, I identified *PSMC3IP* and *MND1* as determinants of PARPi sensitivity in mitotic cells. After establishing that PSMC3IP and MND1 are commonly expressed in mitotic tumour cells and human tumours, I validated the CRISPR screen results and then established that the PARPi and IR sensitivity in *MND1*/*PSMC3IP* defective cells was independent of a previously described role for PMSC3IP and MND1 in ALT. I demonstrated that *PSMC3IP*- or *MND1*-depleted cells accumulate toxic RAD51 foci in response to DNA damage, show impaired homology-directed DNA repair, and become PARPi sensitive. Although RF reversal was also affected in *PSMC3IP*- or *MND1*-depleted cells, the abrogated D-loop formation could be the major cause of PARPi sensitivity; a *PSMC3IP* p.Glu201del D-loop formation mutant associated with ovarian dysgenesis fails to reverse PARPi sensitivity, whereas expression of wild-type PSMC3IP in *PSMC3IP*-defective cells did. These observations are summarised in Figure 6.1, and suggest that meiotic proteins such as MND1 and PSMC3IP could have a greater role in mitotic cells in determining the response to therapeutic DNA damage.

6.2. Remaining questions

Overall, the data from this thesis contributes to the mechanistic understanding of how PARPi response is controlled. Although *MND1* and *PSMC3IP* are classically defined as meiosis-specific genes, my work indicates that both proteins control the DDR in mitotic cells via RAD51 nucleofilament-mediated D-loop formation. Several questions remain to be addressed regarding *MND1* and *PSMC3IP*, as well as “meiosis-specific” genes in general. These are discussed below.

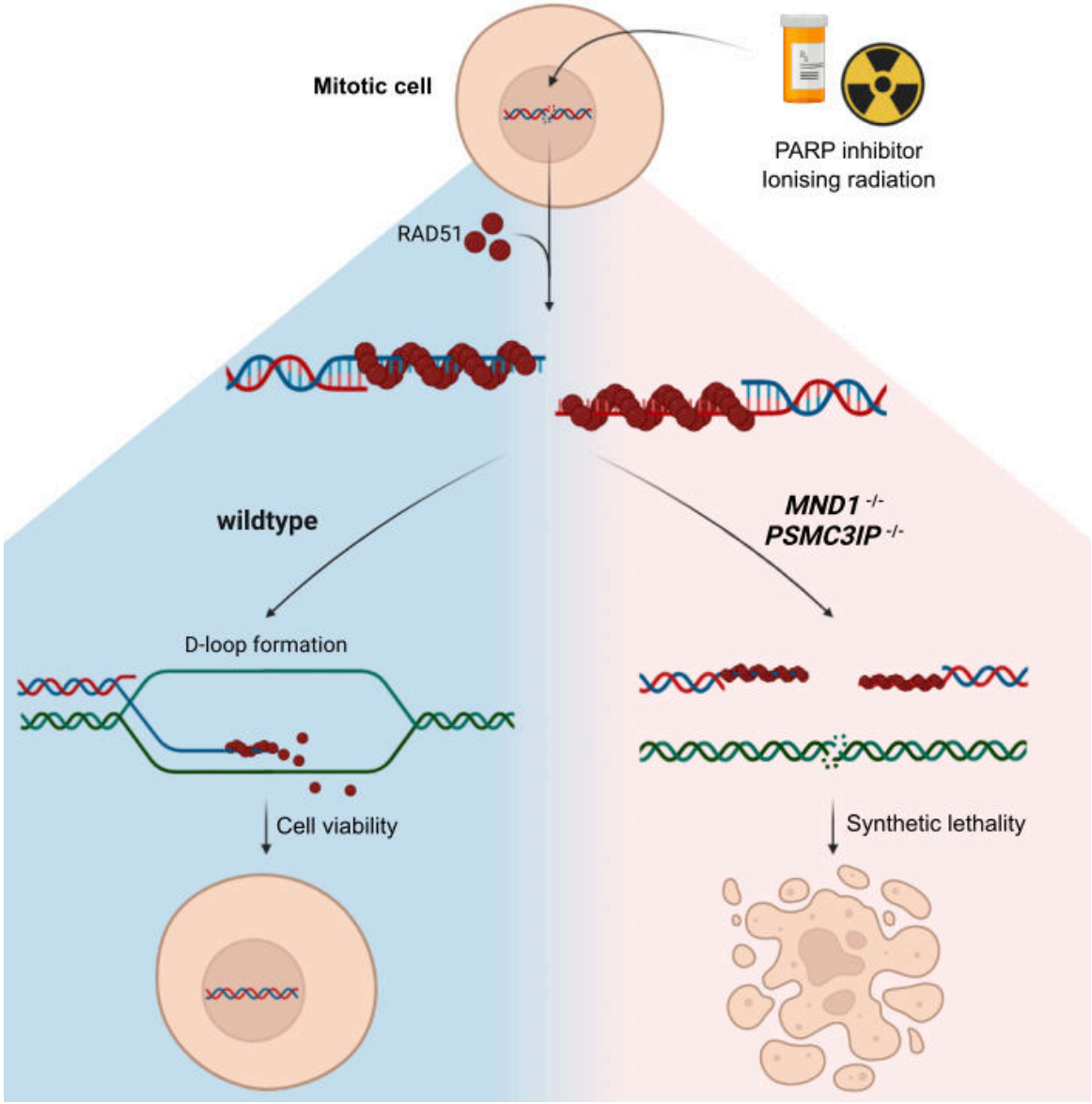

Figure 6.1 Hypothesised mechanism of synthetic lethality upon *MND1* or *PSMC3IP* loss leading to abrogated D-loop formation.
Upon DNA damage with PARP inhibitor or ionising radiation (IR) exposure, DNA repair is initiated with the resection of the double-strand break (DSB), followed by DNA recombination. In the wild-type situation, the RAD51-ssDNA filament performs homology search via D-loop formation, so the DNA damage can be repaired, and the cell survives. Experiments conducted in this thesis indicate that the absence of *MND1* or *PSMC3IP* abrogates D-loop formation. As such, DNA repair cannot be completed, resulting in synthetic lethality.

6.2.1. MND1/PSMC3IP expression in mitotic cells

We, and others, have provided initial evidence that both PSMC3IP and MND1 are expressed in tumour cell lines and tumours, beyond their classical meiotic-specific expression. In order to advance our understanding, it is crucial to investigate the expression patterns and the conditions under which MND1 and PSMC3IP are expressed in mitotic cells. For example, others have proposed that MND1 and PSMC3IP could be regarded as meiosis-specific cancer/testis (meiCT) antigens, and that cancer immunotherapy approaches could be designed to target tumour cells expressing these (Jay et al., 2021). My data suggests that mitotic cells, including non-tumour epithelial cells, (such as MCF10A) express MND1 and PSMC3IP, and use these to conduct HR. If MND1 and PSMC3IP are expressed in normal mitotic tissues (and used to conduct HR), such approaches could conceivably cause systemic toxicity. With this in mind, it seems sensible to therefore define MND1 and PSMC3IP expression at the protein level, in a panel of normal human tissues of different organ origins. Experimentally, antibodies targeting MND1 or PSMC3IP could be used to quantify protein expression in formalin-fixed paraffin embedded (FFPE) tissue sections. Alternatively, antibody free approaches such as the use of mass spec-based proteomics could be used.

6.2.2. Mechanism of dependency on MND1 and PSMC3IP for resistance to PARPi- and IR-induced DNA damage

In this thesis, I established the role of MND1 and PSMC3IP in somatic HR after PARPi- and IR-induced DNA damage in tumour cells, but also in non-tumour cells, such as immortalised breast epithelial cells. My existing data suggests that in mitotic cells, inhibition of RAD51 reverses PARPi sensitivity in *PSMC3IP*-defective

cells and that whilst wild-type PSMC3IP reverses PARPi sensitivity, a PSMC3IP mutant that is known to be defective in D-loop formation (Zhao & Sung, 2015) does not.

Consistent with the previously described important functions of *PSMC3IP* in meiosis, orthologs has been identified in many species in addition to *Homo sapiens*. As demonstrated in Figure 6.2, these species include eukaryotic model organisms *Mus musculus, Danio rerio, Arabidopsis thaliana, Saccharomyces cerevisiae*, and there can be a high degree of PSMC3IP amino acid conservation with *Homo sapiens*; for instance 88.0% identity with *Mus musculus* (mouse). Interestingly, Psmc3ip is not conserved in *Sordaria macrospora*, *Drosophila melanogaster* and *Caenorhabditis elegans*, which also lack *Dmc1* but possess functional *Rad51* (de Massy, 2013). Despite the absence of *Dmc1, Mnd1* and *Psmc3ip,* these organisms are still capable of meiotic recombination and completing meiosis. Perhaps these organisms do not require as much support for strand exchange, or RAD51 is able to compensate for function of these lacking proteins. However, the precise molecular mechanisms and the specific proteins or mechanisms utilised in these organisms, in contrast to those possessing Mnd1 and Psmc3ip, have not been fully elucidated. Further exploration of these differences would be intriguing and may provide valuable insights into fully elucidating the roles of MND1 and PSMC3IP in meiosis.

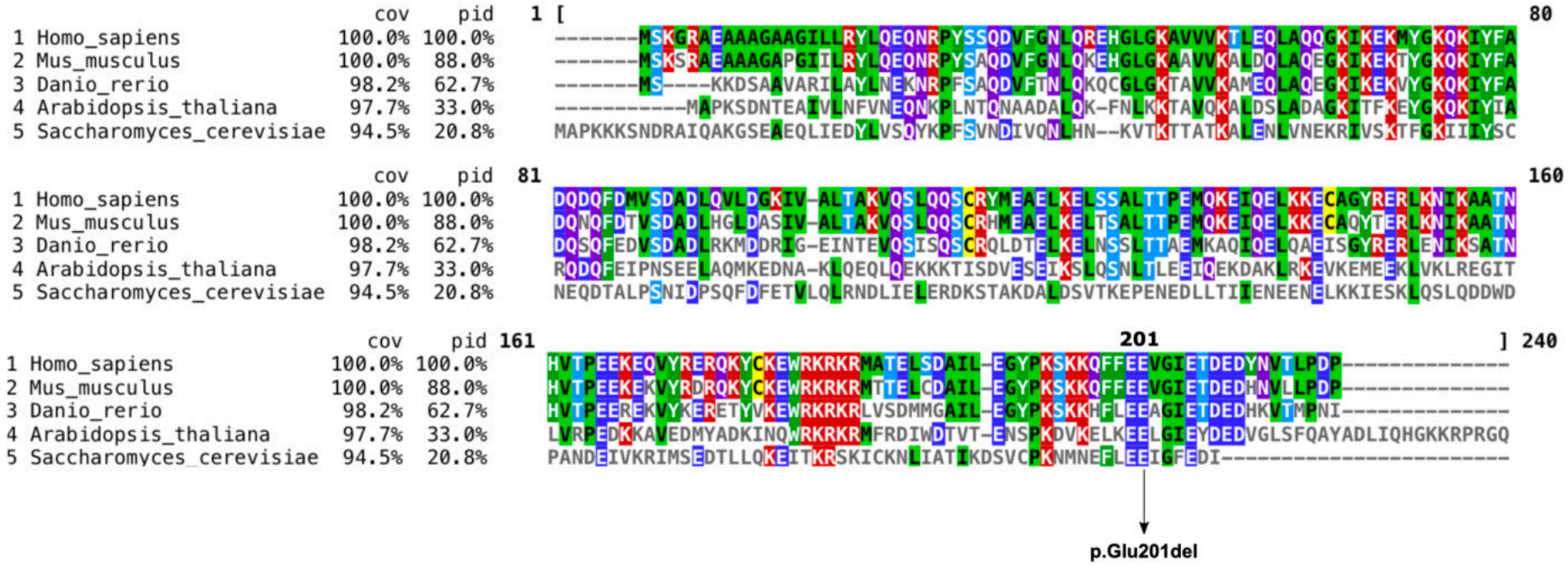

Figure 6.2 Conservation analysis of PSMC3IP between model species.
PSMC3IP homologs from different species are aligned to Homo sapiens to highlight evolutionary conservation. Aligned sequences from species include *Homo sapiens*, *Mus musculus*, *Danio rerio*, *Arabidopsis thaliana* and *Saccharomyces cerevisiae*. Amino acid positions are depicted in black above the alignments, with special annotation for the human p.Glu201del 'D-loop mutant'. Percent coverage (cov) and percent identity (pid) values are calculated with respect to the Homo sapiens reference sequence. Coverage (cov) is calculated as the ratio of the number of residues in a row aligned with a reference row to the length of the ungapped reference row, multiplied by 100. Percentage identity (pid) is calculated as the ratio of the number of identical residues to the length of the ungapped reference row over the aligned region, multiplied by 100. Coloured by identity.

Further experimental work is required in order to conclusively determine whether RAD51 inhibition does indeed reverse the PARPi sensitivity in *PSMC3IP*- or *MND1*-defective cells. The lack of PARPi sensitivity in the BO2-treated wild-type MCF10A TP53$^{-/-}$ cells could be attributed to suboptimal BO2 concentration, possibly leading to insufficient reduction of RAD51 foci levels, and therefore cell viability. Given the HR-proficient nature of wild-type MCF10A TP53$^{-/-}$ cells, they are inherently very resistant to PARPi, especially compared to the *MND1*- and *PSMC3IP*-defective cells. The PARPi doses used in this dose-response experiment might not have been high enough to demonstrate the window of PARPi sensitivity in the wild-type cells. Therefore, the lack of PARPi sensitivity of the BO2-treated wild-type MCF10A cells could be due to insufficient PARPi and/or BO2 concentration used. Assessment of RAD51 foci formation in this context of PARPi dose-response exposure, with dose titration of the RAD51 inhibitor (BO2), is required to optimise the BO2 and PARPi concentrations required for this experiment. MCF10A TP53$^{-/-}$ cells would need to be plated onto coverslips, then pre-treated with various concentrations of BO2 (e.g., 0, 5, 10, 25, 50, 100 μM) for 1 hour. One set of coverslips for each BO2 concentration would then be exposed overnight to the talazoparib doses used in Figure 5.11 (0, 0.01, 0.1, 1 μM), while the other set would remain unexposed to PARPi. Following fixation, immunofluorescence microscopy would be used to assess which doses of BO2 do indeed inhibit RAD51 foci formation, as well as the minimum BO2 dose at which this is achieved – both with and without PARPi. Ideally, this experiment should be performed in the wild-type cells, as well as the *MND1*- and *PSMC3IP*-mutant MCF10A TP53$^{-/-}$ cells, which could provide further insight as to why BO2-treated wild-type MCF10A cells were not sensitive to PARPi.

Further experimental work is also required in order to conclusively determine whether RAD51 foci are indeed elevated in *PSMC3IP*- or *MND1*-defective cells compared to wild-type in response to genotoxic stress. All RAD51 foci experiments were performed in asynchronous cells, and the cell cycle profiles of the different cell models were not characterised. The cell cycle is an important consideration since this can impact the interpretation of RAD51 foci data. RAD51 foci levels vary across different cell cycle phases. During G1 phase, RAD51 foci levels are generally low due to the quiescent state of the cells. As cells progress into S phase, RAD51 foci levels increase as RAD51 is recruited for HR-mediated repair of DNA damage which occurs during DNA replication. RAD51 foci levels remain elevated during G_2 phase due ongoing repair of lesions generated during DNA replication as the cells prepare for subsequent cell division. During mitosis, RAD51 foci levels decrease due to inhibition of HR to prevent inappropriate recombination events that could lead to genomic instability (Chen et al., 1997; Flygare et al., 1996; Yamamoto et al., 1996). In order to account for the variability in RAD51 foci levels at different phases of the cell cycle, characterisation of the cell cycle profiles of the isogenic cell models using the method of flow cytometry could be performed. This approach involves blocking the cells in specific cell cycle phases, staining them with a DNA-specific fluorescent dye, such as propidium iodide, and using flow cytometry to analyse the DNA content of the stained cells. By assessing RAD51 foci levels in response to genotoxic stress at various timepoints throughout the synchronised cell cycle, it will be possible to determine if the observed elevated RAD51 foci levels, particularly four hours post-genotoxic stress, are influenced by the S and G_2 phases when RAD51 foci levels are typically higher. Furthermore, optimisation of IR and PARPi doses is necessary to ensure the induction of RAD51

foci without overwhelming the cells with excessive genotoxic stress. Additionally, assessing RAD51 foci persistence and the kinetics of foci formation and resolution in both synchronous and asynchronous cells is crucial. By comparing RAD51 foci kinetics between the isogenic cell models, valuable insights can be gained regarding the functional significance of *MND1* and *PSMC3IP* in HR-mediated DNA repair. Specifically, analysing the efficiency and speed of HR repair can provide a deeper understanding of the roles played by these genes. Notably, the presence of prolonged RAD51 foci may indicate the persistence of DNA damage or impaired HR processes, highlighting potential consequences associated with the deficiency of these genes.

Although further experiments could be performed in future, the present data in its totality suggests that PSMC3IP-MND1 function in mitotic cells might be similar to that in meiotic cells, which is in RAD51-mediated D-loop formation and filament stabilisation, although this remains to be directly assessed. For instance, D-loop formation can be visualised using electron microscopy. The defective RAD51-mediated HR in *MND1*/*PSMC3IP*-deficient cells might also render cells to be more reliant on RAD51-independent forms of repair, including SSA and MMEJ. In order to assess this, inhibitors of MMEJ and SSA could be used. For example, DNA Polymerase Theta (Polθ), which is encoded by the POLQ gene, is a DNA repair helicase/polymerase that plays a key role in MMEJ (Roerink et al., 2014; Wyatt et al., 2016). A recently reported allosteric inhibitor of Polθ, ART558 (Zatreanu et al., 2021), could be used to assess whether the PARPi sensitivity of *MND1*- or *PSMC3IP*-deficient cells is altered by MMEJ inhibition, or whether the absence of MND1 or PSMC3IP makes cells Polθ-dependent. Alternatively,

additional genetic perturbation experiments could be used to better understand the molecular mechanism of the synthetic lethal effects I have seen. For example, in Chapter 5, I showed that partial inhibition of RAD51 partially reverses the PARPi synthetic lethality of PSMC3IP defective cells; on this basis a suppressor CRISPR screen approach could be used to identify other genes that reverse the PARPi synthetic lethality of the same cells. This experiment could be performed in an isogenic background, using the *PSMC3IP*- or *MND1*-deficient models generated in this thesis using the PARP inhibitors olaparib and talazoparib as selective agents. Alternatively, mass spectrometry could also be performed in this isogenic background for MND1 or PSMC3IP with PARPi. This approach could identify proteins enriched in *MND1*- or *PSMC3IP*-deficient cells upon PARPi exposure, in comparison to wild-type cells.

The proposed future suppressor CRISPR screen would ideally include technical replicates since the absence of technical replicates for the CRISPR screens presented in this thesis represents a noteworthy limitation in the study. Incorporating technical replicates is crucial for several reasons. Firstly, it accounts for inherent biological variability, as individual cells or organisms within a population can respond differently to genetic perturbations. The distinction of authentic genetic effects from random fluctuations is facilitated by the use of replicates. Secondly, technical variability, introduced by experimental procedures, reagents, and instruments, is controlled by replicates to ensure that observed effects are not merely artefacts of the experimental process. Furthermore, noise reduction in the CRISPR screens, which are particularly susceptible to various sources of noise that can affect the data, is achieved by averaging out this noise

through replicates, resulting in more reliable and precise measurements. Replicates are also required for robust statistical analysis for an adequate sample size to calculate measures of variability and significance of the results. True hits are distinguished from false positives, as consistent effects across replicates validate genuine genetic effects. The inclusion of replicates allows for result validation, reproducibility, and increased confidence in the findings, thus strengthening the overall validity of the conclusions. Finally, replicates also enable the assessment of the consistency of genetic effects, leading to more accurate interpretations and insights into gene function and biological mechanisms.

6.2.3. Types of DNA lesions that require MND1 and PSMC3IP for repair

What is not clear is why mitotic cells co-opt parts of the meiotic DNA recombination machinery (MND1 and PSMC3IP) to repair IR- or PARPi-induced DNA damage. Several possible scenarios exist, including: (i) MND1 and PSMC3IP participate in all RAD51-mediated HR reactions in mitotic cells; (ii) MND1 and PSMC3IP are involved in a particular subset of RAD51-mediated HR reactions in mitotic cells, such as those involving PARPi- or IR-induced lesions; or (iii) MND1 and PSMC3IP are involved in a particular subset of RAD51-mediated HR reactions in mitotic transformed cells (all of the cells used in my work were either tumour cell lines or partially transformed cells such as MCF10A cells with a *TP53* mutation). In Chapter 5, I demonstrated that loss of *MND1* or *PSMC3IP* impairs the repair of a DR-GFP synthetic HR reporter substrate, where a blunt ended DSB in GFP is caused by expression of a restriction endonuclease; this suggests that the role of MND1 and PSMC3IP in HR is not restricted to the repair of PARPi- or IR-induced DNA lesions. However, the DR-GFP assay used in this thesis lacked an RPF transfection

control, necessitating consideration of the resulting limitations. Firstly, data interpretation becomes complicated, as changes in DNA repair efficiency cannot be distinguished from variations in transfection efficiency or cell viability, potentially leading to misleading interpretations. Conversely, inclusion of a RFP transfection control would allow these variations in transfection efficiency or cell viability to be accounted for during data analysis, leading to more accurate estimations of DNA repair efficiency. Secondly, the absence of a transfection control hampers comparability with other studies that have appropriately incorporated such controls, impacting validation and reproducibility. The omission of a transfection control also raises questions about the internal validity of the experimental design. Ultimately, concluding that observed effects directly result from the intended experimental manipulations becomes challenging without proper controls.

The line of investigation that HR is not restricted to the repair of PARPi- or IR-induced DNA lesions could be extended. Further drug sensitivity assays with additional DNA damaging agents could be performed using the cell models generated in this thesis. For instance, the sensitivity of the *MND1*- and *PSMC3IP*-defective models could be assessed with agents that impair the progression of RFs, such as HU, aphidocolin, camptothecin, cisplatin and MMC. In addition, these agents impair the progression of RFs via varying mechanisms, which could allow further refinement of a potential mechanism of action for PSMC3IP-MND1. For example, HU stalls RFs by limiting the synthesis of deoxyribonucleotides (Fong et al., 2009), which is distinct from platinum salt-mediated mechanism of RF function impairment via cross-linking DNA (Faivre et al., 2003). The trapping of PARP1 on DNA, the main source of PARPi-induced cytotoxicity, results in DNA damage

associated with the RF, including impairment of nascent DNA strand maturation (Vaitsiankova et al., 2022). Alternatively, Cas9 genomic editing could be used to generate different forms of DSB in *MND1*- or *PSMC3IP*-defective cells and the repair of these DSBs could be assessed.

6.2.4. Effect of inappropriate PSMC3IP and MND1 expression on HR

In this thesis, I have focused on the consequences of *MND1*- and *PSMC3IP*-deficiency on PARPi sensitivity, and ultimately HR. Although the PARPi sensitivity phenotype is a window into the roles of MND1/PSMC3IP in mitosis, it is not clear whether loss of these genes in tumours would represent a practical clinical biomarker of PARPi sensitivity. Indeed, PSMC3IP is amplified and overexpressed in a fraction of basal-like TNBC tumours with a particular mutational signature characterised by allelic-imbalance genomic copy number alterations (Watkins et al., 2015) and therefore, assessing the effects of their overexpression might be more clinically relevant. For example, it would be interesting to assess whether increased activity of MND1 and PSMC3IP would allow tumour cells to tolerate PARPi-induced DNA damage, and potentially act as a mechanism of therapeutic resistance. Given that MND1 and PSMC3IP function as a heterodimer, it could be the case that their dual overexpression is required to enact any increased PSMC3IP function. Upregulated MND1 mRNA expression has also been demonstrated in HGSOC tumours compared to normal tissue (Yeganeh et al., 2017). TNBC and HGSOC show some similarities, in terms of their genome instability phenotype, frequent loss of HR genes, TP53 mutations and copy number alteration landscape; thus adapting to an underlying genome instability may be an important survival requirement for these tumour cells (Hoppe et al., 2018; Lord &

Ashworth, 2017). Perhaps the upregulated expression of MND1 and PSMC3IP in tumours allows their adaptations to deleterious DNA lesions, that would normally invoke HR. Alternatively, it could be the case that MND1/PSMC3IP dual overexpression also drives PARPi sensitivity and HR deficiency. For example, it could be the case that inappropriate expression of MND1/PSMC3IP (i.e., too little or too much) results in HR deficiency. Future experiments to assess the effect of MND1 and/or PSMC3IP overexpression on PARPi response would involve the expression of MND1 and/or PSMC3IP cDNA into wild-type cell lines and carrying out a dose-response survival assays in the presence of PARPi. It would also be interesting to assess RAD51 foci formation and resolution upon PARPi exposure in these cell models of PSMC3IP and/or MND1 overexpression to assess their effects on RAD51-mediated HR more directly.

6.3. Involvement of meiosis genes in somatic HR

My observations indicating the involvement of PSMC3IP and MND1 in somatic HR complement the wider literature indicating that other meiotic proteins could be involved in the DDR of mitotic cancer cells. The most well-characterised of these in HR and cancer is HORMAD1. As mentioned in the introduction section of this thesis, HORMAD1 supports the activity of SPO11 to induce the DSBs required to initiate meiotic HR. RAD51 engagement with sister chromatids, which is the preferred template for somatic HR, is inhibited by HORMAD1 to promote DMC1 activity, an interhomolog-acting DNA recombinase (Niu et al., 2005). PSMC3IP-MND1 further supports DMC1 during this process to orchestrate the localisation of DMC1 on the ssDNA (Zhao et al., 2015) and bring the chromosome homologs in close juxtaposition together (Chen et al., 2004; Pezza et al., 2007). Several groups have identified upregulation of HORMAD1 in cancer, such as

luminal breast (Adelaide et al., 2007), triple-negative breast (Chen et al., 2019; Watkins et al., 2015) and lung (Gao et al., 2018; Nichols et al., 2018), HORMAD1 overexpression results in suppressed RAD51-mediated HR in a panel of TNBC cell lines (Watkins et al., 2015). Correspondingly, enhanced sensitivity to HR defect-targeting agents, such as the PARPi olaparib and talazoparib, was demonstrated in TNBC cell lines upon HORMAD1 overexpression (Watkins et al., 2015). Two distinct studies subsequently contradicted the findings from Watkins et al., whereby HORMAD1 was shown to stimulate HR in lung adenocarcinoma models (Gao et al., 2018; Nichols et al., 2018). HORMAD1 loss was found to enhance IR, camptothecin and PARPi sensitivity. Gao et al. also demonstrated colocalisation of HORMAD1 with the DSB marker γH2AX in response to IR (Gao et al., 2018). The somewhat conflicting data regarding HORMAD1 influence on HR, may be due to inconsistencies in tissue-specific expression of HR pathway regulators targeted by HORMAD1. As such, influence of meiotic genes, such as *HORMAD1* or *MND1*/*PSMC3IP*, on HR may vary between different cancer types, which warrants delineation in future experiments. The common underlying functions of HORMAD1, DMC1 and MND1/PSMC3IP, and even SPO11, in meiotic HR is to promote recombination between homologs, rather than sister chromatids. As such, these proteins could be mediating a similar function in somatic cancer cells, therefore influencing mitotic HR. The reason for their expression in cancer cells is not known. Perhaps cancer cells have an advantage of using homolog rather than sister chromatid for repair. Perhaps there might be reduced energy associated with the meiotic mechanism of HR, whereby a homologous sequence is used as a template, so could be advantageous for cancer cells over the use of the sister chromatid as a template during HR. Experiments conducted in meiotic oocyte cells indicate that

in the absence of *HORMAD1*, increased SCE occurs, supporting the previously described conclusions (Shin et al., 2013). These findings evidence the role of *HORMAD1* to promote repair between homologs, rather than sister chromatids (Latypov et al., 2010). Future experiments would involve determining the CO frequency of human cells which are mutated for *HORMAD1*, *PSMC3IP*, *MND1*, *SPO11* and *DMC1*, in comparison to wild-type cells, via SCE assay. In order to really understand the contribution of meiotic genes, they must be studied in totality, rather than in isolation. Our improved understanding of mitotic HR could help improve our understanding of how these DNA damaging agents are directed for cancer treatment, such as PARPi, in the clinic.

6.4. Final conclusions and future impact

In this thesis, I described how both pre-clinical and clinical studies have not only enhanced our understanding of how PARPi work, but also the most appropriate use of these agents. As a result of these findings, PARPi represent the first DDR-targeting agents approved as anti-cancer therapies. However, PARPi resistance represents a major clinical problem and so understanding how cells respond to PARPi is critical.

Our improved understanding of which genes are involved in HR could further refine the patient criteria for PARPi treatment to potentially include further patients who, under current guidelines, are currently not eligible to receive PARPi. Our improved understanding could also circumvent the problem of PARPi resistance. In contrast to the findings of previous genetic screens, we have reported highly penetrant determinants of PARPi sensitivity, *MND1* and *PSMC3IP*, which were previously thought to be restricted to meiosis. Ultimately, this thesis has contributed to the current knowledge regarding genes which are involved PARPi response, and ultimately in the DDR. Although my experiments focused on *PSMC3IP-MND1*, perhaps many other genes which have been classically associated with meiotic HR, may in fact also have roles in somatic DNA repair, in cancer cells or perhaps even in untransformed cells.

References

Abida, W., Campbell, D., Patnaik, A., Shapiro, J. D., Sautois, B., Vogelzang, N. J., Voog, E. G., Bryce, A. H., McDermott, R., Ricci, F., Rowe, J., Zhang, J., Piulats, J. M., Fizazi, K., Merseburger, A. S., Higano, C. S., Krieger, L. E., Ryan, C. J., Feng, F. Y., Chowdhury, S. (2020). Non-BRCA DNA Damage Repair Gene Alterations and Response to the PARP Inhibitor Rucaparib in Metastatic Castration-Resistant Prostate Cancer: Analysis From the Phase II TRITON2 Study. *Clin Cancer Res*, *26*(11), 2487-2496. https://doi.org/10.1158/1078-0432.CCR-20-0394

Adelaide, J., Finetti, P., Bekhouche, I., Repellini, L., Geneix, J., Sircoulomb, F., Charafe-Jauffret, E., Cervera, N., Desplans, J., Parzy, D., Schoenmakers, E., Viens, P., Jacquemier, J., Birnbaum, D., Bertucci, F., & Chaffanet, M. (2007). Integrated profiling of basal and luminal breast cancers. *Cancer Res*, *67*(24), 11565-11575. https://doi.org/10.1158/0008-5472.CAN-07-2536

Afghahi, A., Timms, K. M., Vinayak, S., Jensen, K. C., Kurian, A. W., Carlson, R. W., Chang, P. J., Schackmann, E., Hartman, A. R., Ford, J. M., & Telli, M. L. (2017). Tumor BRCA1 Reversion Mutation Arising during Neoadjuvant Platinum-Based Chemotherapy in Triple-Negative Breast Cancer Is Associated with Therapy Resistance. *Clin Cancer Res*, *23*(13), 3365-3370. https://doi.org/10.1158/1078-0432.CCR-16-2174

Aguilar-Quesada, R., Munoz-Gamez, J. A., Martin-Oliva, D., Peralta, A., Valenzuela, M. T., Matinez-Romero, R., Quiles-Perez, R., Menissier-de Murcia, J., de Murcia, G., Ruiz de Almodovar, M., & Oliver, F. J. (2007). Interaction between ATM and PARP-1 in response to DNA damage and sensitization of ATM deficient cells through PARP inhibition. *BMC Mol Biol*, *8*, 29. https://doi.org/10.1186/1471-2199-8-29

Aguirre, A. J., Meyers, R. M., Weir, B. A., Vazquez, F., Zhang, C. Z., Ben-David, U., Cook, A., Ha, G., Harrington, W. F., Doshi, M. B., Kost-Alimova, M., Gill, S., Xu, H., Ali, L. D., Jiang, G., Pantel, S., Lee, Y., Goodale, A., Cherniack, A. D., . . . Hahn, W. C. (2016). Genomic Copy Number Dictates a Gene-Independent Cell Response to CRISPR/Cas9 Targeting. *Cancer Discov*, *6*(8), 914-929. https://doi.org/10.1158/2159-8290.CD-16-0154

Al-Zain, A. M., & Symington, L. S. (2021). The dark side of homology-directed repair. *DNA Repair (Amst)*, *106*, 103181. https://doi.org/10.1016/j.dnarep.2021.103181

Alkan, F., Wenzel, A., Anthon, C., Havgaard, J. H., & Gorodkin, J. (2018). CRISPR-Cas9 off-targeting assessment with nucleic acid duplex energy parameters. *Genome Biol*, *19*(1), 177. https://doi.org/10.1186/s13059-018-1534-x

Andegeko, Y., Moyal, L., Mittelman, L., Tsarfaty, I., Shiloh, Y., & Rotman, G. (2001). Nuclear retention of ATM at sites of DNA double strand breaks. *J Biol Chem*, *276*(41), 38224-38230. https://doi.org/10.1074/jbc.M102986200

Arias-Lopez, C., Lazaro-Trueba, I., Kerr, P., Lord, C. J., Dexter, T., Iravani, M., Ashworth, A., & Silva, A. (2006). p53 modulates homologous recombination by transcriptional regulation of the RAD51 gene. *EMBO Rep*, *7*(2), 219-224. https://doi.org/10.1038/sj.embor.7400587

Audeh, M. W., Carmichael, J., Penson, R. T., Friedlander, M., Powell, B., Bell-McGuinn, K. M., Scott, C., Weitzel, J. N., Oaknin, A., Loman, N., Lu, K., Schmutzler, R. K., Matulonis, U., Wickens, M., & Tutt, A. (2010). Oral poly(ADP-ribose) polymerase inhibitor olaparib in patients with BRCA1 or BRCA2 mutations and recurrent ovarian cancer: a proof-of-concept trial. *Lancet*, *376*(9737), 245-251. https://doi.org/10.1016/S0140-6736(10)60893-8

Bajrami, I., Frankum, J. R., Konde, A., Miller, R. E., Rehman, F. L., Brough, R., Campbell, J., Sims, D., Rafiq, R., Hooper, S., Chen, L., Kozarewa, I., Assiotis, I., Fenwick, K., Natrajan, R., Lord, C. J., & Ashworth, A. (2014). Genome-wide profiling of genetic synthetic lethality identifies CDK12 as a novel determinant of PARP1/2 inhibitor sensitivity. *Cancer Res*, *74*(1), 287-297. https://doi.org/10.1158/0008-5472.CAN-13-2541

Banin, S., Moyal, L., Shieh, S., Taya, Y., Anderson, C. W., Chessa, L., Smorodinsky, N. I., Prives, C., Reiss, Y., Shiloh, Y., & Ziv, Y. (1998). Enhanced phosphorylation of p53 by ATM in response to DNA damage. *Science*, *281*(5383), 1674-1677. https://doi.org/10.1126/science.281.5383.1674

Barazas, M., Annunziato, S., Pettitt, S. J., de Krijger, I., Ghezraoui, H., Roobol, S. J., Lutz, C., Frankum, J., Song, F. F., Brough, R., Evers, B., Gogola, E., Bhin, J., van de Ven, M., van Gent, D. C., Jacobs, J. J. L., Chapman, R., Lord, C. J., Jonkers, J., & Rottenberg, S. (2018). The CST Complex Mediates End Protection at Double-Strand Breaks and Promotes PARP Inhibitor Sensitivity in BRCA1-Deficient Cells. *Cell Rep*, *23*(7), 2107-2118. https://doi.org/10.1016/j.celrep.2018.04.046

Barazas, M., Gasparini, A., Huang, Y., Kucukosmanoglu, A., Annunziato, S., Bouwman, P., Sol, W., Kersbergen, A., Proost, N., de Korte-Grimmerink, R., van de Ven, M., Jonkers, J., Borst, G. R., & Rottenberg, S. (2019). Radiosensitivity Is an Acquired Vulnerability of PARPi-Resistant BRCA1-Deficient Tumors. *Cancer Res*, *79*(3), 452-460. https://doi.org/10.1158/0008-5472.CAN-18-2077

Barber, L. J., Sandhu, S., Chen, L., Campbell, J., Kozarewa, I., Fenwick, K., Assiotis, I., Rodrigues, D. N., Reis Filho, J. S., Moreno, V., Mateo, J., Molife, L. R., De Bono, J., Kaye, S., Lord, C. J., & Ashworth, A. (2013). Secondary mutations in BRCA2 associated with clinical resistance to a PARP inhibitor. *J Pathol*, *229*(3), 422-429. https://doi.org/10.1002/path.4140

Barrangou, R., Fremaux, C., Deveau, H., Richards, M., Boyaval, P., Moineau, S., Romero, D. A., & Horvath, P. (2007). CRISPR provides acquired resistance against viruses in prokaryotes. *Science*, *315*(5819), 1709-1712. https://doi.org/10.1126/science.1138140

Baudat, F., Imai, Y., & de Massy, B. (2013). Meiotic recombination in mammals: localization and regulation. *Nat Rev Genet*, *14*(11), 794-806. https://doi.org/10.1038/nrg3573

Baumann, P., Benson, F. E., & West, S. C. (1996). Human Rad51 protein promotes ATP-dependent homologous pairing and strand transfer reactions in vitro. *Cell*, *87*(4), 757-766. https://doi.org/10.1016/s0092-8674(00)81394-x

Beroukhim, R., Mermel, C. H., Porter, D., Wei, G., Raychaudhuri, S., Donovan, J., Barretina, J., Boehm, J. S., Dobson, J., Urashima, M., Mc Henry, K. T., Pinchback, R. M., Ligon, A. H., Cho, Y. J., Haery, L., Greulich, H., Reich, M., Winckler, W., Lawrence, M. S., . . . Meyerson, M. (2010). The landscape of somatic copy-number alteration across human cancers. *Nature*, *463*(7283), 899-905. https://doi.org/10.1038/nature08822

Berti, M., Ray Chaudhuri, A., Thangavel, S., Gomathinayagam, S., Kenig, S., Vujanovic, M., Odreman, F., Glatter, T., Graziano, S., Mendoza-Maldonado, R., Marino, F., Lucic, B., Biasin, V., Gstaiger, M., Aebersold, R., Sidorova, J. M., Monnat, R. J., Jr., Lopes, M., & Vindigni, A. (2013). Human RECQ1 promotes restart of replication forks reversed by DNA topoisomerase I inhibition. *Nat Struct Mol Biol*, *20*(3), 347-354. https://doi.org/10.1038/nsmb.2501

Blomen, V. A., Majek, P., Jae, L. T., Bigenzahn, J. W., Nieuwenhuis, J., Staring, J., Sacco, R., van Diemen, F. R., Olk, N., Stukalov, A., Marceau, C., Janssen, H., Carette, J. E., Bennett, K. L., Colinge, J., Superti-Furga, G., & Brummelkamp, T. R. (2015). Gene essentiality and synthetic lethality in haploid human cells. *Science*, *350*(6264), 1092-1096. https://doi.org/10.1126/science.aac7557

Borst, P., Evers, R., Kool, M., & Wijnholds, J. (2000). A family of drug transporters: the multidrug resistance-associated proteins. *J Natl Cancer Inst*, *92*(16), 1295-1302. https://doi.org/10.1093/jnci/92.16.1295

Bouwman, P., Aly, A., Escandell, J. M., Pieterse, M., Bartkova, J., van der Gulden, H., Hiddingh, S., Thanasoula, M., Kulkarni, A., Yang, Q., Haffty, B. G., Tommiska, J., Blomqvist, C., Drapkin, R., Adams, D. J., Nevanlinna, H., Bartek, J., Tarsounas, M., Ganesan, S., & Jonkers, J. (2010). 53BP1 loss rescues BRCA1 deficiency and is associated with triple-negative and BRCA-mutated breast cancers. Nat Struct Mol Biol, 17(6), 688-695. https://doi.org/10.1038/nsmb.1831

Bramson, J., Prevost, J., Malapetsa, A., Noe, A. J., Poirier, G. G., DesNoyers, S., Alaoui-Jamali, M., & Panasci, L. (1993). Poly(ADP-ribose) polymerase can bind melphalan damaged DNA. *Cancer Res*, *53*(22), 5370-5373. https://www.ncbi.nlm.nih.gov/pubmed/8221673

Breast Cancer Linkage, C. (1999). Cancer risks in BRCA2 mutation carriers. *J Natl Cancer Inst*, *91*(15), 1310-1316. https://doi.org/10.1093/jnci/91.15.1310

Brinkman, E. K., Chen, T., Amendola, M., & van Steensel, B. (2014). Easy quantitative assessment of genome editing by sequence trace

decomposition. *Nucleic Acids Res*, *42*(22), e168. https://doi.org/10.1093/nar/gku936

Bryant, H. E., Schultz, N., Thomas, H. D., Parker, K. M., Flower, D., Lopez, E., Kyle, S., Meuth, M., Curtin, N. J., & Helleday, T. (2005). Specific killing of BRCA2-deficient tumours with inhibitors of poly(ADP-ribose) polymerase. *Nature*, *434*(7035), 913-917. https://doi.org/10.1038/nature03443

Bugreev, D. V., Huang, F., Mazina, O. M., Pezza, R. J., Voloshin, O. N., Camerini-Otero, R. D., & Mazin, A. V. (2014). HOP2-MND1 modulates RAD51 binding to nucleotides and DNA. *Nat Commun*, *5*, 4198. https://doi.org/10.1038/ncomms5198

Bugreev, D. V., Pezza, R. J., Mazina, O. M., Voloshin, O. N., Camerini-Otero, R. D., & Mazin, A. V. (2011). The resistance of DMC1 D-loops to dissociation may account for the DMC1 requirement in meiosis. *Nat Struct Mol Biol*, *18*(1), 56-60. https://doi.org/10.1038/nsmb.1946

Bunting, S. F., Callen, E., Wong, N., Chen, H. T., Polato, F., Gunn, A., Bothmer, A., Feldhahn, N., Fernandez-Capetillo, O., Cao, L., Xu, X., Deng, C. X., Finkel, T., Nussenzweig, M., Stark, J. M., & Nussenzweig, A. (2010). 53BP1 inhibits homologous recombination in Brca1-deficient cells by blocking resection of DNA breaks. Cell, 141(2), 243-254. https://doi.org/10.1016/j.cell.2010.03.012

Caldecott, K. W. (2014). DNA single-strand break repair. *Exp Cell Res*, *329*(1), 2-8. https://doi.org/10.1016/j.yexcr.2014.08.027

Cancer Genome Atlas, N. (2012). Comprehensive molecular portraits of human breast tumours. *Nature*, *490*(7418), 61-70. https://doi.org/10.1038/nature11412

Candelli, A., Holthausen, J. T., Depken, M., Brouwer, I., Franker, M. A., Marchetti, M., Heller, I., Bernard, S., Garcin, E. B., Modesti, M., Wyman, C., Wuite, G. J., & Peterman, E. J. (2014). Visualization and quantification of nascent RAD51 filament formation at single-monomer resolution. *Proc Natl Acad Sci U S A*, *111*(42), 15090-15095. https://doi.org/10.1073/pnas.1307824111

Cerami, E., Gao, J., Dogrusoz, U., Gross, B. E., Sumer, S. O., Aksoy, B. A., Jacobsen, A., Byrne, C. J., Heuer, M. L., Larsson, E., Antipin, Y., Reva, B., Goldberg, A. P., Sander, C., & Schultz, N. (2012). The cBio cancer genomics portal: an open platform for exploring multidimensional cancer genomics data. *Cancer Discov*, *2*(5), 401-404. https://doi.org/10.1158/2159-8290.CD-12-0095

Chabanon, R. M., Muirhead, G., Krastev, D. B., Adam, J., Morel, D., Garrido, M., Lamb, A., Henon, C., Dorvault, N., Rouanne, M., Marlow, R., Bajrami, I., Cardenosa, M. L., Konde, A., Besse, B., Ashworth, A., Pettitt, S. J., Haider, S., Marabelle, A., . . . Postel-Vinay, S. (2019). PARP inhibition enhances tumor cell-intrinsic immunity in ERCC1-deficient non-small cell lung cancer. *J Clin Invest*, *129*(3), 1211-1228. https://doi.org/10.1172/JCI123319

Chavez, A., Scheiman, J., Vora, S., Pruitt, B. W., Tuttle, M., E, P. R. I., Lin, S., Kiani, S., Guzman, C. D., Wiegand, D. J., Ter-Ovanesyan, D., Braff, J. L., Davidsohn, N., Housden, B. E., Perrimon, N., Weiss, R., Aach, J., Collins, J. J., & Church, G. M. (2015). Highly efficient Cas9-mediated transcriptional programming. *Nat Methods*, *12*(4), 326-328. https://doi.org/10.1038/nmeth.3312

Chen, B., Tang, H., Chen, X., Zhang, G., Wang, Y., Xie, X., & Liao, N. (2019). Transcriptomic analyses identify key differentially expressed genes and clinical outcomes between triple-negative and non-triple-negative breast cancer. *Cancer Manag Res*, *11*, 179-190. https://doi.org/10.2147/CMAR.S187151

Chen, Y. K., Leng, C. H., Olivares, H., Lee, M. H., Chang, Y. C., Kung, W. M., Ti, S. C., Lo, Y. H., Wang, A. H., Chang, C. S., Bishop, D. K., Hsueh, Y. P., & Wang, T. F. (2004). Heterodimeric complexes of Hop2 and Mnd1 function with Dmc1 to promote meiotic homolog juxtaposition and strand assimilation. *Proc Natl Acad Sci U S A*, *101*(29), 10572-10577. https://doi.org/10.1073/pnas.0404195101

Cho, N. W., Dilley, R. L., Lampson, M. A., & Greenberg, R. A. (2014). Interchromosomal homology searches drive directional ALT telomere movement and synapsis. *Cell*, *159*(1), 108-121. https://doi.org/10.1016/j.cell.2014.08.030

Choi, E. H., & Kim, K. P. (2019). E2F1 facilitates DNA break repair by localizing to break sites and enhancing the expression of homologous recombination factors. *Exp Mol Med*, *51*(9), 1-12. https://doi.org/10.1038/s12276-019-0307-2

Clauson, C., Scharer, O. D., & Niedernhofer, L. (2013). Advances in understanding the complex mechanisms of DNA interstrand cross-link repair. *Cold Spring Harb Perspect Biol*, *5*(10), a012732. https://doi.org/10.1101/cshperspect.a012732

Clements, K. E., Schleicher, E. M., Thakar, T., Hale, A., Dhoonmoon, A., Tolman, N. J., Sharma, A., Liang, X., Imamura Kawasawa, Y., Nicolae, C. M., Wang, H. G., De, S., & Moldovan, G. L. (2020). Identification of regulators of poly-ADP-ribose polymerase inhibitor response through complementary CRISPR knockout and activation screens. *Nat Commun*, *11*(1), 6118. https://doi.org/10.1038/s41467-020-19961-w

Cloud, V., Chan, Y.-L., Grubb, J., Budke, B., & Bishop, D. K. (2012). Rad51 is an accessory factor for Dmc1-mediated joint molecule formation during meiosis. *Science*, *337*(6099), 1222-1225. https://doi.org/10.1126/science.1219379

Cohen-Sharir, Y., McFarland, J. M., Abdusamad, M., Marquis, C., Bernhard, S. V., Kazachkova, M., Tang, H., Ippolito, M. R., Laue, K., Zerbib, J., Malaby, H. L. H., Jones, A., Stautmeister, L. M., Bockaj, I., Wardenaar, R., Lyons, N., Nagaraja, A., Bass, A. J., Spierings, D. C. J., . . . Ben-David, U. (2021).

Aneuploidy renders cancer cells vulnerable to mitotic checkpoint inhibition. *Nature*, *590*(7846), 486-491. https://doi.org/10.1038/s41586-020-03114-6

Coleman, R. L., Oza, A. M., Lorusso, D., Aghajanian, C., Oaknin, A., Dean, A., Colombo, N., Weberpals, J. I., Clamp, A., Scambia, G., Leary, A., Holloway, R. W., Gancedo, M. A., Fong, P. C., Goh, J. C., O'Malley, D. M., Armstrong, D. K., Garcia-Donas, J., Swisher, E. M., . . . investigators, A. (2017). Rucaparib maintenance treatment for recurrent ovarian carcinoma after response to platinum therapy (ARIEL3): a randomised, double-blind, placebo-controlled, phase 3 trial. *Lancet*, *390*(10106), 1949-1961. https://doi.org/10.1016/S0140-6736(17)32440-6

Colic, M., Wang, G., Zimmermann, M., Mascall, K., McLaughlin, M., Bertolet, L., Lenoir, W. F., Moffat, J., Angers, S., Durocher, D., & Hart, T. (2019). Identifying chemogenetic interactions from CRISPR screens with drugZ. *Genome Med*, *11*(1), 52. https://doi.org/10.1186/s13073-019-0665-3

Collins, N., McManus, R., Wooster, R., Mangion, J., Seal, S., Lakhani, S. R., Ormiston, W., Daly, P. A., Ford, D., Easton, D. F., & et al. (1995). Consistent loss of the wild type allele in breast cancers from a family linked to the BRCA2 gene on chromosome 13q12-13. *Oncogene*, *10*(8), 1673-1675. https://www.ncbi.nlm.nih.gov/pubmed/7731724

Cong, L., Ran, F. A., Cox, D., Lin, S., Barretto, R., Habib, N., Hsu, P. D., Wu, X., Jiang, W., Marraffini, L. A., & Zhang, F. (2013). Multiplex genome engineering using CRISPR/Cas systems. *Science*, *339*(6121), 819-823. https://doi.org/10.1126/science.1231143

Cornelis, R. S., Neuhausen, S. L., Johansson, O., Arason, A., Kelsell, D., Ponder, B. A., Tonin, P., Hamann, U., Lindblom, A., Lalle, P., & et al. (1995). High allele loss rates at 17q12-q21 in breast and ovarian tumors from BRCAl-linked families. The Breast Cancer Linkage Consortium. *Genes Chromosomes Cancer*, *13*(3), 203-210. https://doi.org/10.1002/gcc.2870130310

Cruz, C., Castroviejo-Bermejo, M., Gutierrez-Enriquez, S., Llop-Guevara, A., Ibrahim, Y. H., Gris-Oliver, A., Bonache, S., Morancho, B., Bruna, A., Rueda, O. M., Lai, Z., Polanska, U. M., Jones, G. N., Kristel, P., de Bustos, L., Guzman, M., Rodriguez, O., Grueso, J., Montalban, G., . . . Serra, V. (2018). RAD51 foci as a functional biomarker of homologous recombination repair and PARP inhibitor resistance in germline BRCA-mutated breast cancer. *Ann Oncol*, *29*(5), 1203-1210. https://doi.org/10.1093/annonc/mdy099

Curtis, C., Shah, S. P., Chin, S. F., Turashvili, G., Rueda, O. M., Dunning, M. J., Speed, D., Lynch, A. G., Samarajiwa, S., Yuan, Y., Graf, S., Ha, G., Haffari, G., Bashashati, A., Russell, R., McKinney, S., Group, M., Langerod, A., Green, A., . . . Aparicio, S. (2012). The genomic and transcriptomic architecture of 2,000 breast tumours reveals novel subgroups. Nature, 486(7403), 346-352. https://doi.org/10.1038/nature10983

D'Silva, I., Pelletier, J. D., Lagueux, J., D'Amours, D., Chaudhry, M. A., Weinfeld, M., Lees-Miller, S. P., & Poirier, G. G. (1999). Relative affinities of poly(ADP-ribose) polymerase and DNA-dependent protein kinase for DNA strand interruptions. *Biochim Biophys Acta*, *1430*(1), 119-126. https://doi.org/10.1016/s0167-4838(98)00278-7

Dagogo-Jack, I., & Shaw, A. T. (2018). Tumour heterogeneity and resistance to cancer therapies. *Nat Rev Clin Oncol*, *15*(2), 81-94. https://doi.org/10.1038/nrclinonc.2017.166

Da Ines, O., Degroote, F., Goubely, C., Amiard, S., Gallego, M. E., & White, C. I. (2013). Meiotic recombination in Arabidopsis is catalysed by DMC1, with RAD51 playing a supporting role. *PLoS Genet*, *9*(9), e1003787. https://doi.org/10.1371/journal.pgen.1003787

Davies, A. A., Masson, J. Y., McIlwraith, M. J., Stasiak, A. Z., Stasiak, A., Venkitaraman, A. R., & West, S. C. (2001). Role of BRCA2 in control of the RAD51 recombination and DNA repair protein. *Mol Cell*, *7*(2), 273-282. https://doi.org/10.1016/s1097-2765(01)00175-7

Davies, M. I., Halldorsson, H., Nduka, N., Shall, S., & Skidmore, C. J. (1978). The involvement of poly(adenosine diphosphate-ribose) in deoxyribonucleic acid repair. *Biochem Soc Trans*, *6*(5), 1056-1057. https://doi.org/10.1042/bst0061056

Dawicki-McKenna, J. M., Langelier, M. F., DeNizio, J. E., Riccio, A. A., Cao, C. D., Karch, K. R., McCauley, M., Steffen, J. D., Black, B. E., & Pascal, J. M. (2015). PARP-1 Activation Requires Local Unfolding of an Autoinhibitory Domain. *Mol Cell*, *60*(5), 755-768. https://doi.org/10.1016/j.molcel.2015.10.013

de Bono, J., Mateo, J., Fizazi, K., Saad, F., Shore, N., Sandhu, S., Chi, K. N., Sartor, O., Agarwal, N., Olmos, D., Thiery-Vuillemin, A., Twardowski, P., Mehra, N., Goessl, C., Kang, J., Burgents, J., Wu, W., Kohlmann, A., Adelman, C. A., & Hussain, M. (2020). Olaparib for Metastatic Castration-Resistant Prostate Cancer. *N Engl J Med*, *382*(22), 2091-2102. https://doi.org/10.1056/NEJMoa1911440

de Winter, J. P., & Joenje, H. (2009). The genetic and molecular basis of Fanconi anemia. *Mutat Res*, *668*(1-2), 11-19. https://doi.org/10.1016/j.mrfmmm.2008.11.004

Decker, B., Karyadi, D. M., Davis, B. W., Karlins, E., Tillmans, L. S., Stanford, J. L., Thibodeau, S. N., & Ostrander, E. A. (2016). Biallelic BRCA2 Mutations Shape the Somatic Mutational Landscape of Aggressive Prostate Tumors. *Am J Hum Genet*, *98*(5), 818-829. https://doi.org/10.1016/j.ajhg.2016.03.003

de Massy, B. (2013). Initiation of meiotic recombination: how and where? Conservation and specificities among eukaryotes. *Annu Rev Genet*, *47*, 563-599. https://doi.org/10.1146/annurev-genet-110711-155423

Demple, B., & Harrison, L. (1994). Repair of oxidative damage to DNA: enzymology and biology. *Annu Rev Biochem*, *63*, 915-948. https://doi.org/10.1146/annurev.bi.63.070194.004411

Dev, H., Chiang, T. W., Lescale, C., de Krijger, I., Martin, A. G., Pilger, D., Coates, J., Sczaniecka-Clift, M., Wei, W., Ostermaier, M., Herzog, M., Lam, J., Shea, A., Demir, M., Wu, Q., Yang, F., Fu, B., Lai, Z., Balmus, G., . . . Jackson, S. P. (2018). Shieldin complex promotes DNA end-joining and counters homologous recombination in BRCA1-null cells. *Nat Cell Biol*, *20*(8), 954-965. https://doi.org/10.1038/s41556-018-0140-1

DeWeirdt, P. C., Sangree, A. K., Hanna, R. E., Sanson, K. R., Hegde, M., Strand, C., Persky, N. S., & Doench, J. G. (2020). Genetic screens in isogenic mammalian cell lines without single cell cloning. *Nat Commun*, *11*(1), 752. https://doi.org/10.1038/s41467-020-14620-6

Dilley, R. L., Verma, P., Cho, N. W., Winters, H. D., Wondisford, A. R., & Greenberg, R. A. (2016). Break-induced telomere synthesis underlies alternative telomere maintenance. *Nature*, *539*(7627), 54-58. https://doi.org/10.1038/nature20099

Ding, L., Kim, H. J., Wang, Q., Kearns, M., Jiang, T., Ohlson, C. E., Li, B. B., Xie, S., Liu, J. F., Stover, E. H., Howitt, B. E., Bronson, R. T., Lazo, S., Roberts, T. M., Freeman, G. J., Konstantinopoulos, P. A., Matulonis, U. A., & Zhao, J. J. (2018). PARP Inhibition Elicits STING-Dependent Antitumor Immunity in Brca1-Deficient Ovarian Cancer. *Cell Rep*, *25*(11), 2972-2980 e2975. https://doi.org/10.1016/j.celrep.2018.11.054

Domenichini, S., Raynaud, C., Ni, D. A., Henry, Y., & Bergounioux, C. (2006). Atmnd1-delta1 is sensitive to gamma-irradiation and defective in meiotic DNA repair. DNA Repair (Amst), 5(4), 455-464. https://doi.org/10.1016/j.dnarep.2005.12.007

Drean, A., Williamson, C. T., Brough, R., Brandsma, I., Menon, M., Konde, A., Garcia-Murillas, I., Pemberton, H. N., Frankum, J., Rafiq, R., Badham, N., Campbell, J., Gulati, A., Turner, N. C., Pettitt, S. J., Ashworth, A., & Lord, C. J. (2017). Modeling Therapy Resistance in BRCA1/2-Mutant Cancers. Mol Cancer Ther, 16(9), 2022-2034. https://doi.org/10.1158/1535-7163.MCT-17-0098

Durkacz, B. W., Omidiji, O., Gray, D. A., & Shall, S. (1980). (ADP-ribose)n participates in DNA excision repair. *Nature*, *283*(5747), 593-596. https://doi.org/10.1038/283593a0

Easton, D. F., Ford, D., & Bishop, D. T. (1995). Breast and ovarian cancer incidence in BRCA1-mutation carriers. Breast Cancer Linkage Consortium. *Am J Hum Genet*, *56*(1), 265-271. https://www.ncbi.nlm.nih.gov/pubmed/7825587

Edwards, S. L., Brough, R., Lord, C. J., Natrajan, R., Vatcheva, R., Levine, D. A., Boyd, J., Reis-Filho, J. S., & Ashworth, A. (2008). Resistance to therapy caused by intragenic deletion in BRCA2. *Nature*, *451*(7182), 1111-1115. https://doi.org/10.1038/nature06548

Elstrodt, F., Hollestelle, A., Nagel, J. H., Gorin, M., Wasielewski, M., van den Ouweland, A., Merajver, S. D., Ethier, S. P., & Schutte, M. (2006). BRCA1 mutation analysis of 41 human breast cancer cell lines reveals three new deleterious mutants. *Cancer Res*, *66*(1), 41-45. https://doi.org/10.1158/0008-5472.CAN-05-2853

Eustermann, S., Wu, W. F., Langelier, M. F., Yang, J. C., Easton, L. E., Riccio, A. A., Pascal, J. M., & Neuhaus, D. (2015). Structural Basis of Detection and Signaling of DNA Single-Strand Breaks by Human PARP-1. *Mol Cell*, *60*(5), 742-754. https://doi.org/10.1016/j.molcel.2015.10.032

Faivre, S., Chan, D., Salinas, R., Woynarowska, B., & Woynarowski, J. M. (2003). DNA strand breaks and apoptosis induced by oxaliplatin in cancer cells. *Biochem Pharmacol*, *66*(2), 225-237. https://doi.org/10.1016/s0006-2952(03)00260-0

Fang, P., De Souza, C., Minn, K., & Chien, J. (2019). Genome-scale CRISPR knockout screen identifies TIGAR as a modifier of PARP inhibitor sensitivity. *Commun Biol*, *2*, 335. https://doi.org/10.1038/s42003-019-0580-6

Farmer, H., McCabe, N., Lord, C. J., Tutt, A. N., Johnson, D. A., Richardson, T. B., Santarosa, M., Dillon, K. J., Hickson, I., Knights, C., Martin, N. M., Jackson, S. P., Smith, G. C., & Ashworth, A. (2005). Targeting the DNA repair defect in BRCA mutant cells as a therapeutic strategy. *Nature*, *434*(7035), 917-921. https://doi.org/10.1038/nature03445

Feichtinger, J., & McFarlane, R. J. (2019). Meiotic gene activation in somatic and germ cell tumours. *Andrology*, *7*(4), 415-427. https://doi.org/10.1111/andr.12628

Fidler, I. J. (1978). Tumor heterogeneity and the biology of cancer invasion and metastasis. *Cancer Res*, *38*(9), 2651-2660. https://www.ncbi.nlm.nih.gov/pubmed/354778

Fisher, A. E., Hochegger, H., Takeda, S., & Caldecott, K. W. (2007). Poly(ADP-ribose) polymerase 1 accelerates single-strand break repair in concert with poly(ADP-ribose) glycohydrolase. *Mol Cell Biol*, *27*(15), 5597-5605. https://doi.org/10.1128/MCB.02248-06

Fong, P. C., Boss, D. S., Yap, T. A., Tutt, A., Wu, P., Mergui-Roelvink, M., Mortimer, P., Swaisland, H., Lau, A., O'Connor, M. J., Ashworth, A., Carmichael, J., Kaye, S. B., Schellens, J. H., & de Bono, J. S. (2009). Inhibition of poly(ADP-ribose) polymerase in tumors from BRCA mutation carriers. *N Engl J Med*, *361*(2), 123-134. https://doi.org/10.1056/NEJMoa0900212

Francica, P., Mutlu, M., Blomen, V. A., Oliveira, C., Nowicka, Z., Trenner, A., Gerhards, N. M., Bouwman, P., Stickel, E., Hekkelman, M. L., Lingg, L., Klebic, I., van de Ven, M., de Korte-Grimmerink, R., Howald, D., Jonkers, J., Sartori, A. A., Fendler, W., Chapman, J. R., . . . Rottenberg, S. (2020). Functional Radiogenetic Profiling Implicates ERCC6L2 in Non-homologous End Joining. *Cell Rep*, *32*(8), 108068. https://doi.org/10.1016/j.celrep.2020.108068

Fugger, K., Bajrami, I., Silva Dos Santos, M., Young, S. J., Kunzelmann, S., Kelly, G., Hewitt, G., Patel, H., Goldstone, R., Carell, T., Boulton, S. J., MacRae, J., Taylor, I. A., & West, S. C. (2021). Targeting the nucleotide salvage factor DNPH1 sensitizes BRCA-deficient cells to PARP inhibitors. *Science*, *372*(6538), 156-165. https://doi.org/10.1126/science.abb4542

Gaillard, H., Garcia-Muse, T., & Aguilera, A. (2015). Replication stress and cancer. *Nat Rev Cancer*, *15*(5), 276-289. https://doi.org/10.1038/nrc3916

Gao, J., Aksoy, B. A., Dogrusoz, U., Dresdner, G., Gross, B., Sumer, S. O., Sun, Y., Jacobsen, A., Sinha, R., Larsson, E., Cerami, E., Sander, C., & Schultz, N. (2013). Integrative analysis of complex cancer genomics and clinical profiles using the cBioPortal. *Sci Signal*, *6*(269), pl1. https://doi.org/10.1126/scisignal.2004088

Gao, Y., Kardos, J., Yang, Y., Tamir, T. Y., Mutter-Rottmayer, E., Weissman, B., Major, M. B., Kim, W. Y., & Vaziri, C. (2018). The Cancer/Testes (CT) Antigen HORMAD1 promotes Homologous Recombinational DNA Repair and Radioresistance in Lung adenocarcinoma cells. *Sci Rep*, *8*(1), 15304. https://doi.org/10.1038/s41598-018-33601-w

Garner, E., Kim, Y., Lach, F. P., Kottemann, M. C., & Smogorzewska, A. (2013). Human GEN1 and the SLX4-associated nucleases MUS81 and SLX1 are essential for the resolution of replication-induced Holliday junctions. *Cell Rep.*, *5*(1), 207-215. https://doi.org/10.1016/j.celrep.2013.08.041

Gebre, M., Nomburg, J. L., & Gewurz, B. E. (2018). CRISPR-Cas9 Genetic Analysis of Virus-Host Interactions. *Viruses*, *10*(2). https://doi.org/10.3390/v10020055

German, J. (1993). Bloom syndrome: a mendelian prototype of somatic mutational disease. *Medicine (Baltimore)*, *72*(6), 393-406. https://www.ncbi.nlm.nih.gov/pubmed/8231788

Ghandi, M., Huang, F. W., Jane-Valbuena, J., Kryukov, G. V., Lo, C. C., McDonald, E. R., 3rd, Barretina, J., Gelfand, E. T., Bielski, C. M., Li, H., Hu, K., Andreev-Drakhlin, A. Y., Kim, J., Hess, J. M., Haas, B. J., Aguet, F., Weir, B. A., Rothberg, M. V., Paolella, B. R., . . . Sellers, W. R. (2019). Next-generation characterization of the Cancer Cell Line Encyclopedia. *Nature*, *569*(7757), 503-508. https://doi.org/10.1038/s41586-019-1186-3

Ghezraoui, H., Oliveira, C., Becker, J. R., Bilham, K., Moralli, D., Anzilotti, C., Fischer, R., Deobagkar-Lele, M., Sanchiz-Calvo, M., Fueyo-Marcos, E., Bonham, S., Kessler, B. M., Rottenberg, S., Cornall, R. J., Green, C. M., & Chapman, J. R. (2018). 53BP1 cooperation with the REV7-shieldin complex underpins DNA structure-specific NHEJ. *Nature*, *560*(7716), 122-127. https://doi.org/10.1038/s41586-018-0362-1

Gilbert, L. A., Larson, M. H., Morsut, L., Liu, Z., Brar, G. A., Torres, S. E., Stern-Ginossar, N., Brandman, O., Whitehead, E. H., Doudna, J. A., Lim, W. A., Weissman, J. S., & Qi, L. S. (2013). CRISPR-mediated modular RNA-guided regulation of transcription in eukaryotes. *Cell*, *154*(2), 442-451. https://doi.org/10.1016/j.cell.2013.06.044

Golan, T., Hammel, P., Reni, M., Van Cutsem, E., Macarulla, T., Hall, M. J., Park, J. O., Hochhauser, D., Arnold, D., Oh, D. Y., Reinacher-Schick, A., Tortora, G., Algul, H., O'Reilly, E. M., McGuinness, D., Cui, K. Y., Schlienger, K., Locker, G. Y., & Kindler, H. L. (2019). Maintenance Olaparib for Germline BRCA-Mutated Metastatic Pancreatic Cancer. *N Engl J Med*, *381*(4), 317-327. https://doi.org/10.1056/NEJMoa1903387

Gonzalez-Martin, A., Pothuri, B., Vergote, I., DePont Christensen, R., Graybill, W., Mirza, M. R., McCormick, C., Lorusso, D., Hoskins, P., Freyer, G., Baumann, K., Jardon, K., Redondo, A., Moore, R. G., Vulsteke, C., O'Cearbhaill, R. E., Lund, B., Backes, F., Barretina-Ginesta, P., . . . Investigators, P. E.-O. G.-. (2019). Niraparib in Patients with Newly Diagnosed Advanced Ovarian Cancer. *N Engl J Med*, *381*(25), 2391-2402. https://doi.org/10.1056/NEJMoa1910962

Goodall, J., Mateo, J., Yuan, W., Mossop, H., Porta, N., Miranda, S., Perez-Lopez, R., Dolling, D., Robinson, D. R., Sandhu, S., Fowler, G., Ebbs, B., Flohr, P., Seed, G., Rodrigues, D. N., Boysen, G., Bertan, C., Atkin, M., Clarke, M., . . . investigators, T.-A. (2017). Circulating Cell-Free DNA to Guide Prostate Cancer Treatment with PARP Inhibition. *Cancer Discov*, *7*(9), 1006-1017. https://doi.org/10.1158/2159-8290.CD-17-0261

Gossen, M., & Bujard, H. (1992). Tight control of gene expression in mammalian cells by tetracycline-responsive promoters. *Proc Natl Acad Sci U S A*, *89*(12), 5547-5551. https://doi.org/10.1073/pnas.89.12.5547

Grey, C., Barthès, P., Chauveau-Le Friec, G., Langa, F., Baudat, F., & de Massy, B. (2011). Mouse PRDM9 DNA-binding specificity determines sites of histone H3 lysine 4 trimethylation for initiation of meiotic recombination. *PLoS Biol.*, *9*(10), e1001176. https://doi.org/10.1371/journal.pbio.1001176

Guillemette, S., Serra, R. W., Peng, M., Hayes, J. A., Konstantinopoulos, P. A., Green, M. R., & Cantor, S. B. (2015). Resistance to therapy in BRCA2 mutant cells due to loss of the nucleosome remodeling factor CHD4. *Genes Dev*, *29*(5), 489-494. https://doi.org/10.1101/gad.256214.114

Gunn, A., & Stark, J. M. (2012). I-SceI-based assays to examine distinct repair outcomes of mammalian chromosomal double strand breaks. *Methods Mol Biol*, *920*, 379-391. https://doi.org/10.1007/978-1-61779-998-3_27

Gupta, R., Somyajit, K., Narita, T., Maskey, E., Stanlie, A., Kremer, M., Typas, D., Lammers, M., Mailand, N., Nussenzweig, A., Lukas, J., & Choudhary, C. (2018). DNA Repair Network Analysis Reveals Shieldin as a Key Regulator of NHEJ and PARP Inhibitor Sensitivity. *Cell*, *173*(4), 972-988 e923. https://doi.org/10.1016/j.cell.2018.03.050

Haince, J. F., Kozlov, S., Dawson, V. L., Dawson, T. M., Hendzel, M. J., Lavin, M. F., & Poirier, G. G. (2007). Ataxia telangiectasia mutated (ATM) signaling network is modulated by a novel poly(ADP-ribose)-dependent pathway in the early response to DNA-damaging agents. *J Biol Chem*, *282*(22), 16441-16453. https://doi.org/10.1074/jbc.M608406200

Haince, J. F., McDonald, D., Rodrigue, A., Dery, U., Masson, J. Y., Hendzel, M. J., & Poirier, G. G. (2008). PARP1-dependent kinetics of recruitment of MRE11 and NBS1 proteins to multiple DNA damage sites. *J Biol Chem*, *283*(2), 1197-1208. https://doi.org/10.1074/jbc.M706734200

Hakem, R., de la Pompa, J. L., Elia, A., Potter, J., & Mak, T. W. (1997). Partial rescue of Brca1 (5-6) early embryonic lethality by p53 or p21 null mutation. *Nat Genet*, *16*(3), 298-302. https://doi.org/10.1038/ng0797-298

Hakem, R., de la Pompa, J. L., Sirard, C., Mo, R., Woo, M., Hakem, A., Wakeham, A., Potter, J., Reitmair, A., Billia, F., Firpo, E., Hui, C. C., Roberts, J., Rossant, J., & Mak, T. W. (1996). The tumor suppressor gene Brca1 is required for embryonic cellular proliferation in the mouse. *Cell*, *85*(7), 1009-1023. https://doi.org/10.1016/s0092-8674(00)81302-1

Hanahan, D., & Weinberg, R. A. (2011). Hallmarks of cancer: the next generation. *Cell*, *144*(5), 646-674. https://doi.org/10.1016/j.cell.2011.02.013

Hanzlikova, H., Kalasova, I., Demin, A. A., Pennicott, L. E., Cihlarova, Z., & Caldecott, K. W. (2018). The Importance of Poly(ADP-Ribose) Polymerase as a Sensor of Unligated Okazaki Fragments during DNA Replication. *Mol Cell*, *71*(2), 319-331 e313. https://doi.org/10.1016/j.molcel.2018.06.004

Hart, T., Brown, K. R., Sircoulomb, F., Rottapel, R., & Moffat, J. (2014). Measuring error rates in genomic perturbation screens: gold standards for human functional genomics. *Mol Syst Biol*, *10*, 733. https://doi.org/10.15252/msb.20145216

Hartenian, E., & Doench, J. G. (2015). Genetic screens and functional genomics using CRISPR/Cas9 technology. *FEBS J*, *282*(8), 1383-1393. https://doi.org/10.1111/febs.13248

Hashizume, R., Fukuda, M., Maeda, I., Nishikawa, H., Oyake, D., Yabuki, Y., Ogata, H., & Ohta, T. (2001). The RING heterodimer BRCA1-BARD1 is a ubiquitin ligase inactivated by a breast cancer-derived mutation. *J Biol Chem*, *276*(18), 14537-14540. https://doi.org/10.1074/jbc.C000881200

Hassold, T., & Hunt, P. (2001). To err (meiotically) is human: the genesis of human aneuploidy. Nat Rev Genet, 2(4), 280-291. https://doi.org/10.1038/35066065

Hatakeyama, K., Nemoto, Y., Ueda, K., & Hayaishi, O. (1986). Purification and characterization of poly(ADP-ribose) glycohydrolase. Different modes of action on large and small poly(ADP-ribose). *J Biol Chem*, *261*(32), 14902-14911. https://www.ncbi.nlm.nih.gov/pubmed/3771556

He, Y. J., Meghani, K., Caron, M. C., Yang, C., Ronato, D. A., Bian, J., Sharma, A., Moore, J., Niraj, J., Detappe, A., Doench, J. G., Legube, G., Root, D. E., D'Andrea, A. D., Drane, P., De, S., Konstantinopoulos, P. A., Masson, J. Y., & Chowdhury, D. (2018). DYNLL1 binds to MRE11 to limit DNA end resection in BRCA1-deficient cells. *Nature*, *563*(7732), 522-526. https://doi.org/10.1038/s41586-018-0670-5

Heale, J. T., Ball, A. R., Jr., Schmiesing, J. A., Kim, J. S., Kong, X., Zhou, S., Hudson, D. F., Earnshaw, W. C., & Yokomori, K. (2006). Condensin I interacts with the PARP-1-XRCC1 complex and functions in DNA single-strand break repair. *Mol Cell*, *21*(6), 837-848. https://doi.org/10.1016/j.molcel.2006.01.036

Hennessy, B. T., Timms, K. M., Carey, M. S., Gutin, A., Meyer, L. A., Flake, D. D., 2nd, Abkevich, V., Potter, J., Pruss, D., Glenn, P., Li, Y., Li, J., Gonzalez-Angulo, A. M., McCune, K. S., Markman, M., Broaddus, R. R., Lanchbury, J. S., Lu, K. H., & Mills, G. B. (2010). Somatic mutations in BRCA1 and BRCA2 could expand the number of patients that benefit from poly (ADP ribose) polymerase inhibitors in ovarian cancer. *J Clin Oncol*, *28*(22), 3570-3576. https://doi.org/10.1200/JCO.2009.27.2997

Henry, J. M., Camahort, R., Rice, D. A., Florens, L., Swanson, S. K., Washburn, M. P., & Gerton, J. L. (2006). Mnd1/Hop2 facilitates Dmc1-dependent interhomolog crossover formation in meiosis of budding yeast. Mol Cell Biol, 26(8), 2913-2923. https://doi.org/10.1128/MCB.26.8.2913-2923.2006

Hewitt, G., Borel, V., Segura-Bayona, S., Takaki, T., Ruis, P., Bellelli, R., Lehmann, L. C., Sommerova, L., Vancevska, A., Tomas-Loba, A., Zhu, K., Cooper, C., Fugger, K., Patel, H., Goldstone, R., Schneider-Luftman, D., Herbert, E., Stamp, G., Brough, R., . . . Boulton, S. J. (2021). Defective ALC1 nucleosome remodeling confers PARPi sensitization and synthetic lethality with HRD. *Mol Cell*, *81*(4), 767-783 e711. https://doi.org/10.1016/j.molcel.2020.12.006

Hilario, J., Amitani, I., Baskin, R. J., & Kowalczykowski, S. C. (2009). Direct imaging of human Rad51 nucleoprotein dynamics on individual DNA molecules. *Proc Natl Acad Sci U S A*, *106*(2), 361-368. https://doi.org/10.1073/pnas.0811965106

Hilz, H., & Stone, P. (1976). Poly(ADP-ribose) and ADP-ribosylation of proteins. *Rev Physiol Biochem Pharmacol*, *76*, 1-58, 177. https://doi.org/10.1007/BFb0027686

Hine, C. M., Li, H., Xie, L., Mao, Z., Seluanov, A., & Gorbunova, V. (2014). Regulation of Rad51 promoter. *Cell Cycle*, *13*(13), 2038-2045. https://doi.org/10.4161/cc.29016

Holliday, R. (2007). A mechanism for gene conversion in fungi. *Genet. Res.*, *89*(5-6), 285-307. https://doi.org/10.1017/S0016672308009476

Holm, J. B., Humphrys, M. S., Robinson, C. K., Settles, M. L., Ott, S., Fu, L., Yang, H., Gajer, P., He, X., McComb, E., Gravitt, P. E., Ghanem, K. G., Brotman, R. M., & Ravel, J. (2019). Ultrahigh-Throughput Multiplexing and Sequencing of >500-Base-Pair Amplicon Regions on the Illumina HiSeq 2500 Platform. *mSystems*, *4*(1). https://doi.org/10.1128/mSystems.00029-19

Hong, S., Sung, Y., Yu, M., Lee, M., Kleckner, N., & Kim, K. P. (2013). The logic and mechanism of homologous recombination partner choice. *Mol. Cell*, *51*(4), 440-453. https://doi.org/10.1016/j.molcel.2013.08.008

Hoppe, M. M., Sundar, R., Tan, D. S. P., & Jeyasekharan, A. D. (2018). Biomarkers for Homologous Recombination Deficiency in Cancer. *J Natl Cancer Inst*, *110*(7), 704-713. https://doi.org/10.1093/jnci/djy085

Horlbeck, M. A., Gilbert, L. A., Villalta, J. E., Adamson, B., Pak, R. A., Chen, Y., Fields, A. P., Park, C. Y., Corn, J. E., Kampmann, M., & Weissman, J. S. (2016). Compact and highly active next-generation libraries for CRISPR-mediated gene repression and activation. *Elife*, *5*. https://doi.org/10.7554/eLife.19760

Hu, K., Ghandi, M., & Huang, F. W. (2021). Integrated evaluation of telomerase activation and telomere maintenance across cancer cell lines. *Elife*, *10*. https://doi.org/10.7554/eLife.66198

Huang, F., Mazina, O. M., Zentner, I. J., Cocklin, S., & Mazin, A. V. (2012). Inhibition of homologous recombination in human cells by targeting RAD51 recombinase. *J Med Chem*, *55*(7), 3011-3020. https://doi.org/10.1021/jm201173g

Huang, F., Motlekar, N. A., Burgwin, C. M., Napper, A. D., Diamond, S. L., & Mazin, A. V. (2011). Identification of specific inhibitors of human RAD51 recombinase using high-throughput screening. *ACS Chem Biol*, *6*(6), 628-635. https://doi.org/10.1021/cb100428c

Hunter, N. (2015). Meiotic Recombination: The Essence of Heredity. *Cold Spring Harb Perspect Biol*, *7*(12). https://doi.org/10.1101/cshperspect.a016618

Ip, S. C. Y., Rass, U., Blanco, M. G., Flynn, H. R., Skehel, J. M., & West, S. C. (2008). Identification of Holliday junction resolvases from humans and yeast. *Nature*, *456*(7220), 357-361. https://doi.org/10.1038/nature07470

Jackson, A. L., Bartz, S. R., Schelter, J., Kobayashi, S. V., Burchard, J., Mao, M., Li, B., Cavet, G., & Linsley, P. S. (2003). Expression profiling reveals off-target gene regulation by RNAi. *Nat Biotechnol*, *21*(6), 635-637. https://doi.org/10.1038/nbt831

Jackson, S. P., & Bartek, J. (2009). The DNA-damage response in human biology and disease. *Nature*, *461*(7267), 1071-1078. https://doi.org/10.1038/nature08467

Jamal, K., Galbiati, A., Armenia, J., Illuzzi, G., Hall, J., Bentouati, S., Barrell, D., Ahdesmäki, M., O'Connor, M. J., Leo, E., & Forment, J. V. (2022). Drug-gene interaction screens coupled to tumour data analyses identify the most clinically-relevant cancer vulnerabilities driving sensitivity to PARP inhibition. *bioRxiv*, 2022.2007.2029.501846. https://doi.org/10.1101/2022.07.29.501846

Jaspers, J. E., Kersbergen, A., Boon, U., Sol, W., van Deemter, L., Zander, S. A., Drost, R., Wientjens, E., Ji, J., Aly, A., Doroshow, J. H., Cranston, A., Martin, N. M., Lau, A., O'Connor, M. J., Ganesan, S., Borst, P., Jonkers, J., & Rottenberg, S. (2013). Loss of 53BP1 causes PARP inhibitor resistance in Brca1-mutated mouse mammary tumors. *Cancer Discov*, *3*(1), 68-81. https://doi.org/10.1158/2159-8290.CD-12-0049

Jay, A., Reitz, D., Namekawa, S. H., & Heyer, W. D. (2021). Cancer testis antigens and genomic instability: More than immunology. *DNA Repair (Amst)*, *108*, 103214. https://doi.org/10.1016/j.dnarep.2021.103214

Jiang, Y., & Chu, W. K. (2018). Potential Roles of the Retinoblastoma Protein in Regulating Genome Editing. *Front Cell Dev Biol*, *6*, 81. https://doi.org/10.3389/fcell.2018.00081

Jinek, M., Chylinski, K., Fonfara, I., Hauer, M., Doudna, J. A., & Charpentier, E. (2012). A programmable dual-RNA-guided DNA endonuclease in adaptive bacterial immunity. *Science*, *337*(6096), 816-821. https://doi.org/10.1126/science.1225829

Johannes, J. W., Balazs, A., Barratt, D., Bista, M., Chuba, M. D., Cosulich, S., Critchlow, S. E., Degorce, S. L., Di Fruscia, P., Edmondson, S. D., Embrey, K., Fawell, S., Ghosh, A., Gill, S. J., Gunnarsson, A., Hande, S. M., Heightman, T. D., Hemsley, P., Illuzzi, G., . . . Zheng, X. (2021). Discovery of 5-{4-[(7-Ethyl-6-oxo-5,6-dihydro-1,5-naphthyridin-3-yl)methyl]piperazin-1-yl}-N-m ethylpyridine-2-carboxamide (AZD5305): A PARP1-DNA Trapper with High Selectivity for PARP1 over PARP2 and Other PARPs. *J Med Chem*, *64*(19), 14498-14512. https://doi.org/10.1021/acs.jmedchem.1c01012

Johnson, R. D., & Jasin, M. (2000). Sister chromatid gene conversion is a prominent double-strand break repair pathway in mammalian cells. *EMBO J*, *19*(13), 3398-3407. https://doi.org/10.1093/emboj/19.13.3398

Jumper, J., Evans, R., Pritzel, A., Green, T., Figurnov, M., Ronneberger, O., Tunyasuvunakool, K., Bates, R., Zidek, A., Potapenko, A., Bridgland, A., Meyer, C., Kohl, S. A. A., Ballard, A. J., Cowie, A., Romera-Paredes, B., Nikolov, S., Jain, R., Adler, J., . . . Hassabis, D. (2021). Highly accurate protein structure prediction with AlphaFold. *Nature*, *596*(7873), 583-589. https://doi.org/10.1038/s41586-021-03819-2

Kadyk, L. C., & Hartwell, L. H. (1992). Sister chromatids are preferred over homologs as substrates for recombinational repair in Saccharomyces cerevisiae. *Genetics*, *132*(2), 387-402. https://doi.org/10.1093/genetics/132.2.387

Kao, H.-I., Campbell, J. L., & Bambara, R. A. (2004). Dna2p helicase/nuclease is a tracking protein, like FEN1, for flap cleavage during Okazaki fragment maturation. *J. Biol. Chem.*, *279*(49), 50840-50849. https://doi.org/10.1074/jbc.M409231200

Karimian, M., Nikzad, H., Azami-Tameh, A., Taherian, A., Darvishi, F. Z., & Haghighatnia, M. J. (2015). SPO11-C631T Gene Polymorphism: Association With Male Infertility and an in Silico-Analysis. *J Family Reprod Health*, *9*(4), 155-163. https://www.ncbi.nlm.nih.gov/pubmed/27047561

Kashima, L., Idogawa, M., Mita, H., Shitashige, M., Yamada, T., Ogi, K., Suzuki, H., Toyota, M., Ariga, H., Sasaki, Y., & Tokino, T. (2012). CHFR protein regulates mitotic checkpoint by targeting PARP-1 protein for ubiquitination

and degradation. *J Biol Chem*, *287*(16), 12975-12984. https://doi.org/10.1074/jbc.M111.321828

Kaufman, B., Shapira-Frommer, R., Schmutzler, R. K., Audeh, M. W., Friedlander, M., Balmana, J., Mitchell, G., Fried, G., Stemmer, S. M., Hubert, A., Rosengarten, O., Steiner, M., Loman, N., Bowen, K., Fielding, A., & Domchek, S. M. (2015). Olaparib monotherapy in patients with advanced cancer and a germline BRCA1/2 mutation. *J Clin Oncol*, *33*(3), 244-250. https://doi.org/10.1200/JCO.2014.56.2728

Keeney, S., Giroux, C. N., & Kleckner, N. (1997). Meiosis-specific DNA double-strand breaks are catalyzed by Spo11, a member of a widely conserved protein family. *Cell*, *88*(3), 375-384. https://doi.org/10.1016/s0092-8674(00)81876-0

Khodyreva, S. N., Prasad, R., Ilina, E. S., Sukhanova, M. V., Kutuzov, M. M., Liu, Y., Hou, E. W., Wilson, S. H., & Lavrik, O. I. (2010). Apurinic/apyrimidinic (AP) site recognition by the 5'-dRP/AP lyase in poly(ADP-ribose) polymerase-1 (PARP-1). *Proc Natl Acad Sci U S A*, *107*(51), 22090-22095. https://doi.org/10.1073/pnas.1009182107

Kinzler, K. W., & Vogelstein, B. (1997). Cancer-susceptibility genes. Gatekeepers and caretakers. *Nature*, *386*(6627), 761, 763. https://doi.org/10.1038/386761a0

Kolinjivadi, A. M., Sannino, V., De Antoni, A., Zadorozhny, K., Kilkenny, M., Techer, H., Baldi, G., Shen, R., Ciccia, A., Pellegrini, L., Krejci, L., & Costanzo, V. (2017). Smarcal1-Mediated Fork Reversal Triggers Mre11-Dependent Degradation of Nascent DNA in the Absence of Brca2 and Stable Rad51 Nucleofilaments. *Mol Cell*, *67*(5), 867-881 e867. https://doi.org/10.1016/j.molcel.2017.07.001

Kondrashova, O., Nguyen, M., Shield-Artin, K., Tinker, A. V., Teng, N. N. H., Harrell, M. I., Kuiper, M. J., Ho, G. Y., Barker, H., Jasin, M., Prakash, R., Kass, E. M., Sullivan, M. R., Brunette, G. J., Bernstein, K. A., Coleman, R. L., Floquet, A., Friedlander, M., Kichenadasse, G., . . . Group, A. S. (2017). Secondary Somatic Mutations Restoring RAD51C and RAD51D Associated with Acquired Resistance to the PARP Inhibitor Rucaparib in High-Grade Ovarian Carcinoma. *Cancer Discov*, *7*(9), 984-998. https://doi.org/10.1158/2159-8290.CD-17-0419

Koob, L., Friskes, A., van Bergen, L., Feringa, F. M., van den Broek, B., Koeleman, E. S., van Beek, E., Schubert, M., Blomen, V. A., Brummelkamp, T. R., Krenning, L., & Medema, R. H. (2023). MND1 enables homologous recombination in somatic cells primarily outside the context of replication. Mol Oncol. https://doi.org/10.1002/1878-0261.13448

Kowalczykowski, S. C. (2015). An Overview of the Molecular Mechanisms of Recombinational DNA Repair. *Cold Spring Harb Perspect Biol*, *7*(11). https://doi.org/10.1101/cshperspect.a016410

Kramer, K. M., Brock, J. A., Bloom, K., Moore, J. K., & Haber, J. E. (1994). Two different types of double-strand breaks in Saccharomyces cerevisiae are

repaired by similar RAD52-independent, nonhomologous recombination events. *Mol Cell Biol*, *14*(2), 1293-1301. https://doi.org/10.1128/mcb.14.2.1293-1301.1994

Krastev, D. B., Li, S., Sun, Y., Wicks, A. J., Hoslett, G., Weekes, D., Badder, L. M., Knight, E. G., Marlow, R., Pardo, M. C., Yu, L., Talele, T. T., Bartek, J., Choudhary, J. S., Pommier, Y., Pettitt, S. J., Tutt, A. N. J., Ramadan, K., & Lord, C. J. (2022). The ubiquitin-dependent ATPase p97 removes cytotoxic trapped PARP1 from chromatin. *Nat Cell Biol*, *24*(1), 62-73. https://doi.org/10.1038/s41556-021-00807-6

Krastev, D. B., Wicks, A. J., & Lord, C. J. (2021). PARP Inhibitors - Trapped in a Toxic Love Affair. *Cancer Res*, *81*(22), 5605-5607. https://doi.org/10.1158/0008-5472.CAN-21-3201

Kuchenbaecker, K. B., Hopper, J. L., Barnes, D. R., Phillips, K. A., Mooij, T. M., Roos-Blom, M. J., Jervis, S., van Leeuwen, F. E., Milne, R. L., Andrieu, N., Goldgar, D. E., Terry, M. B., Rookus, M. A., Easton, D. F., Antoniou, A. C., Brca, Consortium, B. C., McGuffog, L., Evans, D. G., . . . Olsson, H. (2017). Risks of Breast, Ovarian, and Contralateral Breast Cancer for BRCA1 and BRCA2 Mutation Carriers. *JAMA*, *317*(23), 2402-2416. https://doi.org/10.1001/jama.2017.7112

Kumar, R., Bourbon, H.-M., & de Massy, B. (2010). Functional conservation of Mei4 for meiotic DNA double-strand break formation from yeasts to mice. *Genes Dev.*, *24*(12), 1266-1280. https://doi.org/10.1101/gad.571710

Kumar, R., Oliver, C., Brun, C., Juarez-Martinez, A. B., Tarabay, Y., Kadlec, J., & de Massy, B. (2018). Mouse REC114 is essential for meiotic DNA double-strand break formation and forms a complex with MEI4. Life Sci Alliance, 1(6), e201800259. https://doi.org/10.26508/lsa.201800259

Latypov, V., Rothenberg, M., Lorenz, A., Octobre, G., Csutak, O., Lehmann, E., Loidl, J., & Kohli, J. (2010). Roles of Hop1 and Mek1 in meiotic chromosome pairing and recombination partner choice in Schizosaccharomyces pombe. *Mol Cell Biol*, *30*(7), 1570-1581. https://doi.org/10.1128/MCB.00919-09

Ledermann, J., Harter, P., Gourley, C., Friedlander, M., Vergote, I., Rustin, G., Scott, C., Meier, W., Shapira-Frommer, R., Safra, T., Matei, D., Macpherson, E., Watkins, C., Carmichael, J., & Matulonis, U. (2012). Olaparib maintenance therapy in platinum-sensitive relapsed ovarian cancer. *N Engl J Med*, *366*(15), 1382-1392. https://doi.org/10.1056/NEJMoa1105535

Ledermann, J., Harter, P., Gourley, C., Friedlander, M., Vergote, I., Rustin, G., Scott, C. L., Meier, W., Shapira-Frommer, R., Safra, T., Matei, D., Fielding, A., Spencer, S., Dougherty, B., Orr, M., Hodgson, D., Barrett, J. C., & Matulonis, U. (2014). Olaparib maintenance therapy in patients with platinum-sensitive relapsed serous ovarian cancer: a preplanned retrospective analysis of outcomes by BRCA status in a randomised phase 2 trial. *Lancet Oncol*, *15*(8), 852-861. https://doi.org/10.1016/S1470-2045(14)70228-1

Lemacon, D., Jackson, J., Quinet, A., Brickner, J. R., Li, S., Yazinski, S., You, Z., Ira, G., Zou, L., Mosammaparast, N., & Vindigni, A. (2017). MRE11 and EXO1 nucleases degrade reversed forks and elicit MUS81-dependent fork rescue in BRCA2-deficient cells. *Nat Commun*, *8*(1), 860. https://doi.org/10.1038/s41467-017-01180-5

Leongamornlert, D., Mahmud, N., Tymrakiewicz, M., Saunders, E., Dadaev, T., Castro, E., Goh, C., Govindasami, K., Guy, M., O'Brien, L., Sawyer, E., Hall, A., Wilkinson, R., Easton, D., Collaborators, U., Goldgar, D., Eeles, R., & Kote-Jarai, Z. (2012). Germline BRCA1 mutations increase prostate cancer risk. *Br J Cancer*, *106*(10), 1697-1701. https://doi.org/10.1038/bjc.2012.146

Leu, J. Y., Chua, P. R., & Roeder, G. S. (1998). The meiosis-specific Hop2 protein of S. cerevisiae ensures synapsis between homologous chromosomes. *Cell*, *94*(3), 375-386. https://doi.org/10.1016/s0092-8674(00)81480-4

Leung, A. K. (2014). Poly(ADP-ribose): an organizer of cellular architecture. *J Cell Biol*, *205*(5), 613-619. https://doi.org/10.1083/jcb.201402114

Lheureux, S., Bruce, J. P., Burnier, J. V., Karakasis, K., Shaw, P. A., Clarke, B. A., Yang, S. Y., Quevedo, R., Li, T., Dowar, M., Bowering, V., Pugh, T. J., & Oza, A. M. (2017). Somatic BRCA1/2 Recovery as a Resistance Mechanism After Exceptional Response to Poly (ADP-ribose) Polymerase Inhibition. *J Clin Oncol*, *35*(11), 1240-1249. https://doi.org/10.1200/JCO.2016.71.3677

Li, B., Navarro, S., Kasahara, N., & Comai, L. (2004). Identification and biochemical characterization of a Werner's syndrome protein complex with Ku70/80 and poly(ADP-ribose) polymerase-1. *J Biol Chem*, *279*(14), 13659-13667. https://doi.org/10.1074/jbc.M311606200

Li, M., & Yu, X. (2013). Function of BRCA1 in the DNA damage response is mediated by ADP-ribosylation. *Cancer Cell*, *23*(5), 693-704. https://doi.org/10.1016/j.ccr.2013.03.025

Li, W., Xu, H., Xiao, T., Cong, L., Love, M. I., Zhang, F., Irizarry, R. A., Liu, J. S., Brown, M., & Liu, X. S. (2014). MAGeCK enables robust identification of essential genes from genome-scale CRISPR/Cas9 knockout screens. *Genome Biol*, *15*(12), 554. https://doi.org/10.1186/s13059-014-0554-4

Li, Z., Golub, E. I., Gupta, R., & Radding, C. M. (1997). Recombination activities of HsDmc1 protein, the meiotic human homolog of RecA protein. *Proc Natl Acad Sci U S A*, *94*(21), 11221-11226. https://doi.org/10.1073/pnas.94.21.11221

Libby, B. J., Reinholdt, L. G., & Schimenti, J. C. (2003). Positional cloning and characterization of Mei1, a vertebrate-specific gene required for normal meiotic chromosome synapsis in mice. *Proc. Natl. Acad. Sci. U. S. A.*, *100*(26), 15706-15711. https://doi.org/10.1073/pnas.2432067100

Lieber, M. R. (2010). The mechanism of double-strand DNA break repair by the nonhomologous DNA end-joining pathway. *Annu Rev Biochem*, *79*, 181-211. https://doi.org/10.1146/annurev.biochem.052308.093131

Lin, F. L., Sperle, K., & Sternberg, N. (1984). Model for homologous recombination during transfer of DNA into mouse L cells: role for DNA ends in the recombination process. *Mol Cell Biol*, *4*(6), 1020-1034. https://doi.org/10.1128/mcb.4.6.1020-1034.1984

Lindahl, T. (1974). An N-glycosidase from Escherichia coli that releases free uracil from DNA containing deaminated cytosine residues. *Proc Natl Acad Sci U S A*, *71*(9), 3649-3653. https://doi.org/10.1073/pnas.71.9.3649

Lindahl, T. (1993). Instability and decay of the primary structure of DNA. *Nature*, *362*(6422), 709-715. https://doi.org/10.1038/362709a0

Lindahl, T., & Nyberg, B. (1972). Rate of depurination of native deoxyribonucleic acid. *Biochemistry*, *11*(19), 3610-3618. https://doi.org/10.1021/bi00769a018

Lisby, M., Barlow, J. H., Burgess, R. C., & Rothstein, R. (2004). Choreography of the DNA damage response: spatiotemporal relationships among checkpoint and repair proteins. *Cell*, *118*(6), 699-713. https://doi.org/10.1016/j.cell.2004.08.015

Litton, J. K., Rugo, H. S., Ettl, J., Hurvitz, S. A., Goncalves, A., Lee, K. H., Fehrenbacher, L., Yerushalmi, R., Mina, L. A., Martin, M., Roche, H., Im, Y. H., Quek, R. G. W., Markova, D., Tudor, I. C., Hannah, A. L., Eiermann, W., & Blum, J. L. (2018). Talazoparib in Patients with Advanced Breast Cancer and a Germline BRCA Mutation. *N Engl J Med*, *379*(8), 753-763. https://doi.org/10.1056/NEJMoa1802905

Liu, C., Wu, J., Paudyal, S. C., You, Z., & Yu, X. (2013). CHFR is important for the first wave of ubiquitination at DNA damage sites. *Nucleic Acids Res*, *41*(3), 1698-1710. https://doi.org/10.1093/nar/gks1278

Llop-Guevara, A., Loibl, S., Villacampa, G., Vladimirova, V., Schneeweiss, A., Karn, T., Zahm, D. M., Herencia-Ropero, A., Jank, P., van Mackelenbergh, M., Fasching, P. A., Marme, F., Stickeler, E., Schem, C., Dienstmann, R., Florian, S., Nekljudova, V., Balmana, J., Hahnen, E., . . . Serra, V. (2021). Association of RAD51 with homologous recombination deficiency (HRD) and clinical outcomes in untreated triple-negative breast cancer (TNBC): analysis of the GeparSixto randomized clinical trial. *Ann Oncol*, *32*(12), 1590-1596. https://doi.org/10.1016/j.annonc.2021.09.003

Loeb, L. A., Springgate, C. F., & Battula, N. (1974). Errors in DNA replication as a basis of malignant changes. *Cancer Res*, *34*(9), 2311-2321. https://www.ncbi.nlm.nih.gov/pubmed/4136142

Lomonosov, M., Anand, S., Sangrithi, M., Davies, R., & Venkitaraman, A. R. (2003). Stabilization of stalled DNA replication forks by the BRCA2 breast cancer susceptibility protein. *Genes Dev*, *17*(24), 3017-3022. https://doi.org/10.1101/gad.279003

Lord, C. J., & Ashworth, A. (2016). BRCAness revisited. *Nat Rev Cancer*, *16*(2), 110-120. https://doi.org/10.1038/nrc.2015.21

Lord, C. J., & Ashworth, A. (2017). PARP inhibitors: Synthetic lethality in the clinic. *Science*, *355*(6330), 1152-1158. https://doi.org/10.1126/science.aam7344

Lord, C. J., McDonald, S., Swift, S., Turner, N. C., & Ashworth, A. (2008). A high-throughput RNA interference screen for DNA repair determinants of PARP inhibitor sensitivity. *DNA Repair (Amst)*, *7*(12), 2010-2019. https://doi.org/10.1016/j.dnarep.2008.08.014

Lovejoy, C. A., & Cortez, D. (2009). Common mechanisms of PIKK regulation. *DNA Repair (Amst)*, *8*(9), 1004-1008. https://doi.org/10.1016/j.dnarep.2009.04.006

Lucchesi, J. C. (1968). Synthetic lethality and semi-lethality among functionally related mutants of Drosophila melanfgaster. *Genetics*, *59*(1), 37-44. https://doi.org/10.1093/genetics/59.1.37

Ludwig, T., Chapman, D. L., Papaioannou, V. E., & Efstratiadis, A. (1997). Targeted mutations of breast cancer susceptibility gene homologs in mice: lethal phenotypes of Brca1, Brca2, Brca1/Brca2, Brca1/p53, and Brca2/p53 nullizygous embryos. *Genes Dev*, *11*(10), 1226-1241. https://doi.org/10.1101/gad.11.10.1226

Luscher, B., Ahel, I., Altmeyer, M., Ashworth, A., Bai, P., Chang, P., Cohen, M., Corda, D., Dantzer, F., Daugherty, M. D., Dawson, T. M., Dawson, V. L., Deindl, S., Fehr, A. R., Feijs, K. L. H., Filippov, D. V., Gagne, J. P., Grimaldi, G., Guettler, S., . . . Ziegler, M. (2021). ADP-ribosyltransferases, an update on function and nomenclature. *FEBS J*. https://doi.org/10.1111/febs.16142

Luscher, B., Ahel, I., Altmeyer, M., Ashworth, A., Bai, P., Chang, P., Cohen, M., Corda, D., Dantzer, F., Daugherty, M. D., Dawson, T. M., Dawson, V. L., Deindl, S., Fehr, A. R., Feijs, K. L. H., Filippov, D. V., Gagne, J. P., Grimaldi, G., Guettler, S., . . . Ziegler, M. (2022). ADP-ribosyltransferases, an update on function and nomenclature. *FEBS J*, *289*(23), 7399-7410. https://doi.org/10.1111/febs.16142

Lux, M. P., Fasching, P. A., & Beckmann, M. W. (2006). Hereditary breast and ovarian cancer: review and future perspectives. *J Mol Med (Berl)*, *84*(1), 16-28. https://doi.org/10.1007/s00109-005-0696-7

Mah, L. J., El-Osta, A., & Karagiannis, T. C. (2010). gammaH2AX: a sensitive molecular marker of DNA damage and repair. *Leukemia*, *24*(4), 679-686. https://doi.org/10.1038/leu.2010.6

Mali, P., Aach, J., Stranges, P. B., Esvelt, K. M., Moosburner, M., Kosuri, S., Yang, L., & Church, G. M. (2013). CAS9 transcriptional activators for target specificity screening and paired nickases for cooperative genome engineering. *Nat Biotechnol*, *31*(9), 833-838. https://doi.org/10.1038/nbt.2675

Marston, N. J., Richards, W. J., Hughes, D., Bertwistle, D., Marshall, C. J., & Ashworth, A. (1999). Interaction between the product of the breast cancer susceptibility gene BRCA2 and DSS1, a protein functionally conserved from

yeast to mammals. *Mol. Cell. Biol.*, *19*(7), 4633-4642. https://doi.org/10.1128/MCB.19.7.4633

Marusyk, A., Almendro, V., & Polyak, K. (2012). Intra-tumour heterogeneity: a looking glass for cancer? *Nat Rev Cancer*, *12*(5), 323-334. https://doi.org/10.1038/nrc3261

Maya-Mendoza, A., Moudry, P., Merchut-Maya, J. M., Lee, M., Strauss, R., & Bartek, J. (2018). High speed of fork progression induces DNA replication stress and genomic instability. *Nature*, *559*(7713), 279-284. https://doi.org/10.1038/s41586-018-0261-5

McCabe, N., Turner, N. C., Lord, C. J., Kluzek, K., Bialkowska, A., Swift, S., Giavara, S., O'Connor, M. J., Tutt, A. N., Zdzienicka, M. Z., Smith, G. C., & Ashworth, A. (2006). Deficiency in the repair of DNA damage by homologous recombination and sensitivity to poly(ADP-ribose) polymerase inhibition. *Cancer Res*, *66*(16), 8109-8115. https://doi.org/10.1158/0008-5472.CAN-06-0140

McGranahan, N., & Swanton, C. (2017). Clonal Heterogeneity and Tumor Evolution: Past, Present, and the Future. *Cell*, *168*(4), 613-628. https://doi.org/10.1016/j.cell.2017.01.018

Merajver, S. D., Frank, T. S., Xu, J., Pham, T. M., Calzone, K. A., Bennett-Baker, P., Chamberlain, J., Boyd, J., Garber, J. E., Collins, F. S., & et al. (1995). Germline BRCA1 mutations and loss of the wild-type allele in tumors from families with early onset breast and ovarian cancer. *Clin Cancer Res*, *1*(5), 539-544. https://www.ncbi.nlm.nih.gov/pubmed/9816013

Mijic, S., Zellweger, R., Chappidi, N., Berti, M., Jacobs, K., Mutreja, K., Ursich, S., Ray Chaudhuri, A., Nussenzweig, A., Janscak, P., & Lopes, M. (2017). Replication fork reversal triggers fork degradation in BRCA2-defective cells. *Nat Commun*, *8*(1), 859. https://doi.org/10.1038/s41467-017-01164-5

Miki, Y., Swensen, J., Shattuck-Eidens, D., Futreal, P. A., Harshman, K., Tavtigian, S., Liu, Q., Cochran, C., Bennett, L. M., Ding, W., & et al. (1994). A strong candidate for the breast and ovarian cancer susceptibility gene BRCA1. *Science*, *266*(5182), 66-71. https://doi.org/10.1126/science.7545954

Mimitou, E. P., & Symington, L. S. (2008). Sae2, Exo1 and Sgs1 collaborate in DNA double-strand break processing. *Nature*, *455*(7214), 770-774. https://doi.org/10.1038/nature07312

Mirman, Z., Sasi, N. K., King, A., Chapman, J. R., & de Lange, T. (2022). 53BP1-shieldin-dependent DSB processing in BRCA1-deficient cells requires CST-Polalpha-primase fill-in synthesis. *Nat Cell Biol*, *24*(1), 51-61. https://doi.org/10.1038/s41556-021-00812-9

Mirza, M. R., Monk, B. J., Herrstedt, J., Oza, A. M., Mahner, S., Redondo, A., Fabbro, M., Ledermann, J. A., Lorusso, D., Vergote, I., Ben-Baruch, N. E., Marth, C., Madry, R., Christensen, R. D., Berek, J. S., Dorum, A., Tinker, A. V., du Bois, A., Gonzalez-Martin, A., . . . Investigators, E.-O. N. (2016). Niraparib Maintenance Therapy in Platinum-Sensitive, Recurrent Ovarian

Cancer. *N Engl J Med*, *375*(22), 2154-2164. https://doi.org/10.1056/NEJMoa1611310

Modrich, P., & Lahue, R. (1996). Mismatch repair in replication fidelity, genetic recombination, and cancer biology. *Annu Rev Biochem*, *65*, 101-133. https://doi.org/10.1146/annurev.bi.65.070196.000533

Moore, K., Colombo, N., Scambia, G., Kim, B. G., Oaknin, A., Friedlander, M., Lisyanskaya, A., Floquet, A., Leary, A., Sonke, G. S., Gourley, C., Banerjee, S., Oza, A., Gonzalez-Martin, A., Aghajanian, C., Bradley, W., Mathews, C., Liu, J., Lowe, E. S., . . . DiSilvestro, P. (2018). Maintenance Olaparib in Patients with Newly Diagnosed Advanced Ovarian Cancer. *N Engl J Med*, *379*(26), 2495-2505. https://doi.org/10.1056/NEJMoa1810858

Moore, K. N., Secord, A. A., Geller, M. A., Miller, D. S., Cloven, N., Fleming, G. F., Wahner Hendrickson, A. E., Azodi, M., DiSilvestro, P., Oza, A. M., Cristea, M., Berek, J. S., Chan, J. K., Rimel, B. J., Matei, D. E., Li, Y., Sun, K., Luptakova, K., Matulonis, U. A., & Monk, B. J. (2019). Niraparib monotherapy for late-line treatment of ovarian cancer (QUADRA): a multicentre, open-label, single-arm, phase 2 trial. *Lancet Oncol*, *20*(5), 636-648. https://doi.org/10.1016/S1470-2045(19)30029-4

Murai, J., Huang, S. Y., Das, B. B., Renaud, A., Zhang, Y., Doroshow, J. H., Ji, J., Takeda, S., & Pommier, Y. (2012). Trapping of PARP1 and PARP2 by Clinical PARP Inhibitors. *Cancer Res*, *72*(21), 5588-5599. https://doi.org/10.1158/0008-5472.CAN-12-2753

Murai, J., Huang, S. Y., Renaud, A., Zhang, Y., Ji, J., Takeda, S., Morris, J., Teicher, B., Doroshow, J. H., & Pommier, Y. (2014). Stereospecific PARP trapping by BMN 673 and comparison with olaparib and rucaparib. *Mol Cancer Ther*, *13*(2), 433-443. https://doi.org/10.1158/1535-7163.MCT-13-0803

Murai, J., Zhang, Y., Morris, J., Ji, J., Takeda, S., Doroshow, J. H., & Pommier, Y. (2014). Rationale for poly(ADP-ribose) polymerase (PARP) inhibitors in combination therapy with camptothecins or temozolomide based on PARP trapping versus catalytic inhibition. *J Pharmacol Exp Ther*, *349*(3), 408-416. https://doi.org/10.1124/jpet.113.210146

Nakatani, Y., & Ogryzko, V. (2003). Immunoaffinity purification of mammalian protein complexes. *Methods Enzymol*, *370*, 430-444. https://doi.org/10.1016/S0076-6879(03)70037-8

Nassif, N., Penney, J., Pal, S., Engels, W. R., & Gloor, G. B. (1994). Efficient copying of nonhomologous sequences from ectopic sites via P-element-induced gap repair. *Mol Cell Biol*, *14*(3), 1613-1625. https://doi.org/10.1128/mcb.14.3.1613-1625.1994

Neale, M. J., & Keeney, S. (2006). Clarifying the mechanics of DNA strand exchange in meiotic recombination. *Nature*, *442*(7099), 153-158. https://doi.org/10.1038/nature04885

Negrini, S., Gorgoulis, V. G., & Halazonetis, T. D. (2010). Genomic instability--an evolving hallmark of cancer. *Nat Rev Mol Cell Biol*, *11*(3), 220-228. https://doi.org/10.1038/nrm2858

Nichols, B. A., Oswald, N. W., McMillan, E. A., McGlynn, K., Yan, J., Kim, M. S., Saha, J., Mallipeddi, P. L., LaDuke, S. A., Villalobos, P. A., Rodriguez-Canales, J., Wistuba, II, Posner, B. A., Davis, A. J., Minna, J. D., MacMillan, J. B., & Whitehurst, A. W. (2018). HORMAD1 Is a Negative Prognostic Indicator in Lung Adenocarcinoma and Specifies Resistance to Oxidative and Genotoxic Stress. *Cancer Res*, *78*(21), 6196-6208. https://doi.org/10.1158/0008-5472.CAN-18-1377

Nimonkar, A. V., Genschel, J., Kinoshita, E., Polaczek, P., Campbell, J. L., Wyman, C., Modrich, P., & Kowalczykowski, S. C. (2011). BLM-DNA2-RPA-MRN and EXO1-BLM-RPA-MRN constitute two DNA end resection machineries for human DNA break repair. *Genes Dev*, *25*(4), 350-362. https://doi.org/10.1101/gad.2003811

Nimonkar, A. V., & Kowalczykowski, S. C. (2009). Second-end DNA capture in double-strand break repair: how to catch a DNA by its tail. *Cell Cycle*, *8*(12), 1816-1817. https://doi.org/10.4161/cc.8.12.8935

Niu, H., Wan, L., Baumgartner, B., Schaefer, D., Loidl, J., & Hollingsworth, N. M. (2005). Partner choice during meiosis is regulated by Hop1-promoted dimerization of Mek1. *Mol Biol Cell*, *16*(12), 5804-5818. https://doi.org/10.1091/mbc.e05-05-0465

Noordermeer, S. M., Adam, S., Setiaputra, D., Barazas, M., Pettitt, S. J., Ling, A. K., Olivieri, M., Alvarez-Quilon, A., Moatti, N., Zimmermann, M., Annunziato, S., Krastev, D. B., Song, F., Brandsma, I., Frankum, J., Brough, R., Sherker, A., Landry, S., Szilard, R. K., . . . Durocher, D. (2018). The shieldin complex mediates 53BP1-dependent DNA repair. *Nature*, *560*(7716), 117-121. https://doi.org/10.1038/s41586-018-0340-7

Norquist, B., Wurz, K. A., Pennil, C. C., Garcia, R., Gross, J., Sakai, W., Karlan, B. Y., Taniguchi, T., & Swisher, E. M. (2011). Secondary somatic mutations restoring BRCA1/2 predict chemotherapy resistance in hereditary ovarian carcinomas. *J Clin Oncol*, *29*(22), 3008-3015. https://doi.org/10.1200/JCO.2010.34.2980

Nowell, P. C. (1976). The clonal evolution of tumor cell populations. *Science*, *194*(4260), 23-28. https://doi.org/10.1126/science.959840

Oh, J. M., Venters, C. C., Di, C., Pinto, A. M., Wan, L., Younis, I., Cai, Z., Arai, C., So, B. R., Duan, J., & Dreyfuss, G. (2020). U1 snRNP regulates cancer cell migration and invasion in vitro. *Nat Commun*, *11*(1), 1. https://doi.org/10.1038/s41467-019-13993-7

Oka, S., Kato, J., & Moss, J. (2006). Identification and characterization of a mammalian 39-kDa poly(ADP-ribose) glycohydrolase. *J Biol Chem*, *281*(2), 705-713. https://doi.org/10.1074/jbc.M510290200

Olivieri, M., Cho, T., Alvarez-Quilon, A., Li, K., Schellenberg, M. J., Zimmermann, M., Hustedt, N., Rossi, S. E., Adam, S., Melo, H., Heijink, A. M., Sastre-Moreno, G., Moatti, N., Szilard, R. K., McEwan, A., Ling, A. K., Serrano-Benitez, A., Ubhi, T., Feng, S., . . . Durocher, D. (2020). A Genetic Map of the Response to DNA Damage in Human Cells. *Cell*, *182*(2), 481-496 e421. https://doi.org/10.1016/j.cell.2020.05.040

Orr-Weaver, T. L., Szostak, J. W., & Rothstein, R. J. (1981). Yeast transformation: a model system for the study of recombination. *Proc Natl Acad Sci U S A*, *78*(10), 6354-6358. https://doi.org/10.1073/pnas.78.10.6354

Oza, A. M., Tinker, A. V., Oaknin, A., Shapira-Frommer, R., McNeish, I. A., Swisher, E. M., Ray-Coquard, I., Bell-McGuinn, K., Coleman, R. L., O'Malley, D. M., Leary, A., Chen, L. M., Provencher, D., Ma, L., Brenton, J. D., Konecny, G. E., Castro, C. M., Giordano, H., Maloney, L., . . . Kristeleit, R. S. (2017). Antitumor activity and safety of the PARP inhibitor rucaparib in patients with high-grade ovarian carcinoma and a germline or somatic BRCA1 or BRCA2 mutation: Integrated analysis of data from Study 10 and ARIEL2. *Gynecol Oncol*, *147*(2), 267-275. https://doi.org/10.1016/j.ygyno.2017.08.022

Pantelidou, C., Sonzogni, O., De Oliveria Taveira, M., Mehta, A. K., Kothari, A., Wang, D., Visal, T., Li, M. K., Pinto, J., Castrillon, J. A., Cheney, E. M., Bouwman, P., Jonkers, J., Rottenberg, S., Guerriero, J. L., Wulf, G. M., & Shapiro, G. I. (2019). PARP Inhibitor Efficacy Depends on CD8(+) T-cell Recruitment via Intratumoral STING Pathway Activation in BRCA-Deficient Models of Triple-Negative Breast Cancer. *Cancer Discov*, *9*(6), 722-737. https://doi.org/10.1158/2159-8290.CD-18-1218

Parkes, E. E., Walker, S. M., Taggart, L. E., McCabe, N., Knight, L. A., Wilkinson, R., McCloskey, K. D., Buckley, N. E., Savage, K. I., Salto-Tellez, M., McQuaid, S., Harte, M. T., Mullan, P. B., Harkin, D. P., & Kennedy, R. D. (2017). Activation of STING-Dependent Innate Immune Signaling By S-Phase-Specific DNA Damage in Breast Cancer. *J Natl Cancer Inst*, *109*(1). https://doi.org/10.1093/jnci/djw199

Parvanov, E. D., Petkov, P. M., & Paigen, K. (2010). Prdm9 controls activation of mammalian recombination hotspots. *Science*, *327*(5967), 835. https://doi.org/10.1126/science.1181495

Patch, A. M., Christie, E. L., Etemadmoghadam, D., Garsed, D. W., George, J., Fereday, S., Nones, K., Cowin, P., Alsop, K., Bailey, P. J., Kassahn, K. S., Newell, F., Quinn, M. C., Kazakoff, S., Quek, K., Wilhelm-Benartzi, C., Curry, E., Leong, H. S., Australian Ovarian Cancer Study, G., . . . Bowtell, D. D. (2015). Whole-genome characterization of chemoresistant ovarian cancer. *Nature*, *521*(7553), 489-494. https://doi.org/10.1038/nature14410

Patel, K. J., Yu, V. P., Lee, H., Corcoran, A., Thistlethwaite, F. C., Evans, M. J., Colledge, W. H., Friedman, L. S., Ponder, B. A., & Venkitaraman, A. R. (1998). Involvement of Brca2 in DNA repair. *Mol Cell*, *1*(3), 347-357. https://doi.org/10.1016/s1097-2765(00)80035-0

Peng, M., Bakker, J. L., Dicioccio, R. A., Gille, J. J., Zhao, H., Odunsi, K., Sucheston, L., Jaafar, L., Mivechi, N. F., Waisfisz, Q., & Ko, L. (2013). Inactivating Mutations in GT198 in Familial and Early-Onset Breast and Ovarian Cancers. *Genes Cancer*, *4*(1-2), 15-25. https://doi.org/10.1177/1947601913486344

Peng, M., Yang, Z., Zhang, H., Jaafar, L., Wang, G., Liu, M., Flores-Rozas, H., Xu, J., Mivechi, N. F., & Ko, L. (2013). GT198 Splice Variants Display Dominant-Negative Activities and Are Induced by Inactivating Mutations. *Genes Cancer*, *4*(1-2), 26-38. https://doi.org/10.1177/1947601913486345

Petrucelli, N., Daly, M. B., & Pal, T. (1993). BRCA1- and BRCA2-Associated Hereditary Breast and Ovarian Cancer. In M. P. Adam, D. B. Everman, G. M. Mirzaa, R. A. Pagon, S. E. Wallace, L. J. H. Bean, K. W. Gripp, & A. Amemiya (Eds.), *GeneReviews((R))*. https://www.ncbi.nlm.nih.gov/pubmed/20301425

Pettitt, S. J., Frankum, J. R., Punta, M., Lise, S., Alexander, J., Chen, Y., Yap, T. A., Haider, S., Tutt, A. N. J., & Lord, C. J. (2020). Clinical BRCA1/2 Reversion Analysis Identifies Hotspot Mutations and Predicted Neoantigens Associated with Therapy Resistance. *Cancer Discov*, *10*(10), 1475-1488. https://doi.org/10.1158/2159-8290.CD-19-1485

Pettitt, S. J., Krastev, D. B., Brandsma, I., Drean, A., Song, F., Aleksandrov, R., Harrell, M. I., Menon, M., Brough, R., Campbell, J., Frankum, J., Ranes, M., Pemberton, H. N., Rafiq, R., Fenwick, K., Swain, A., Guettler, S., Lee, J. M., Swisher, E. M., . . . Lord, C. J. (2018). Genome-wide and high-density CRISPR-Cas9 screens identify point mutations in PARP1 causing PARP inhibitor resistance. *Nat Commun*, *9*(1), 1849. https://doi.org/10.1038/s41467-018-03917-2

Pettitt, S. J., Rehman, F. L., Bajrami, I., Brough, R., Wallberg, F., Kozarewa, I., Fenwick, K., Assiotis, I., Chen, L., Campbell, J., Lord, C. J., & Ashworth, A. (2013). A genetic screen using the PiggyBac transposon in haploid cells identifies Parp1 as a mediator of olaparib toxicity. *PLoS One*, *8*(4), e61520. https://doi.org/10.1371/journal.pone.0061520

Petukhova, G. V., Romanienko, P. J., & Camerini-Otero, R. D. (2003). The Hop2 protein has a direct role in promoting interhomolog interactions during mouse meiosis. *Dev Cell*, *5*(6), 927-936. https://doi.org/10.1016/s1534-5807(03)00369-1

Pezza, R. J., Voloshin, O. N., Vanevski, F., & Camerini-Otero, R. D. (2007). Hop2/Mnd1 acts on two critical steps in Dmc1-promoted homologous pairing. *Genes Dev*, *21*(14), 1758-1766. https://doi.org/10.1101/gad.1562907

Pishvaian, M. J., Biankin, A. V., Bailey, P., Chang, D. K., Laheru, D., Wolfgang, C. L., & Brody, J. R. (2017). BRCA2 secondary mutation-mediated resistance to platinum and PARP inhibitor-based therapy in pancreatic cancer. *Br J Cancer*, *116*(8), 1021-1026. https://doi.org/10.1038/bjc.2017.40

Plummer, R., Lorigan, P., Steven, N., Scott, L., Middleton, M. R., Wilson, R. H., Mulligan, E., Curtin, N., Wang, D., Dewji, R., Abbattista, A., Gallo, J., & Calvert, H. (2013). A phase II study of the potent PARP inhibitor, Rucaparib (PF-01367338, AG014699), with temozolomide in patients with metastatic melanoma demonstrating evidence of chemopotentiation. *Cancer Chemother Pharmacol*, *71*(5), 1191-1199. https://doi.org/10.1007/s00280-013-2113-1

Pommier, Y., O'Connor, M. J., & de Bono, J. (2016). Laying a trap to kill cancer cells: PARP inhibitors and their mechanisms of action. *Sci Transl Med*, *8*(362), 362ps317. https://doi.org/10.1126/scitranslmed.aaf9246

Powers, N. R., Parvanov, E. D., Baker, C. L., Walker, M., Petkov, P. M., & Paigen, K. (2016). The meiotic recombination activator PRDM9 trimethylates both H3K36 and H3K4 at recombination hotspots in vivo. *PLoS Genet.*, *12*(6), e1006146. https://doi.org/10.1371/journal.pgen.1006146

Pujade-Lauraine, E., Ledermann, J. A., Selle, F., Gebski, V., Penson, R. T., Oza, A. M., Korach, J., Huzarski, T., Poveda, A., Pignata, S., Friedlander, M., Colombo, N., Harter, P., Fujiwara, K., Ray-Coquard, I., Banerjee, S., Liu, J., Lowe, E. S., Bloomfield, R., . . . investigators, S. O. E.-O. (2017). Olaparib tablets as maintenance therapy in patients with platinum-sensitive, relapsed ovarian cancer and a BRCA1/2 mutation (SOLO2/ENGOT-Ov21): a double-blind, randomised, placebo-controlled, phase 3 trial. *Lancet Oncol*, *18*(9), 1274-1284. https://doi.org/10.1016/S1470-2045(17)30469-2

Purnell, M. R., Stone, P. R., & Whish, W. J. (1980). ADP-ribosylation of nuclear proteins. *Biochem Soc Trans*, *8*(2), 215-227. https://doi.org/10.1042/bst0080215

Qiu, S., Jiang, G., Cao, L., & Huang, J. (2021). Replication Fork Reversal and Protection. *Front Cell Dev Biol*, *9*, 670392. https://doi.org/10.3389/fcell.2021.670392

Quereda, V., Bayle, S., Vena, F., Frydman, S. M., Monastyrskyi, A., Roush, W. R., & Duckett, D. R. (2019). Therapeutic Targeting of CDK12/CDK13 in Triple-Negative Breast Cancer. *Cancer Cell*, *36*(5), 545-558 e547. https://doi.org/10.1016/j.ccell.2019.09.004

Ramalingam, S. S., Blais, N., Mazieres, J., Reck, M., Jones, C. M., Juhasz, E., Urban, L., Orlov, S., Barlesi, F., Kio, E., Keiholz, U., Qin, Q., Qian, J., Nickner, C., Dziubinski, J., Xiong, H., Ansell, P., McKee, M., Giranda, V., & Gorbunova, V. (2017). Randomized, Placebo-Controlled, Phase II Study of Veliparib in Combination with Carboplatin and Paclitaxel for Advanced/Metastatic Non-Small Cell Lung Cancer. *Clin Cancer Res*, *23*(8), 1937-1944. https://doi.org/10.1158/1078-0432.CCR-15-3069

Ramalingam, S. S., Novello, S., Guclu, S. Z., Bentsion, D., Zvirbule, Z., Szilasi, M., Bernabe, R., Syrigos, K., Byers, L. A., Clingan, P., Bar, J., Vokes, E. E., Govindan, R., Dunbar, M., Ansell, P., He, L., Huang, X., Sehgal, V., Glasgow, J., . . . Mazieres, J. (2021). Veliparib in Combination With Platinum-Based Chemotherapy for First-Line Treatment of Advanced

Squamous Cell Lung Cancer: A Randomized, Multicenter Phase III Study. *J Clin Oncol*, *39*(32), 3633-3644. https://doi.org/10.1200/JCO.20.03318

Ran, F. A., Hsu, P. D., Wright, J., Agarwala, V., Scott, D. A., & Zhang, F. (2013). Genome engineering using the CRISPR-Cas9 system. *Nat Protoc*, *8*(11), 2281-2308. https://doi.org/10.1038/nprot.2013.143

Ray Chaudhuri, A., Callen, E., Ding, X., Gogola, E., Duarte, A. A., Lee, J. E., Wong, N., Lafarga, V., Calvo, J. A., Panzarino, N. J., John, S., Day, A., Crespo, A. V., Shen, B., Starnes, L. M., de Ruiter, J. R., Daniel, J. A., Konstantinopoulos, P. A., Cortez, D., . . . Nussenzweig, A. (2016). Replication fork stability confers chemoresistance in BRCA-deficient cells. *Nature*, *535*(7612), 382-387. https://doi.org/10.1038/nature18325

Ray Chaudhuri, A., Hashimoto, Y., Herrador, R., Neelsen, K. J., Fachinetti, D., Bermejo, R., Cocito, A., Costanzo, V., & Lopes, M. (2012). Topoisomerase I poisoning results in PARP-mediated replication fork reversal. *Nat Struct Mol Biol*, *19*(4), 417-423. https://doi.org/10.1038/nsmb.2258

Ray Chaudhuri, A., & Nussenzweig, A. (2017). The multifaceted roles of PARP1 in DNA repair and chromatin remodelling. *Nat Rev Mol Cell Biol*, *18*(10), 610-621. https://doi.org/10.1038/nrm.2017.53

Ray-Coquard, I., Pautier, P., Pignata, S., Perol, D., Gonzalez-Martin, A., Berger, R., Fujiwara, K., Vergote, I., Colombo, N., Maenpaa, J., Selle, F., Sehouli, J., Lorusso, D., Guerra Alia, E. M., Reinthaller, A., Nagao, S., Lefeuvre-Plesse, C., Canzler, U., Scambia, G., . . . Investigators, P.-. (2019). Olaparib plus Bevacizumab as First-Line Maintenance in Ovarian Cancer. *N Engl J Med*, *381*(25), 2416-2428. https://doi.org/10.1056/NEJMoa1911361

Richardson, C., & Jasin, M. (2000). Frequent chromosomal translocations induced by DNA double-strand breaks. *Nature*, *405*(6787), 697-700. https://doi.org/10.1038/35015097

Robert, I., Dantzer, F., & Reina-San-Martin, B. (2009). Parp1 facilitates alternative NHEJ, whereas Parp2 suppresses IgH/c-myc translocations during immunoglobulin class switch recombination. *J Exp Med*, *206*(5), 1047-1056. https://doi.org/10.1084/jem.20082468

Robson, M., Im, S. A., Senkus, E., Xu, B., Domchek, S. M., Masuda, N., Delaloge, S., Li, W., Tung, N., Armstrong, A., Wu, W., Goessl, C., Runswick, S., & Conte, P. (2017). Olaparib for Metastatic Breast Cancer in Patients with a Germline BRCA Mutation. *N Engl J Med*, *377*(6), 523-533. https://doi.org/10.1056/NEJMoa1706450

Roerink, S. F., van Schendel, R., & Tijsterman, M. (2014). Polymerase theta-mediated end joining of replication-associated DNA breaks in C. elegans. *Genome Res*, *24*(6), 954-962. https://doi.org/10.1101/gr.170431.113

Romanienko, P. J., & Camerini-Otero, R. D. (2000). The mouse Spo11 gene is required for meiotic chromosome synapsis. *Mol Cell*, *6*(5), 975-987. https://doi.org/10.1016/s1097-2765(00)00097-6

Rondinelli, B., Gogola, E., Yucel, H., Duarte, A. A., van de Ven, M., van der Sluijs, R., Konstantinopoulos, P. A., Jonkers, J., Ceccaldi, R., Rottenberg, S., & D'Andrea, A. D. (2017). EZH2 promotes degradation of stalled replication forks by recruiting MUS81 through histone H3 trimethylation. *Nat Cell Biol*, *19*(11), 1371-1378. https://doi.org/10.1038/ncb3626

Roos, W. P., & Kaina, B. (2006). DNA damage-induced cell death by apoptosis. *Trends Mol Med*, *12*(9), 440-450. https://doi.org/10.1016/j.molmed.2006.07.007

Rottenberg, S., Jaspers, J. E., Kersbergen, A., van der Burg, E., Nygren, A. O., Zander, S. A., Derksen, P. W., de Bruin, M., Zevenhoven, J., Lau, A., Boulter, R., Cranston, A., O'Connor, M. J., Martin, N. M., Borst, P., & Jonkers, J. (2008). High sensitivity of BRCA1-deficient mammary tumors to the PARP inhibitor AZD2281 alone and in combination with platinum drugs. *Proc Natl Acad Sci U S A*, *105*(44), 17079-17084. https://doi.org/10.1073/pnas.0806092105

Roy, S., & Schlacher, K. (2019). SIRF: A Single-cell Assay for in situ Protein Interaction with Nascent DNA Replication Forks. *Bio Protoc*, *9*(18), e3377. https://doi.org/10.21769/BioProtoc.3377

Ryan, C. J., Bajrami, I., & Lord, C. J. (2018). Synthetic Lethality and Cancer - Penetrance as the Major Barrier. Trends Cancer, 4(10), 671-683. https://doi.org/10.1016/j.trecan.2018.08.003

Sakai, W., Swisher, E. M., Jacquemont, C., Chandramohan, K. V., Couch, F. J., Langdon, S. P., Wurz, K., Higgins, J., Villegas, E., & Taniguchi, T. (2009). Functional restoration of BRCA2 protein by secondary BRCA2 mutations in BRCA2-mutated ovarian carcinoma. *Cancer Res*, *69*(16), 6381-6386. https://doi.org/10.1158/0008-5472.CAN-09-1178

Sakai, W., Swisher, E. M., Karlan, B. Y., Agarwal, M. K., Higgins, J., Friedman, C., Villegas, E., Jacquemont, C., Farrugia, D. J., Couch, F. J., Urban, N., & Taniguchi, T. (2008). Secondary mutations as a mechanism of cisplatin resistance in BRCA2-mutated cancers. *Nature*, *451*(7182), 1116-1120. https://doi.org/10.1038/nature06633

San Filippo, J., Sung, P., & Klein, H. (2008). Mechanism of eukaryotic homologous recombination. *Annu Rev Biochem*, *77*, 229-257. https://doi.org/10.1146/annurev.biochem.77.061306.125255

Sancar, A. (1996). DNA excision repair. *Annu Rev Biochem*, *65*, 43-81. https://doi.org/10.1146/annurev.bi.65.070196.000355

Sansam, C. L., & Pezza, R. J. (2015). Connecting by breaking and repairing: mechanisms of DNA strand exchange in meiotic recombination. *FEBS J*, *282*(13), 2444-2457. https://doi.org/10.1111/febs.13317

Sartori, A. A., Lukas, C., Coates, J., Mistrik, M., Fu, S., Bartek, J., Baer, R., Lukas, J., & Jackson, S. P. (2007). Human CtIP promotes DNA end resection. *Nature*, *450*(7169), 509-514. https://doi.org/10.1038/nature06337

Satoh, M. S., & Lindahl, T. (1992). Role of poly(ADP-ribose) formation in DNA repair. *Nature*, *356*(6367), 356-358. https://doi.org/10.1038/356356a0

Schlacher, K., Wu, H., & Jasin, M. (2012). A distinct replication fork protection pathway connects Fanconi anemia tumor suppressors to RAD51-BRCA1/2. *Cancer Cell*, *22*(1), 106-116. https://doi.org/10.1016/j.ccr.2012.05.015

Schmid, J. A., Berti, M., Walser, F., Raso, M. C., Schmid, F., Krietsch, J., Stoy, H., Zwicky, K., Ursich, S., Freire, R., Lopes, M., & Penengo, L. (2018). Histone Ubiquitination by the DNA Damage Response Is Required for Efficient DNA Replication in Unperturbed S Phase. *Mol Cell*, *71*(6), 897-910 e898. https://doi.org/10.1016/j.molcel.2018.07.011

Schroeder, T. M., & Kurth, R. (1971). Spontaneous chromosomal breakage and high incidence of leukemia in inherited disease. *Blood*, *37*(1), 96-112. https://www.ncbi.nlm.nih.gov/pubmed/5539134

Schwacha, A., & Kleckner, N. (1997). Interhomolog bias during meiotic recombination: meiotic functions promote a highly differentiated interhomolog-only pathway. *Cell*, *90*(6), 1123-1135. https://doi.org/10.1016/s0092-8674(00)80378-5

Scully, R., Ganesan, S., Vlasakova, K., Chen, J., Socolovsky, M., & Livingston, D. M. (1999). Genetic analysis of BRCA1 function in a defined tumor cell line. *Mol Cell*, *4*(6), 1093-1099. https://doi.org/10.1016/s1097-2765(00)80238-5

Shalem, O., Sanjana, N. E., Hartenian, E., Shi, X., Scott, D. A., Mikkelson, T., Heckl, D., Ebert, B. L., Root, D. E., Doench, J. G., & Zhang, F. (2014). Genome-scale CRISPR-Cas9 knockout screening in human cells. *Science*, *343*(6166), 84-87. https://doi.org/10.1126/science.1247005

Sharan, S. K., Morimatsu, M., Albrecht, U., Lim, D. S., Regel, E., Dinh, C., Sands, A., Eichele, G., Hasty, P., & Bradley, A. (1997). Embryonic lethality and radiation hypersensitivity mediated by Rad51 in mice lacking Brca2. *Nature*, *386*(6627), 804-810. https://doi.org/10.1038/386804a0

Shen, S. X., Weaver, Z., Xu, X., Li, C., Weinstein, M., Chen, L., Guan, X. Y., Ried, T., & Deng, C. X. (1998). A targeted disruption of the murine Brca1 gene causes gamma-irradiation hypersensitivity and genetic instability. *Oncogene*, *17*(24), 3115-3124. https://doi.org/10.1038/sj.onc.1202243

Shen, Y., Rehman, F. L., Feng, Y., Boshuizen, J., Bajrami, I., Elliott, R., Wang, B., Lord, C. J., Post, L. E., & Ashworth, A. (2013). BMN 673, a novel and highly potent PARP1/2 inhibitor for the treatment of human cancers with DNA repair deficiency. *Clin Cancer Res*, *19*(18), 5003-5015. https://doi.org/10.1158/1078-0432.CCR-13-1391

Shibata, A. (2017). Regulation of repair pathway choice at two-ended DNA double-strand breaks. Mutat Res, 803-805, 51-55. https://doi.org/10.1016/j.mrfmmm.2017.07.011

Shin, Y. H., McGuire, M. M., & Rajkovic, A. (2013). Mouse HORMAD1 is a meiosis i checkpoint protein that modulates DNA double- strand break repair during

female meiosis. *Biol Reprod*, *89*(2), 29. https://doi.org/10.1095/biolreprod.112.106773

Shkundina, I. S., Gall, A. A., Dick, A., Cocklin, S., & Mazin, A. V. (2021). New RAD51 Inhibitors to Target Homologous Recombination in Human Cells. *Genes (Basel)*, *12*(6). https://doi.org/10.3390/genes12060920

Sigurdsson, S., Van Komen, S., Petukhova, G., & Sung, P. (2002). Homologous DNA pairing by human recombination factors Rad51 and Rad54. *J. Biol. Chem.*, *277*(45), 42790-42794. https://doi.org/10.1074/jbc.M208004200

Skidmore, C. J., Davies, M. I., Goodwin, P. M., Halldorsson, H., Lewis, P. J., Shall, S., & Zia'ee, A. A. (1979). The involvement of poly(ADP-ribose) polymerase in the degradation of NAD caused by gamma-radiation and N-methyl-N-nitrosourea. *Eur J Biochem*, *101*(1), 135-142. https://doi.org/10.1111/j.1432-1033.1979.tb04225.x

Soule, H. D., Maloney, T. M., Wolman, S. R., Peterson, W. D., Jr., Brenz, R., McGrath, C. M., Russo, J., Pauley, R. J., Jones, R. F., & Brooks, S. C. (1990). Isolation and characterization of a spontaneously immortalized human breast epithelial cell line, MCF-10. *Cancer Res*, *50*(18), 6075-6086. https://www.ncbi.nlm.nih.gov/pubmed/1975513

Stadler, Z. K., Salo-Mullen, E., Patil, S. M., Pietanza, M. C., Vijai, J., Saloustros, E., Hansen, N. A., Kauff, N. D., Kurtz, R. C., Kelsen, D. P., Offit, K., & Robson, M. E. (2012). Prevalence of BRCA1 and BRCA2 mutations in Ashkenazi Jewish families with breast and pancreatic cancer. *Cancer*, *118*(2), 493-499. https://doi.org/10.1002/cncr.26191

Stanzione, M., Baumann, M., Papanikos, F., Dereli, I., Lange, J., Ramlal, A., Tränkner, D., Shibuya, H., de Massy, B., Watanabe, Y., Jasin, M., Keeney, S., & Tóth, A. (2016). Meiotic DNA break formation requires the unsynapsed chromosome axis-binding protein IHO1 (CCDC36) in mice. *Nat. Cell Biol.*, *18*(11), 1208-1220. https://doi.org/10.1038/ncb3417

Stratton, M. R., Campbell, P. J., & Futreal, P. A. (2009). The cancer genome. *Nature*, *458*(7239), 719-724. https://doi.org/10.1038/nature07943

Sturzenegger, A., Burdova, K., Kanagaraj, R., Levikova, M., Pinto, C., Cejka, P., & Janscak, P. (2014). DNA2 cooperates with the WRN and BLM RecQ helicases to mediate long-range DNA end resection in human cells. *J. Biol. Chem.*, *289*(39), 27314-27326. https://doi.org/10.1074/jbc.M114.578823

Sugiyama, T., Kantake, N., Wu, Y., & Kowalczykowski, S. C. (2006). Rad52-mediated DNA annealing after Rad51-mediated DNA strand exchange promotes second ssDNA capture. *EMBO J.*, *25*(23), 5539-5548. https://doi.org/10.1038/sj.emboj.7601412

Sugiyama, T., New, J. H., & Kowalczykowski, S. C. (1998). DNA annealing by RAD52 protein is stimulated by specific interaction with the complex of replication protein A and single-stranded DNA. *Proc. Natl. Acad. Sci. U. S. A.*, *95*(11), 6049-6054. https://doi.org/10.1073/pnas.95.11.6049

Sugiyama, T., Zaitseva, E. M., & Kowalczykowski, S. C. (1997). A single-stranded DNA-binding protein is needed for efficient presynaptic complex formation by the Saccharomyces cerevisiae Rad51 protein. *J Biol Chem*, *272*(12), 7940-7945. https://doi.org/10.1074/jbc.272.12.7940

Swisher, E. M., Lin, K. K., Oza, A. M., Scott, C. L., Giordano, H., Sun, J., Konecny, G. E., Coleman, R. L., Tinker, A. V., O'Malley, D. M., Kristeleit, R. S., Ma, L., Bell-McGuinn, K. M., Brenton, J. D., Cragun, J. M., Oaknin, A., Ray-Coquard, I., Harrell, M. I., Mann, E., . . . McNeish, I. A. (2017). Rucaparib in relapsed, platinum-sensitive high-grade ovarian carcinoma (ARIEL2 Part 1): an international, multicentre, open-label, phase 2 trial. *Lancet Oncol*, *18*(1), 75-87. https://doi.org/10.1016/S1470-2045(16)30559-9

Sy, S. M., Huen, M. S., & Chen, J. (2009). PALB2 is an integral component of the BRCA complex required for homologous recombination repair. Proc Natl Acad Sci U S A, 106(17), 7155-7160. https://doi.org/10.1073/pnas.0811159106

Szostak, J. W., Orr-Weaver, T. L., Rothstein, R. J., & Stahl, F. W. (1983). The double-strand-break repair model for recombination. *Cell*, *33*(1), 25-35. https://doi.org/10.1016/0092-8674(83)90331-8

Taglialatela, A., Alvarez, S., Leuzzi, G., Sannino, V., Ranjha, L., Huang, J. W., Madubata, C., Anand, R., Levy, B., Rabadan, R., Cejka, P., Costanzo, V., & Ciccia, A. (2017). Restoration of Replication Fork Stability in BRCA1- and BRCA2-Deficient Cells by Inactivation of SNF2-Family Fork Remodelers. *Mol Cell*, *68*(2), 414-430 e418. https://doi.org/10.1016/j.molcel.2017.09.036

Taylor, A. M., Shih, J., Ha, G., Gao, G. F., Zhang, X., Berger, A. C., Schumacher, S. E., Wang, C., Hu, H., Liu, J., Lazar, A. J., Cancer Genome Atlas Research, N., Cherniack, A. D., Beroukhim, R., & Meyerson, M. (2018). Genomic and Functional Approaches to Understanding Cancer Aneuploidy. *Cancer Cell*, *33*(4), 676-689 e673. https://doi.org/10.1016/j.ccell.2018.03.007

Ter Brugge, P., Kristel, P., van der Burg, E., Boon, U., de Maaker, M., Lips, E., Mulder, L., de Ruiter, J., Moutinho, C., Gevensleben, H., Marangoni, E., Majewski, I., Jozwiak, K., Kloosterman, W., van Roosmalen, M., Duran, K., Hogervorst, F., Turner, N., Esteller, M., . . . Jonkers, J. (2016). Mechanisms of Therapy Resistance in Patient-Derived Xenograft Models of BRCA1-Deficient Breast Cancer. *J Natl Cancer Inst*, *108*(11). https://doi.org/10.1093/jnci/djw148

Thompson, D., Easton, D. F., & Breast Cancer Linkage, C. (2002). Cancer Incidence in BRCA1 mutation carriers. *J Natl Cancer Inst*, *94*(18), 1358-1365. https://doi.org/10.1093/jnci/94.18.1358

Tibbetts, R. S., Brumbaugh, K. M., Williams, J. M., Sarkaria, J. N., Cliby, W. A., Shieh, S. Y., Taya, Y., Prives, C., & Abraham, R. T. (1999). A role for ATR in the DNA damage-induced phosphorylation of p53. *Genes Dev.*, *13*(2), 152-157. https://doi.org/10.1101/gad.13.2.152

Tirkkonen, M., Johannsson, O., Agnarsson, B. A., Olsson, H., Ingvarsson, S., Karhu, R., Tanner, M., Isola, J., Barkardottir, R. B., Borg, A., & Kallioniemi, O. P. (1997). Distinct somatic genetic changes associated with tumor progression in carriers of BRCA1 and BRCA2 germ-line mutations. *Cancer Res*, *57*(7), 1222-1227. https://www.ncbi.nlm.nih.gov/pubmed/9102202

Tsubouchi, H., & Roeder, G. S. (2002). The Mnd1 protein forms a complex with hop2 to promote homologous chromosome pairing and meiotic double-strand break repair. *Mol Cell Biol*, *22*(9), 3078-3088. https://doi.org/10.1128/MCB.22.9.3078-3088.2002

Turner, N. C., Lord, C. J., Iorns, E., Brough, R., Swift, S., Elliott, R., Rayter, S., Tutt, A. N., & Ashworth, A. (2008). A synthetic lethal siRNA screen identifying genes mediating sensitivity to a PARP inhibitor. *EMBO J*, *27*(9), 1368-1377. https://doi.org/10.1038/emboj.2008.61

Tutt, A., & Ashworth, A. (2002). The relationship between the roles of BRCA genes in DNA repair and cancer predisposition. *Trends Mol Med*, *8*(12), 571-576. https://doi.org/10.1016/s1471-4914(02)02434-6

Tutt, A., Gabriel, A., Bertwistle, D., Connor, F., Paterson, H., Peacock, J., Ross, G., & Ashworth, A. (1999). Absence of Brca2 causes genome instability by chromosome breakage and loss associated with centrosome amplification. *Curr Biol*, *9*(19), 1107-1110. https://doi.org/10.1016/s0960-9822(99)80479-5

Tutt, A., Robson, M., Garber, J. E., Domchek, S. M., Audeh, M. W., Weitzel, J. N., Friedlander, M., Arun, B., Loman, N., Schmutzler, R. K., Wardley, A., Mitchell, G., Earl, H., Wickens, M., & Carmichael, J. (2010). Oral poly(ADP-ribose) polymerase inhibitor olaparib in patients with BRCA1 or BRCA2 mutations and advanced breast cancer: a proof-of-concept trial. *Lancet*, *376*(9737), 235-244. https://doi.org/10.1016/S0140-6736(10)60892-6

Tutt, A. N. J., Garber, J. E., Kaufman, B., Viale, G., Fumagalli, D., Rastogi, P., Gelber, R. D., de Azambuja, E., Fielding, A., Balmana, J., Domchek, S. M., Gelmon, K. A., Hollingsworth, S. J., Korde, L. A., Linderholm, B., Bandos, H., Senkus, E., Suga, J. M., Shao, Z., . . . Investigators. (2021). Adjuvant Olaparib for Patients with BRCA1- or BRCA2-Mutated Breast Cancer. *N Engl J Med*, *384*(25), 2394-2405. https://doi.org/10.1056/NEJMoa2105215

Tzelepis, K., Koike-Yusa, H., De Braekeleer, E., Li, Y., Metzakopian, E., Dovey, O. M., Mupo, A., Grinkevich, V., Li, M., Mazan, M., Gozdecka, M., Ohnishi, S., Cooper, J., Patel, M., McKerrell, T., Chen, B., Domingues, A. F., Gallipoli, P., Teichmann, S., . . . Yusa, K. (2016). A CRISPR Dropout Screen Identifies Genetic Vulnerabilities and Therapeutic Targets in Acute Myeloid Leukemia. *Cell Rep*, *17*(4), 1193-1205. https://doi.org/10.1016/j.celrep.2016.09.079

Vaitsiankova, A., Burdova, K., Sobol, M., Gautam, A., Benada, O., Hanzlikova, H., & Caldecott, K. W. (2022). PARP inhibition impedes the maturation of nascent DNA strands during DNA replication. *Nat Struct Mol Biol*, *29*(4), 329-338. https://doi.org/10.1038/s41594-022-00747-1

van Asperen, C. J., Brohet, R. M., Meijers-Heijboer, E. J., Hoogerbrugge, N., Verhoef, S., Vasen, H. F., Ausems, M. G., Menko, F. H., Gomez Garcia, E. B., Klijn, J. G., Hogervorst, F. B., van Houwelingen, J. C., van't Veer, L. J., Rookus, M. A., van Leeuwen, F. E., & Netherlands Collaborative Group on Hereditary Breast, C. (2005). Cancer risks in BRCA2 families: estimates for sites other than breast and ovary. *J Med Genet*, *42*(9), 711-719. https://doi.org/10.1136/jmg.2004.028829

van der Heijden, T., Seidel, R., Modesti, M., Kanaar, R., Wyman, C., & Dekker, C. (2007). Real-time assembly and disassembly of human RAD51 filaments on individual DNA molecules. *Nucleic Acids Res*, *35*(17), 5646-5657. https://doi.org/10.1093/nar/gkm629

van Wijk, L. M., Vermeulen, S., Meijers, M., van Diest, M. F., Ter Haar, N. T., de Jonge, M. M., Solleveld-Westerink, N., van Wezel, T., van Gent, D. C., Kroep, J. R., Bosse, T., Gaarenstroom, K. N., Vrieling, H., & Vreeswijk, M. P. G. (2020). The RECAP Test Rapidly and Reliably Identifies Homologous Recombination-Deficient Ovarian Carcinomas. *Cancers (Basel)*, *12*(10). https://doi.org/10.3390/cancers12102805

Verma, P., Zhou, Y., Cao, Z., Deraska, P. V., Deb, M., Arai, E., Li, W., Shao, Y., Puentes, L., Li, Y., Patankar, S., Mach, R. H., Faryabi, R. B., Shi, J., & Greenberg, R. A. (2021). ALC1 links chromatin accessibility to PARP inhibitor response in homologous recombination-deficient cells. *Nat Cell Biol*, *23*(2), 160-171. https://doi.org/10.1038/s41556-020-00624-3

Vujanovic, M., Krietsch, J., Raso, M. C., Terraneo, N., Zellweger, R., Schmid, J. A., Taglialatela, A., Huang, J. W., Holland, C. L., Zwicky, K., Herrador, R., Jacobs, H., Cortez, D., Ciccia, A., Penengo, L., & Lopes, M. (2017). Replication Fork Slowing and Reversal upon DNA Damage Require PCNA Polyubiquitination and ZRANB3 DNA Translocase Activity. *Mol Cell*, *67*(5), 882-890 e885. https://doi.org/10.1016/j.molcel.2017.08.010

Wang, J., Aroumougame, A., Lobrich, M., Li, Y., Chen, D., Chen, J., & Gong, Z. (2014). PTIP associates with Artemis to dictate DNA repair pathway choice. *Genes Dev*, *28*(24), 2693-2698. https://doi.org/10.1101/gad.252478.114

Wang, M., Wu, W., Wu, W., Rosidi, B., Zhang, L., Wang, H., & Iliakis, G. (2006). PARP-1 and Ku compete for repair of DNA double strand breaks by distinct NHEJ pathways. *Nucleic Acids Res*, *34*(21), 6170-6182. https://doi.org/10.1093/nar/gkl840

Wang, T. C., & Smith, K. C. (1986). Postreplication repair in ultraviolet-irradiated human fibroblasts: formation and repair of DNA double-strand breaks. *Carcinogenesis*, *7*(3), 389-392. https://doi.org/10.1093/carcin/7.3.389

Ward, J. F. (1988). DNA damage produced by ionizing radiation in mammalian cells: identities, mechanisms of formation, and reparability. *Prog Nucleic Acid Res Mol Biol*, *35*, 95-125. https://doi.org/10.1016/s0079-6603(08)60611-x

Watkins, J., Weekes, D., Shah, V., Gazinska, P., Joshi, S., Sidhu, B., Gillett, C., Pinder, S., Vanoli, F., Jasin, M., Mayrhofer, M., Isaksson, A., Cheang, M.

C., Mirza, H., Frankum, J., Lord, C. J., Ashworth, A., Vinayak, S., Ford, J. M., . . . Tutt, A. N. (2015). Genomic Complexity Profiling Reveals That HORMAD1 Overexpression Contributes to Homologous Recombination Deficiency in Triple-Negative Breast Cancers. *Cancer Discov*, *5*(5), 488-505. https://doi.org/10.1158/2159-8290.CD-14-1092

Weinfeld, M., Chaudhry, M. A., D'Amours, D., Pelletier, J. D., Poirier, G. G., Povirk, L. F., & Lees-Miller, S. P. (1997). Interaction of DNA-dependent protein kinase and poly(ADP-ribose) polymerase with radiation-induced DNA strand breaks. *Radiat Res*, *148*(1), 22-28. https://www.ncbi.nlm.nih.gov/pubmed/9216614

West, S. C., Blanco, M. G., Chan, Y. W., Matos, J., Sarbajna, S., & Wyatt, H. D. (2015). Resolution of Recombination Intermediates: Mechanisms and Regulation. *Cold Spring Harb Symp Quant Biol*, *80*, 103-109. https://doi.org/10.1101/sqb.2015.80.027649

Wielckens, K., Schmidt, A., George, E., Bredehorst, R., & Hilz, H. (1982). DNA fragmentation and NAD depletion. Their relation to the turnover of endogenous mono(ADP-ribosyl) and poly(ADP-ribosyl) proteins. *J Biol Chem*, *257*(21), 12872-12877. https://www.ncbi.nlm.nih.gov/pubmed/6813330

Winter, C., Nilsson, M. P., Olsson, E., George, A. M., Chen, Y., Kvist, A., Torngren, T., Vallon-Christersson, J., Hegardt, C., Hakkinen, J., Jonsson, G., Grabau, D., Malmberg, M., Kristoffersson, U., Rehn, M., Gruvberger-Saal, S. K., Larsson, C., Borg, A., Loman, N., & Saal, L. H. (2016). Targeted sequencing of BRCA1 and BRCA2 across a large unselected breast cancer cohort suggests that one-third of mutations are somatic. Ann Oncol, 27(8), 1532-1538. https://doi.org/10.1093/annonc/mdw209

Wooster, R., Bignell, G., Lancaster, J., Swift, S., Seal, S., Mangion, J., Collins, N., Gregory, S., Gumbs, C., & Micklem, G. (1995). Identification of the breast cancer susceptibility gene BRCA2. *Nature*, *378*(6559), 789-792. https://doi.org/10.1038/378789a0

Wu, L., & Hickson, I. D. (2002). The Bloom's syndrome helicase stimulates the activity of human topoisomerase IIIalpha. *Nucleic Acids Res*, *30*(22), 4823-4829. https://doi.org/10.1093/nar/gkf611

Wu, L., & Hickson, I. D. (2003). The Bloom's syndrome helicase suppresses crossing over during homologous recombination. *Nature*, *426*(6968), 870-874. https://doi.org/10.1038/nature02253

Wyatt, D. W., Feng, W., Conlin, M. P., Yousefzadeh, M. J., Roberts, S. A., Mieczkowski, P., Wood, R. D., Gupta, G. P., & Ramsden, D. A. (2016). Essential Roles for Polymerase theta-Mediated End Joining in the Repair of Chromosome Breaks. *Mol Cell*, *63*(4), 662-673. https://doi.org/10.1016/j.molcel.2016.06.020

Wyatt, H. D., Sarbajna, S., Matos, J., & West, S. C. (2013). Coordinated actions of SLX1-SLX4 and MUS81-EME1 for Holliday junction resolution in human cells. *Mol Cell*, *52*(2), 234-247. https://doi.org/10.1016/j.molcel.2013.08.035

Wyllie, A. H., Kerr, J. F., & Currie, A. R. (1980). Cell death: the significance of apoptosis. *Int Rev Cytol*, *68*, 251-306. https://doi.org/10.1016/s0074-7696(08)62312-8

Xia, B., Sheng, Q., Nakanishi, K., Ohashi, A., Wu, J., Christ, N., Liu, X., Jasin, M., Couch, F. J., & Livingston, D. M. (2006). Control of BRCA2 cellular and clinical functions by a nuclear partner, PALB2. *Mol. Cell*, *22*(6), 719-729. https://doi.org/10.1016/j.molcel.2006.05.022

Xiong, Y., Guo, Y., Liu, Y., Wang, H., Gong, W., Liu, Y., Wang, X., Gao, Y., Yu, F., Su, D., Wang, F., Zhu, Y., Zhao, Y., Wu, Y., Qin, Z., Sun, X., Ren, B., Jiang, B., Jin, W., . . . Jiang, B. (2020). Pamiparib is a potent and selective PARP inhibitor with unique potential for the treatment of brain tumor. *Neoplasia*, *22*(9), 431-440. https://doi.org/10.1016/j.neo.2020.06.009

Yang, H., Jeffrey, P. D., Miller, J., Kinnucan, E., Sun, Y., Thoma, N. H., Zheng, N., Chen, P.-L., Lee, W.-H., & Pavletich, N. P. (2002). BRCA2 function in DNA binding and recombination from a BRCA2-DSS1-ssDNA structure. *Science*, *297*(5588), 1837-1848. https://doi.org/10.1126/science.297.5588.1837

Yang, Z., Peng, M., Cheng, L., Jones, K., Maihle, N. J., Mivechi, N. F., & Ko, L. (2016). GT198 Expression Defines Mutant Tumor Stroma in Human Breast Cancer. *Am J Pathol*, *186*(5), 1340-1350. https://doi.org/10.1016/j.ajpath.2016.01.006

Yarden, R. I., Pardo-Reoyo, S., Sgagias, M., Cowan, K. H., & Brody, L. C. (2002). BRCA1 regulates the G2/M checkpoint by activating Chk1 kinase upon DNA damage. *Nat Genet*, *30*(3), 285-289. https://doi.org/10.1038/ng837

Yeganeh, P. N., Richardson, C., Bahrani-Mostafavi, Z., Tait, D. L., & Mostafavi, M. T. (2017). Dysregulation of AKT3 along with a small panel of mRNAs stratifies high-grade serous ovarian cancer from both normal epithelia and benign tumor tissues. *Genes Cancer*, *8*(11-12), 784-798. https://doi.org/10.18632/genesandcancer.164

Yu, V. P., Koehler, M., Steinlein, C., Schmid, M., Hanakahi, L. A., van Gool, A. J., West, S. C., & Venkitaraman, A. R. (2000). Gross chromosomal rearrangements and genetic exchange between nonhomologous chromosomes following BRCA2 inactivation. *Genes Dev*, *14*(11), 1400-1406. https://www.ncbi.nlm.nih.gov/pubmed/10837032

Yun, M. H., & Hiom, K. (2009). CtIP-BRCA1 modulates the choice of DNA double-strand-break repair pathway throughout the cell cycle. *Nature*, *459*(7245), 460-463. https://doi.org/10.1038/nature07955

Zack, T. I., Schumacher, S. E., Carter, S. L., Cherniack, A. D., Saksena, G., Tabak, B., Lawrence, M. S., Zhsng, C. Z., Wala, J., Mermel, C. H., Sougnez, C., Gabriel, S. B., Hernandez, B., Shen, H., Laird, P. W., Getz, G., Meyerson, M., & Beroukhim, R. (2013). Pan-cancer patterns of somatic copy number alteration. *Nat Genet*, *45*(10), 1134-1140. https://doi.org/10.1038/ng.2760

Zahradka, P., & Ebisuzaki, K. (1982). A shuttle mechanism for DNA-protein interactions. The regulation of poly(ADP-ribose) polymerase. *Eur J Biochem*, *127*(3), 579-585. https://www.ncbi.nlm.nih.gov/pubmed/6293817

Zatreanu, D., Robinson, H. M. R., Alkhatib, O., Boursier, M., Finch, H., Geo, L., Grande, D., Grinkevich, V., Heald, R. A., Langdon, S., Majithiya, J., McWhirter, C., Martin, N. M. B., Moore, S., Neves, J., Rajendra, E., Ranzani, M., Schaedler, T., Stockley, M., . . . Lord, C. J. (2021). Poltheta inhibitors elicit BRCA-gene synthetic lethality and target PARP inhibitor resistance. *Nat Commun*, *12*(1), 3636. https://doi.org/10.1038/s41467-021-23463-8

Zellweger, R., Dalcher, D., Mutreja, K., Berti, M., Schmid, J. A., Herrador, R., Vindigni, A., & Lopes, M. (2015). Rad51-mediated replication fork reversal is a global response to genotoxic treatments in human cells. *J Cell Biol*, *208*(5), 563-579. https://doi.org/10.1083/jcb.201406099

Zhao, W., Saro, D., Hammel, M., Kwon, Y., Xu, Y., Rambo, R. P., Williams, G. J., Chi, P., Lu, L., Pezza, R. J., Camerini-Otero, R. D., Tainer, J. A., Wang, H. W., & Sung, P. (2014). Mechanistic insights into the role of Hop2-Mnd1 in meiotic homologous DNA pairing. *Nucleic Acids Res*, *42*(2), 906-917. https://doi.org/10.1093/nar/gkt924

Zhao, W., Steinfeld, J. B., Liang, F., Chen, X., Maranon, D. G., Jian Ma, C., Kwon, Y., Rao, T., Wang, W., Sheng, C., Song, X., Deng, Y., Jimenez-Sainz, J., Lu, L., Jensen, R. B., Xiong, Y., Kupfer, G. M., Wiese, C., Greene, E. C., & Sung, P. (2017). BRCA1-BARD1 promotes RAD51-mediated homologous DNA pairing. *Nature*, *550*(7676), 360-365. https://doi.org/10.1038/nature24060

Zhao, W., & Sung, P. (2015). Significance of ligand interactions involving Hop2-Mnd1 and the RAD51 and DMC1 recombinases in homologous DNA repair and XX ovarian dysgenesis. *Nucleic Acids Res*, *43*(8), 4055-4066. https://doi.org/10.1093/nar/gkv259

Zhou, B. B., & Elledge, S. J. (2000). The DNA damage response: putting checkpoints in perspective. *Nature*, *408*(6811), 433-439. https://doi.org/10.1038/35044005

Zhu, Z., Chung, W.-H., Shim, E. Y., Lee, S. E., & Ira, G. (2008). Sgs1 helicase and two nucleases Dna2 and Exo1 resect DNA double-strand break ends. *Cell*, *134*(6), 981-994. https://doi.org/10.1016/j.cell.2008.08.037

Zickler, D., & Kleckner, N. (1999). Meiotic chromosomes: integrating structure and function. Annu Rev Genet, 33, 603-754. https://doi.org/10.1146/annurev.genet.33.1.603

Zimmermann, M., Murina, O., Reijns, M. A. M., Agathanggelou, A., Challis, R., Tarnauskaite, Z., Muir, M., Fluteau, A., Aregger, M., McEwan, A., Yuan, W., Clarke, M., Lambros, M. B., Paneesha, S., Moss, P., Chandrashekhar, M., Angers, S., Moffat, J., Brunton, V. G., . . . Durocher, D. (2018). CRISPR screens identify genomic ribonucleotides as a source of PARP-trapping lesions. *Nature*, *559*(7713), 285-289. https://doi.org/10.1038/s41586-018-0291-z

Zou, L., & Elledge, S. J. (2003). Sensing DNA damage through ATRIP recognition of RPA-ssDNA complexes. *Science*, *300*(5625), 1542-1548. https://doi.org/10.1126/science.1083430